
GAZİ ÜNİVERSİTESİ
Gazi
1926

POWDER BED SELECTIVE LASER MELTING/SINTERING OF HIGH-TECHNICAL CERAMIC MATERIALS

A THESIS SUBMITTED TO
THE GRADUATE SCHOOL OF NATURAL AND APPLIED SCIENCES
OF
GAZİ UNIVERSITY

BY

Mohamed EID SAIED ABDELMOULA

IN PARTIAL FULFILLMENT OF THE REQUIREMENTS
FOR
THE DEGREE OF DOCTOR OF PHILOSOPHY
IN
MECHANICAL ENGINEERING

OCTOBER 2022

ETHICAL STATEMENT

I hereby declare that in this thesis study I prepared in accordance with thesis writing rules of Gazi University Graduate School of Natural and Applied Sciences.

- All data, information and documents presented in this thesis have been obtained within the scope of academic rules and ethical conduct,
- All information, documents, assessments, and results have been presented in accordance with scientific ethical conduct and moral rules,
- All material used in this thesis that are not original to this work have been fully cited and referenced,
- No change has been made in the data used,
- The work presented in this thesis is original,

or else, I admit all loss of rights to be incurred against me.

Mohamed EID SAIED ABDELMOULA

13/10/2022

TEKNİK SERAMİK MALZEMELERİN TOZ YATAĞINDA SEÇİCİ LAZER ERGİTME/SİNTERLEMESİ

(Doktora Tezi)

Mohamed EID SAIED ABDELMOULA

GAZİ ÜNİVERSİTESİ

FEN BİLİMLERİ ENSTİTÜSÜ

Ekim 2022

ÖZET

Doğrudan Toz Yataklı Seçici Lazer İşleme (D-PBSLP), seramik malzemelerin Eklemeli İmalatı için gelecek vadeden bir teknik olarak kabul edilir. Seramik malzemelerin D-PBSLP'sinde başarılı olmak için proses parametrelerine uygun değerlerin kullanılması gerekmektedir. Seramik malzemelerin başarılı D-PBSLP'si için uygun proses parametrelerini elde etmek ve deneysel araştırma boyunca bir kılavuz olarak kullanılmak üzere sayısal bir model geliştirilmiştir. Bu çalışmada model malzeme olarak alümina ve SiC kullanılmıştır. Farklı yapı yönelimleri ile çok katmanlı taramanın PBSLP araştırmasında geliştirilen sayısal modelin kullanılması, yapı yönelimi ve tarama stratejilerinin, basılı numunelerin gelişmiş termal stresini ve çatlamasını kontrol etmek için gerekli olduğunu ortaya koymaktadır. D-PBSLP alümina için, doğrusal 45° tarama stratejisi, araştırılan diğer tarama stratejilerine kıyasla en umut verici sonuçları vermiştir. Ayrıca, 400 mm/s'lik yüksek bir tarama hızı kullanıldığında, 100, 200 ve 300 mm/s'ye kıyasla %85'lik yüksek bir bağıl yoğunluk ölçülmesiyle yüksek kalitede alümina numuneleri basmak mümkün olduğu kanaatine varılmıştır. Sayısal modelin öngördüğü optimal tarama stratejileri, tarama hızı ve diğer parametre değerleri belirlendikten sonra, süreç parametreleri Taguchi optimizasyon yöntemi ve Paetro ANOVA analizi kullanılarak optimize edildi. 210 W lazer gücü, 400 mm/sn tarama hızı ve 30 µm tarama alanı %94,5 yüksek yoğunluklu alümina numunelerinin yazdırılması için en uygun proses parametresi olduğu anlaşılmıştır. Bası testi ve mikrosertlik ölçümü kullanılarak mekanik performans değerlendirildi. Test edilen numuneler, literatürde bildirilen değerle aynı olan 2180 HV'lik bir mikrosertlik değeri vermiştir. Buna karşılık, elde edilen bası dayanımı, literatürde bildirilen değerlerle karşılaştırıldığında en düşük olan yaklaşık 140 MPa'dır. Tarama stratejileri araştırıldığında ve incelenen diğer tarama stratejilerinin kıyaslandığında SiC'nin D-PBSLP'si için eğimli zikzak tarama stratejisinin önerildiği sonucuna varıldı. Daha sonra farklı katman kalınlıkları 22, 30 ve 40 µm ile 100, 250 ve 500 mm/s gibi farklı değerler dikkate alınarak tarama hızı incelenmiştir. Düşük tarama hızları ve 22 ve 30 µm gibi düşük katman kalınlıkları kullanılarak, sonuçların gösterdiği gibi, SiC numunelerini %85 kısmi yoğunluğa sahip başarılı bir şekilde basmak mümkün olmuştur. Numunlerde %87'lik bir nispi yoğunluğa ulaşmak, 45W'lık bir lazer gücü, 100 mm/sn'lik bir tarama hızı ve 40 µm'lik bir tarama alanı ile sonuçlanan proses parametrelerinin optimizasyonunu ile elde edilmiştir. Mekanik performans, 1,4 MPa'lık düşük bir bası dayanımına sahip olduğu değerlendirildi. Sonuç olarak, mekanik performansı artırmak için ikincil işlemler kullanılması önerilmektedir.

Bilim Kodu	:	91438
Anahtar Kelimeler	:	Eklemeli imalat, seramik, numerik analiz, lazer
Sayfa Adedi	:	254
Danışman	:	Doç. Dr. Gökhan KÜÇÜKTÜRK

POWDER BED SELECTIVE LASER MELTING/SINTERING OF HIGH-TECHNICAL CERAMIC MATERIALS

(Ph. D. Thesis)

Mohamed EID SAIED ABDELMOULA

GAZİ UNIVERSITY

GRADUATE SCHOOL OF NATURAL AND APPLIED SCIENCES

October 2022

ABSTRACT

Direct-Powder Bed Selective Laser Processing (D-PBSLP) is considered a promising technique for Additive Manufacturing (AM) of Ceramic materials. To be successful in the D-PBSLP of ceramic materials, it is necessary to use the proper values for the process parameters. A numerical model has been developed to obtain the proper process parameters for successful D-PBSLP of ceramic materials to be used as a guide through the experimental investigation. Alumina and SiC were used as model materials in this study. Using the developed numerical model in the PBSLP investigation of multi-layer scanning with different build orientations reveals that the build orientation and scanning strategies are essential for controlling the printed samples' developed thermal stress and cracking. For D-PBSLP alumina, the Linear 45° scanning strategy produced the most promising results compared to other investigated scanning strategies. In addition, by using a high scanning speed of 400 mm/s, it was possible to print alumina samples of high quality, as measured by a high relative density of 85 %, compared to 100, 200, and 300 mm/s. After determining the optimal scanning strategies, scanning speed, and other parameter values as predicted by the numerical mode, the process parameters were optimized using the Taguchi optimization method and Paetro ANOVA analysis. Laser power of 210 W, scanning speed of 400 mm/s, and hatching space of 30 µm were the optimal process parameter settings for printing alumina samples with a high density of 94.5 %. Utilizing the compressive test and microhardness measurement, the mechanical performance was evaluated. The tested samples yielded a microhardness value of 2180 HV, identical to the value reported in the literature. In contrast, the obtained compressive strength was approximately 140 MPa, which is low compared to the values reported in the literature. The same procedure was followed while investigating D-PBSLP of SiC. The scanning strategies investigation concluded that the inclined zigzag scanning strategy is recommended for D-PBSLP of SiC, as it overcomes nearly all of the obstacles encountered by the other investigated scanning strategies. Then the scanning speed considering different values such as 100, 250, and 500 mm/s with different layer thicknesses of 22, 30, and 40 µm. Using low scanning speeds and low layer thicknesses, such as 22 and 30 µm, it was possible to successfully print SiC samples with a relative density of 85 %, as demonstrated by the results. Attaining a relative density of 87 % required optimization of the process parameters, resulting in a laser power of 45W, a scanning speed of 100 mm/s, and a hatching space of 40 µm. The mechanical performance was evaluated using a compressive test, which revealed a low compressive strength of 1.4 MPa; consequently, postprocessing should be considered to enhance the mechanical performance.

Science Code : 91438
Key Words : Additive manufacturing, ceramics, numerical analysis, laser
Page Number : 254
Supervisor : Assoc. Prof. Dr. Gökhan KÜÇÜKTÜRK

ACKNOWLEDGMENT

After a long and incredible journey, I was able to complete the research for this dissertation. This task was difficult and fraught with challenges. I am filled with thoughtfulness and the desire to perform high-quality work. Ultimately. I could say that I have attained my objectives and am completely satisfied with my accomplishments.

I did not accomplish this work alone, but numerous individuals supported me on this Journey. My most heartfelt gratitude and appreciation are extended to my supervisor, Assoc. Prof. Dr. Gökhan KÜÇÜKTÜRK gave me the opportunity to be a part of the DOC 3D PRINTING team and provided me with invaluable guidance throughout my dissertation.

Many thanks and great appreciation to Dr. David GROSSIN for his unwavering support and guidance throughout this study, as well as his invaluable assistance in completing the majority of the work contained in this dissertation.

Meanwhile, tremendous and unlimited Thanks are also extended to Dr. Fabrice PETIT and Dr. Enrique JUSTE. It was a great honour for me to work with them, as their experience and intelligence greatly enriched me. In addition, they provided substantial assistance in completing this dissertation's work.

My most appreciation and gratitude are also extended to Guillaume Gentil, who contributed significantly to the success of this project. Without his assistance, I would be unable to complete a significant portion of this work.

In the meantime, I must express my gratitude to Duran KAYA, the project officer at “Gazi University”, for his unwavering support and assistance throughout my time in Turkey.

In addition, I owe a debt of gratitude to my family in Egypt, including my father’s spirit, my mother, my wife, and my brothers, for their tremendous support during the difficult times the world was experiencing during the fight against COVID-19.

Lastly, I would like to extend a special thank you to all of my DOC 3D PRINTING project colleagues who contributed to enriching both the scientific and social moments.

CONTENTS

Page

Page

Page

Page

Page

LIST OF TABLES

Table **Page**

Table **Page**

Table **Page**

LIST OF FIGURES

Figure **Page**

Figure **Page**

Figure **Page**

Figure **Page**

Figure **Page**

Figure **Page**

Figure **Page**

Figure **Page**

Figure **Page**

Figure **Page**

Figure **Page**

1. INTRODUCTION

Ceramics are regarded as one of the most important classes of materials due to their robust physical and mechanical properties, which make them highly desirable in advanced markets such as aerospace, defence, automotive, and medicine. Due to the recent manufacturing revolution and the emergence of Industry 4.0, conventional manufacturing techniques of ceramic materials are unable to respond to the changing demands, which include the manufacturing of immensely complicated designs. Consequently, it became necessary to investigate the processing of ceramic materials using alternative techniques, such as Additive Manufacturing (AM).

The successful application of AM to ceramic materials processing will accelerate the growth of numerous industries to a high level of sophistication as it will enable the design of objects with an infinite degree of complexity. Even though AM has reached a highly advanced level in other material classes, such as polymers and metals, there are still several obstacles to its effective application in ceramics, despite the enormous benefits that can be realized through this application.

In this scope, the Development Of Ceramics 3D-Printing, Additive Manufacturing (DOC-3D PRINTING) project (https://cordis.europa.eu/project/id/764935), funded by the European Commission through the Marie Sklodowska-Curie Actions (grant number 764935), aimed to develop the AM of ceramics materials by investigating the most appropriate AM techniques. These include binder jetting (BJ), powder bed fusion (PBF), robocasting, stereolithography (SLA) and direct energy deposition (DED). DOC-3D PRINTING encompasses all facets of AM of ceramics, including the production of feedstocks, the development of novel processes/technologies, and the evaluation of commercialized products. Fourteen early-stage researchers (ESRs) are working on five packages, including materials feedstock, process equipment, design products, testing standards, modelling, and characterization. The entire group comprises six academic, one non-profit, and seven non-academic partners with varied experiences.

This dissertation focuses on the process parameters for high technical ceramic materials using the PBF technique, specifically the direct-PBF (D-PBF). D-PBF is regarded as the

most promising technique for ceramics AM because it can process ceramic materials without requiring any powder preparation or post-processing techniques such as drying, debinding, and sintering. This primarily represents the nominal goal of "one-step ceramic AM" that nearly all researchers in the field of ceramic AM seek to achieve. In addition, D-PBF is ideally suited for manufacturing ceramic materials for diverse applications, such as structural and thermally resistant components.

PBF merely employs a laser beam to scan an entire powder bed, layer by layer, until the part is finished. Despite its simplicity, the application of the PBF technique currently faces various challenges. One of these challenges is the high melting/sintering point of ceramics, which necessitates using lasers with a high energy density and results in thermal shocks that cause material cracking. Another challenge is that the accumulation of heat within the printed object is a further issue, as it causes the scanning temperature to rise well above ceramic materials' boiling or decomposition point. The absorptivity of ceramic materials to the employed laser depends on the laser's wavelength; therefore, the absorptivity should be altered in some instances. In addition, selecting appropriate process parameters is regarded as one of the most significant obstacles to the PBF success of ceramics. Also, a particular baseplate is needed to ensure the adhesion of the first printed layers. Ultimately, the obtained density and mechanical properties of the 3D-printed parts are still far outside the norm.

Numerous studies have been conducted to overcome the challenges mentioned above. Most of these studies attempted to modify the feedstock by combining it with another material acting as a binder. However, they continue to use a long-winded manufacturing process that includes feedstock preparation and post-processing, such as drying, debinding and sintering to achieve the desired final shape. In addition, they were confronted with the shrinkage issue in the printed part dimensions, which is regarded as the most significant barrier for other AM techniques, and the need to perform additional processes to increase the final density, such as the infiltration process.

The research focus on D-PBF of ceramics is deemed low, and only a few studies have investigated this technique from various perspectives. By developing a preheating system, some research has focused on reducing the temperature gradient that occurs during the PBF of ceramics. Other studies focused on improving powder absorptivity to be suitable for the currently available PBF printers, which are equipped with Nd-Yag or fibre lasers that are

unsuitable for oxides ceramics. The remaining studies attempted D-PBF of a few ceramic materials but did not investigate the process in detail.

By reviewing the state of the art regarding D-PBF of ceramics as described in chapter 2, it was determined that despite the numerous advantages of this technology, three main limitations hinder the effective application of direct-PBF to ceramic materials. The first and most significant limitation is the printing itself, i.e., obtaining a ceramic shape with as much defined shape as possible. As evidenced by the literature, many studies have only reported the printing of a few layers and not an entire part. The second limitation is the low relative density for ceramic parts printed with D-PBF, where the density ranges from 50 to 75 % of the relative density, and this is a severe issue as it affects the mechanical properties. The third limitation is the thermal shock of the material, which causes high thermal stress and cracking.

This dissertation presents new findings to overcome the limitations mentioned above: successful printing, low relative density, and the reduction of thermal shocks and cracks. This was accomplished primarily by comprehensively examining the process parameters, including laser power, scanning speed, hatching distance, layer thickness, and scanning strategies. Due to the lack of systematic and comprehensive studies addressing the topic, direct-PBF is considered to be a very complex task; therefore, it was necessary to develop a tool to guide the research progress; this was achieved by developing a numerical simulation model throughout this dissertation. The numerical model can simulate the D-PBF process for any ceramic material and provide a thorough understanding of the effect of each process parameter.

Aluminum Oxide (Alumina) and Silicon Carbide (SiC), both of which are highly technical ceramics, were investigated in this dissertation. SiC D-PBF was conducted at CIRIMAT (Université de Toulouse, France), while Alumina D-PBF was conducted at the Belgian Ceramic Research Center (BCRC). The influence of process parameters on each material was studied in depth, resulting in identifying the optimal set of process parameters for each material, capable of significantly overcoming the previously described limitations.

Using the methodology outlined in this dissertation, ceramic parts with a density of 95 % for alumina and 90 % for SiC were manufactured without any post-processing techniques. The

level of cracks was significantly reduced and controlled. In addition, complex designs could be printed thanks to the optimization of process parameters efficiently. Focusing on producing a more suitable ceramic powder for the D-PBF technique could result in a further increase in density and should be considered in a future study.

Importance of research

Ceramics Materials are a very important class of materials that are employed in a variety of high-tech applications, including defence, medical, and aerospace. Using conventional techniques to process ceramics is a time-consuming and costly process. In addition, these approaches have limitations when it comes to high-complexity, multi-faceted designs. Additive Manufacturing (AM) of Ceramics can not only overcome the limitations of conventional manufacturing techniques, but also offer numerous other advantages. Different AM techniques, such as binder jetting, extrusion, fused deposition modelling, and powder bed selective laser processing (PBSLP), can be used to manufacture ceramics (PBSLP). PBSLP is the only additive manufacturing technique that can enable AM of ceramics in a single step, as opposed to other processes (binder jetting, extrusion, fused deposition modelling) that require feedstock preparation and postprocessing to produce the final shape. However, the application of PBSLP in ceramics meets numerous problems, such as the high melting point of ceramics, the development of thermal stress and cracking, and laser absorption. The significance of this research is to overcome the previously mentioned challenges and outline a clear path for applying the PBSLP to ceramics. The success of PBSLP in the AM of ceramics would greatly advance the AM of ceramics and eliminate the requirement for numerous processes currently utilized in the AM of ceramics and this was achieved by investigating the PBSLP from every conceivable angle in order to eliminate any obstacles to its practical application in the AM of ceramics.

2. LITERATURE REVIEW

This chapter provides an overview of ceramic materials, Additive Manufacturing (AM), and their applications. In addition, it offers a comprehensive introduction to the AM techniques, Direct-Powder Bed Fusion (D-PBF), utilized throughout this dissertation. This chapter discusses the primary materials studied in this dissertation, Aluminum Oxide (Alumina) and Silicon Carbide (SiC), as well as prior research on the application of D-PBF to these materials.

2.1. Ceramics

Ceramics are a class of materials that are neither metallic nor organic; they can be crystalline, glassy, or both; and they are renowned for being extremely hard and nonreactive. Due to their unique material properties, ceramics are precious in high-value markets such as the aerospace and medical industries. In addition to dishes, bricks, and glass, ceramics can also be found in the form of human bones and teeth. Ceramics are used as semiconductors and insulators in electronics, as well as spark plugs, brakes, and self-lubricating bearings in automobiles.

Typically, ceramic materials are categorized based on their applications or chemical compositions [1]. Based on their intended use, ceramics can be categorized as either traditional or advanced (high technical). Advanced ceramics include alumina, zirconia, silicon carbide, silicon nitride, and other substances. Ceramics can be categorized into distinct material group sets, such as oxides ceramics, carbide ceramics, and nitride ceramics, based on their composition. Advanced ceramics have superior properties to other materials, including low weight, high hardness, high modulus of elasticity, excellent dimensional, chemical, and thermal stability, and high wear and corrosion resistance [2]. These properties made advanced ceramics superior candidates for various highly advanced applications.

Ceramics can be shaped using conventional techniques such as tape casting, pressing, and extrusion [2–7]. These techniques form the feedstock material by blending the ceramic powder with solvents and organic compounds. The shape is achieved following drying, debinding, and sintering[8]. The lengthy manufacturing route (preparing the feedstock,

processing, drying, and sintering), dimension shrinkage, co-sintering issues, and limited complexity represent the most significant challenges for these techniques.

AM technology can not only overcome the obstacles mentioned earlier, but it can also significantly improve ceramics manufacturing by providing a short and rapid manufacturing cycle and the flexibility to manufacture highly complex designs with increased reliability [9]. Moreover, AM can ensure the homogeneity of structures because it allows for more efficient material mixing.

2.2. Additive Manufacturing

2.2.1. Introduction

AM is a rapidly growing manufacturing approach that offers many advantages, including flexibility and complexity. AM is defined by ISO/ASTM 52900 [10] as "the process of joining materials to make parts from 3D model data, typically layer by layer, as opposed to subtractive and formative manufacturing techniques." Charles Hull introduced AM in 1983 using a technique known as stereolithography (SLA) [11]. Other techniques were subsequently developed based on different physical or chemical principles of various materials. In recent years, AM technologies have developed significantly and are now widely utilized in various research and industries. To obtain the 3D shape from the 3D model, the AM comprises the following steps: 1) Creating the 3D file, 2) slicing the 3D file into multiple layers, and 3) fabricating the component layer by layer [12, 13]. Figure 2.1 depicts these steps.

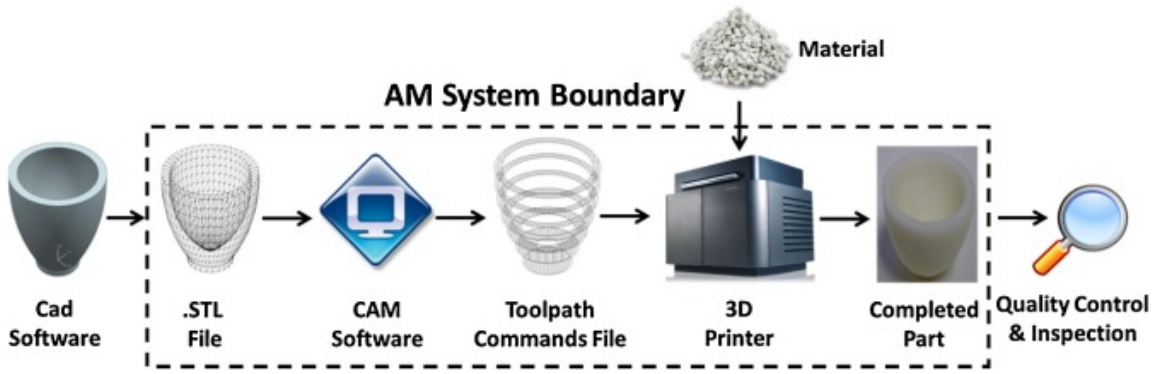

Figure 2.1. The AM process steps, from the 3D model to the final 3D part [13].

AM has demonstrated its efficacy as a highly advanced technology due to the enormous benefits it can provide [14, 15]. These benefits include design flexibility, rapid prototyping, a short manufacturing route, and cost-effectiveness, and it allowed AM to rapidly invade numerous high-tech industries, including aerospace, defence, automotive, and biomedical. Moreover, AM has enabled many industries to manufacture their needs domestically rather than relying on a third party. AM has supported the proliferation of home-based manufacturing for prototyping and other purposes and allowed manufacturing companies to have their products designed online by the customer, who chooses the product's shape and dimensions and initiates production. It can be concluded that AM altered the traditional conception of design and manufacturing. Currently, numerous companies manufacture AM printers ranging from desktop to industrial size. 3D Systems (US), Lithoz (Austria), Admatec (Netherlands), 3D-Ceram (France), Electro-Optical Systems EOS (Germany), and General Electrical (US) are the most well-known companies.

Despite the immense and unquantifiable benefits AM provides, it still faces numerous limitations that impede its tremendous progress [16, 17]. Porosities formation within the material, anisotropic properties, crack formations, and shrinkage in dimensions for certain materials, a large window of process parameters that should be optimized for each material, a restricted build size, high equipment costs, post-processing requirements, and high cost of powder preparation for certain high-advanced materials that require expensive techniques, are some of these limitations. In addition, additive manufacturing is still inefficient for mass production compared to other conventional techniques. Enhancing the reliability of AM by focusing on the raw materials to ensure their efficiency and performance stability over time (and production batches) is also a crucial requirement. Another significant limitation is the selection of AM techniques, which largely depends on the technical requirements and the needed mechanical and physical properties. The following section provides an overview of each AM technique, including its applications, suitable materials, benefits, and limitations.

2.2.2. AM classification

As depicted in Figure 2.2, the ISO/ASTM 52900 standard [10] identifies seven techniques for additive manufacturing, including material jetting (MJ), vat-polymerization, binder jetting (BJ), fused deposition modeling (FDM), direct energy deposition (DED), sheet lamination, and powder bed fusion.

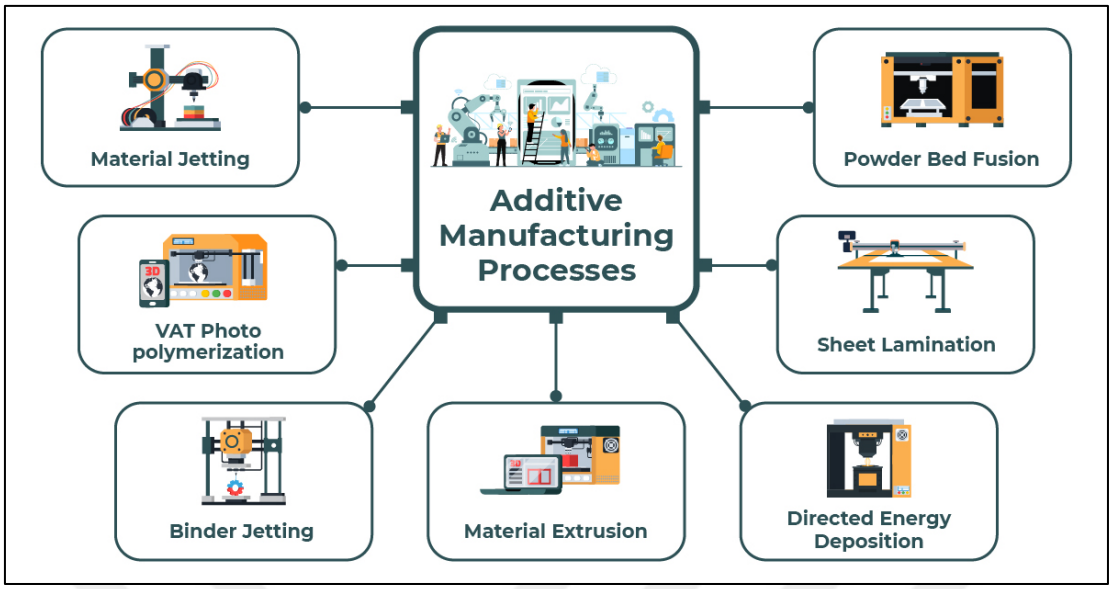

Figure 2.2. AM techniques as defined by ISO/ASTM 52900 [18].

Numerous previous researchers have described a variety of classification criteria for AM techniques. One of these criteria is the starting material or feedstock used for printing, by which AM techniques are categorized as liquid-based, filament/paste-based, powder-based, and solid-sheet-based [19]. Figure 2.3 illustrates the classification of additive manufacturing techniques according to the feedstock material.

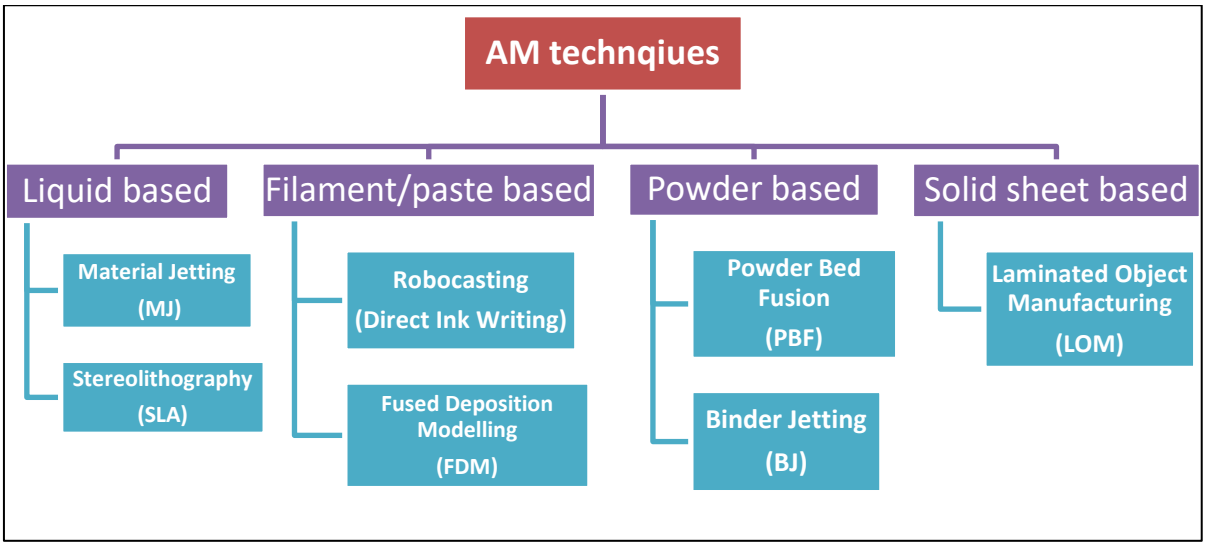

Figure 2.3. AM classification based on the feedstock material [13].

Moreover, and based on additional criteria, AM techniques can be divided into single-step and multi-step AM techniques [20], with the single step implying that the final shape can be used directly after the printing process and the multi-step requiring additional post-

processing steps. Nevertheless, this classification depends on the initial feedstock. The final shape does not require postprocessing when the PBF technique prints metallic powder. However, when the PBF is used to print ceramic powder mixed with another binding material, the final shape requires postprocessing (drying, debinding, and sintering).

Therefore, the feedstock material should be specified when classifying AM techniques according to the number of steps. In addition, AM techniques can be subdivided into direct and indirect techniques, similar to the classification based on the number of steps. Indirect refers to the use of two or more materials as AM feedstock. In the case of printing ceramic materials using PBF techniques, for example, researchers combined the ceramic powder with another binding material to prevent thermal shocks and cracks. This mixing primarily intends to overcome obstacles associated with the base material's printability. Additional post-treatments, such as drying, debinding, and sintering, are required to achieve the final shape. Therefore, the classification of AM techniques as either direct or indirect techniques should also specify the feedstock. In this scope, Zocca et al. [21] proposed an additional classification of AM techniques for ceramic materials based on the feedstock (solid or liquid), part size, surface quality, precision, feedstock cost, process cost, and level of densification.

The classification of AM into direct and indirect techniques was considered in this dissertation, and because the focus of this dissertation was on printing ceramic materials without the addition of any other material to act as a binder using a laser source, the direct-PBF (D-PBF) technique was regarded to be the AM technique used in this dissertation.

In addition, PBF can be classified into three distinct techniques, Selective Laser Melting (SLM), Selective Laser Sintering (SLS), and Electron Beam Melting (EBM) [22]. It became necessary to specify which technique should be used. EBM cannot be used with ceramics because it relies on an electron beam, and ceramics have a low electrical conductivity. However, both SLS and SLM are capable of printing ceramics. SLM can be used with ceramic materials with a melting phase, such as alumina, whereas SLS can be used with materials that do not melt, such as SiC. In order to avoid confusion, this dissertation refers to SLM and SLS by the term Direct-Powder Bed Selective Laser Processing (D-PBSLP).

2.2.3. AM of ceramic materials

Several AM techniques, including BJ, FDM, SLA, PBSLP, and robocasting (Direct ink writing), can be utilized for the AM of ceramics. These techniques have their advantages and disadvantages when applied to the AM of ceramics, and only certain ceramic materials can be manufactured using a specific technique based on their specifications. In addition, the characteristics of the employed technique determine the properties of printed parts. The subsequent sections provide an overview of each technique.

Binder jetting

Binder Jetting (BJ) was developed in 1993 at the Massachusetts Institute of Technology [23] as a powder-based additive manufacturing (AM) technique that creates three-dimensional objects by selectively depositing a binder layer-by-layer onto a powder bed. Due to the powdered nature of Binder's feedstock, BJ can process a wide range of commercial materials, including metals, ceramics, and biomaterials. Several postprocessing operations, such as debinding and sintering, are required to obtain the final shape [24] after manufacturing a "green body." Figure 2.4 depicts a diagrammatic illustration of the BJ technique.

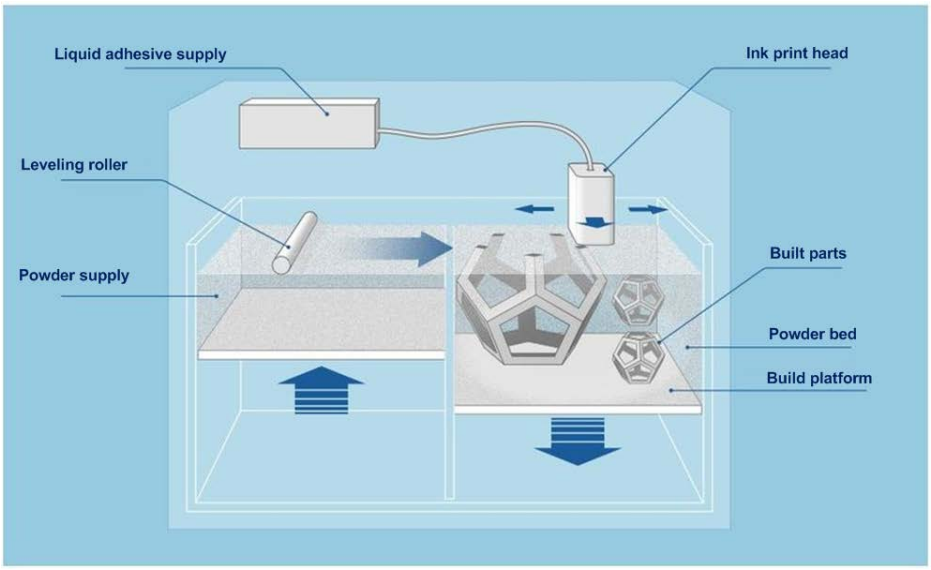

Figure 2.4. Binder jetting technique [24].

BJ is widely used in the AM of ceramics, and numerous studies [25–28] have reported the AM of various ceramic materials using the BJ technique. This is primarily due to BJ's

capacity to process various ceramic materials with larger scale and more intricate designs than possible with conventional techniques. Figure 2.5 depicts alumina ceramic components manufactured using the BJ technique.

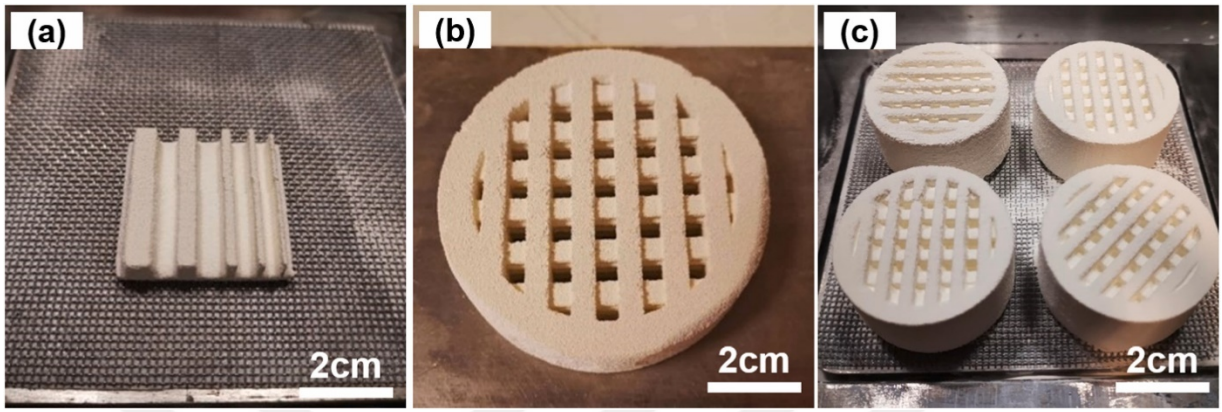

Figure 2.5. Printed green body of different complex shape parts: (a): Benchmark; (b): Large size scaffold; (c): Small size scaffolds [29].

It is unnecessary to perform powder preparation to obtain suitable feedstock for BJ; however, good powder bed and packing properties are required.

BJ has many advantages, such as the ability to fabricate ceramics on a macro scale, which is exceedingly difficult with conventional techniques due to their brittle and hard nature, mainly when producing complex geometries [25]. In addition, it is compatible with nearly any powdered feedstock and can incorporate functionally graded materials. BJ systems also have a relatively high build rate compared to other printing processes, such as MJ, because they only need to print a portion of the part's total volume's binder [30]. However, these advantages do not come without a price; the BJ technique faces obstacles and has limitations. One of these constraints is the requirement for post-processing. As BJ creates a component of powder particles bonded together with a binder, this is commonly referred to as a "green" part, which requires post-processing to acquire its final properties. Figure 2.6 illustrates the BJ-produced green body and the final sintered shape.

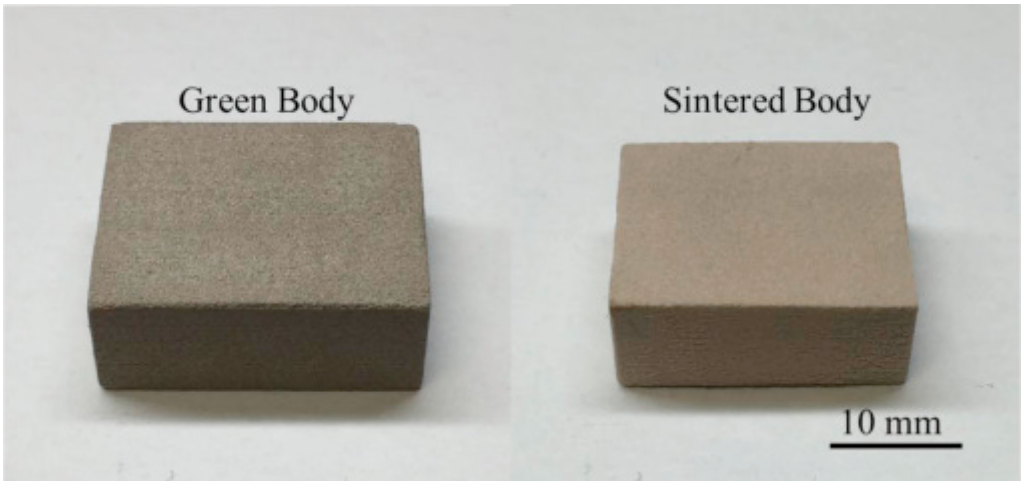

Figure 2.6. Green body and final sintered body manufactured using BJ technique [25].

In addition, the final properties depend on numerous process parameters, such as the raw material, powder bed formation, build parameters, and post-processing techniques [30]. In order to print ceramic components with desirable final properties, a number of factors should be precisely handled. In addition, the final properties determine the application space for BJ components.

Fused deposition modeling

Fused deposition modeling (FDM) was developed by Stratasys Inc. (US) in the 1990s [31, 32] and is widely used by numerous industries that rely on AM technology for prototyping in a variety of thermoplastics. This is primarily attributable to FDM's ability to produce complex geometries with various materials.

FDM is currently utilized extensively for modeling, prototyping, and manufacturing applications. By modifying the feedstock, FDM can be used to process a variety of polymers, ceramics, and metals [33–35]. Figure 1.7 depicts a schematic representation of FDM technology, in which the material is melted into a liquid state in a liquefier head and then selectively deposited on the printer bed via a nozzle to create 3D objects directly from a CAD model, layer by layer.

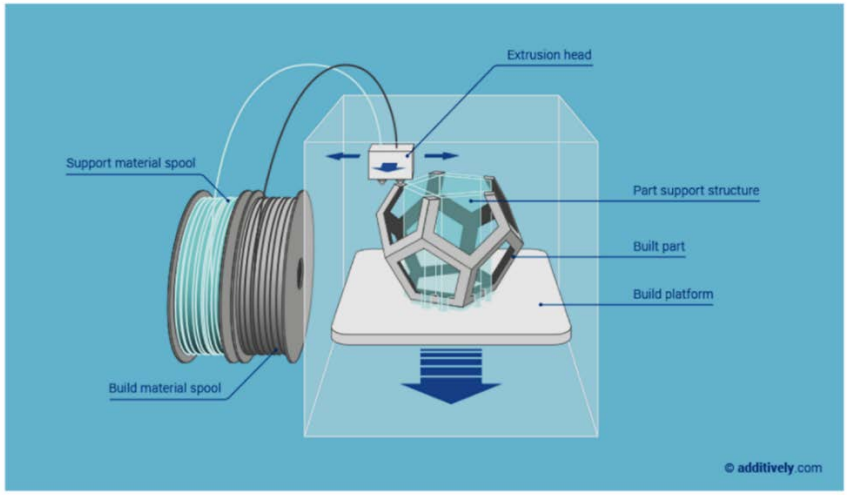

Figure 2.7. FDM technique [33].

FDM is used in the AM of ceramics by using polymeric filaments containing ceramic powders as a feedstock, as shown in Figure 2.8. Many ceramic materials can be printed using FDM, such as alumina, zirconia and SiC [34, 35]. Figure 2.8 shows typical alumina ceramic printed using the FDM [36].

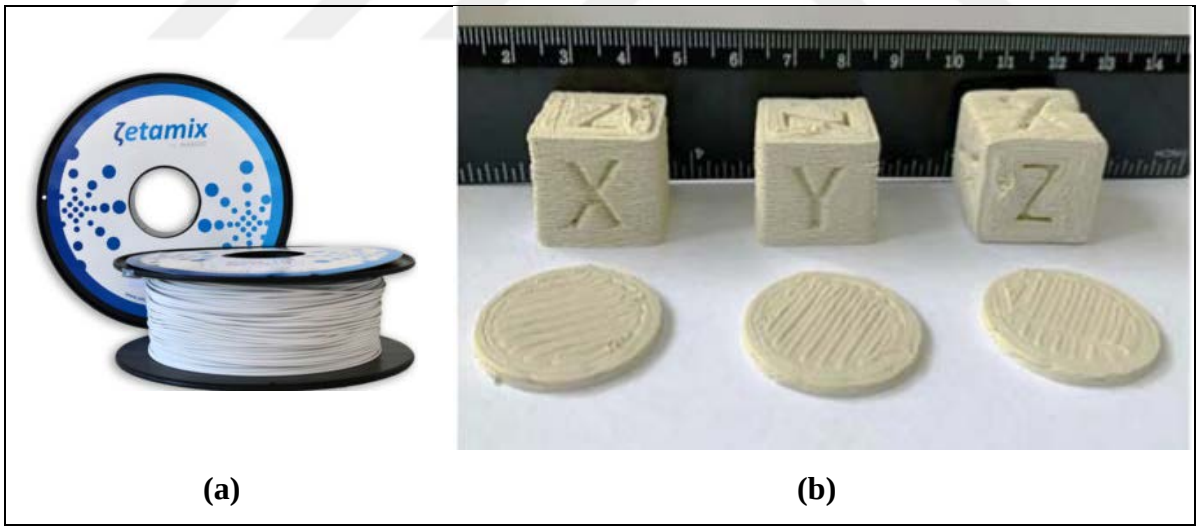

Figure 2.8. Alumina filament from zetamix [37] (a); Printed alumina samples using the FDM technique [36] (b).

The ceramic AM through the FDM technique is considered liquid-based and, therefore, can avoid the issues arising with ceramic powders. Additionally, it provides better shaping ability enabled by the soluble and cross-linkable precursors [34, 35, 38, 39]. This process's solidification upon deposition characteristic is a significant advantage that significantly reduces the drying process's need [40]. However, there are still many limitations to this

technique. One of these limitations is the feedstock preparation which is considered a complex process. The ceramic material content inside the filament should be less than 30% because higher ceramic content increases the brittleness of the composite and reduces mechanical performance. Additionally, the ceramic powder particle size should be controlled not to close the nozzle during deposition [41]. The low printing resolution, staircase effect and inherent anisotropy of the printed parts, caused by the filament-based layer-by-layer printing process, are also severe limitations [34].

As the case with BJ, the final properties of ceramic parts printed with FDM depend on the filament build parameters and post-processing methods, and they should be optimized for obtaining ceramic parts with good final properties.

Robocasting (Direct ink writing)

Robocasting or Direct ink writing (DIW) is a procedure that arose two decades ago [42] as a separate AM technique. Green 3D objects are created in a way similar to the FDM of ceramics by extruding a filament of paste (known as "ink") through a fine nozzle while a computer controls the position of the nozzle following a CAD model. In contrast to fused deposition, robocasting relies on rheology rather than solidification to print self-supporting components. Figure 2.9 depicts the robocasting method.

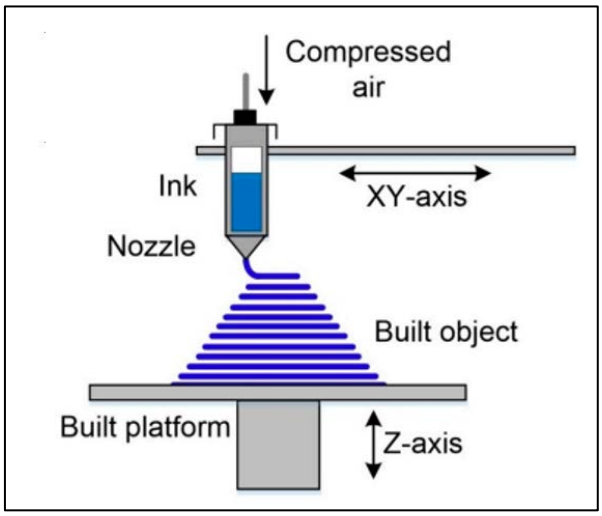

Figure 2.9. Schematic representation of the robocasting technique [43].

The real advantage of robocasting resides in the technique's ability to print various materials, including metals, composites, ceramics, biomaterials, and shape memory alloys [44–48]. Figure 2.10 displays ceramic components that were printed via robocasting.

For additive manufacturing of ceramic materials employing robocasting, the ink's qualities and composition are crucial considerations. Inks must be homogeneous, devoid of air bubbles, contain a high-volume proportion of ceramic powder, and possess the required flow properties for extrusion while retaining their shape after printing. Additionally, the ink must be very shear-thinning and self-supporting during printing to be extruded via nozzles. Various methods, such as pastes with a very high solids loading [42], have been investigated to meet each of these conditions.

(a) **(b)**

Figure 2.10. Ceramic parts printed using the robocasting technique, Scaffolds for human mandibular defect reconstruction, as sintered: (a); Boron carbide: (b) [49].

AM of ceramics using robocasting provides numerous benefits, including the versatility to be used with various materials. In addition, functionally graded components with complicated, smooth compositional gradients have been printed in a manner that has not been replicated by any other approach [50, 51]. Due to the layer-by-layer nature of robocasting, parts will always have stepped edges, and supports must be produced to enable significant overhangs or massive spanning portions [52]. In addition, post-treatment is required to eliminate the binder and join the ceramic particles.

Stereolithography

Stereolithography (SLA) is a liquid-based additive manufacturing (AM) process that was introduced in the late 1980s and created by 3D Systems in 1986; it was the first commercially

available solid free-form technique [53]. SLA utilizes photocurable resin containing photopolymerizable monomers as its feedstock. These resin layers solidify when exposed to light or a laser, allowing a 3D item to be constructed layer by layer [54]. Figure 2.11 depicts a schematic illustration of the SLA technique.

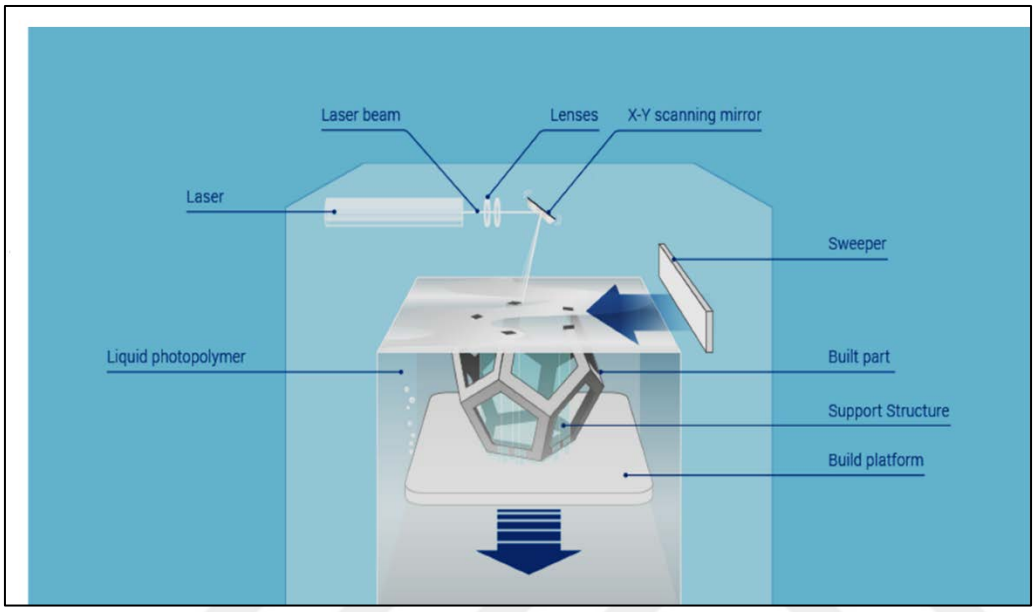

Figure 2.11. Schematic representation of SLA technique [33].

The additive manufacturing (AM) of ceramic materials using SLA can be achieved by mixing the resin with ceramic powder and then selectively solidifying the resin using a UV light or laser source based on the layer information obtained from the 3D sliced model [55]. This procedure is continued layer by layer to create complex-shaped ceramic green components, which, after undergoing multiple thermal treatments, are transformed into ceramic solids. Various ceramic materials can be processed, including Al2O3, ZrO2, and Si3N4 [56–58]. Figure 2.12 depicts ceramic components manufactured with SLA. Typically, SLA-based AM of ceramics requires preparing the ceramic-suspension resin in a manner that permits the transformation of the ceramic green body into a dense structure through sintering; consequently, feedstock preparation is an essential step for the SLA-based AM of ceramics.

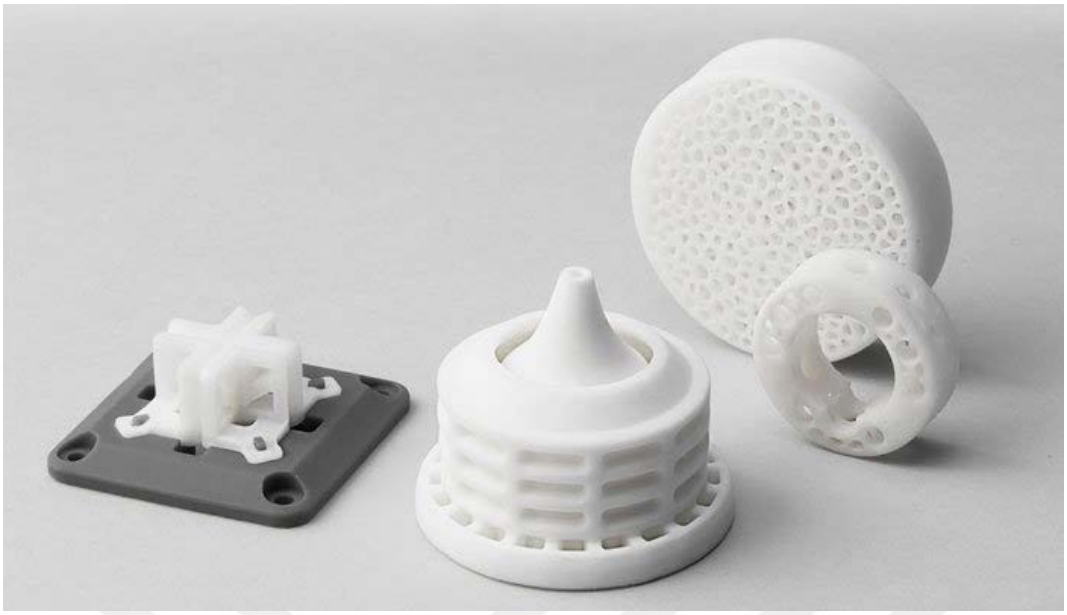

Figure 2.12. Ceramic parts printed using Robocasting technique [59].

SLA is regarded as the most effective and adaptable ceramic additive manufacturing (AM) process due to its ability to capture microscale details with efficient manufacturing accuracy [53]. Moreover, compared to other AM techniques, SLA produces the highest surface quality and dimensional accuracy; consequently, it is widely utilized for producing microscopic ceramic structures [60].

Despite the previously described benefits of SLA, there are numerous disadvantages. One of these limitations is that SLA cannot be utilized for multi-material printing because it fabricates parts from a single liquid material, and using several materials in SLA is problematic due to contamination between material systems [61]. Darker ceramic materials, such as SiC, are challenging to treat with SLA due to the light attenuation of highly loaded slurries and the light absorption by the darker particles, which precludes the formation of a suitable layer height for printing. To minimize light attenuation, coarser particles might be employed; however, this negatively impacts the sintering process required to generate dense parts [62].

Powder bed selective laser processing

PBSLP is one of the earliest and remains one of the most versatile AM techniques, being well-suited for polymers and metals and, to a lesser extent, ceramics and composites. PBSLP

processes are of great interest across many industries as a means of direct manufacturing [65]. There are increasing machine variants for fusing powders using different energy sources. The most active area of development is for metal PBSLP processes using lasers. Figure 2.13 depicts a schematic illustration of the PBSLP technique.

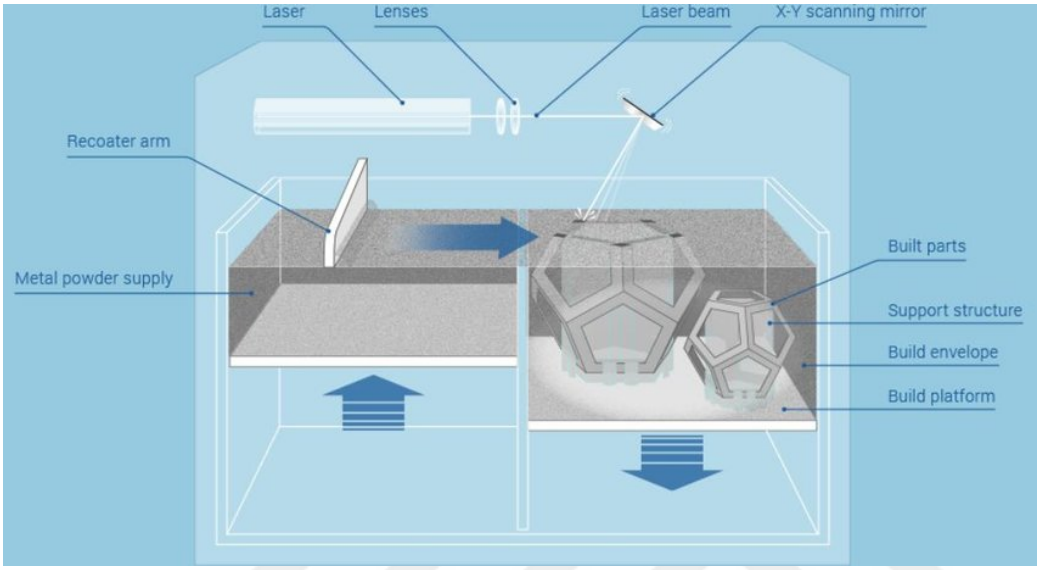

Figure 2.13. Schematic representation for the PBSLP technique [59].

As previously described in section 1.2.2, the PBSLP can be utilized for the AM of ceramics in two ways: direct and indirect. The indirect-PBSLP (In-PBSLP) utilizes a mixture of ceramic powder and other additives that act as a binder, followed by a laser system to selectively scan the powder layer by layer, according to the data from the 3D CAD model [63, 64]. In order to achieve the final shape, postprocessing, including debinding (to remove the binder) and sintering (to consolidate the ceramic particles together), should be applied. The obtained part is called the green part because it contains ceramic powder with a binding material. This method is plagued by difficulties such as a lengthy powder preparation process, posttreatment, shrinkage, and degradation [63, 65–68]. Figure 2.14 depicts alumina components manufactured using the In-PBSLP method.

Figure 2.14. Alumina parts printed using In-PBSLP technique [69].

In contrast, direct-PBSLP (D-PBSLP) utilizes a ceramic powder, without any additives, as feedstock, and then the laser scans the powder, layer by layer, based on the CAD 3D model. Therefore, no post-processing or shrinkage is required to achieve the final shape [70]. However, this technique faces numerous obstacles, including ceramic laser interaction, thermal shock, high thermal stress, and cracks [71–73]. Figure 2.15 shows samples of alumina printed using the D-PBSLP method.

Figure 2.15. Alumina parts printed using the D-PBSLP technique [74].

Comparison between ceramic AM techniques

Since its original conception in 1990 [75, 76], the AM has been evolving to address the obstacles that impede its application in ceramics. All the employed techniques, including PBSLP [77–79], BJ [80–84], DIW [43, 85], FDM [86–90], and SLA [91–94], confront obstacles that prevent their effective application in AM of ceramics. This section compares and contrasts each technique's advantages and disadvantages to evaluate its relative strengths.

The comparison considered different aspects, including feedstock preparation, postprocessing, and confronting challenges. Table 2.1 summarize the comparison between the different AM techniques used for ceramics.

Table 2.1. Comparison of the AM techniques used for ceramics.

Item	In-PBSLP	D-PBSLP	SLA	DIW	FDM	BJ
Feedstock preparation	The feedstock combines ceramic powder with polymer powder or by coating ceramic powder particles with a polymer layer.	Pure ceramic powder is directly processable.	The feedstock is created by mixing ceramic powder and a photosensitive resin to create a ceramic slurry.	Ceramic powder and the gelling agent are combined to create ceramic ink.	Ceramic powder is mixed with a polymer to produce the feedstock, which is then formed into a filament.	The ceramic powder can be directly processed.
Postprocessing	Debinding and sintering are required to achieve the desired shape.	No postprocessing is needed.	Debinding and sintering are required to achieve the desired shape.	Drying, debinding, and sintering are necessary to attain the final form.	Debinding and sintering are required to achieve the desired shape.	Debinding and sintering are required to achieve the desired shape.
Challenges	• Long manufacturing route • Need for postprocessing. • Shrinkage	• Thermal shock • High thermal stress • Cracks	• Long manufacturing route • Need for postprocessing. • shrinkage	• Long manufacturing route • Need for postprocessing. • shrinkage	• Long manufacturing route • Need for postprocessing. • Shrinkage	• Long manufacturing route • Need for postprocessing. • Low surface roughness
Ref.	[68]		[97]	[96]	[95]	[80]

Table 2.1 demonstrates that nearly all AM techniques for ceramics require initial powder preparation (mixing the ceramic powder with other additives) and postprocessing (debinding and sintering) to create the final shapes. Only D-PBSLP does not necessitate feedstock preparation or postprocessing; if postprocessing is employed, it is only to improve the mechanical or physical properties. However, the difficulties encountered with the D-PBLSP technique are considered significant obstacles that may impede ceramic AM's advancement. The following section focuses on the D-PBSLP of ceramics, specifically the materials investigated in this dissertation (alumina and SiC), and presents previous studies conducted on this topic and how they attempted to overcome the challenges mentioned earlier.

2.3. D-PBSLP of Ceramics

As described in section 2.2.3. , D-PBSLP is one of the advanced techniques used extensively in AM. It uses a laser beam to selectively scan the powder bed based on the 3D CAD model's data. After the current layer has been scanned, a new layer is deposited and scanned. These steps are repeated until all sliced layers have been completed. To be utilized effectively in AM, it is necessary to consider the appropriate PBSLP parameters. The most important D-PBSLP parameters include laser power, scanning speed, scanning strategies, layer thickness, and hatching space (Figure 2.16). Here is a concise explanation of these parameters:

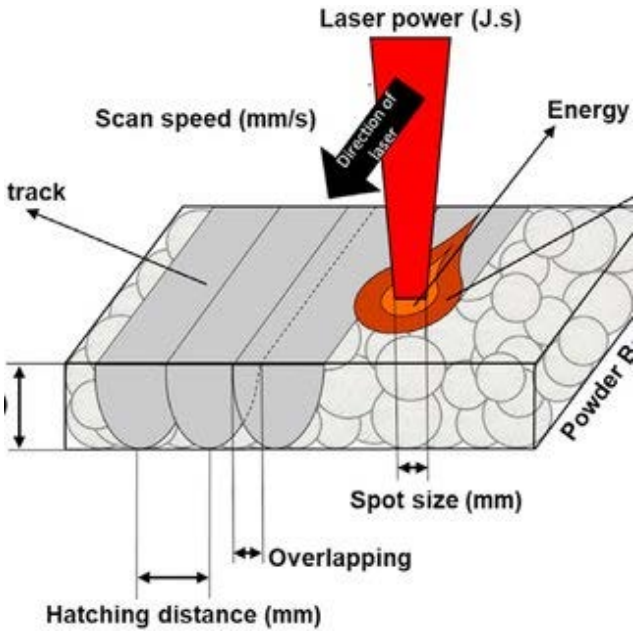

Figure 2.16. Schematic representation of the D-PBSLP process parameters [20].

Laser power, W

Laser power is the heat transfer rate from the beam to the powder bed. When scanning a material, it is essential to use the appropriate power; otherwise, structural issues may arise. Low laser power results in insufficient melting/sintering of the material, whereas high beam power results in an unstable melt pool that has a negative effect on the manufactured part or creates pores due to material evaporation.

Scanning speed, mm/s

Scanning speed is the rate at which the laser moves across the powder bed, scanning the powder layer. Using the correct scanning speed; otherwise, the same issues as described previously may occur.

Scanning strategies:

The scanning strategy is the tool path by which the laser selectively scans the powder layer based on the sliced layer data. The scanning strategy is regarded as an essential parameter because it substantially affects the obtained properties of the printed part, necessitating careful consideration when selecting it.

Layer thickness t (µm):

The layer thickness is the height of the deposited powder layer. It should be carefully chosen to preserve interlayer adhesion. Increasing the layer thickness can reduce the building time, but it will affect the part's resolution and mechanical properties. In addition, a thin layer can significantly improve a part's resolution while increasing its construction time.

Hatching (distance) space h (µm):

Hatching space (distance) is the distance between two adjacent scanning paths; thus, it controls the connection between adjacent paths and significantly affects the printed part's mechanical properties.

As previously described, D-PBSLP is considered the best AM technique for ceramic materials. However, the application of this technique in ceramics faces various challenges, such as the high melting/sintering point of ceramic materials, thermal shocks, the development of cracks, and laser interaction with ceramic materials [98–101].

The high melting/sintering point of ceramic materials combined with a rapid increase in temperature induces a high thermal shock in the material [74, 102], resulting in the initiation and formation of cracks. Ceramic materials' low thermal conductivity keeps the heat generated by the laser heat source within the material and prevents its diffusion. Consequently, nonuniform heating and cracking may develop [68, 103].

For laser-material interaction, ceramic materials absorb light energy of varying wavelengths based on their optical properties [104, 105]. For instance, the absorptivity of oxide ceramics is exceptionally high for lasers with a wavelength of 10.64 μm and extremely low for lasers with a wavelength of 1.064 μm, while carbides ceramics display the opposite behaviour (Figure 2.17 shows the absorptivity of different materials with different wavelengths). Therefore, the laser source that should be utilized with oxide ceramics is one with a long wavelength, such as a CO2 laser (10.64 μm). This notion is supported by the research of Pham et al. [105], who examined the milling of alumina and Silicon Nitride using an Nd-Yag laser with a wavelength of 1.064 μm, and they discovered that the machining accuracy is highly dependent on the laser absorptivity, with Silicon Nitride (which has a high absorptivity for the used laser) providing superior laser milling accuracy than Alumina (has low absorptivity for the used laser).

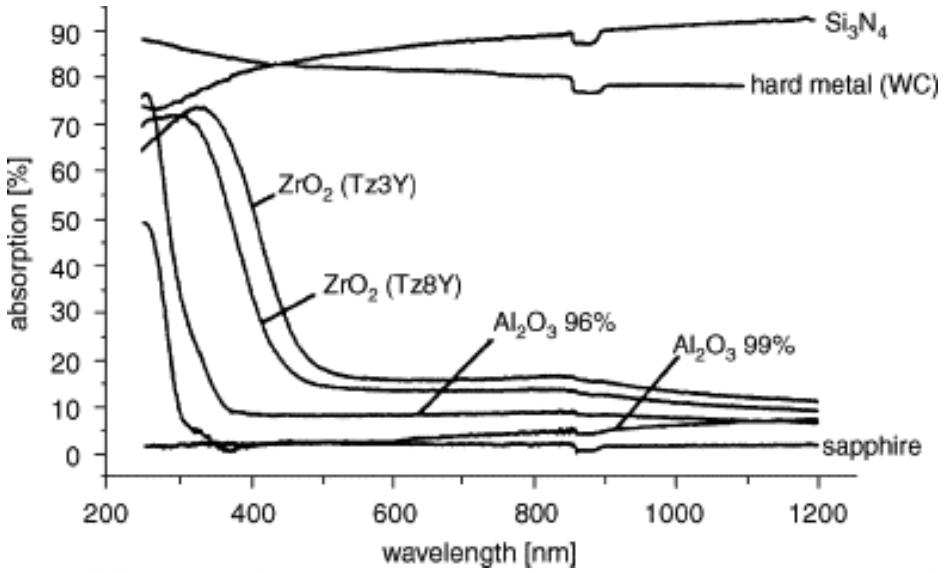

Figure 2.17. Absorptivity of different materials at different wavelengths [105].

Therefore, it is advised to use the appropriate laser for the printing material; however, nearly all PBSLP printers on the market or in research labs are equipped with an Nd-YAG or fiber laser with a wavelength of 1.064 µm, which is unsuitable for oxide ceramics such as Alumina. Table 2.2 summarizes the absorptivity of the two materials considered in this dissertation (alumina and SiC) for lasers with wavelengths of 1.064 µm and 10.64 µm.

Table 2.2. Absorptivity of Alumina and SiC at different laser types [108].

Material	Nd-Yag laser (1.064 µm)	CO2 laser (10.64 µm)
Alumina	0.03	0.96
SiC	0.78	0.66

Since the purpose of this dissertation is to investigate the D-PBSLP of alumina and SiC ceramic materials, it is necessary to review the prior research on these two materials to provide a context for what was done and the shortcomings that needed to be addressed; this is covered in the following two sections.

2.3.1. D-PBSLP of Alumina

Alumina is a chemical compound that can be formed by oxidizing aluminium; its chemical formula is Al_2O_3. Alumina is typically extracted from bauxite, a naturally occurring ore containing variable amounts of hydrous (water-containing) aluminium oxides. Alumina possesses outstanding mechanical and physical properties, such as high strength and

hardness, electrical insulation, corrosion resistance, biocompatibility, and heat resistance. Table 2.3 provides a summary of alumina's mechanical and physical characteristics.

Table 2.3. Alumina material properties.

No	Property	value	Unit	Ref.
1	Density	3.9	Kg/cm^3	[106]
2	Thermal conductivity	40	W/m. K	
3	Hardness	1500	Kg/mm^2	
4	Elastic Modulus	370	GPa	
5	Tensile strength	262	MPa	
6	Thermal expansion coefficient	8×10^{-6}	/°C	
7	Melting point	2072	°C	

Due to its superior properties, alumina is the most widely used advanced ceramic material on the planet and is utilized in various applications. These applications include fillers, catalysis, gas purification, electrical insulation, abrasion protection, coatings, and medical and aerospace uses [107–111].

D-PBSLP has excellent potential for the additive manufacturing of alumina, where final 3D shapes can be obtained without feedstock preparation or post-processing. However, D-PBSLP faces numerous obstacles, including, as previously described, thermal shock, thermal stress, cracks, and laser interaction with powder. In addition, the process parameters (laser power, scanning speed, hatching distance, and scanning strategies) should be thoroughly investigated and studied to determine their optimal values.

The cracking of ceramic materials is considered the most significant challenge for D-PBSLP of ceramics, as it alters the mechanical performance and prevents the use of ceramics in numerous applications, such as structurally resistant applications. According to Zheng et al. [102], who investigated the cracks developed during D-PBSLP of alumina, two types of cracking primarily occur during AM of ceramics utilizing D-PBSLP techniques: longitudinal and transverse cracks. This study considered zigzag and island scanning strategies, and pure alumina powder was used as the feedstock. As seen in Figure 2.18, most cracks were transverse (perpendicular to the laser path) and longitudinal (parallel to the laser path). The transverse cracks were primarily caused by the high-temperature gradient along the scanning path, while the transfer cracks were caused by the solidification progress along the scanning path. Regarding the effect of scanning strategies, the zigzag strategy revealed both transverse

and longitudinal cracks, whereas the island strategy revealed only transverse cracks. Because the scanning path in the zigzag strategy is so lengthy, the effect of the temperature gradient was more significant than in the island strategy, which utilized a shorter scanning path.

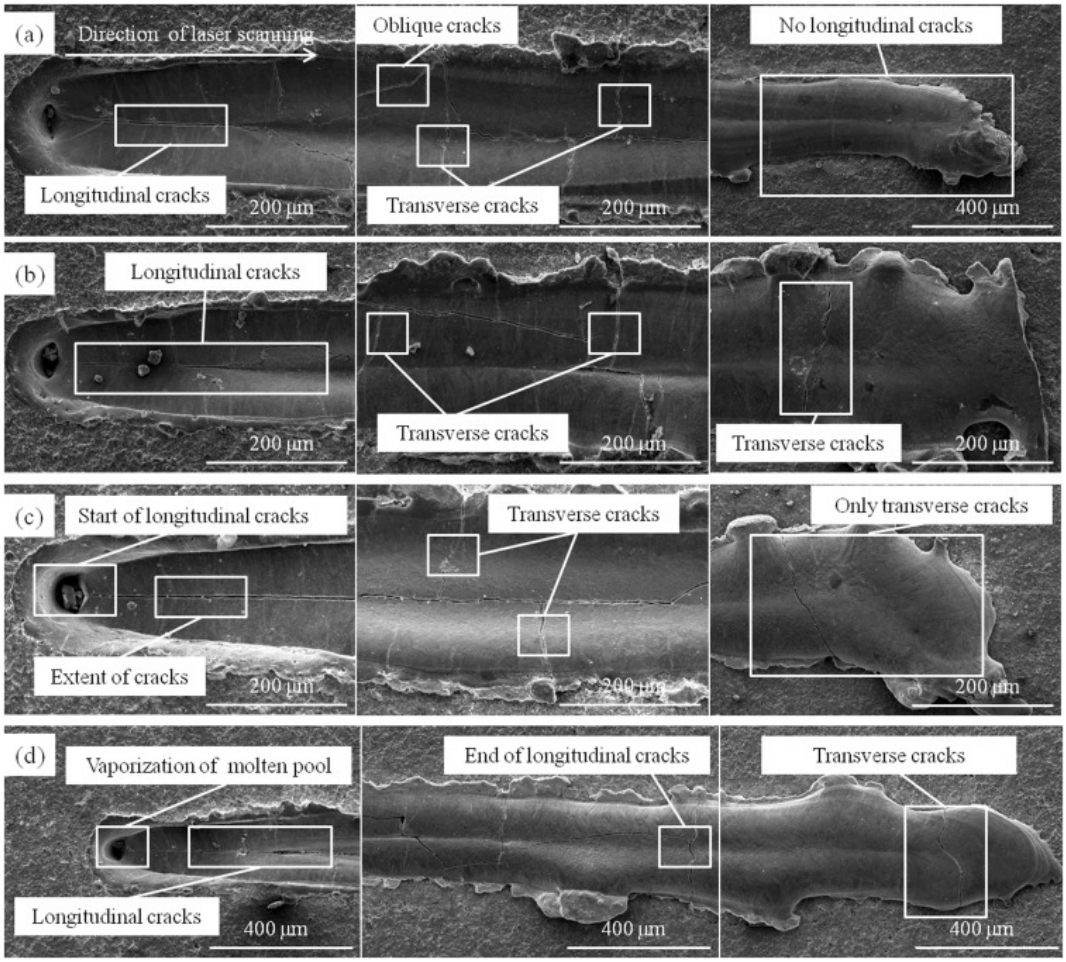

Figure 2.18. Cracks developed during D-PBSLP of alumina as reported by Zheng et al. [102].

Some studies were conducted to address this obstacle to overcome the problem of thermal shock and cracks. Hagedorn et al. [77] developed a preheating system to preheat the layer powder temperature with a CO2 laser before scanning with an Nd-Yag laser to reduce thermal shocks and cracks. Figure 2.19 depicts the constructed system.

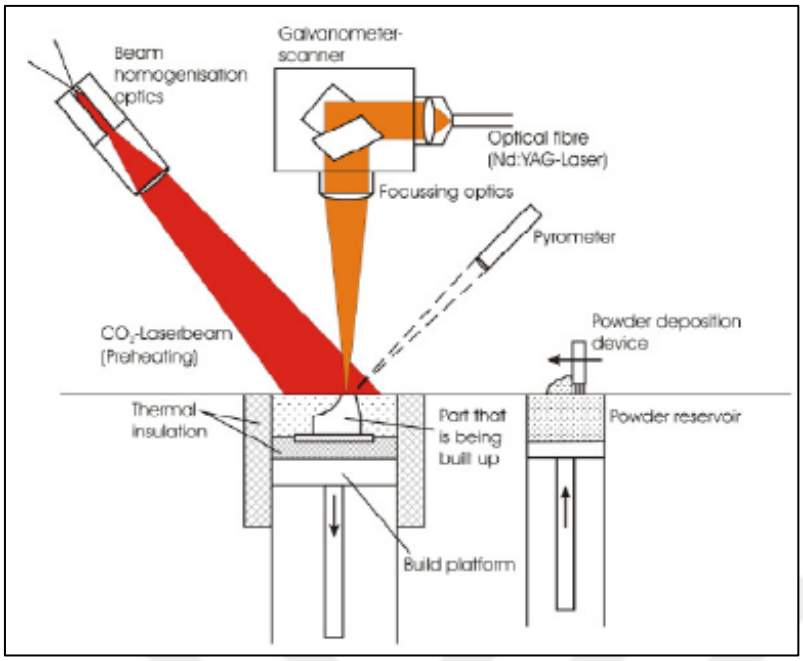

Figure 2.19. Preheating system developed by Hagedorn et al. [77].

As shown in Figure 2.20(a), they could print various alumina layers and discovered that cracks were significantly reduced but still present. It was determined that these cracks formed due to the deposition of cold powder on the previously scanned hot layer. This issue can be resolved by installing a heating system in the powder tank. Figure 2.20(b) depicts the temperature distribution of the powder bed, in which the preheated powder layer is obvious.

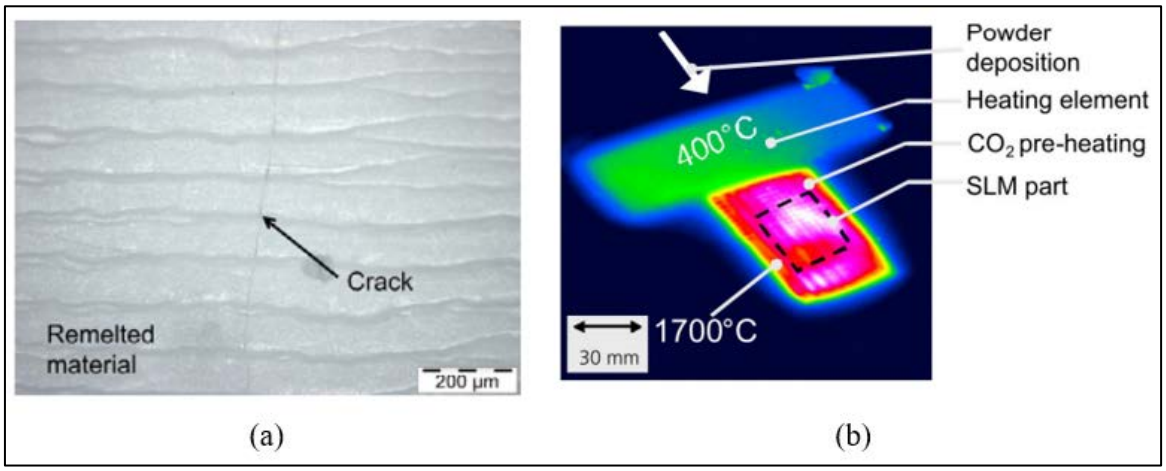

Figure 2.20. Cracks developed in the printed aluminium layers (a); temperature distribution of the powder bed obtained using thermal camera (b) [77].

Wilkes et al. [99] investigate the potential AM of zirconia and alumina mixtures using the preheating system described by Hagedorn et al. [77], illustrated in Figure 2.19. Figure 2.21 depicts the zirconia-alumina mixture.

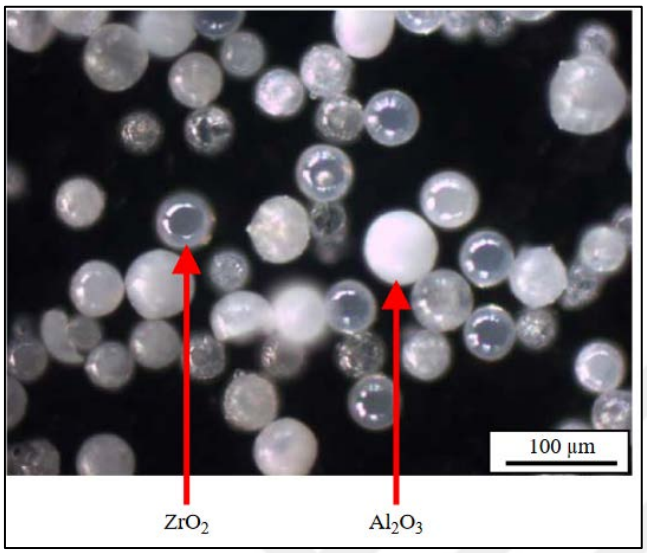

Figure 2.21. Detailed photo of the alumina-zirconia mixture used for D-PBSLP [99].

As depicted in Figure 1.22, the results demonstrated that preheating could nearly eliminate the occurrence of cracks in the printed samples. In addition, 3D parts could be printed, as depicted in Figure 2.23. Although this method achieves a promising result for applying D-PBSLP to an alumina-zirconia mixture, it does not consider printing alumina or zirconia solely, which is regarded as the primary objective of ceramics AM.

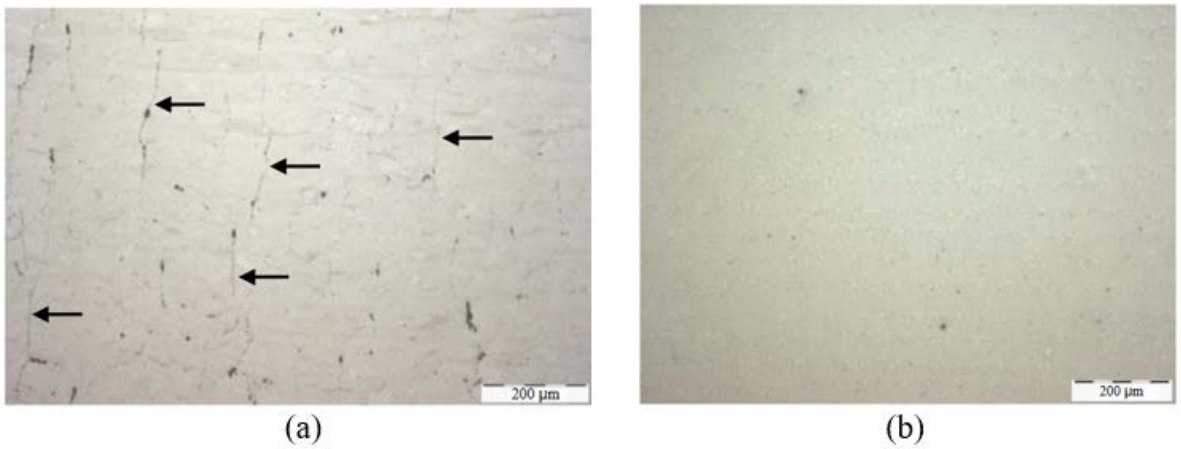

Figure 2.22. SEM images for alumina-zirconia sample printed with D-PBSLP technique; without preheating (a), with preheating up to 1715 °C (b) [99].

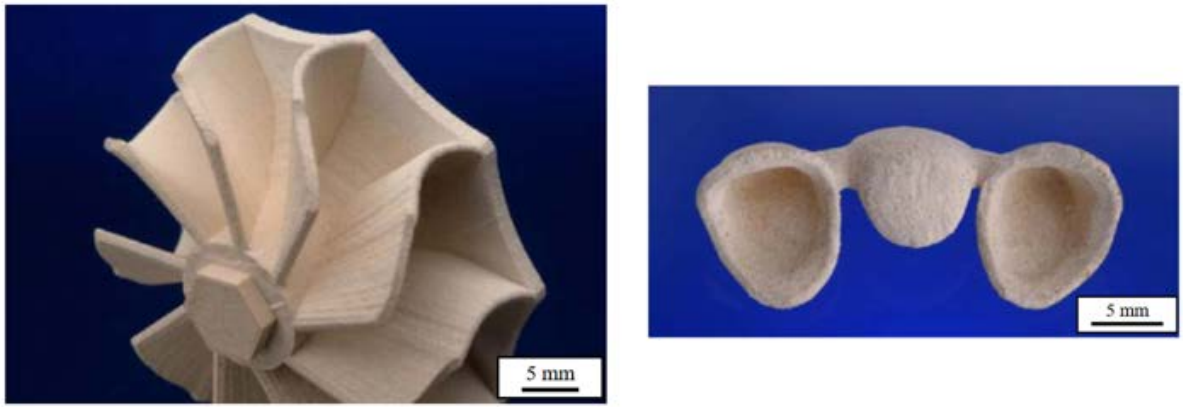

Figure 2.23. 3D parts printed using D-PBSLP and alumina-zirconia mixture (80 wt.% zirconia/20 wt.% alumina) as a feedstock without preheating [99].

Liu et al. [112] developed a preheating system for yttria-stabilized zirconia (YSZ) powder, as depicted in Figure 2.24, in accordance with the same concept described by Hagedorn et al. [77]. The powder bed was preheated with an Nd-YAG laser prior to fiber laser scanning. They could print YSZ components with 84% relative density and fewer cracks. However, as a result of the preheating, the printed components were surrounded by sintered powder, as seen in Figure 2.25.

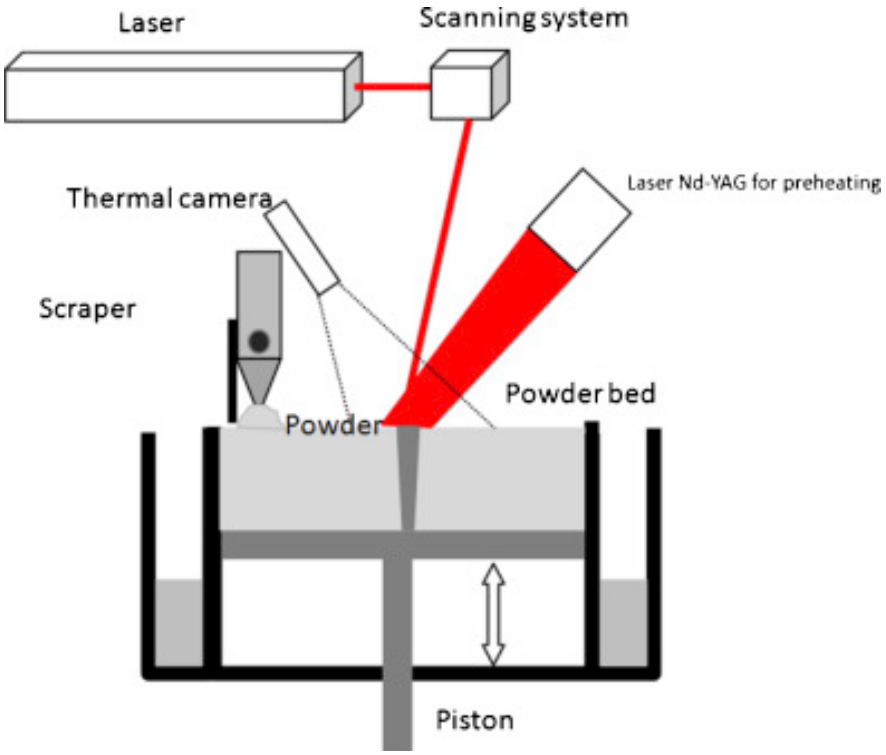

Figure 2.24. Preheating system developed by Liu et al. [112].

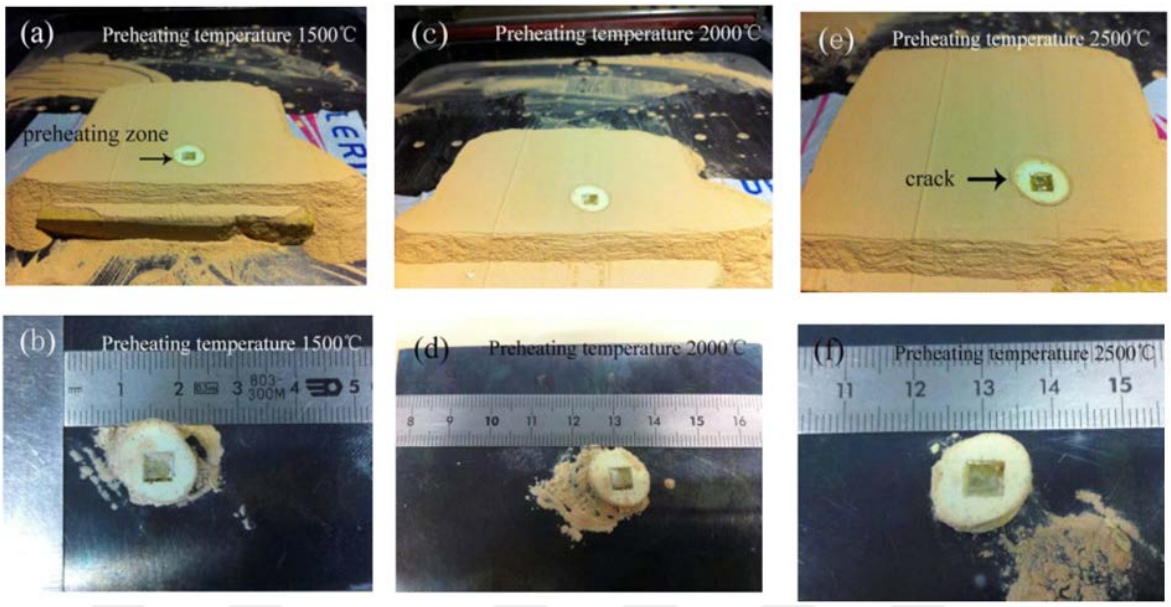

Figure 2.25. Yttria-stabilized zirconia printed utilizing the preheating system developed by Liu et al. [112].

Cracking is not the primary defect experienced in D-PBSLP of ceramics. Balling is another severe problem, resulting from various factors such as inappropriate process parameters, high surface tension and viscosity of molten ceramics. Qiu et al. [73] investigated the balling phenomena and cracks resulting from alumina D-PBSLP. They found that due to the high surface tension and high viscosity of molten alumina, the top surface of the printed samples displayed balling phenomena (Figure 2.26). The high surface tension of alumina prevents the molten particles from merging, and the high viscosity of molten alumina prevents the molten alumina particles from spreading through the surface. In addition, they revealed that the scanning speed and laser power play a significant role in regulating the balling phenomenon; therefore, laser power and scanning speed should be appropriately selected. In addition, the results demonstrated that the formation of both longitudinal and transfer cracks could be controlled with the right powder size, powder bed uniformity, and laser parameters.

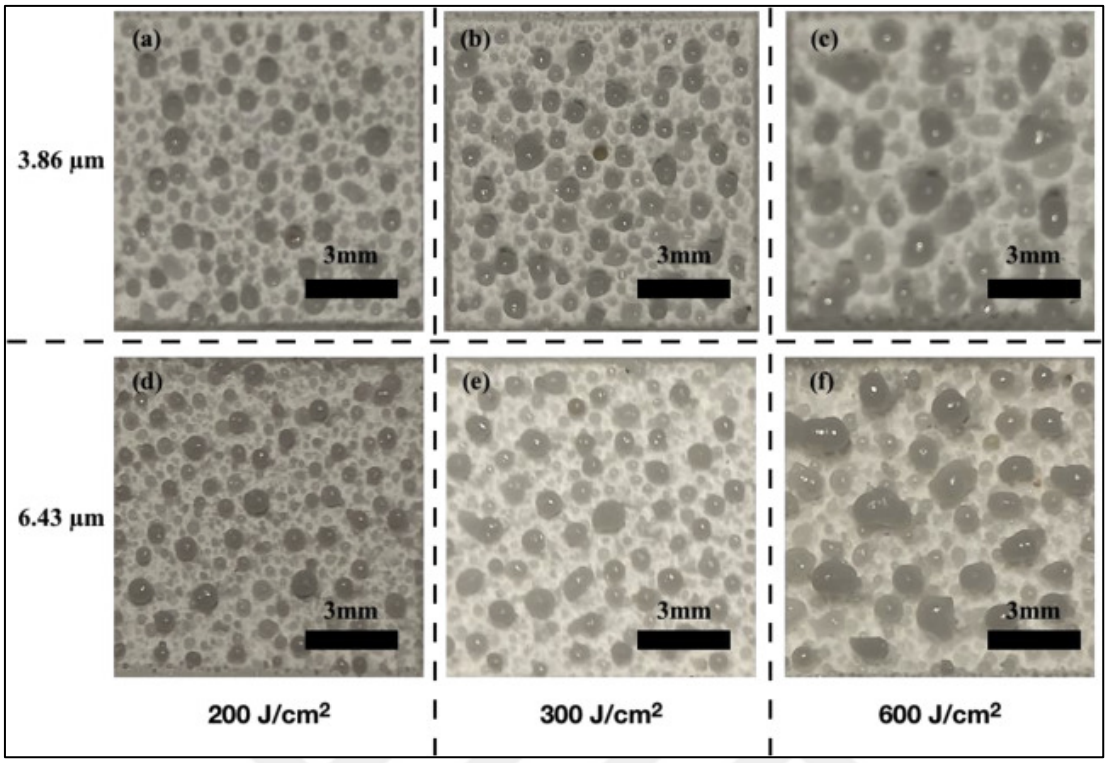

Figure 2.26. Balling of alumina samples at different hatch spaces: (a) 0.15 mm; (b) 0.10 mm; (c) 0.05 mm; (d) 0.15 mm; (d) 0.10 mm; (e) 0.05 mm, and with different particle size (3.86 and 6.43 µm) [73].

Ceramics-laser interaction (absorptivity) is also a significant challenge, as described previously, and some researchers have utilized additives mixed with ceramic powder to improve the interaction. Juste et al. [74] investigated the AM of alumina using the D-PBSLP technique. They used a printer equipped with an Nd-Yag laser with a wavelength of 1.064 µm, and the absorption of this laser by alumina was only 3%. Therefore, they attempted to increase the absorptivity by combining alumina powder with a tiny amount of graphite (0.1 vol%) and spray-drying the mixture, and as a result, the absorptivity increased to 50 %. Figure 2.27 demonstrates that alumina samples could be printed using different process parameters. Nonetheless, the samples exhibited a top surface with waviness and periodic damage along the build directions. As shown in Figure 2.28, complex shapes were also printed to demonstrate the developed method's capability to process ceramic materials highly.

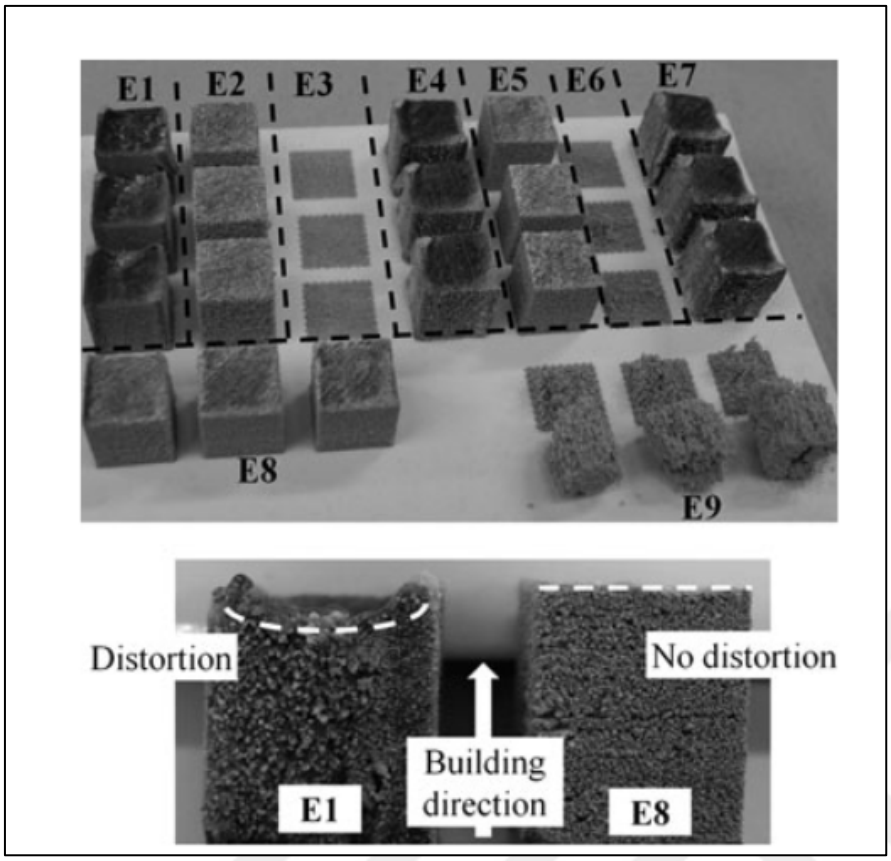

Figure 2.27. 3D alumina cubes printed using D-PBSLP technique utilizing spray-dried alumina powder mixed with graphite as developed by Juste et al. [74].

Figure 2.28. Alumina complex designs printed utilizing the technique described by Juste et al.[74].

Liu et al. [72] investigated the D-PBLSP of alumina by enhancing the alumina-laser sintering with boron carbide (B4C). The effect of varying B4C concentrations on alumina's microstructure was investigated. The results demonstrated a remarkable improvement in alumina sintering and densification, and the process window was expanded, as seen in Figure 2.29.

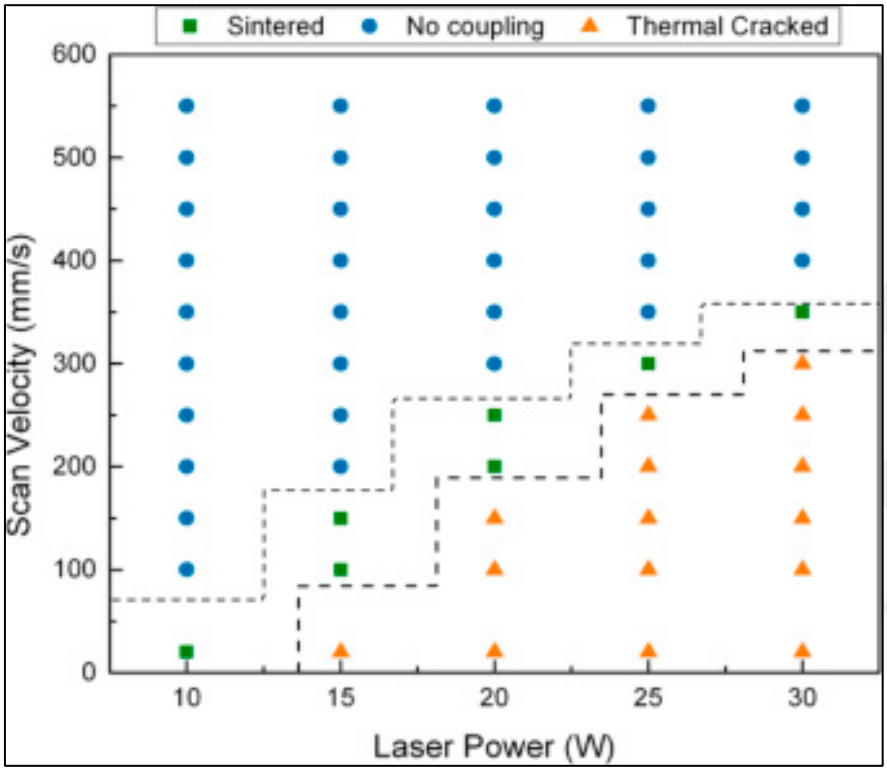

Figure 2.29. Process window for D-PBSLP of alumina as obtained by Liu et al.[72].

Figure 2.30 depicts the printed alumina samples, where it can be observed that increasing the amount of B4C led to darker-coloured samples that could be lightened through heat treatment and oxidation of B4C. Although the technique developed by Liu et al. [72] produced promising outcomes, the low relative density and shrinkage were the most significant drawbacks.

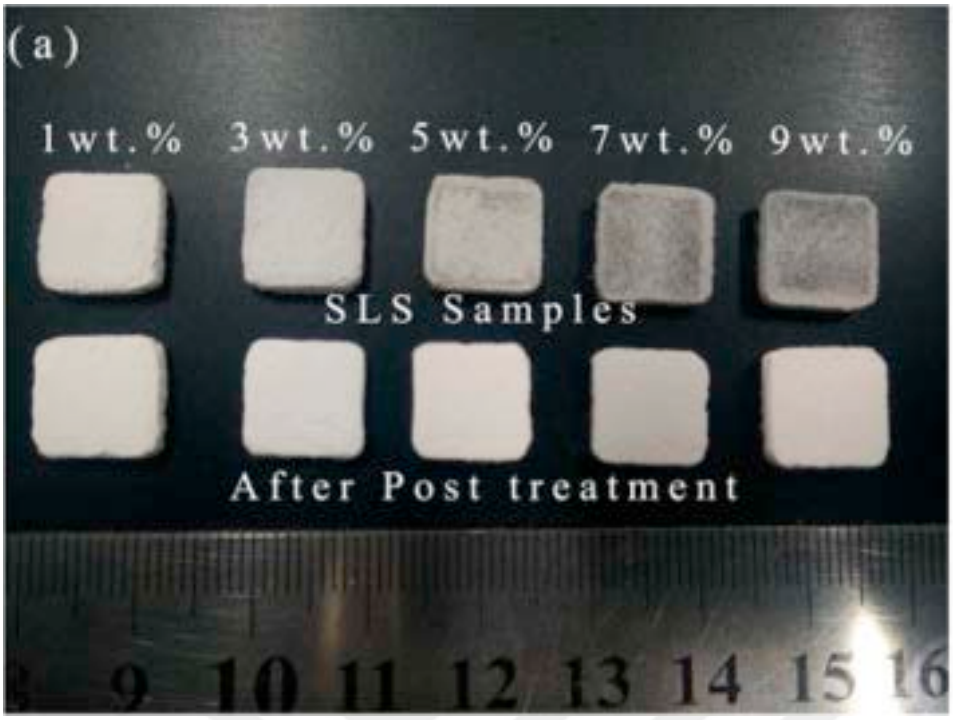

Figure 2.30. Alumina samples obtained by D-PBSLP technique utilizing alumina mixed with B4C as a sintering enhancer [72].

For the effective application of D-PBSLP on ceramics, the appropriate values of process parameters are an additional crucial factor. However, it has not been thoroughly investigated, and most studies used random values for these parameters. Shishkovsky et al. [113] used the PBSLP technique to investigate the direct AM of zirconia mixed with aluminium (in some cases, alumina). They investigated the effect of various process parameters on the obtained monolayer (one path) and discovered the significance of using the proper parameter values. The limitation of this study is that it focused on additive manufacturing of composite materials rather than ceramics. In a separate study, Fayed et al. [114] examined the D-PBSLP of monolayer alumina using a 50 MPa compaction die to form a 3 mm thick, 50×50 mm square layer. The layer's surface roughness, thickness, deformation, density, porosity, and hardness were then analyzed using various process parameters after it was sintered. The results demonstrated that both laser power and scanning speed significantly impact the quality of the sintered layer.

Moreover, Fan et al. [115] investigated the D-PBLSP of alumina, considering only a single path experimentally and numerically using a model developed specifically for this study. As shown in Figure 1.31, they could obtain a process map that specifies the laser power and scanning speeds required to melt alumina continuously. This study's flaw is that it only

considered a single track and not the entire component, which is a completely different process involving numerous obstacles such as heat accumulation, layer deposition, adhesion, thermal shock, and cracks. The feedstock used in this study was 99.8% pure alpha-alumina powder with a d50 of 20 µm.

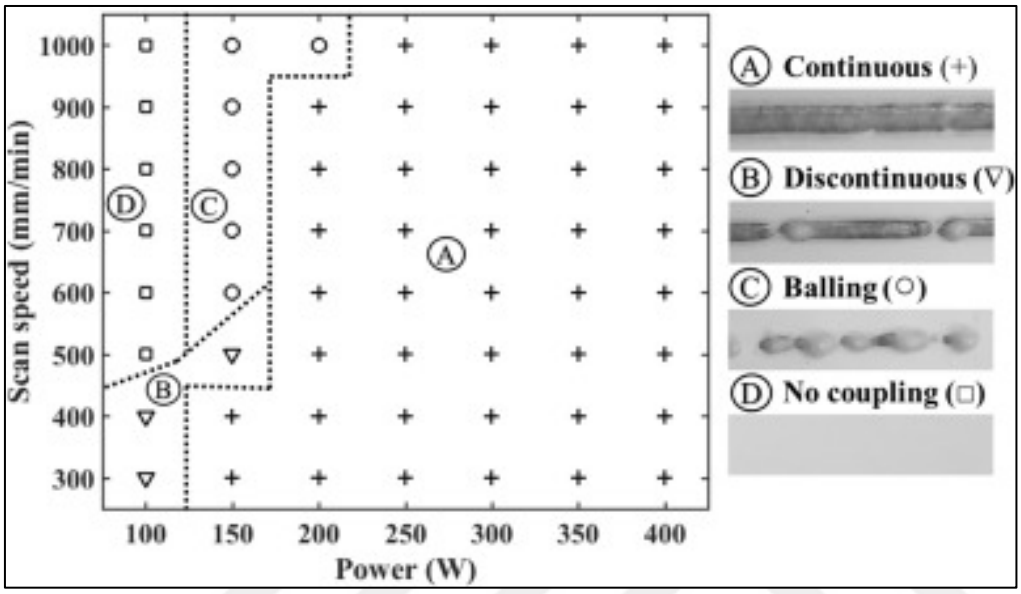

Figure 2.31. Window map for alumina considering single path [115].

A simulation was also used to investigate ceramics' D-PBSLP and analyze the impact of various process factors. Zhang et al.[116] used simulation to investigate alumina's thermal behaviour and solidification during D-PBSLP by developing a Finite Element Model (FEM). They discovered that the temperature of the printed part gradually increases over time due to heat accumulation during the printing process, which corresponded with the thermal camera measurements of the temperature history during scanning. In addition, as depicted in Figure 1.32, the results demonstrated the importance of the laser power and scanning speed on the obtained melt pool dimensions.

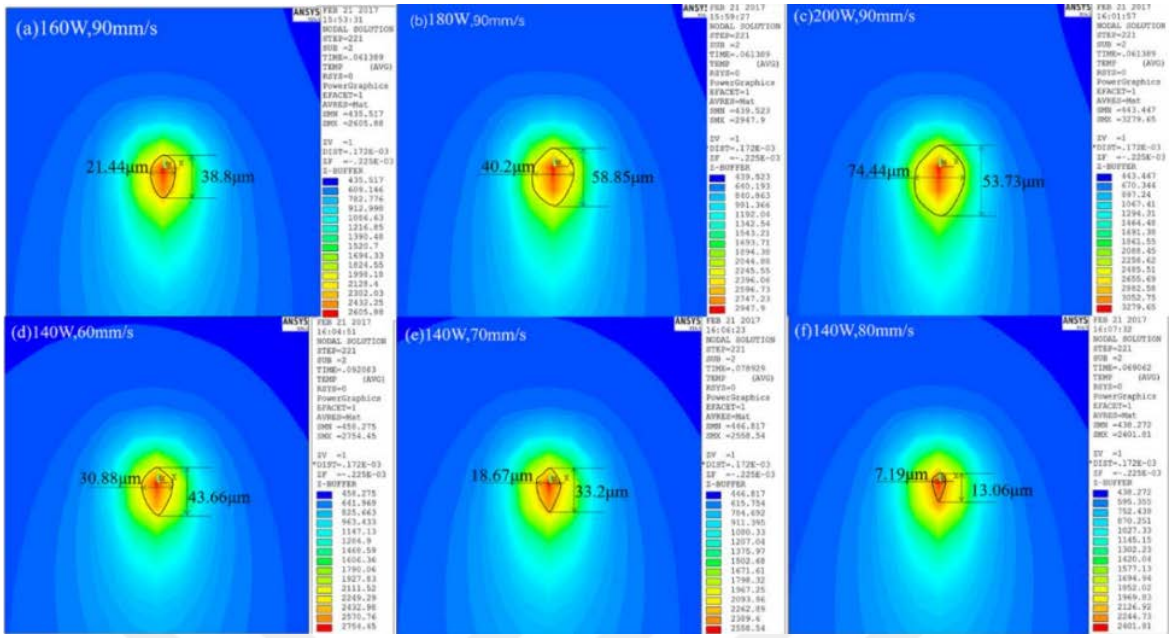

Figure 2.32. Molten pool dimensions obtained at different laser powers and scanning speeds [116].

Chen et al.[117] investigated the influence of various process parameters on temperature distribution, melt pool profiles, and bead shapes during D-PBSLP of alumina by developing a three-dimensional finite element thermomechanical model. Figure 2.33 depicts the transformation of the shape of the melt pool as a function of various process parameters; it is evident that increasing the scanning speed resulted in an unstable melt pool.

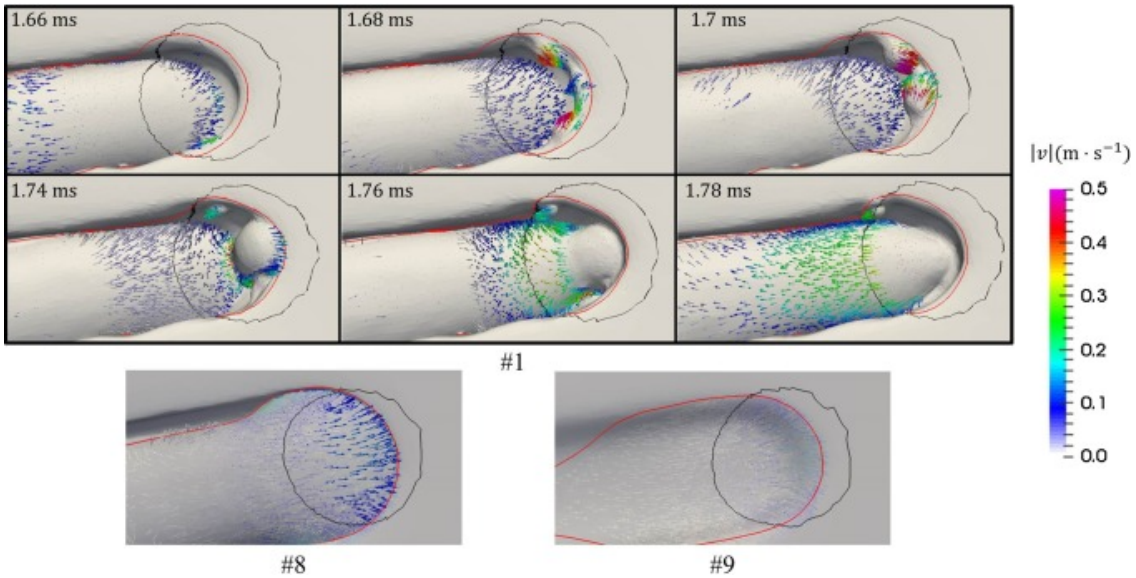

Figure 2.33. Molten pool shape obtained at different parameter values as described in [117].

2.3.2. D-BPSLP of SiC

SiC is one of the essential technical ceramics. It comprises Silicon (Si) and Carbon (C) atoms with a covalent bond and a grey-white hue. It is referred to as alpha-SiC and is formed at temperatures above 2000 °C. It existed in various crystal structures. SiC is lightweight and possesses exceptional properties. Table 2.4 summarizes the fundamental physical and mechanical properties of SiC. Through the chemical reaction between Si and C, SiC can be produced (densified). Figure 2.34 depicts the phase diagram of the binary Si and C system, which illustrates the different phases that can be formed with different Si and C compositions [118].

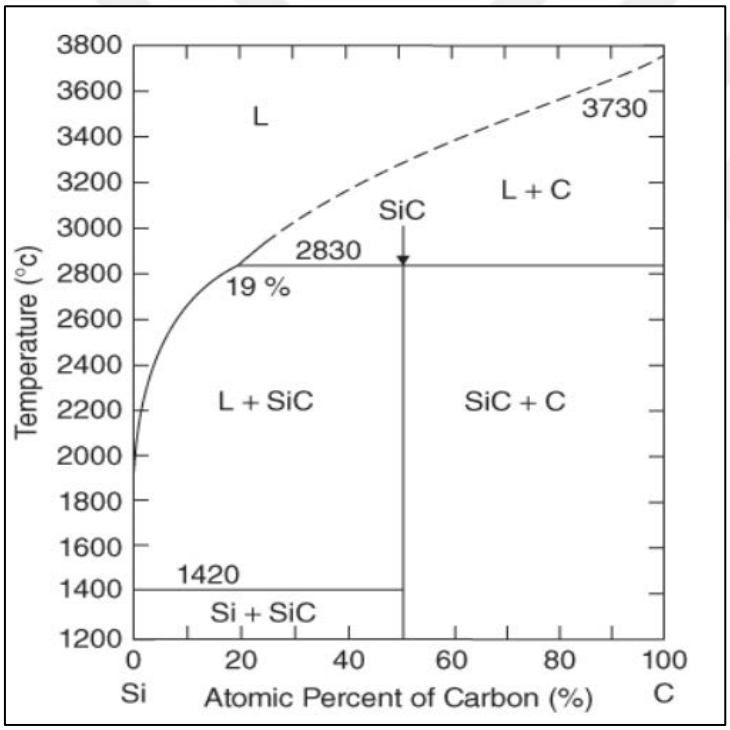

Figure 2.34. Phase diagram of the Si–C binary system [118].

Table 2.4. Material properties of SiC.

No	Property	Value	Unit	Ref.
1	Density	3.21	kg/cm^3	[119]
2	Thermal conductivity	120	W/m. K	
3	Hardness	2800	Kg/mm^2	
4	Elastic Modulus	410	GPa	
5	Ultimate strength	550	MPa	
6	Thermal expansion coefficient	4×10^{-6}	/°C	
7	Decomposition point	> 2800	°C	

SiC is used in numerous applications due to its excellent properties, such as its high mechanical stiffness, low density, wide bandgap, low thermal expansion coefficient, high thermal stability, and resistance to corrosive environments [120]. These applications include high-power microwave devices for commercial and military systems, high-temperature electronics, space telescope mirrors, and laser mirrors [121, 122]. SiC is also used in micro-electro-mechanical sensor devices for hostile environments, gas and chemical sensors for internal combustion engines, furnaces, boilers, and solar-blind UV photodetectors [123].

SiC research rate in PBSLP is generally considered to be low. As SiC begins to decompose at 2800 K [124], no study has previously focused on the D-PBSLP of SiC components, as this is a challenging task. All previous research was limited to the Indirect-PBSLP of SiC, regardless of application. Some studies, for instance, focused on the PBSLP of SiC particulates for composite material applications. Suocheng et al.[125] investigated how to improve SiC/Si composites produced by PBSLP incorporating reaction-bonded (RB) processes. Subrata and Partha [126] examined the developed fissures in SiC particulate manufactured by PBSLP for use in an aluminium-based metal matrix composite. Hon and Gill [127] applied the PBSLP techniques to produce SiC particulates in composite material. Xiong et al. [128] studied the effects of dual binders on the accuracy, microstructure and mechanical properties of SiC particulates used in composites. Nelson et al. [129] investigated the PBSLP of SiC powders coated with polymer. Hua et al. [130] studied the silicon effect on the microstructure, and mechanical and thermal properties of Carbon fiber reinforced silicon carbide composite (Cf/SiC) manufactured by PBSLP. Laizhen et al. [131] studied the cracks developed in SiC particulates produced by PBSLP to be used in metal matrix composites. Xiong et al. [132] studied the effects of binders on the dimensional accuracy and mechanical properties of SiC particulates used in composite materials manufactured by PBSLP.

For In-PBSLP of SiC 3D shapes, many previous studies focused on printing SiC through mixing SiC powder with other additives to bond SiC particles together and then applying post-processing for debinding and sintering the particles. This process is often accompanied by shrinkage in the dimensions of the manufactured parts, changes in the mechanical and physical properties, and production parts with low relative density. Birmingham et al. [133] investigated the indirect PBSLP of SiC by scanning the Si powder in an acetylene (C2H2)

chamber where SiC could be formed by the reaction of Si with the carbon in the atmosphere, but very light and porous SiC parts were obtained, as can be seen in Figure 2.35.

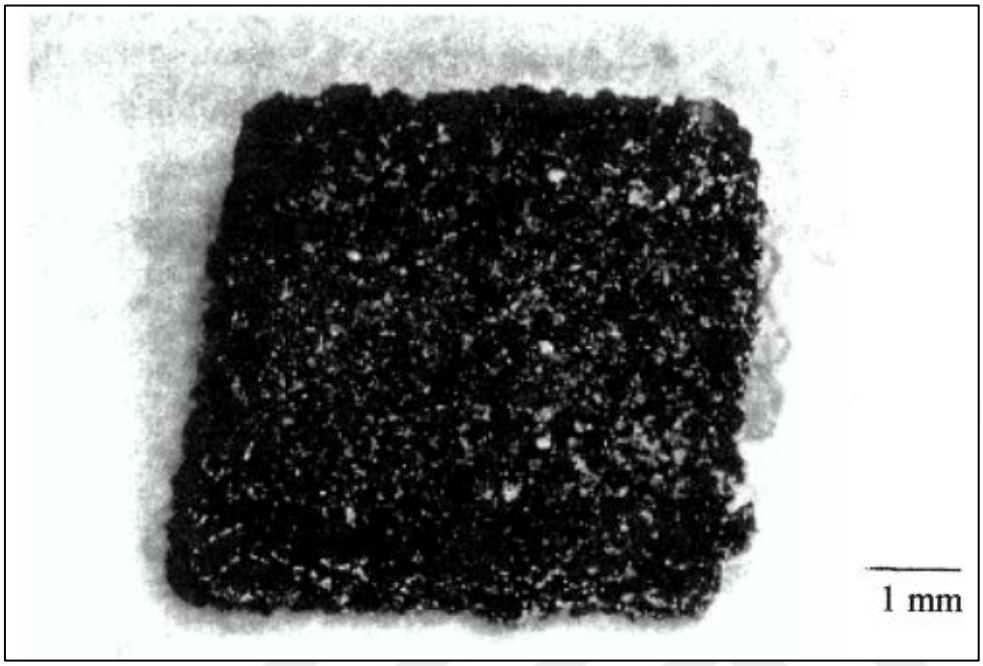

Figure 2.35. SiC part (5×5×1 mm3) printed using In-PBSLP technique as described by Birmingham et al. [133].

To increase the density obtained by indirect PBSLP of SiC, Hon et al. [134] manufactured SiC/Polyamide composites by blending 50vol.% polyamide with 50 vol.% SiC. After the PBSLP, postprocessing was used to reach the final shape. However, the polymer was still included in the final product, affecting the obtained mechanical properties. In another study carried out by Löschau et al. [135], they tried to improve the mechanical and thermal properties of SiC parts produced through indirect-PBSLP by using silicon infiltration.

Additionally, previous studies [138,139] developed laser sintering to produce SiC parts using a mixture of Si and SiC. For example, Meyers. et al. [136, 137] mixed SiC with Si and then laser sintered where Si melted and resolidified again from primary SiC. After that, the Si-SiC performs were impregnated in a phenolic resin that pyrolyzed into porous carbon, reacted with Si, and transferred into secondary SiC. They could obtain a fully dense reaction bonded silicon carbide part with up to 84 vol% SiC. However, the problem with this process is the postprocessing steps followed to achieve high dense SiC.

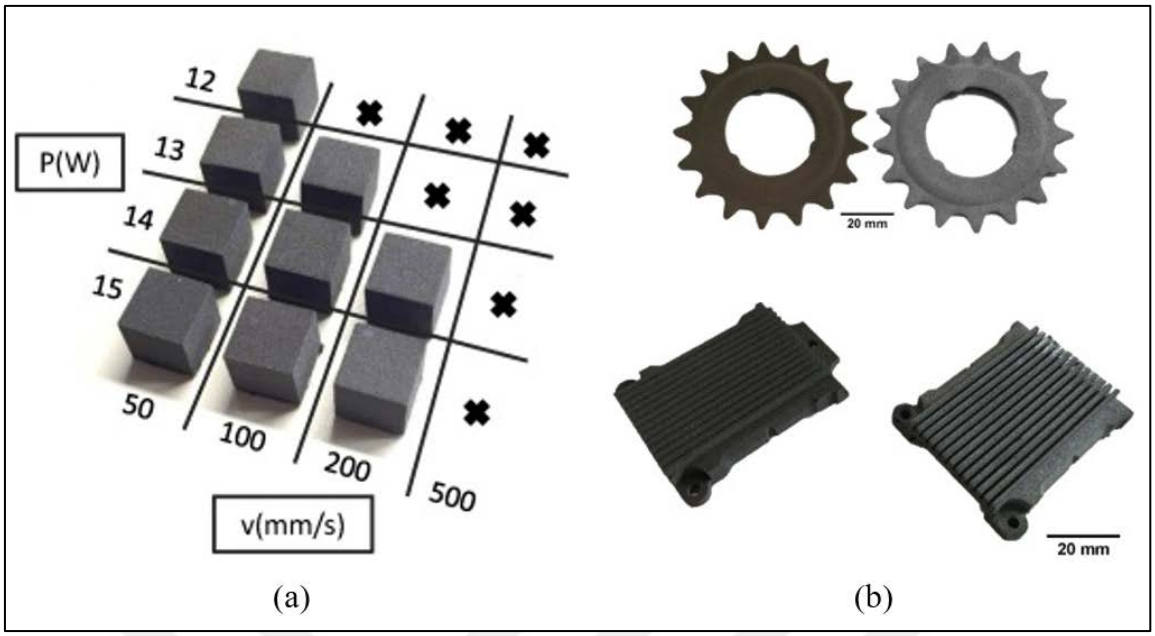

Figure 2.36. Si-SiC part manufactured using In-PBSLP technique; cubes (a), complex shapes (b) [138, 139].

2.3.3. Shortcomings in the state of the art

Reviewing the literature on D-PBSLP of alumina revealed that the focus is limited, and there is an immediate need to investigate this technique in-depth, particularly the process parameters that were not adequately considered. As previously described, the process parameters consist of laser power, scanning speed, hatching space (distance), scanning strategies, and build orientations. These process parameters are dependent on each other and should be considered jointly, as any change in the value of any process parameter should be accompanied by changes in the other parameters.

For SiC, it can be observed that all previous studies have focused on In-PBSLP, while D-PBSLP has never been considered. Therefore, it is essential to investigate the possibility of SiC D-PBSLP. SiC is a covalent ceramic that does not have a melting phase under normal atmospheric conditions; instead, it decomposes into liquid silicon and solid carbon at temperatures above 2545°C [140, 141]. As a result, the manufacturing of 3D SiC components by D-PBSLP is considered to be challenging. It is believed that investigating and optimizing the process parameters is the key to having a successful D-PBSLP of SiC; therefore, it will be studied by a thorough investigation and optimization of the process

parameters (scanning strategies, laser power, scanning speed, hatching distance and layer thickness).

In addition, it is essential to note that the scanning strategy is one of the most process parameters, and its effect is completely ignored, as no previous studies have investigated its effect on D-PBSLP of ceramic materials deeply. This dissertation filled this gap by considering the scanning strategies as the first parameter to investigate, as it does not have a value to manipulate but rather a type to choose based on its performance during D-PBSLP.

2.4. Research Objectives

Based on the introduction and literature review presented, a gap in the D-PBSLP of ceramic materials should be investigated and addressed. The vast majority of previous research has focused on indirect PBSLP, which requires feedstock material preparation and post-processing operations. In addition, a comprehensive study of the effect of process parameters, particularly scanning strategies, is required. This dissertation examines the effect of scanning strategies and other process parameters for D-PBSLP of SiC and alumina to provide a guide for selecting the appropriate parameters. D-PBSLP of Alumina was conducted at the Belgian Ceramic Research Centre (BCRC, Mons, Belgium). The study's initial emphasis was on examining scanning strategies to determine their effectiveness with alumina and select the optimal strategy. The remaining process parameters were then investigated and optimized. The PBSLP of SiC was carried out in CIRIMAT (Université de Toulouse, France), and the same procedure described previously with alumina was followed.

Since the D-PBSLP is considered a challenging process and numerous factors directly affect it, there is a pressing need for a numerical tool to predict the effect of these process parameters and aid in interpreting and guiding experimental results. Therefore, the following are the objectives of this study:

i. Developing a numerical model to be used as a guide through the experimental work and help to understand the obtained results.
ii. Investigate the effect of the process parameters on the D-PBSLP of alumina and SiC.
iii. Optimizing the process parameters to reach the optimal combination values for D-PBSLP of alumina and SiC.

iv. Mechanical performance evaluation of alumina and SiC parts printed with D-PBSLP technique.

2.5. Dissertation Outlines

The dissertation consists of seven chapters, including the following: introduction, methodologies, results, and conclusion. The description of each chapter is as follows:

Chapter 1: Introduction

This chapter introduces the dissertation topic, its importance, and other definitions related to the dissertation topic.

Chapter 2: Literature Review

This chapter presents the literature review of the previous studies regarding the dissertation topic, the classification of ceramic materials with an emphasis on alumina and SiC, Additive Manufacturing of Ceramics. Finally, the research objectives are included.

Chapter 3: Research Methodology

This chapter describes the research methodologies utilized in this dissertation, including numerical model development, PBSLP printers, experimental analysis devices, used feedstock materials (powder), and optimization techniques. In addition, the evaluation methods for mechanical performance are presented in this chapter.

Chapter 4: Numerical Model Validation

This chapter discusses and evaluates the development of the numerical model and its validation with the experimental results. The numerical model results that included Alumina and SiC as powder materials were used to interpret the experimental data better.

Chapter 5: Multi-layer simulation of D-PBSLP

This chapter presents an initial numerical investigation for D-PBSLP of alumina and SiC, including ceramic-laser interaction, numerical investigation of scanning strategies, and multilayer simulation.

Chapter 6: D-PBSLP of Alumina

This chapter discusses the experimental and numerical results obtained for alumina. It began with the prediction of process parameter values using the developed numerical model, and the obtained parameters from the numerical model served as a guide throughout the experimental study. In addition, numerical simulation was used to improve the interpretability of the experimental outcomes. Lastly, optimization of process parameters using optimization techniques and mechanical performance evaluation were presented.

Chapter 7: D-PBSLP of SiC.

The contents of chapter 7 are similar to those of chapter 6, except that it is dedicated to SiC.

Chapter 8: Conclusion and Future work

In this chapter, the major conclusions drawn from this dissertation are presented. In addition, future research directions were highlighted.

3. RESEARCH METHODOLOGY

This chapter describes the methodologies used to conduct the research covered in this dissertation, including numerical model development, powder feedstock preparation, PBSLP printers, and characterization and analysis instruments. In addition, the optimization techniques used to optimize the process parameters are detailed. Methods for evaluating mechanical performance are also described.

3.1. Numerical Procedure

The success of any material's PBSLP is dependent mainly on the use of appropriate parameter combinations. PBSLP parameters include laser power (p), scanning speed (v), hatching distance (space) (h), layer thickness (t), and scanning strategy. These parameters are dependent on each other. This implies that changing the value of one parameter necessitates altering the values of the remaining parameters. The method of trial and error is expensive and time-consuming. Consequently, there is a need for a numerical tool that can simulate the PBSLP, describe the effect of any parameter change, and facilitate a more accurate interpretation of the experimental results. In addition, the numerical model should be able to obtain an initial value for the process parameters, which serves as a guide for the experimental work.

3.1.1. Model development

The laser melting/sintering of powder particles is a complex process, and in order to model it mathematically, the following assumptions were considered during model development: (1) the powder bed is a homogeneous and continuous medium; (2) the laser heat source has a uniform heat distribution; (4) the melting/sintering pool top surface is flat; (5) no evaporation losses were considered; and (6) heat transfer by radiation and convection was considered.

In PBSLP, heat is transferred from the laser source to the powder bed via conduction, with a portion of the laser power used to melt/sinter the powder particles and the remainder reflected into the printer chamber. Heat transfer can be described using the energy equation (2.1) [115].

$$\rho C_p \frac{\partial T}{\partial t} = \nabla . (k \nabla T) + S_h \quad (2.1)$$

ρ is the powder density, T is the temperature, C_p is the powder specific heat, k is the thermal conductivity, and S_h is the laser heat source.

The laser heat source is assumed to have a Gaussian distribution and is described by the equation (2.2) [115]:

$$S_h = AI_o\alpha \, exp\,(-2\,\frac{(x - v_x t)^2 + \left(y - v_y t\right)^2}{R^2} - \alpha z) \quad (2.2)$$

Where A is the powder absorptivity, I_o is laser density, α is the absorption coefficient, R is the laser radius, and v is the laser scanning speed. It is important to mention the difference between absorptivity and absorption coefficient. Absorptivity measures how strongly a material absorbs light at a specific wavelength, whereas the absorption coefficient determines how deeply a specific wavelength of light can penetrate a material before being absorbed. According to Fan et al. [115], the absorption coefficient of alumina was considered, whereas, for SiC, the absorption coefficient was considered according to [142]. The laser's intensity is expressed as:

$$I_o = \frac{P}{\pi R^2} \quad (2.3)$$

$$R = \frac{D_b}{2} \quad (2.4)$$

P and D_b in equation (2.4) is the laser power and laser beam diameter, respectively. Equations (2.3) and (2.4) were used for D-PBSLP of Alumina.

For laser sintering simulation (D-PBSLP of SiC), the laser intensity can be expressed as [143]:

$$I_o = \frac{2 \times P}{\pi\, \omega^2} \tag{2.5}$$

$$\omega = \frac{D_b}{2 \times 2.146} \tag{2.6}$$

Where ω is the laser characteristic radius, the factor of 2.146 in Equation (2.6) was derived from calculating the distance from the laser center at which the laser intensity distribution has I/I0 = $1/e^2$ (0.135). This allows I_0 to be easily and more accurately calculated using the characteristic radius according to [143].

The scanning speed vectors control the laser movement on the powder bed v_x and v_y in equation (2.2). Through this movement control, the scanning strategies can be simulated. The initial position of the laser beam is adjusted by the coordinates x, y and z described in equation (2.2).

A User-Defined Function (UDF) for the laser heat source S_h, laser characteristics and powder properties, as a function of temperature, were developed, written, and compiled to be solved using ANSYS FLUENT. Table 3.2 and Table 3.1 summarize the physical properties of alumina and SiC, respectively.

Table 3.1. Physical properties of Alumina used in the numerical model.

Property	Value	Ref.
Density, kg/m^3	3910	BCRC, measured
Specific heat J/kg-k	= 3×10^{-13} T^5 - 3×10^{-9} T^4 + 5×10^{-6} T^3 -0.0073T^2 + 5.0097 T- 190.71, (T ≤ 2450) = 1360, (T > 2450) (T, temperature in K)	[115]
Thermal conductivity W/kg-K (T, temperature in K)	= -3×10^{-15} T^5 - 3×10^{-11} T^4 -10^{-7} T^3 +0.0002T^2 -0.203 T+ 79.673, (T ≤ 2450) = 5.5, (T > 2450) (T, temperature in K)	
Melting point, K	> 2327	
Latent heat of melting, J/kg	1137900	
Absorptivity at 1046 µm wavelength[1]	0.5	measured at BCRC
Absorptivity/CO2 laser[2]	0.96	[144]
Absorptivity/Fiber laser[2]	0.03	

[1]This absorptivity for the modified spray dried alumina.
[2]This absorptivity for pure alumina powder.

Table 3.2. Physical properties of SiC used in the numerical model.

Property	Value	Ref.
Density, kg/m^3	3210	Mersen Boostec®
Specific heat J/kg-K (T, temperature in K)	= -0.0005 T^2 +1.2911 T+ 337.13, (T ≤ 1273.15) = 0.0201 T + 1285.9, (1273.15 < T < 2200) = 1330, (T > 2200)	Mersen Boostec®, [38-39]
Thermal conductivity W/kg-K (T, temperature in K)	= 0.0002 T^2 -0.4427 T +295.88, (T ≤ 1273.15) = -8E-05 T +5.676, (1273.15 < T < 2200) = 5.5, (T > 2200)	Mersen Boostec®, [38-39]
Sintering point, K	>2525	Mersen Boostec®
Latent heat of sintering, J/kg	370000	[38-39]
Absorptivity at 1046 µm wavelength	0.55	CIRIMAT, measured

The initial and the boundary conditions which were considered in this study are according to equations (2.7) and (2.8), respectively [147]. Figure 3.1 shows the initial and boundary conditions applied in the developed numerical model.

$$T(x,y,z)_{t=0} = T_O \tag{2.7}$$

$$-k\left(\frac{\partial T}{\partial z}\right) = \dot{S_h} - h_{cov}(T_a - T_s) - \sigma\mathcal{E}(T_a^4 - T_s^4) \tag{2.8}$$

Where T_O is the room temperature and is set to 300 K, h_{cov} is the heat convection coefficient, T_a is the powder layer's initial temperature, T_s is the temperature of the surroundings, $\mathcal{E}$ is the radiation coefficient, and σ is the Stefan-Boltzmann constant.

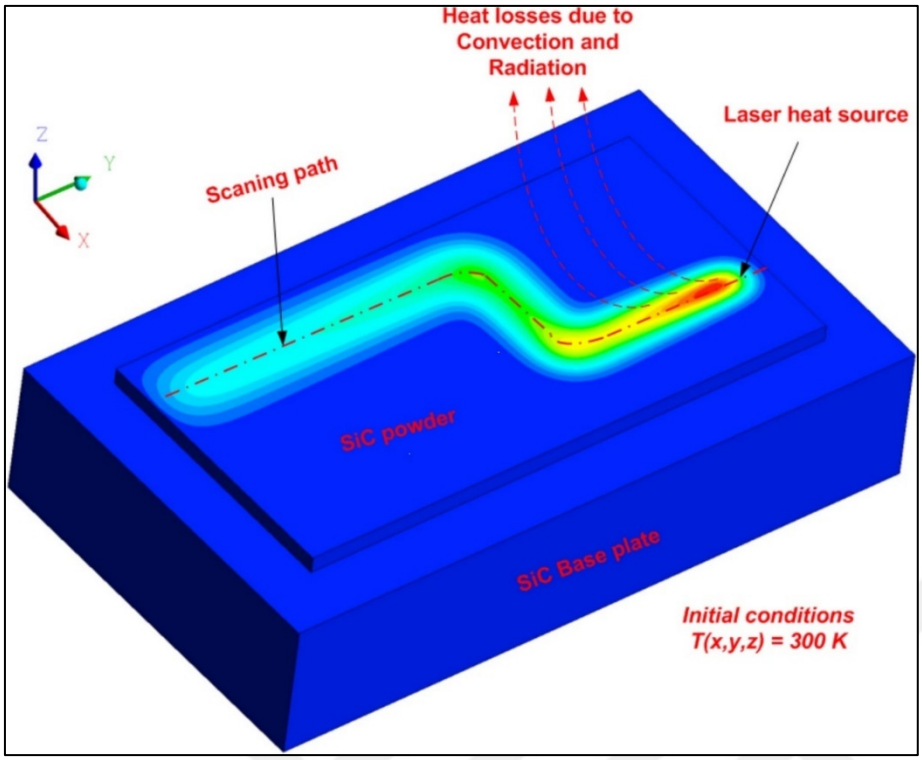

Figure 3.1. Initial and boundary conditions are used in the developed model.

The melting/sintering and solidification during PBSLP were modelled using the enthalpy technique described in [148]. This technique is predicated primarily on the material enthalpy, defined as the system's total heat content, and can be expressed by the sum of the system's internal energy and the product of the pressure and volume, as shown in the equation (2.9). Additionally, the enthalpy can be expressed by the system's sensible heat and latent heat content, as defined by the equation (2.10).

$$H=U+PV \tag{2.9}$$

$$H=h+\Delta H \tag{2.10}$$

Where U represents internal energy, P represents pressure, V represents volume change, h represents sensible heat, and ΔH represents latent heat. h and ΔH can be expressed as follows, as per [148]:

$$h= h_{ref} + C_p \Delta T \tag{2.11}$$

$$\Delta H=\beta L \tag{2.12}$$

Where h_{ref}, L, and β represent the reference enthalpy, the latent heat, and the liquid fraction, respectively. The liquid fraction could be determined as follows [148]:

$$\beta = \frac{T - T_{solidus}}{T_{liquidus} - T_{solidus}} \tag{2.13}$$

The temperature T can be calculated by solving equation (2.1) and then used to measure β, which defines the melting/sintering or solidification region within the solution domain according to equation (2.14):

$$\beta = \begin{cases} < 1 & solid\ region \\ = 0 & transition\ region \\ > 1 & melting\ region \end{cases} \tag{2.14}$$

Utilizing a coupled thermal-mechanical analysis, Finite Element Analysis (FEA) was used to calculate the thermal stress and distortion developed in the 3D-printed part. The FEA is predicated primarily on the stress-strain relationship. After yielding, this relation is considered to be a nonlinear, plastic region. As described in [149], the bilinear plasticity model was used to characterize the relationship between stress and strain.

The mechanical properties of alumina used in the calculation of residual stress and distortion are expressed as a function of temperature according to [150–153], whereas the mechanical properties of SiC are expressed according to [145, 146].

3.1.2. Model geometry

The developed model is solved within the domain of the model geometry. In order to simulate a real-world situation, it is essential to consider geometry with great precision. As depicted in Figure 3.2, PBSLP consists of three primary components: the scanned powder, the surrounding powder, and the baseplate. As can be seen in Figure 3.3, the model geometry considered in this dissertation reflects these three primary components: the scanned powder, the surrounding (unscanned) powder, and the baseplate. Changing the model's dimensions permits the simulation of a single scanning path, multiple scanning paths (scanning strategy simulation), and multi-layer simulation. The dimensions of the model are summarized in Table 3.3.

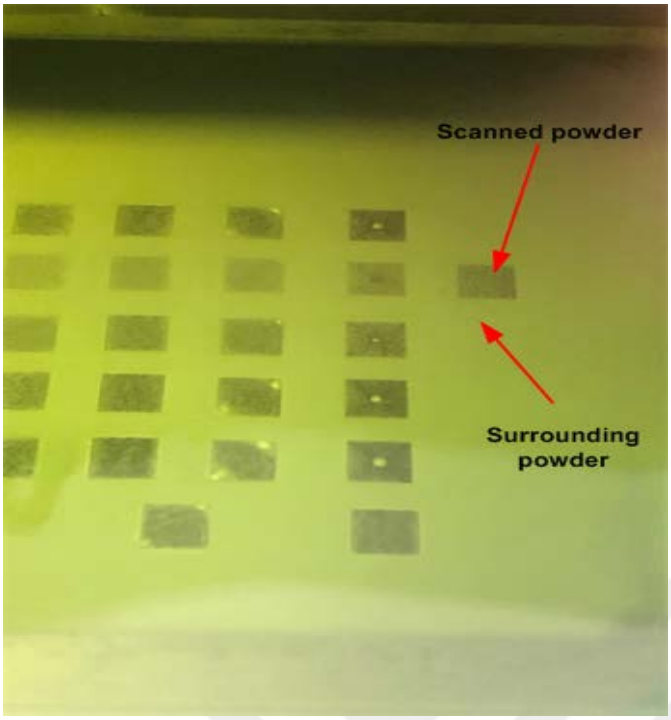

Figure 3.2. Real PBSLP powder bed.

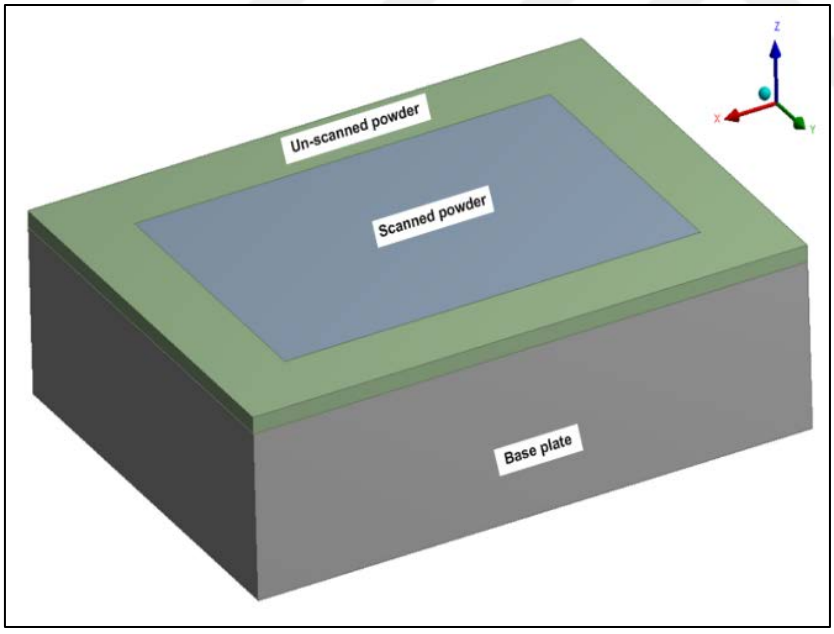

Figure 3.3. The model geometries used in this study.

Table 3.3. Model geometry dimensions

Parameter	Base plate	Powder layer
Length (mm)	4	3
Width (mm)	2.5	1.5
Thickness (mm)	1	Variable

3.1.3. Computational domain

The computational domain (the mesh) is the field at which the previously described governing equations are solved, and it is responsible for the accuracy of the numerical model's output. Therefore, the model geometry should have been carefully meshed. The heat is transferred from the laser source to the powder layer, then to the surrounding powder and the baseplate. To allow for this heat transfer, it is necessary to define the contacting surfaces between model geometry components. Figure 3.4 depicts the computational domain (mesh) where the ANSYS Mechanical Meshing Tool was used. Consideration was given to a fine discretization for the powder layer and a coarser discretization for the unscanned powder and the baseplate.

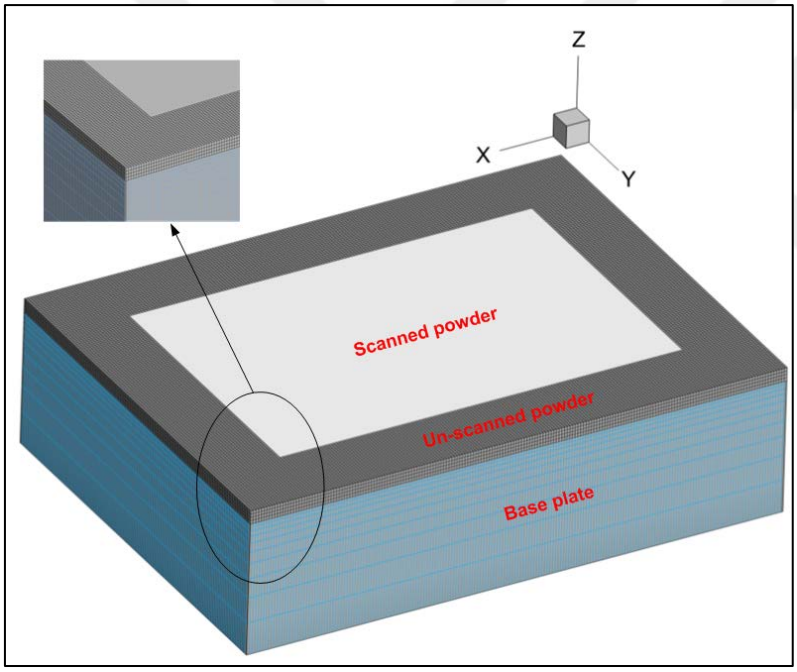

Figure 3.4. The computational domain (the mesh) used in the analysis (not to scale).

3.2. PBSLP Feedstock Material and Printers

As previously described in Chapter 1, the majority of the PBSLP feedstock is a powder. To obtain high-quality samples, it is crucial to have powders with attractive characteristics. These characteristics include proper powder particle size distribution (PSD), powder morphology, and powder flowability. In this dissertation, the ceramic materials, alumina and SiC were investigated. In this section, both SiC and alumina powder are described.

3.2.1. Alumina powder

As described in Chapter 2, the Nd-Yag or fiber laser absorption by Alumina is extremely low, reaching 3%. Since all PBSLP printers on the market are equipped with Nd-Yag or fiber laser, the absorptivity of the alumina powder should be enhanced for the PBSLP technique to be successful. Several methodologies enhance ceramic powder's absorptivity, including using absorptivity enhancers and calcination [20, 154]. Using absorptivity enhancers to improve the absorptivity of a powder is an appropriate technique because it employs a small amount of another material to increase absorptivity without affecting the powder's properties. Numerous previous studies [155–157] have utilized this technique to print ceramic powder using the PBSLP method. In addition, powder morphology is a significant factor that should be considered. The powder's morphology substantially impacts the powder's flowability on the printer bed and, consequently, the density of the printed parts [158, 159]. It has been reported that the spherical powder shape is highly recommended in PBSLP due to its good flowability compared to other shapes that experience low flowability due to interaction between powder particles [68]. The spray-drying method or high-temperature plasma technology can be used to produce spherical powder from ceramic materials. The spray-drying method produces a fully spherical powder shape with a controlled particle size distribution; however, the obtained density is relatively low due to the powder's porous structure [160], whereas plasma technology can produce a solid-spherical powder shape, which can significantly increase the density of the 3D-printed ceramic shapes [161, 162]. Spray drying technique mainly depends on producing dry granules from slurry, as it rapidly dries droplets with hot gas and pressure. Four steps comprise the entire procedure: preparation of the powder slurry, atomization of the feeding slurry, contact of slurry droplet with air, droplet drying, and separation of dried particles from the hot gas [163]. Ceramic powder, water, and dispersant are typically combined to produce powder slurry (with specified wt.%). After preparing the powder slurry, the suspension containing well-dispersed particles is pumped into a nozzle and the liquid feedstock is ejected as a spray of droplets. In a chamber, where the liquid phase evaporates, droplets are dried, resulting in the formation of dried granules.

The spray drying technique was used in this study to prepare alumina feedstock for the D-PBSLP by increasing alumina's absorptivity. Alpha-alumina powder (P172LSB, Alteo, France) was used as the raw material. The powder slurry was made by combining 1200g of

alumina powder with 44.8 wt.% water and 1 wt.% carboxylic acid dispersant (Dolapix CE64, Zschimmer & Schwarz, Germany) relative to the alumina powder weight. The slurry was then ball-milled for 12 hours with alumina balls to break up agglomerates. The preparation of the slurry is depicted graphically in Figure 3.5.

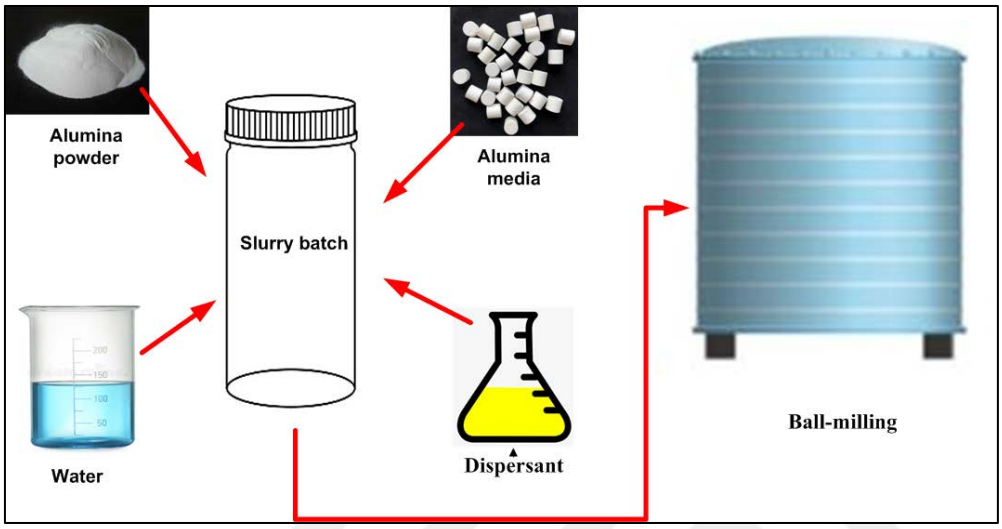

Figure 3.5. Graphical representation for the alumina powder slurry preparation method.

In order to increase the powder absorptivity, a graphite-based colloidal suspension (AQUADAG 18%, Acheson) was added to the powder slurry following the milling step and mixed uniformly in order to introduce dopant into the powders. The volume percentage of dopant (relative to the volume of ceramics) is determined to be 0.1 vol%.

The well-dispersed particle suspension is then pumped into the atomizer, which ejects the liquid feedstock as a spray of droplets. The droplets are dried in a chamber where the liquid phase evaporates, forming dried granules. Spray drying was conducted with a Niro machine (GEA, Germany) available at the Belgium Ceramic Research Centre for this study (BCRC). The spray dryer (Niro, GEA, Germany) employed in this study is depicted graphically in Figure 3.6.

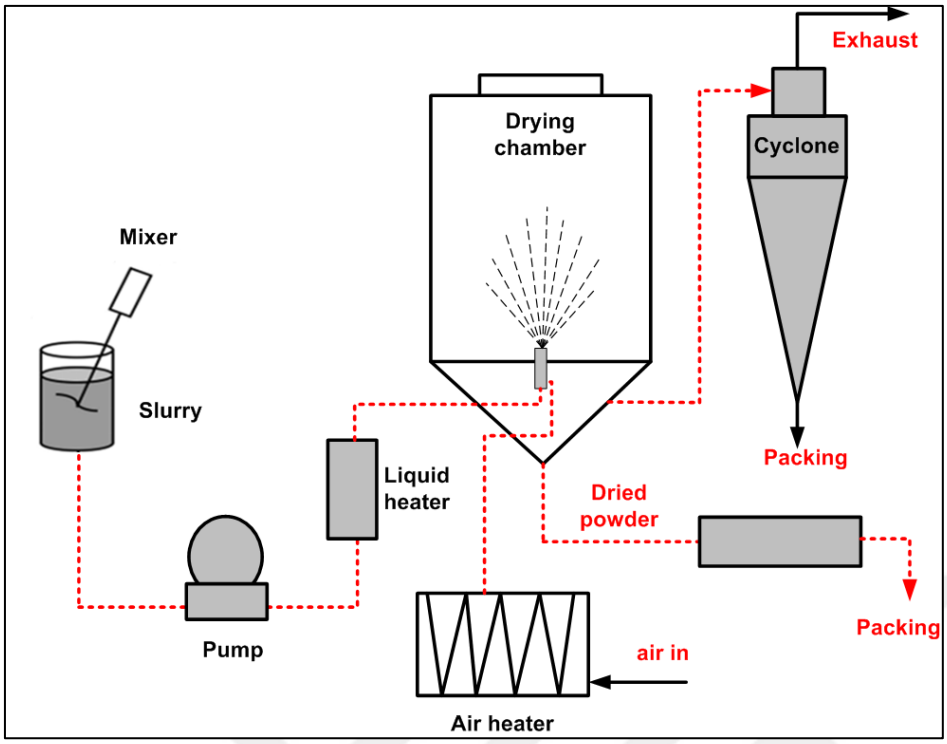

Figure 3.6. Graphical representation for the spray-dryer (Niro, GEA, Germany) used in this study.

Numerous factors, including inlet temperature, solid loading of the suspension, feeding rate, and organic content, affect the quality of the spray-drying process and the properties of the final dried products. For this work, the inlet temperature ranged between 210°C and 225°C, and the outlet temperature was maintained at approximately 95°C. The intake air flow rate was 60 L/min, and the suspension feeding rate was 25 rpm.

After spray drying, both the main and cyclone fraction powders were dried at 100 °C to remove any remaining moisture, as it is considered a crucial step since the powder's flowability is affected by moisture content. Moisture can create bridges between powder particles, reducing their flowability, but it can also act as a lubricant to reduce interparticle friction [164, 165]. Before printing, therefore, the powders were dried to remove any residual moisture [166, 167]. The spray-dried technique yields two primary powder categories; the main part and cyclonic part are referred to as Al-M and Al-C, respectively. In addition, the main part was divided into two batches after sieving at 100 µm to determine the effect of granule size. The fine fraction is designated as Al-MF, while the coarse fraction (powder sizes greater than 100 µm) is designated as Al-MC. The raw alumina powder is designated as Al-raw. The spray-dried alumina powder was evaluated using various characterization

techniques, including SEM images, PSD, and a flowability test. The outcomes of these characterizations are presented in Chapter 6.

The baseplate is an additional aspect that contributes to the success of the ceramic D-PBLSP. To ensure adherence of the first printed layers to the printer baseplate, the material of the baseplate must be compatible with the feedstock. Since the printer's metallic baseplate is made of metal, an alumina-based material baseplate was adhered to the printer's metallic baseplate, as shown in Figure 3.7, and utilized for alumina D-PBSLP.

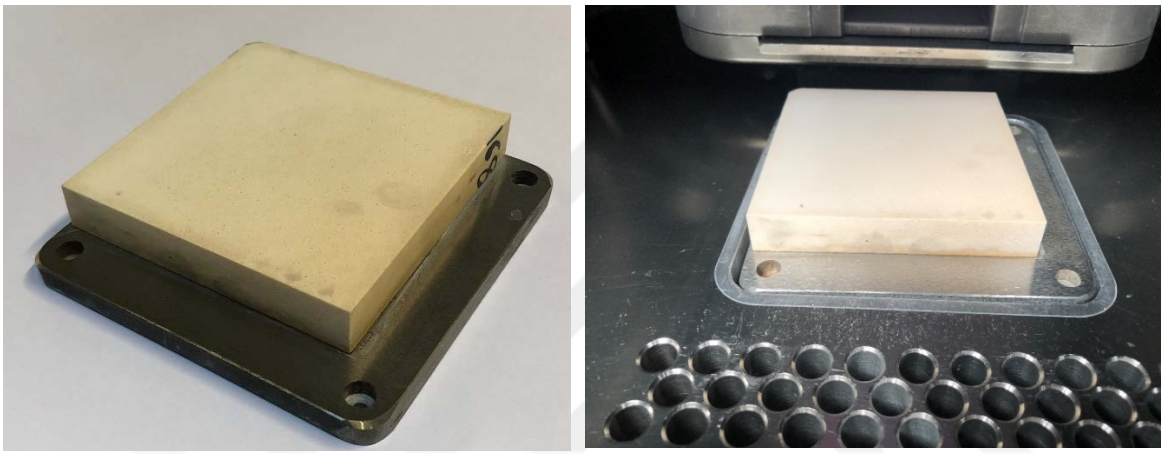

(a) (b)

Figure 3.7. Alumina baseplate used for PBSLP of Alumina (a), Alumina baseplate loaded into the printer bed (b).

3.2.2. SiC powder

The alpha SiC powder with a purity of 98.5 % (Mersen Boostec®, France) without any additives was used for D-PBSLP of SiC. Since the SiC powder absorptivity to fiber laser is as high as 70 %, there was no need to increase its absorptivity or do any further powder preparation prior to its usage in SiC D-PBSLP. SiC circular plates (Mersen Boostec®, France) with a diameter of 65 mm were utilized as a baseplate to ensure that the first printed layers would stick adequately to the printer bed (the same powder material). The circular SiC plates have adhered to the printer's metallic baseplate with Permabond adhesive liquid. Figure 3.8 depicts the SiC baseplate mounted to the metallic baseplate of the printer.

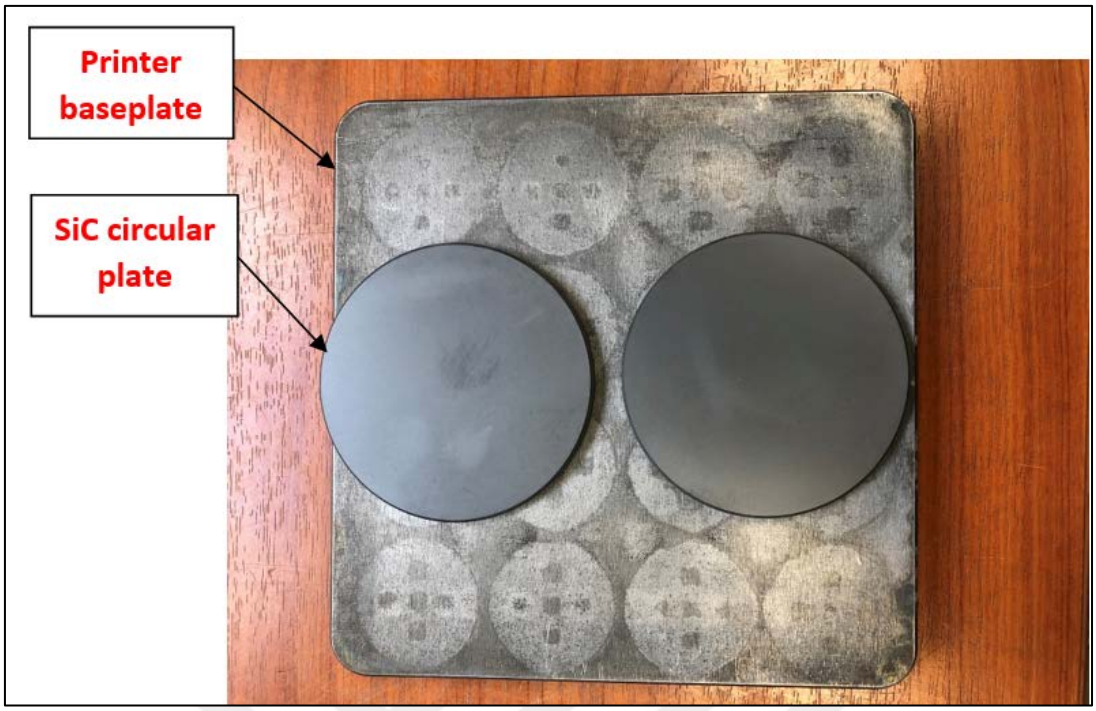

Figure 3.8. SiC circular plates attached to the metallic baseplate.

3.2.3. PBSLP printers

For the D-PBSLP of alumina, the SLM printer (SLM 125, Renishaw®, UK) available at BCRC was utilized (Figure 3.9). This printer has an Nd-Yag laser with a wavelength of 1070 nm, and Table 3.4 summarises its specifications. To prevent oxidation during printing, inert gas (Argon) was employed.

For the D-PBSLP of SiC, the CIRIMAT SLM printer (ProX® DMP200, 3D Systems, US) was utilized (Figure 3.9). This printer is equipped with a fiber laser with a wavelength of 1060 nm and a laser spot size of 70 µm, and Table 3.4 summarises its specifications. The Phoenix 3D printer is equipped with a compaction cylinder that can compact the layer powder after layering to increase the powder bed's packing density and, consequently, the printed samples' density. The compaction mechanism is depicted in Figure 3.10.

Figure 3.9. PBSLP printer used for Alumina and SiC.

Table 3.4. Renishaw® SLM 125 and Phoenix 3D printer specifications.

No	Item	Renishaw® SLM 125 printer	ProX® DMP 200
		Range	Range
1	Laser power	Up 200 W	Up 300 W
2	Laser spot size	35:200 µm	70:200 µm
4	Building volume	100×100 ×100 mm^3	140 × 140 × 125 mm^3
5	Inert gas	Argon	Argon

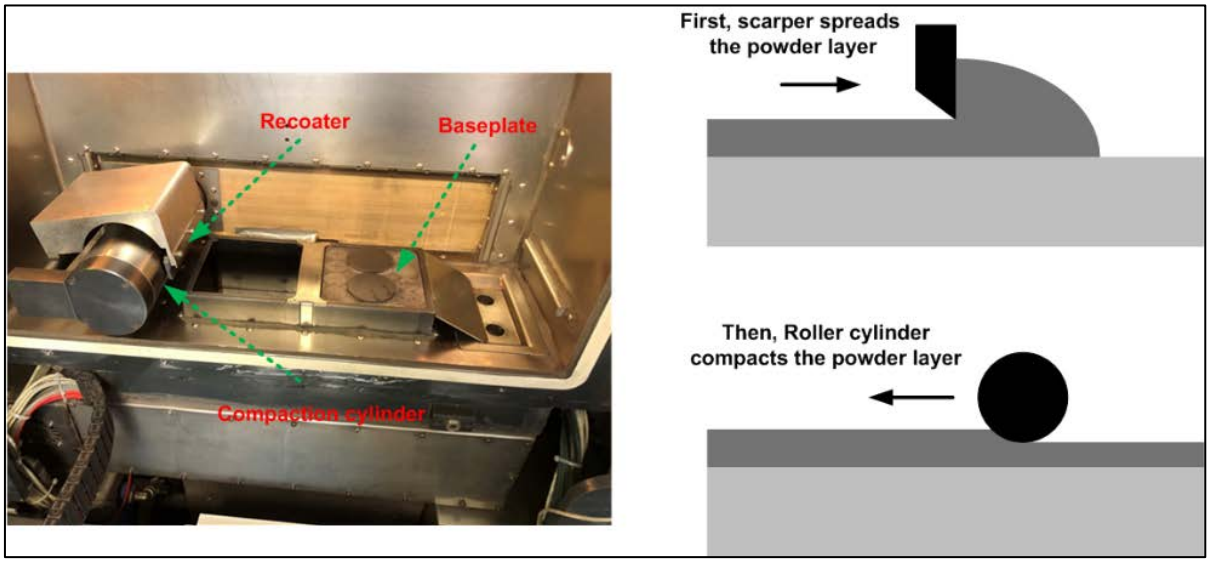

Figure 3.10. The layering and the compaction system in ProX® DMP 200 printer.

Various scanning strategies, including linear, concentric, and island, are available on these printers. Figure 3.11 depicts the scanning strategies investigated for alumina PBSLP,

including zigzag with different orientations, concentric out-in, island concentric, and island-linear. Figure 3.12 illustrates the investigated scanning strategies for SiC PBSLP, including linear, inclined-zigzag, concentric out-to-in, and hexagonal. For the hexagonal strategy, the hexagon size was 700 µm, and the scanning pattern within the hexagon was a 45°-inclined zigzag repeated randomly until the powder layer was scanned.

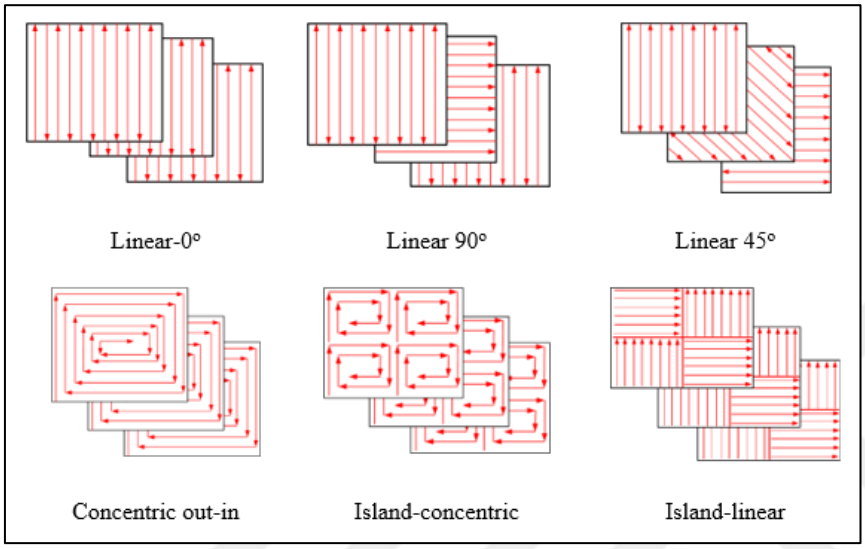

Figure 3.11. Scanning strategies investigated for PBSLP of Alumina.

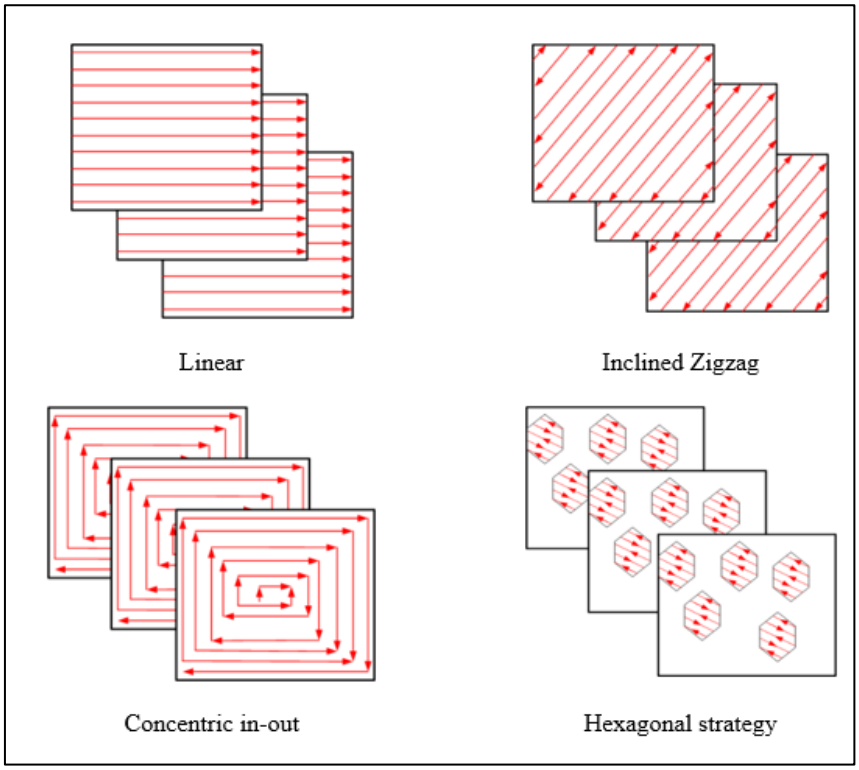

Figure 3.12. Scanning strategies investigated for PBSLP of SiC.

3.3. Characterization Methods and Instruments

Several characterisation techniques were used to assess the quality of the printed samples, including relative density measurements, SEM imaging, optical microscopic imaging, XRD analysis, Ramon spectrum, and mechanical testing (microhardness measurement, compression test, and flexural test). The sections below present each characterization technique in detail. Several characterization methods, including relative density measurements, SEM imaging, optical microscopic imaging, XRD analysis, and mechanical testing (microhardness measurement, compression test, and flexural test), were utilized (microhardness measurement, compression test, and flexural test). The sections below describe each method of characterization in detail.

3.3.1. PBSLP feedstock characterization

The feedstock (powder) characteristics are crucial for the effectiveness of additive manufacturing (AM) materials utilizing the PBSLP process. A suitable powder property will significantly impact the printed components' resulting properties (relative density and mechanical performance). The powder must have an appropriate particle size distribution (PSD), morphology, flowability, and absorbency to be suitable for the PBSLP. The subsequent subsections detail the technique utilized to measure/evaluate the previously described attributes.

Previous research [68] indicated that the optimal PSD for the PBSLP approach should be in the region of tens of microns. Low PSD induced powder particle aggregation, which hindered smooth deposition and impaired the quality of the powder bed. In addition, employing a PSD higher than 100 μm with the PBSLP approach is impractical because the majority of powder particles will end up in the excess powder tank due to the tiny layer thickness (typically, the layer thickness in the PBSLP technique varies from 20 to 100 μm). Several approaches, including laser analysis, image analysis, sieve analysis, and viscous fluid analysis [170], can be used to determine powder particle size distribution (PSD). The Mastersizer MS 3000 (Malvern Panalytical®) laser particle size analyzer was utilized to measure the particle size distribution of alumina and SiC powder in this dissertation.

Powder morphology (shape) is the essential powder property since it significantly impacts powder flowability. Numerous prior PBSLP tests have indicated that having a spherical powder form dramatically improves the powder's flowability and significantly contributes to achieving the desired powder bed quality. Due to the internal friction between the powder particles, irregular powder forms have a negative impact on flowability. As indicated in the sections that follow, scanning electron microscopy (SEM) was utilized to investigate the morphology of alumina and SiC powders.

Powder flowability is also an important factor for the efficacy of PBSLP, as it significantly impacts powder bed quality. Possessing excellent powder flowability will significantly improve the powder layering and packing density of the powder bed. There are numerous methods for determining the powder's flowability, including the angle of repose, Hall flow meter, carr index, and Hauser ratio. In this research, the angle of repose was regarded as a simple and reliable approach for measuring the flowability of SiC powder while for alumina powder, Hall flow meter was used to evaluate the powder flowability. The angle of repose is the slope of a stepped material from a horizontal plane. At this point, the angle of repose can be determined by allowing the powder to flow from a funnel onto a smooth baseplate until it piles without falling [171]. Figure 3.13 depicts a schematic illustration of the angle of repose measurement. The value of the angle of repose is mainly governed by the internal friction between particles, the baseplate's roughness, and the powder-flowing funnel's height. The flowability indexing is described in Table 3.5 based on the angle of repose value [172].

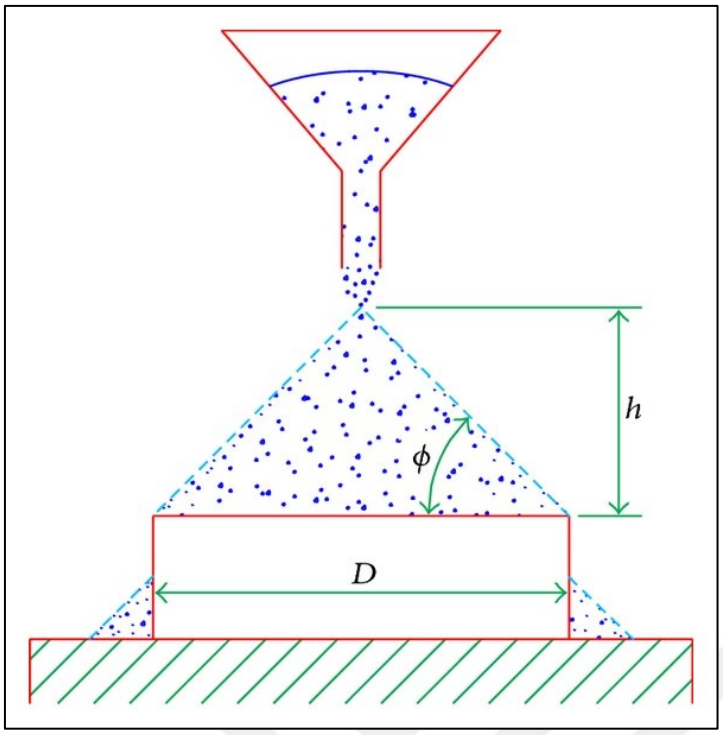

Figure 3.13. Angle of repose [171].

Table 3.5. Flowability indexing using the angle of repose [172].

No	Flowability	The angle of repose (degrees)
1	Excellent	25-30
2	Good	31-35
3	Fair	36-40
4	Passable- may hang up	41-45
5	Poor	46-55
6	Very poor	56-65
7	Very, very poor	> 66

3.3.2. Relative density and porosity evaluation

The first parameter determining the quality of a printed sample, particularly for ceramic materials, is the obtained relative density. In this dissertation, the Archimedes method was utilized for measuring relative density for alumina and SiC printed samples. For alumina, dry samples were weighed in the air before being placed under a vacuum. After achieving a suitable vacuum condition in a closed container, the water flow was opened to fill all interior pores with water. Afterwards, the samples were measured in the air and underwater. The relative density and porosity level were determined using these three measurements. Figure 3.14 (a) depicts the weighting balance (Bp 110 S, Sartorius, Germany) used to measure the relative density of alumina samples.

For SiC samples, samples were first weighed in air and then measured in water and from these two readings, the relative density is calculated directly from the user balance. Figure 3.14 (c) depicts the weighting balance (AS 220R2, RADWAG, UK) utilized to measure the relative density of SiC samples.

(a) (b) (c)

Figure 3.14. Relative density measurement; Balance used to measure the relative density of alumina samples (a), the apparatus used to vacuum alumina samples (b), and the balance used to measure the SiC sample's relative density(c).

Micro-computed tomography (Micro-CT) analysis was used to understand the porosity distribution within the samples. Micro-CT is a high-resolution 3D image analysis technique that uses X-rays to detect the interior of an object slice by slice. Micro-CT utilizes a series of X-ray-obtained 2D images, which allow for the visualization of internal sample details. In addition, using the 2D images, a 3D visualization of the entire sample can be created, allowing for a high-resolution look inside the component. In addition, it can provide volumetric information about the sample, including the porosity level and its distribution within the sample.

In this dissertation, Micro-CT was performed at Université de Toulouse (France) using the Micro-CT facility (Phoenix Nanotom, Baker Hughes, USA). As the specimen rotated 360 degrees, a cone-shaped X-ray beam with an energy of 80 KeV was transmitted and produced 1440 images (7.5 m/voxel). A volume image stack was created using Datos X (Pheonix X-ray system) and VG Studio Max (Volume Graphic GmbH, Germany).

3.3.3. Optical microscopic analysis

Using a series of lenses that magnify the sample surfaces, the optical microscope can be used to obtain an initial investigation of the sample surfaces. The sample is positioned beneath the lens, and a highly magnified image of the examined surface is visible to the human eye. It is possible to examine the sample at various magnifications. In this dissertation, samples of alumina and SiC were examined using the 3D laser scanning microscope (VKX-250, Keyence, Japan) available at the BCRC. It employs double-telecentric lenses and an advanced triangulation algorithm (multi-triangulation algorithm) to generate a 3D view of surface textures; it can be used for profile, height difference, planarity, volume, area, and surface roughness measurements. In addition, surface roughness measurements for alumina and SiC samples were performed using this microscope. Figure depicts the optical microscope (KEYENCE VR-3000) utilized in this dissertation to examine the samples' top surface and surface roughness measurements.

Figure 3.15. The optical microscope (KEYENCE VR-3000) used to check the samples.

3.3.4. Scanning electron microscopy (SEM) analysis

The SEM is a high-resolution electron microscope that can examine the surfaces of samples. It utilizes a low-energy electron beam to scan the sample's surface regularly. It relies on applying kinetic energy to the sample surfaces via the electron beam. When an electron beam strikes the surface of a sample, two types of electrons are reflected: secondary electrons and backscattered electrons. A detector collects reflected secondary electrons from the sample's

top surface to generate a high-magnification image of the sample's surface. The nature of an area is determined by the number of secondary electrons reflected from it, with a high number of secondary electrons reflected from raised surfaces and a low number reflected from depressed surfaces. Consequently, raised surfaces will appear brighter than depressed ones [173].

The back-scattered electrons are reflected from areas below the surface and can be used to view the crystalized elements if the instrument is supplied with a back-scattered element detector. Figure 3.16 describes the working principle for SEM [173].

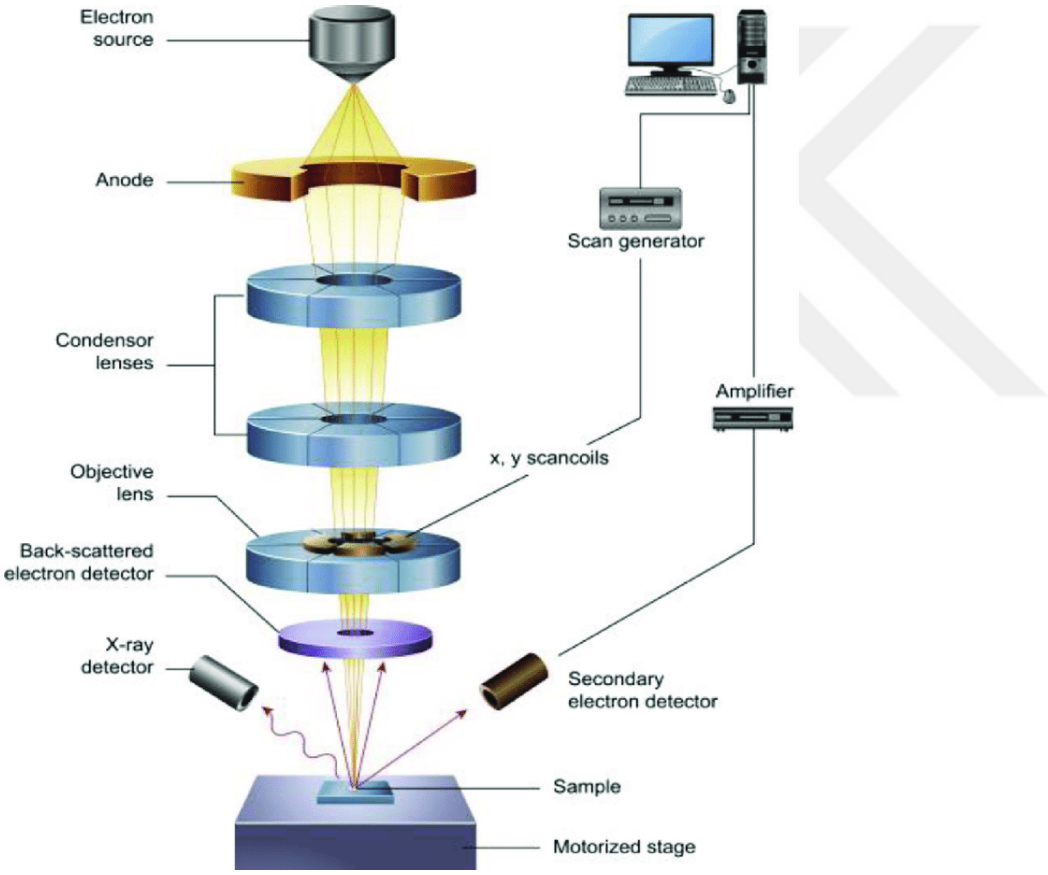

Figure 3.16. The scanning electron microscope working principle [173].

For alumina samples, the electron microscope (Tescan, Czech Republic) was used for SEM analysis, while the electron microscope (SU500, HITACHI, Japan) was utilized for SiC samples.

3.3.5. X-ray diffraction (XRD) analysis

X-ray diffraction (XRD) is a non-destructive technique used to analyze the material's structure and identify the phases present in the sample. It consists of irradiating the sample with X-rays and measuring the intensity and scattering angles of X-rays reflected from the sample. Since the wavelength of X-rays is nearly identical to the distance between atoms, the diffraction angle of a molecule's atoms will influence the diffraction angle. The XRD is illustrated in Figure 2.17a.

When X-ray beams strike atoms within a material, the direction of the beam changes by an angle, θ, from its original direction; this angle is known as the diffraction angle (θ). At a specific diffraction angle, the diffracted beams then interfere with one another; constructive interference occurs if the interfering beams have the same wavelength; destructive interference (the beams cancel each other) occurs if the wavelengths differ.

During the Constructive interference (Figure 3.17b), beams with the same wavelength combine and a new beam with a greater amplitude are generated. This high amplitude at a particular diffraction angle (θ) is converted to a stronger signal, and its wavelength (λ) is measured by a detector. Afterwards, the angle of diffraction (θ) is used to determine the distance between atomic planes (d) utilizing Bragg's law, $\sin\theta = n\lambda/2d$ (Figure 3.17b), and this distance is then used to determine the crystalline structure or composition [173]. BRUKER D8-Advance (D8-Advance, BRUKER, US) at CIRIMAT was used for the XRD analysis of SiC and alumina samples.

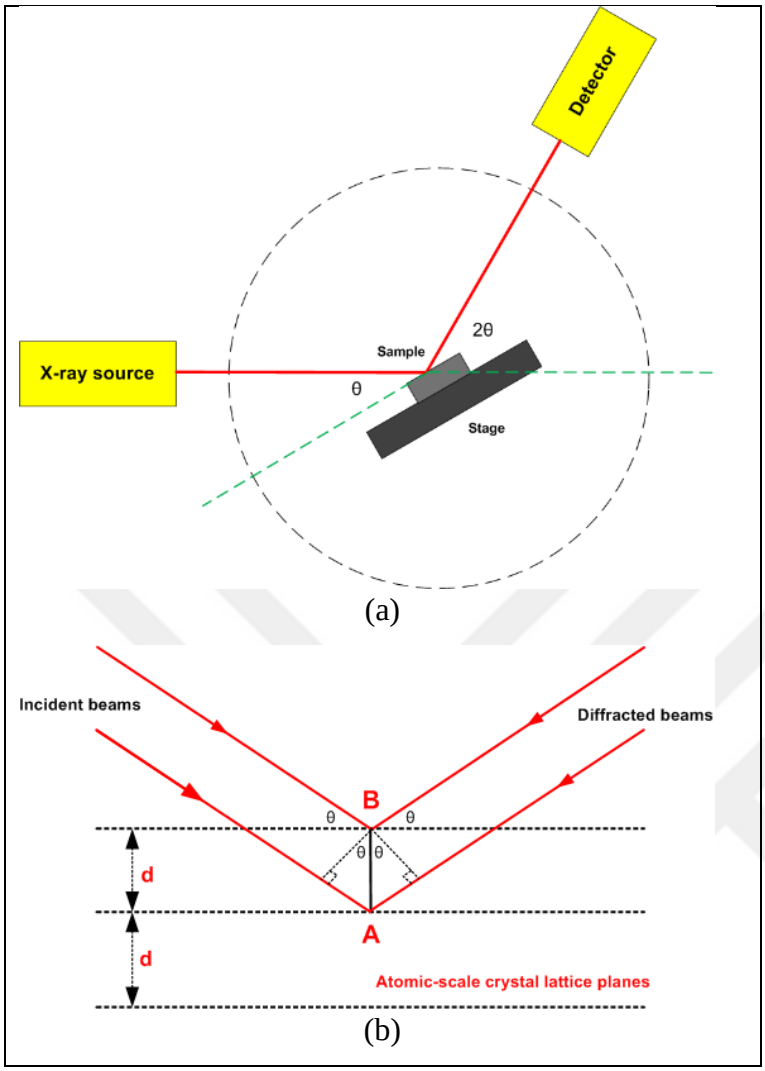

Figure 3.17. Schematic diagram of XRD (a), Schematic illustration of Bragg condition and Bragg's law (b).

3.3.6. XRD-Rietveld refinement

Hugo Rietveld initially described the Rietveld refinement, which is used to characterize crystalline materials. In The Rietveld Refinement, the pattern characteristics that resulted from x-ray diffraction, such as the height, width, and positions of intensity peaks, are used to define numerous aspects of the material's structure. Using the least squares method, the Rietveld refinement technique compares a theoretical pattern profile to a measured profile and refines it. The Rietveld refinement technique can be utilized for a variety of purposes, such as quantitative phase analysis, unit cell size determination, and residual strain measurement [174].

In this dissertation, the Rietveld refinement was used to determine the phases within SiC samples after PBSLP since SiC can decompose into Si and carbon if the temperature during PBSLP exceeds its decomposition point. The Rietveld refinement for SiC dramatically aids in identifying the optimal SiC PBSLP process parameters (Laser power, scanning speed, hatching distance, layer thickness, and scanning strategies).

MAUD (Material Analysis Using Diffraction) software was utilized for the Rietveld refinement. Before using MAUD software for refinement, the software should be calibrated with LaB6 powder XRD diffraction to form a virtual XRD instrument. This is primarily because numerous XRD instrument-related parameters within MAUD should be adjusted during this calibration. After MAUD has been calibrated and a virtual XRD machine has been created, it can be used for refinement.

3.4. Optimization Techniques

Optimization mainly refers to determining the values of process input which can achieve the maximization or minimization of the desired output through a mathematical formulation (techniques) which describes the process and predict its output. The input parameters and their levels, the objective function (minimization or maximization of the output), and the governing constraints are required to use the optimization techniques. The optimization techniques can guide the experimental investigation to reduce its cost and control or eliminate any risk. As the objective of this dissertation is to optimize the PBSLP of SiC and alumina, Taguchi optimization and Pareto ANOVA techniques were used for this purpose.

3.4.1. Taguchi optimization technique

The Taguchi optimization technique, which Dr. Genichi Taguchi developed, is regarded as one of the most effective experimental optimization methodologies for minimizing the number of experiments and identifying the effect of each process parameter on the output. Taguchi optimization method has many benefits, including the ability to consider materials, manufacturing process, and parameters at the design stage, the ability to investigate multiple process parameters simultaneously, and insensitivity to variations in production and user environments [175, 176]. Both control and uncontrollable factors can be considered, and products can be regulated so that they do not deviate from their intended functional

characteristic. Since the Taguchi optimization method can shorten the design and manufacturing stages development cycle, it is widely used in the industry.

Three distinct phases comprise the Taguchi optimization method procedure. The first stage is the design phase, which entails executing the system in which the experiments will be conducted, identifying all the factors (process parameters) that influence the process, determining the range of each factor (levels) included in the experiments, and identifying the response factors. The second stage is the conduction stage, which consists of various steps. In the first step, the orthogonal array (OA) is constructed based on the factors and levels of each factor. The design of the OA should incorporate all feasible treatments that address all factors and levels under consideration. The second step entails conducting experiments in accordance with the OA and determining the response factors for each treatment. The second stage is the most crucial and must be executed with care. All possible factors should be considered during the design phase, as this greatly aids in the early identification of ineffective factors. The final phase is the analysis and optimization phase, which consists of response factor analysis (data analysis), determining the optimal factor value, and conducting a confirmation test using the optimal factor value. In addition, this phase involves establishing a connection between the factors and the response output.

This study used the Taguchi optimization method to optimize the PBSLP process parameters (laser power, scanning speed, and hatching distance) to achieve the highest relative density and the least amount of SiC decomposition. In addition, for PBSLP of alumina, the process parameters were optimized to achieve the highest relative density for alumina.

3.4.2. Pareto ANOVA

Pareto ANOVA is a technique used to analyze data for process optimization, and it can also provide the contribution of each parameter to the response functions straightforwardly [177, 178]. The Signal-to-Noise (S/N) response data can be calculated for each response function and serve as the foundation for the Pareto ANOVA analysis. Consider the sum of all S/N ratio values at the same level of the input parameter when calculating the S/N response data. After calculating the S/N response data for each input parameter, the sum of squares of differences is computed using the following formula for each input parameter.

$$S_d^A = (A_1 - A_2)^2 + (A_1 - A_3)^2 + (A_2 - A_3)^2 \quad (2.16)$$

Where S_d^A represents the squares of difference for a particular input parameter, and the squares of difference for the other input parameters can be calculated similarly. The percentage contribution for each input parameter is computed by comparing the percentage summation of the squares of differences to the total summation for all input parameters. The Pareto diagram is drawn with the percentage contribution for each input parameter considered. In the Pareto diagram, the input parameters are ordered such that the parameter with the most significant contribution comes first, followed by other parameters bd on their contributions.

3.5. Mechanical Characterization

It is essential to investigate the mechanical performance of alumina and SiC samples to determine the effect of the used process parameters and to compare the mechanical performance of the PBSLP technique with that of other conventional techniques. This dissertation utilized microhardness and compressive testing for the mechanical performance evaluation.

3.5.1. Microhardness measurement

Given that ceramic materials are well-known for their high hardness, it is essential to evaluate the hardness of the printed samples and compare it to traditional techniques. Due to the small size of the printed samples (10×10×10 mm3), it is suggested that microhardness be used to evaluate the hardness of the samples. As depicted in Figure 3.18a, the microhardness of alumina samples was measured in CIRIMAT using a Vickers microhardness tester (HM-200, Mitutoyo, Japan). Figure 3.18b demonstrates that, due to the small size of the samples, which made it difficult to fix the sample for microhardness testing, the samples were embedded in plastic resin to form a small cylinder with a diameter of 25.4 mm that could be easily fixed on the tester.

The Vickers hardness method employs a diamond indenter shaped like a right pyramid with a square base and a 136° angle between opposing faces. The loads applied during Vickers microhardness testing are extremely light, ranging between 10g and 1kg. Different loads,

including 100, 200, and 300g, were applied to examine the relationship between microhardness and applied load. The load is applied to the sample's surface for 10 to 20 seconds. After the applied load is removed, the projected area of the indentation is computed using an optical measurement through the tester, and the Vickers Hardness (HV) is computed using the following formula [179]:

$$HV = 1.854\, F/d^2 \tag{2.15}$$

where F represents the applied load (kg), and d2 represents the indentation's projected area (mm2), as shown in Figure 3.18c. Figure 3.18d depicts the indentation formed in a sample of alumina.

(a)

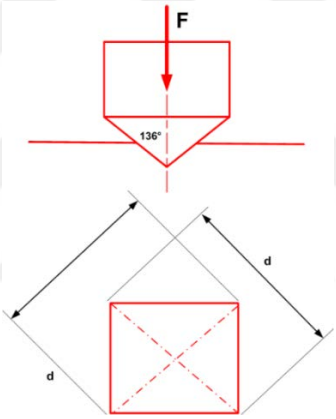

(b)

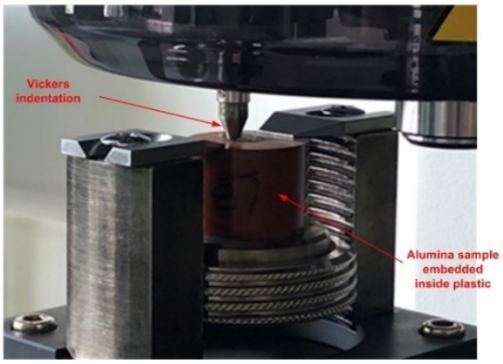

(c)

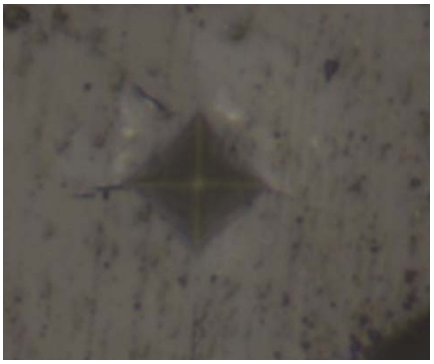

(d)

Figure 3.18. Vickers microhardness tester (HM-200, Mitutoyo, Japan) (a), Schematic diagram of the Vickers microhardness (b), Vickers Hardness indentation applied on alumina sample (c). The indentation shape on alumina sample (d).

3.5.2. Compressive test

It is important to evaluate the compressive strength of alumina and SiC samples printed using PBSLP, as the high compressive strength of ceramic materials is one of their most valuable advantages compared to other material classes. Compressive strength is a material's resistance to failure (breakage) under compression load. The primary purpose of the compression test is to determine the material's behaviour under a compression load and to determine various material properties, such as the stress-strain curve, elastic modulus, yield strength, compressive strength, and passion ratio. Cubes, cylinders, or other shapes as described in [180] may be used to represent the compressive load specimen. The cylindrical compressive test specimens used in this dissertation have a diameter of 10 mm and a length of 20 mm.

The compression tests were performed using a Z100 Universal testing machine (Zwick, Germany) with a 100 kN cell force, and the top head of the machine was lowered at a rate of 0.5-1 mm/min until failure occurred. The compressive strength can be calculated using the following equation:

$$\sigma_c = F_{max}/A \tag{2.16}$$

σ_c represents the compressive strength, F_{max} is the maximum compressive load, and A is the cross-sectional area of the compressive sample.

4. NUMERICAL MODEL VALIDATION

In order to effectively employ the numerically developed model for process parameter investigation and PBSLP simulation, it is essential to verify that the numerical model's results correspond to the experimental results. This can be accomplished by validating the numerical model with experimental data, as described in this chapter.

4.1. Numerical Solution Procedure

ANSYS FLUENT was used to solve the developed numerical model. The process parameters (laser power, scanning speed, layer thickness, hatching distance, and scanning strategies) were considered through the UDF, which was developed to simulate the melting/sintering process. Figure 4.1 shows the steps followed to solve the developed numerical model. A mesh density test was carried out to avoid inaccurate results from low-quality meshing. Three different meshes, A, B, and C (Table 4.1), were investigated regarding the convergence in the obtained results from each mesh. The maximum temperature obtained during scanning was used as a testing criterion. Table 4.1 summarizes the obtained maximum temperature for each mesh, and the maximum temperature for mesh A and B was 2376.3 K and 2379.4 K, respectively, with an error of 0.1% between the two values. Any discretization after level B will give accurate results; therefore, mesh C was used for this study. Two important factors that significantly affect the accuracy of the results are the time step size and the number of iterations per time step. They were considered, selected, and tested to ensure that they did not affect the accuracy of the results. The time step size was 0.00001s, while 20 iterations per time step were used. Finally, the results were measured when the temperature history became stable, as shown in Figure 4.2.

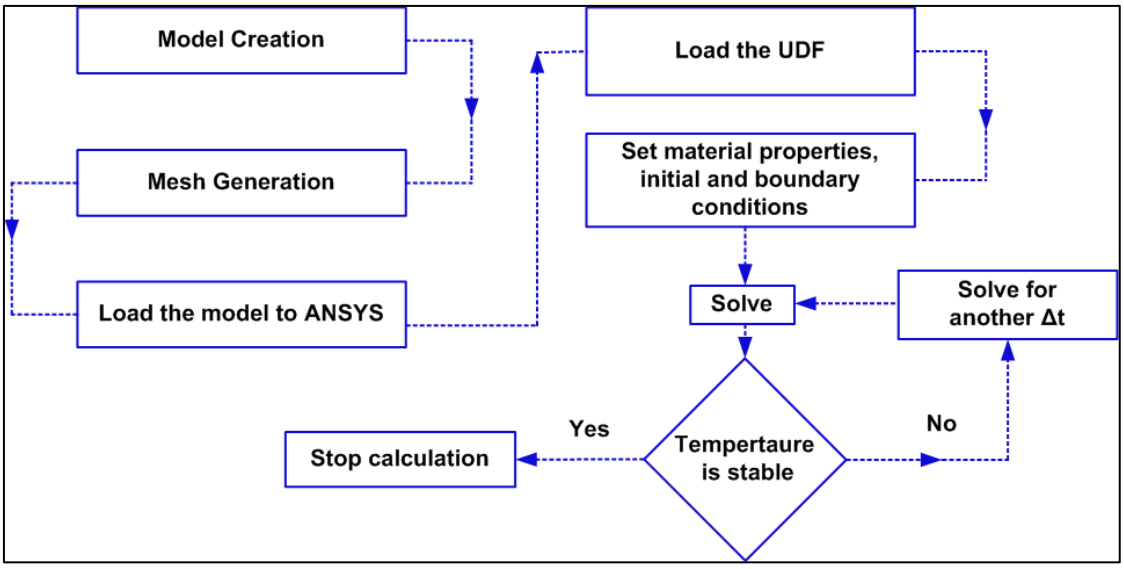

Figure 4.1. Numerical procedure followed during the model solution.

Table 4.1. Mesh density analysis test.

Mesh	A	B	C
Mesh top view	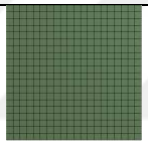	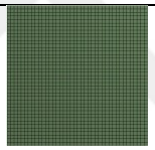	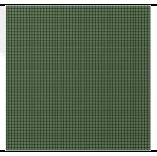
Element size, µm	5	2.5	2
Time per time step, sec	3.92	6.89	8.4
Temperature, K	2343.7	2376.4	2379.4
Number of cores*	48		

* 2×Intel® Xeon® Gold 6252 Processor (48 cores) is used for calculation with 96 Gb RAM.

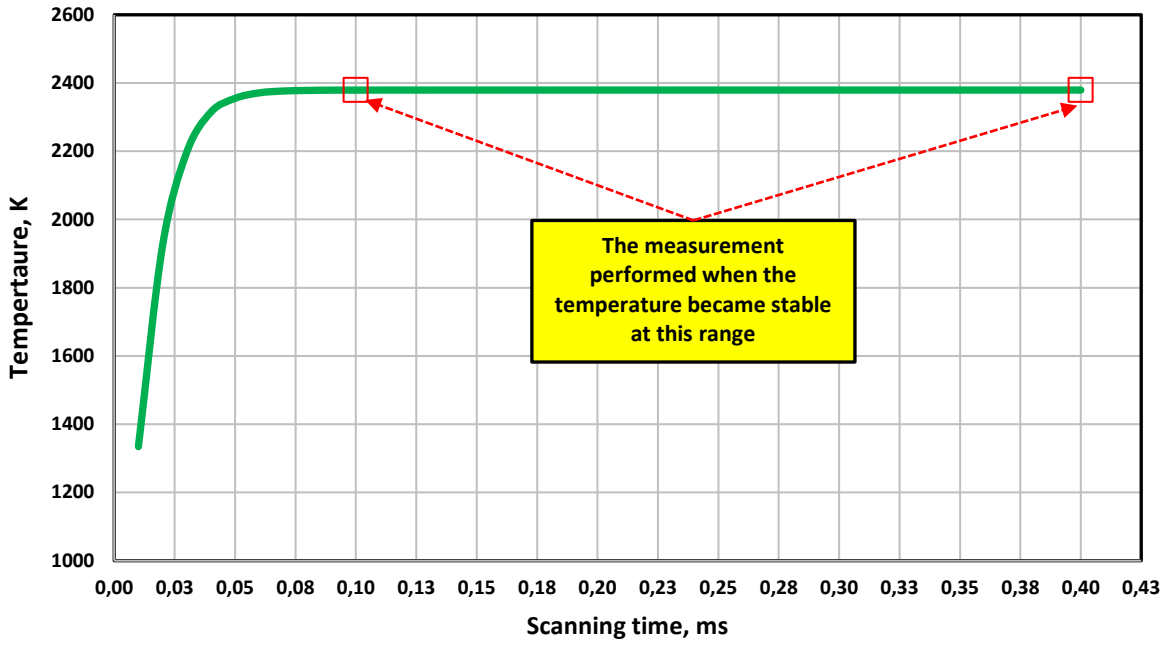

Figure 4.2. Temperature history for one path (laser track) during the scanning process.

4.2. Model Validation with Alumina

In order to validate the model, the process parameters used in the experimental study should be the same as those used in the numerical model. for this purpose, the spray-dried alumina powder was loaded into the Renishaw® SLM 125 printer and scanned. The process parameters are a laser power of 95W, scanning speed of 200 mm/s, hatching distance of 50µm and layer thickness of 100 µm. Two adjacent melting paths' width was measured using SEM analysis, which recorded 142.9 µm. The numerical model was solved to make two adjacent paths using the same conditions, which were used experimentally. It gave a width of 131.5 µm for the two adjacent melting paths, close to the experimental results with a calculation error of 8% (Figure 4.3a and b). It can be concluded that the numerical model was validated with experimental results and can be used for process parameters evaluation and PBSLP simulation.

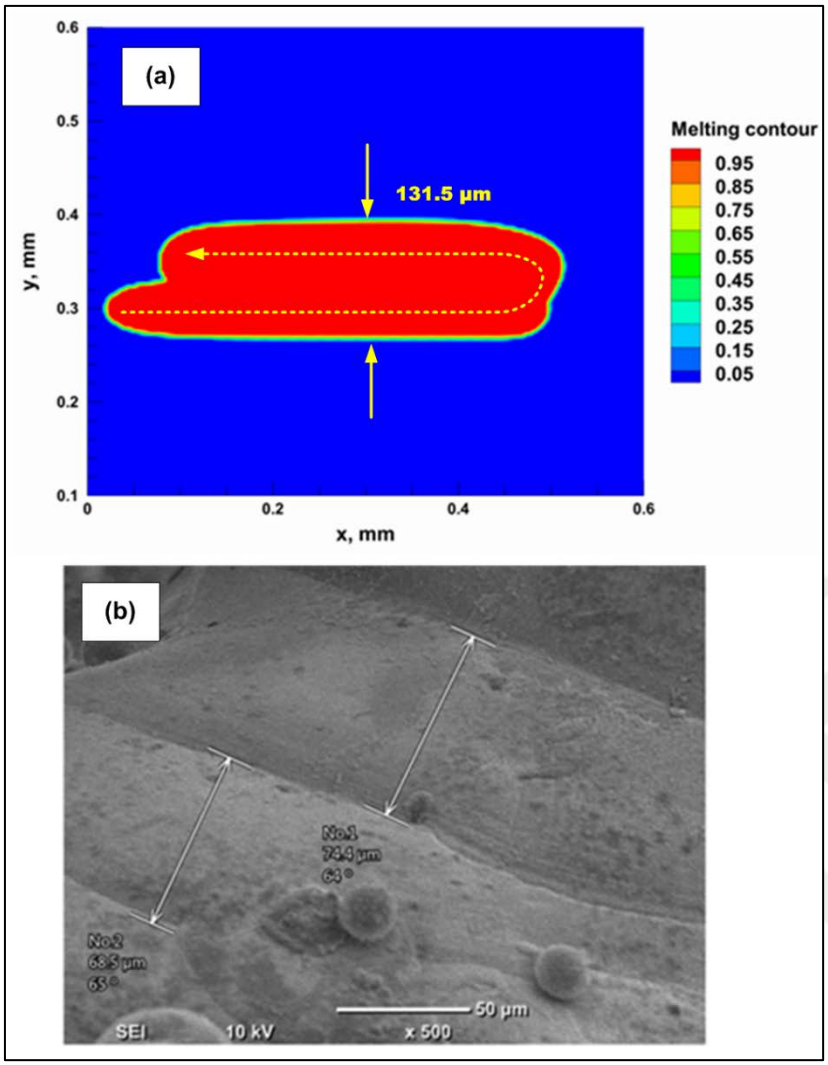

Figure 4.3. Comparison of the experimental data with numerical model: (a) two adjacent melting paths width measured using SEM, (b) two adjacent melting path widths measured numerically,

In addition, the numerical model was validated by considering the temperature distribution. The temperature contour of the laser spot obtained from the numerical model was compared with experimental data. This experimental data is a contour of a laser spot temperature distribution measured using a TVS-2300ST thermal camera manufactured by Avio Nippon Avionics Co., Ltd [143, 181]. The results indicated a perfect similarity between the two results, with a calculation error of 1.24% (Figure 4.4).

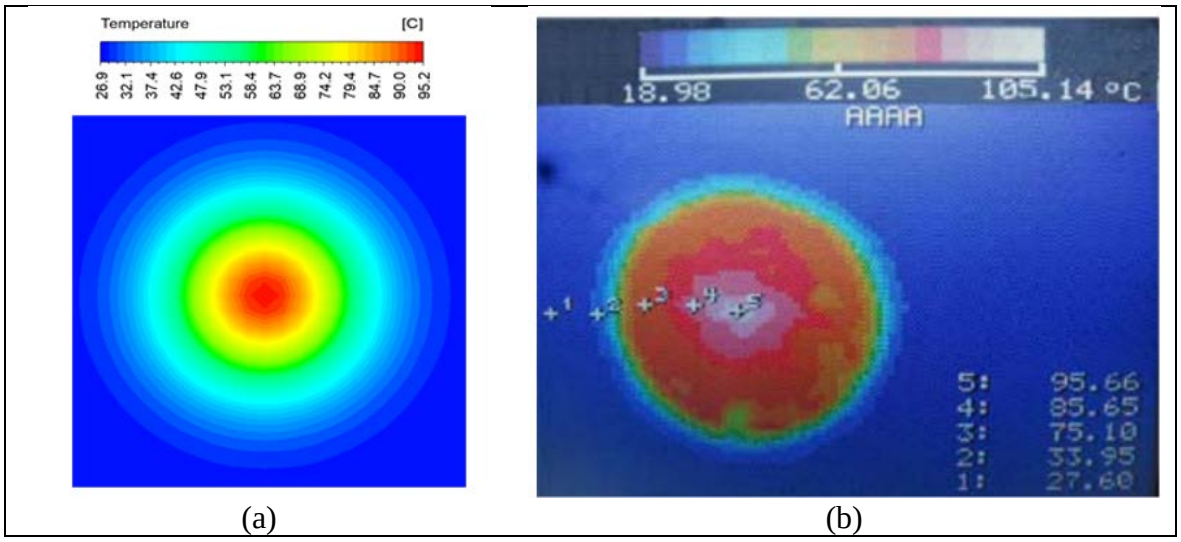

Figure 4.4. Comparison of the experimental laser spot temperature contour, captured using a thermal camera [143, 181] with the temperature distribution of the laser spot as predicted by the developed numerical model

To confirm the validation of the model, another validation was carried out where the results from the numerical model were compared with the available data from Zhang et al.[147]. The comparison indicated a good agreement between obtained results from the numerical model and Zhang et al.[147] Moreover, the maximum error was 3.34%. Figure 4.5 shows the comparison of the two results.

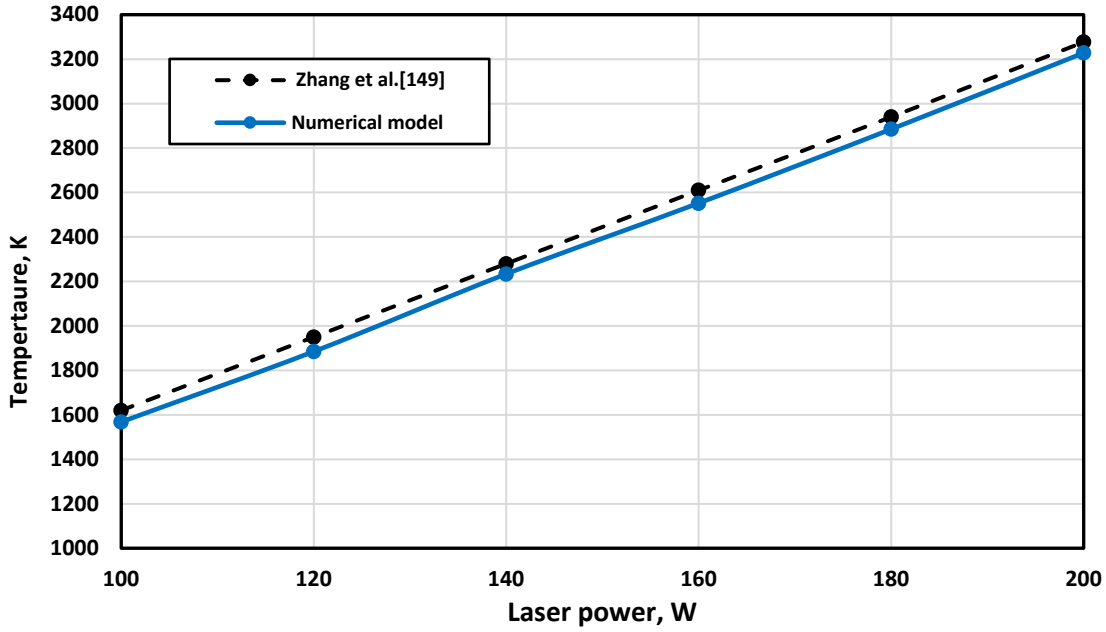

Figure 4.5. Comparison of the maximum temperature obtained from the numerical model with the experimental data [147].

4.3. Model Validation with SiC

For SiC, the results obtained from the numerical model were compared with those obtained experimentally. The width of sintered scanning path was used for this comparison. As shown in Figure 4.6, different sets of laser power and scanning speed (45W-250 mm/s, 30W-100mm/s, 35W-100 mm/s and 30W-50mm/s) are expressed in terms of laser energy density (LED) (LED = laser power /scanning speed) were used. A good agreement between the results from the developed model and the experimental data was obtained, especially at a lower value of LED, where the minimum error is 7.9 %. The maximum obtained error was 13.7 % due to many reasons, such as the change in the powder absorptivity with the temperature, where the absorptivity increases with the increase of temperature.

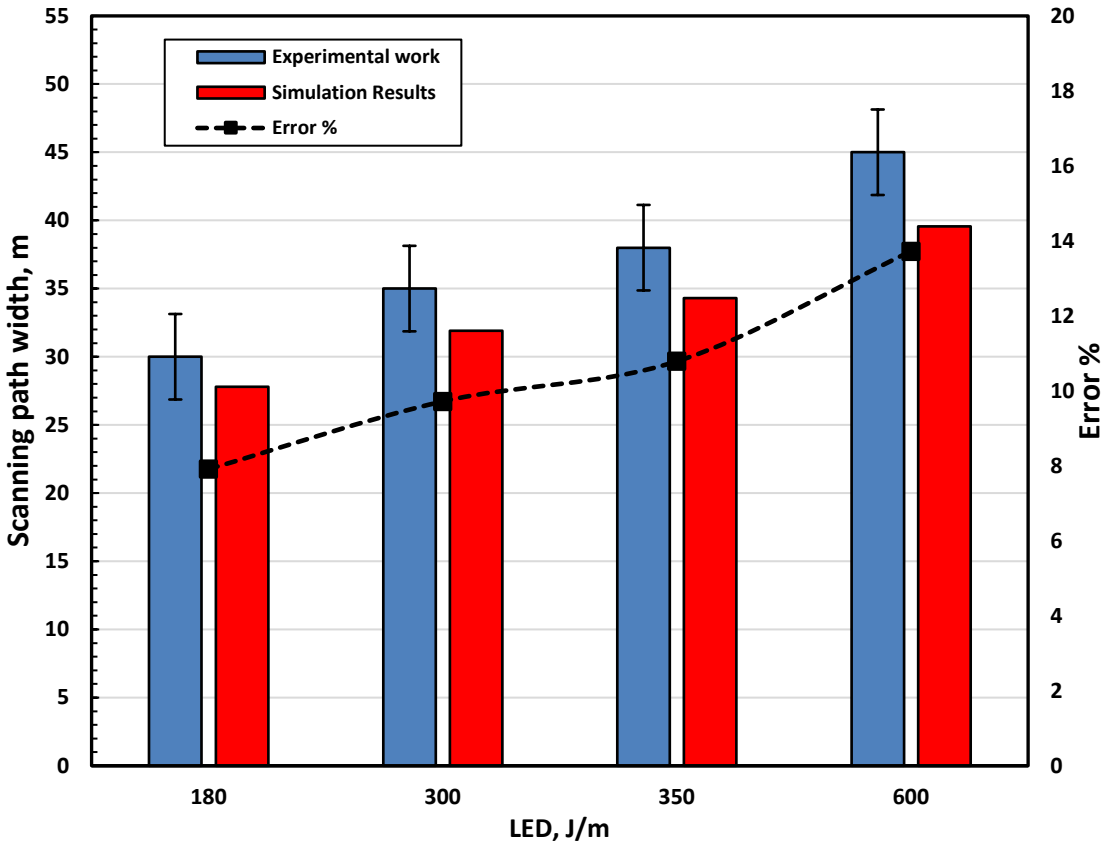

Figure 4.6. Comparison of the scanning path width obtained experimentally with the simulation results at different.

4.4. Conclusion

It can be concluded from the comparison between results obtained from the numerical model and the experimental results that the numerical model was validated and can be used effectively to evaluate the process parameters and simulate the PBSLP of alumina and SiC.

5. D-PBSLP: MULTI-LAYER SIMULATION

This chapter presents a multi-layer simulation of PBSLP to provide an in-depth understanding of the process, residual stress, and distortion. There are two sections in this chapter. Multilayer simulation of alumina PBSLP is the topic of Section 5.1. Section 5.2 demonstrates the multilayer simulation of SiC's PBSLP.

5.1. Multi-Layer PBSLP Simulation of Alumina

5.1.1. Alumina laser interaction

As explained in Chapter 2, the absorption of alumina varies with laser wavelength. For instance, alumina has outstanding absorption for high-wavelength lasers, such as CO_2 lasers (10.64 µm), but poor absorption for low-wavelength lasers, such as Nd-YAG laser (1.064 µm). Utilizing the numerical model, the PBSLP of Alumina using CO_2 laser and Nd-YAG laser was compared. The influence of laser power and scanning speed on the PBSLP of alumina was studied, while other parameters, including laser spot diameter and layer thickness, remained constant. Table 5.1 summarizes the range of laser power, scanning speed, and other process parameters used to explore the laser interaction with alumina.

Table 5.1. Process parameters used for multi-layer simulation of PBSLP of alumina.

Parameters	CO2 laser	Nd-YAG laser
Laser power range (W)	15 – 40	100 - 200
Scanning speed range (mm/s)	500 - 1000	50 - 100
Laser spot diameter, µm	100	100
Layer thickness, µm	50	50

In this investigation, the Nd-YAG laser's laser power varied from 100 W to 200 W, while the scanning speed varied from 50 mm/s to 100 mm/s. The range of CO_2 laser power was 15 to 40 W, and the range of scanning speed was 500 to 1000 mm/s. Figure 5.1 and Figure 5.2 depict the temperature obtained using Nd-YAG and CO_2 lasers with varying powers and scanning speeds. In the PBSLP of alumina, any laser power with scanning speed values that gave a temperature within the grey area may be employed. The melting defined this grey region and boiling limits of alumina according to [105], where values below this region are

insufficient to melt the powder and values beyond it results in material boiling and evaporation. In addition, the CO_2 laser utilized much lower laser power values than the Nd:YAG laser, and the scanning rates employed with the CO_2 laser are far faster than those used with the Nd-YAG laser. This is partly because the absorptivity of alumina to the Nd-YAG laser is extremely low, reaching just 3%, whereas the absorptivity of alumina to the CO_2 laser is extremely high, reaching 96% [182].

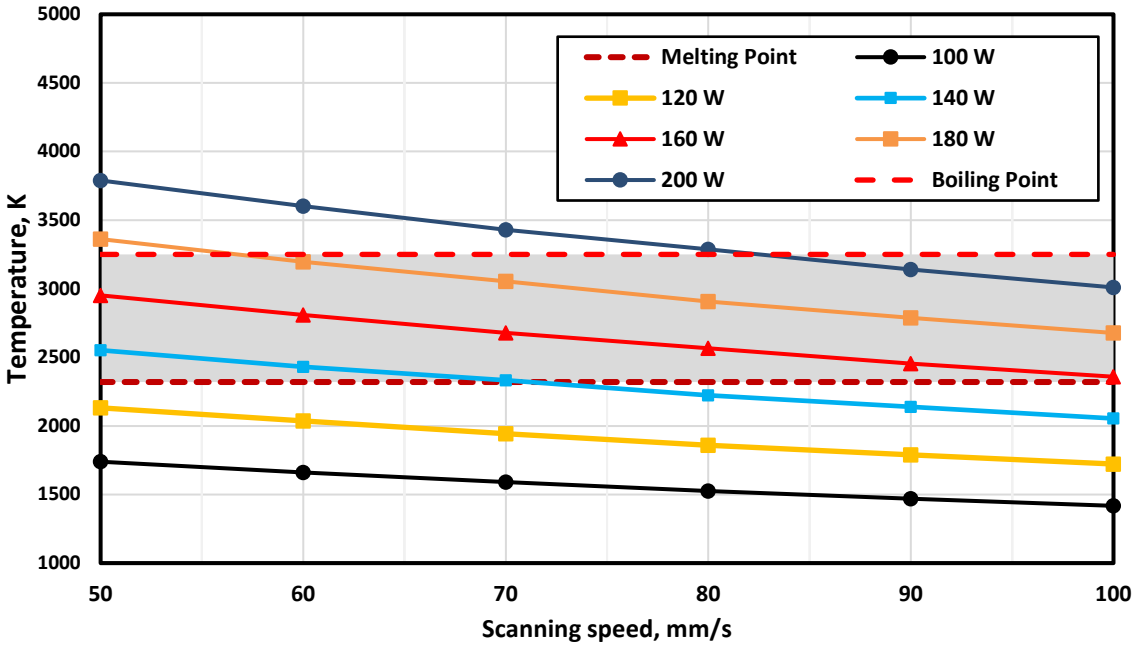

Figure 5.1. The maximum temperature obtained using Nd-YAG laser at different laser powers and scanning speeds.

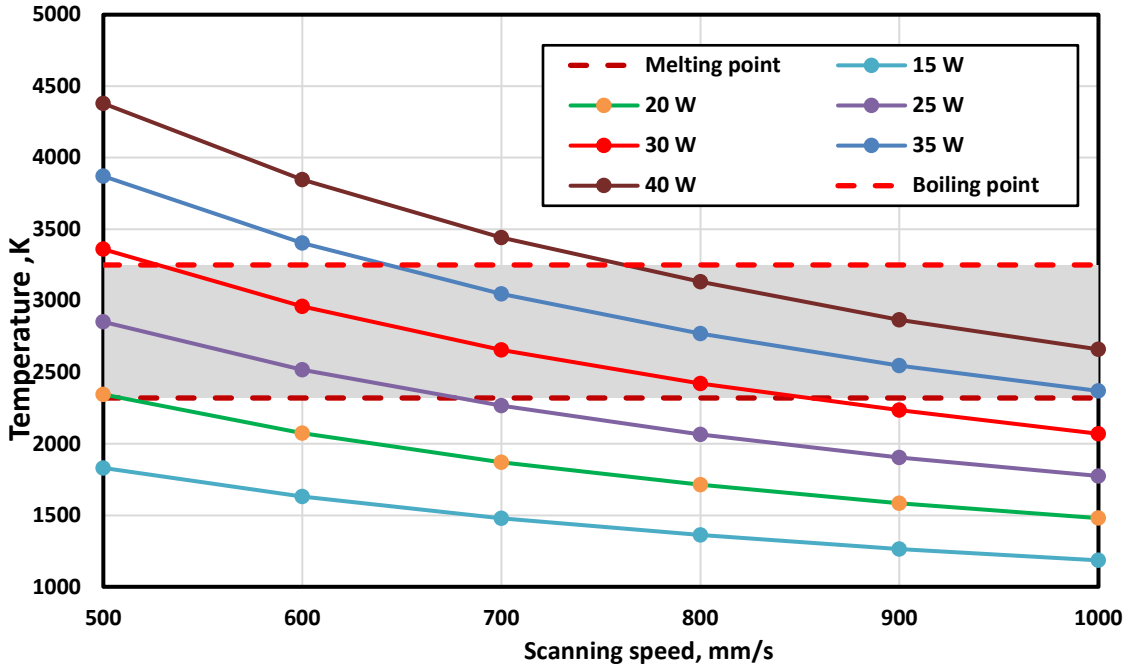

Figure 5.2. The maximum temperature obtained at different powers and scanning speeds using a CO2 laser.

5.1.2. Scanning strategies investigation: Numerical analysis

In this investigation, the CO_2 laser was considered, and the process parameters were selected according to Figure 4.2 and are reported in Table 4.2. The numerical model was employed to examine the effect of scanning strategies on the PBSLP of alumina. As illustrated in Figure 4.3, several scanning strategies were examined. The UDF was enhanced with a particular subroutine to control the laser beam's movement to follow the scanning strategy. The temperature contour and history were considered to evaluate each scanning strategy's effect.

Table 5.2. PBSLP parameters used for PBSLP of alumina scanning strategies investigation.

No	Process parameter	Value
2	Laser power	30 W
4	Scanning speed	700 mm/s
5	Hatching space	50 µm
6	Layer thickness	50 µm

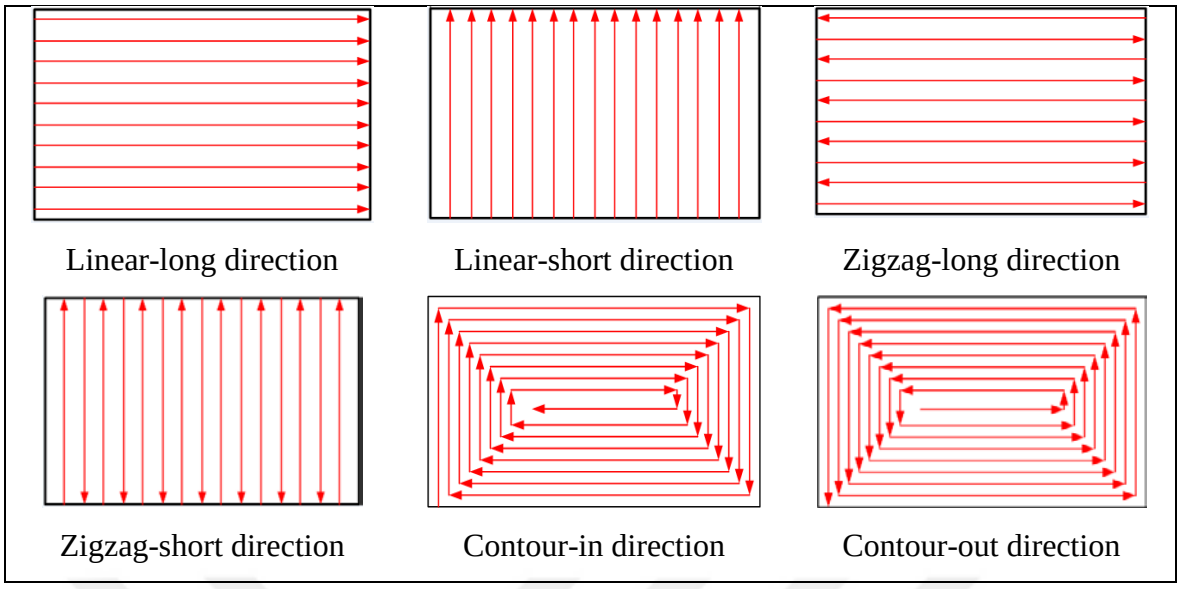

Figure 5.3. The scanning strategies investigated for PBSLP of alumina using the numerical model.

Linear scanning

Figure 5.4 depicts the temperature contour for the linear strategies in which the laser heat source followed the scanning strategy. Figure 5.5 depicts the temperature history's fluctuation with scanning time. When the laser beam started to scan the layer, the temperature increased to 2665°C. The temperature remained at this level until the end of the first path, at which point the laser source was relocated to initiate a new path. This was repeated until the entire layer had been scanned. At the beginning of each new path, the temperature decreased dramatically, falling below the melting point. This was mostly due to the laser source moving to start a new path (new position). The abrupt drop in temperature might damage the edge quality by causing defects near the part's edge (in micro-scale). As a result, contour scanning is advised when linear strategies are employed for the PBSLP of alumina.

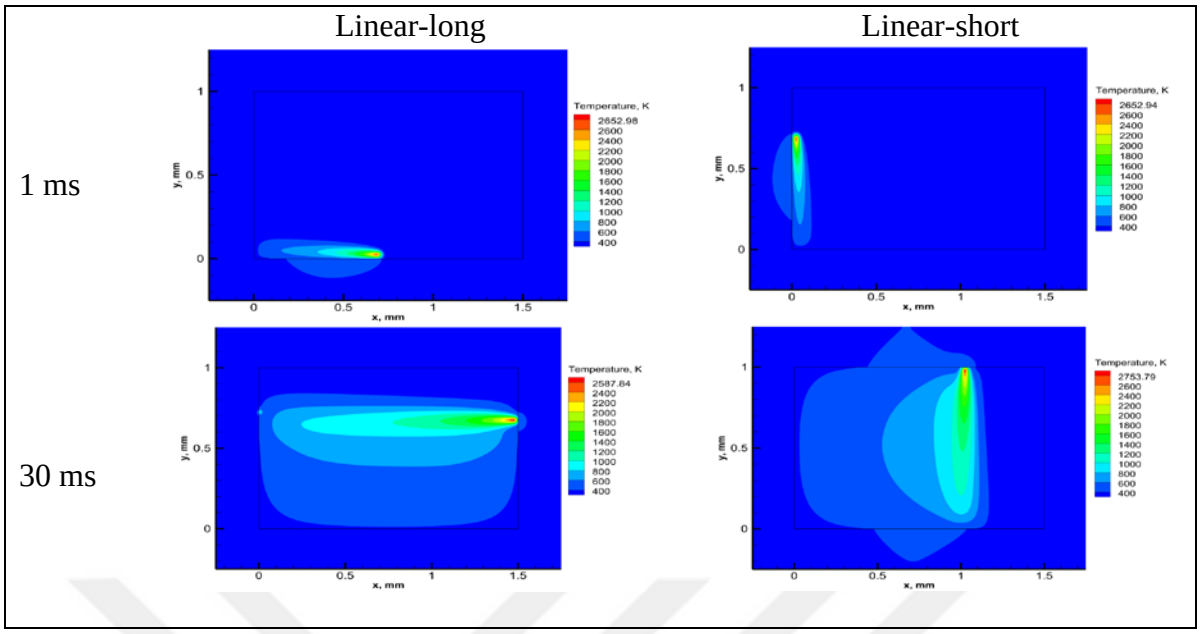

Figure 5.4. The temperature distribution contour for the linear scanning strategies at different scanning times.

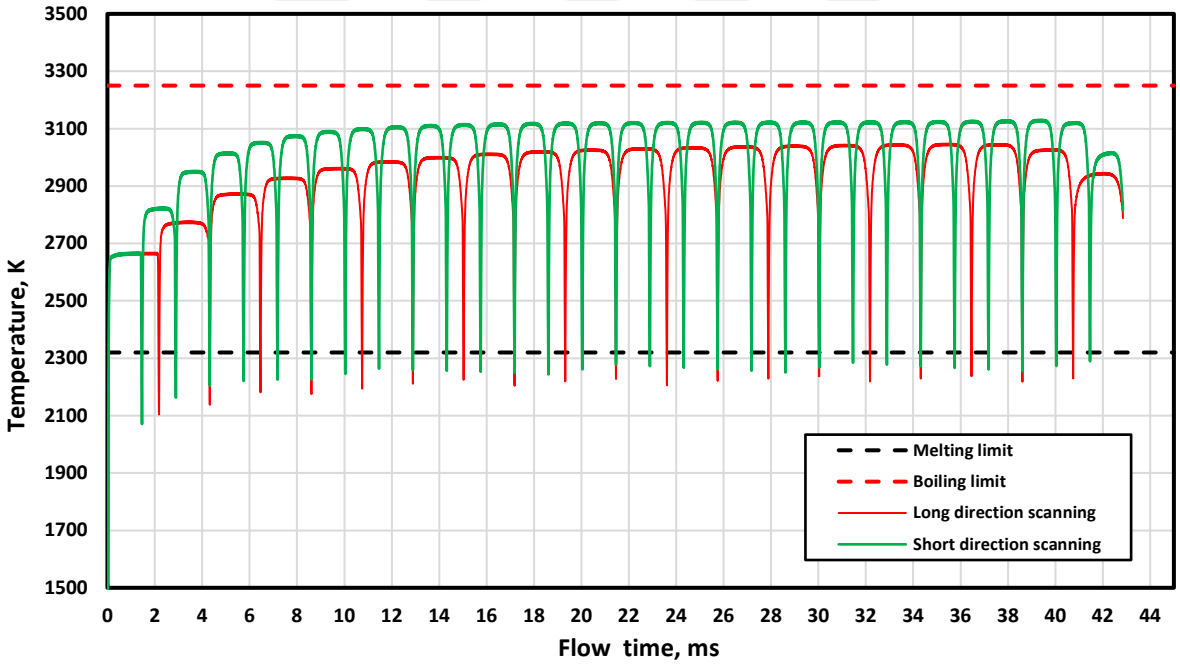

Figure 5.5. The temperature history for the linear scanning strategies.

Zigzag scanning

Figure 5.6 depicts the temperature distribution, while Figure 5.7 depicts the temperature history for the zigzag scanning strategy. As with the linear scanning strategy, when the laser began scanning the powder, the temperature surged sharply to 2665°C and remained at this

level until the completion of the first route. The laser beam then shifted to scan a new path where the temperature decreased dramatically before increasing sharply (the laser went to a new point). The shift in temperature happened as a result of the proximity of the laser beam's new position to the old position, which retained heat from the prior scan. This technique was repeated until the scanning of all layers was complete. In linear scanning, the temperature dropped below the boiling point during the scanning process. However, in the case of zigzag scanning, the temperature was close to boiling. As a result, the zigzag technique overcame the linear strategy's difficulty (unscanned powder surrounding the layer contour) and may be employed well for alumina without needing contour scanning.

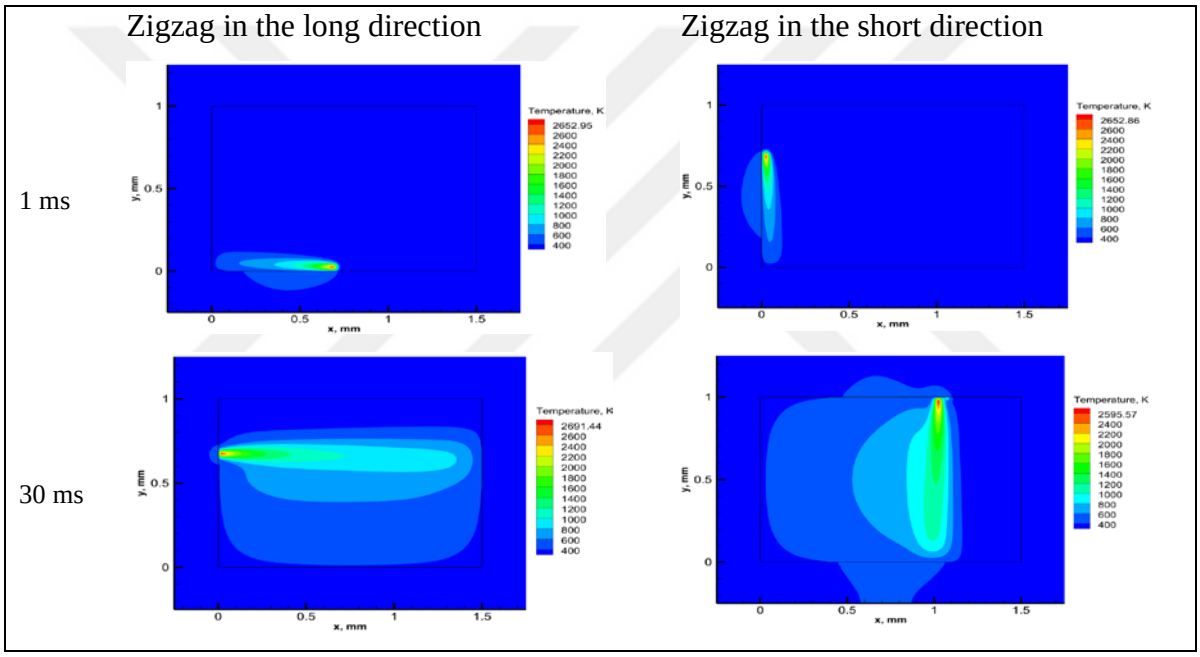

Figure 5.6. The zigzag scanning strategies' temperature distribution at different scanning times.

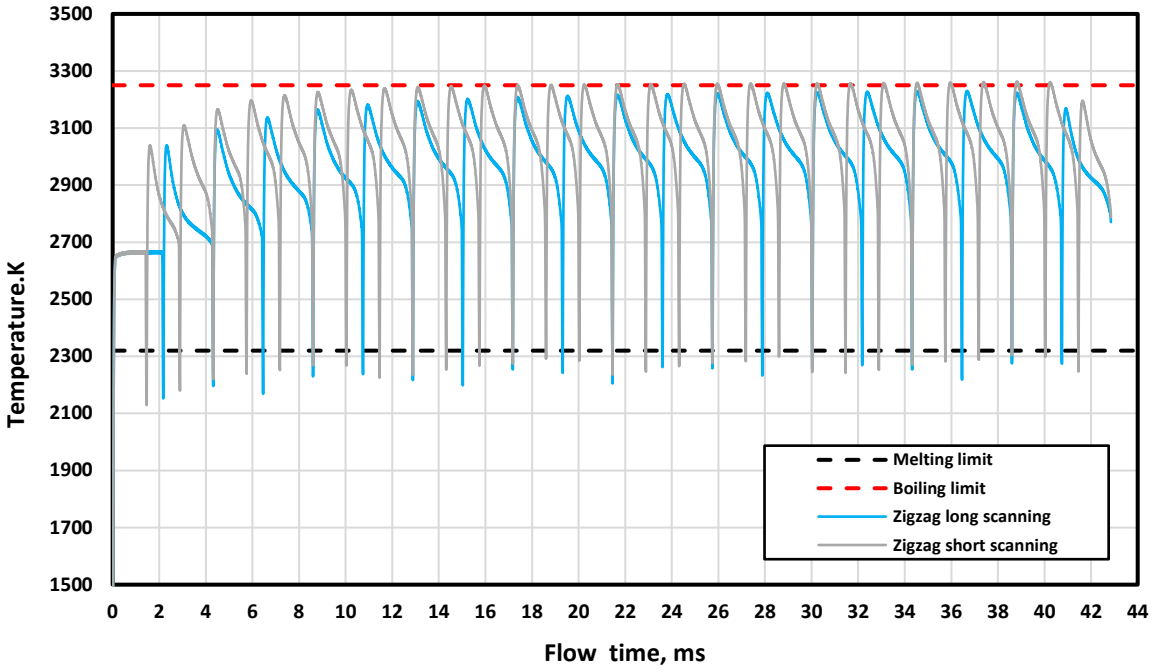

Figure 5.7. The temperature history for the zigzag scanning strategies.

Contour scanning

Figure 5.8 and Figure 5.9 depict, respectively, the temperature contour and history of the contour scanning approach. As illustrated in Figure 5.9, contour scanning induced temperature changes between the melting and boiling limits, with several peaks-up caused by a change in laser beam direction and peaks-down caused by the start of a new path. In addition, with the contour out-in technique, heat accumulated within the part due to the short scanning paths at the end of the layer scanning, resulting in a temperature increase over the boiling point. The contour in-out strategy had no heat accumulation and performed better than the contour out-in strategy. Laser beam direction changes mostly induce temperature peaks in the contour strategy. To control the temperature peaks, developing a new scanning strategy is necessary.

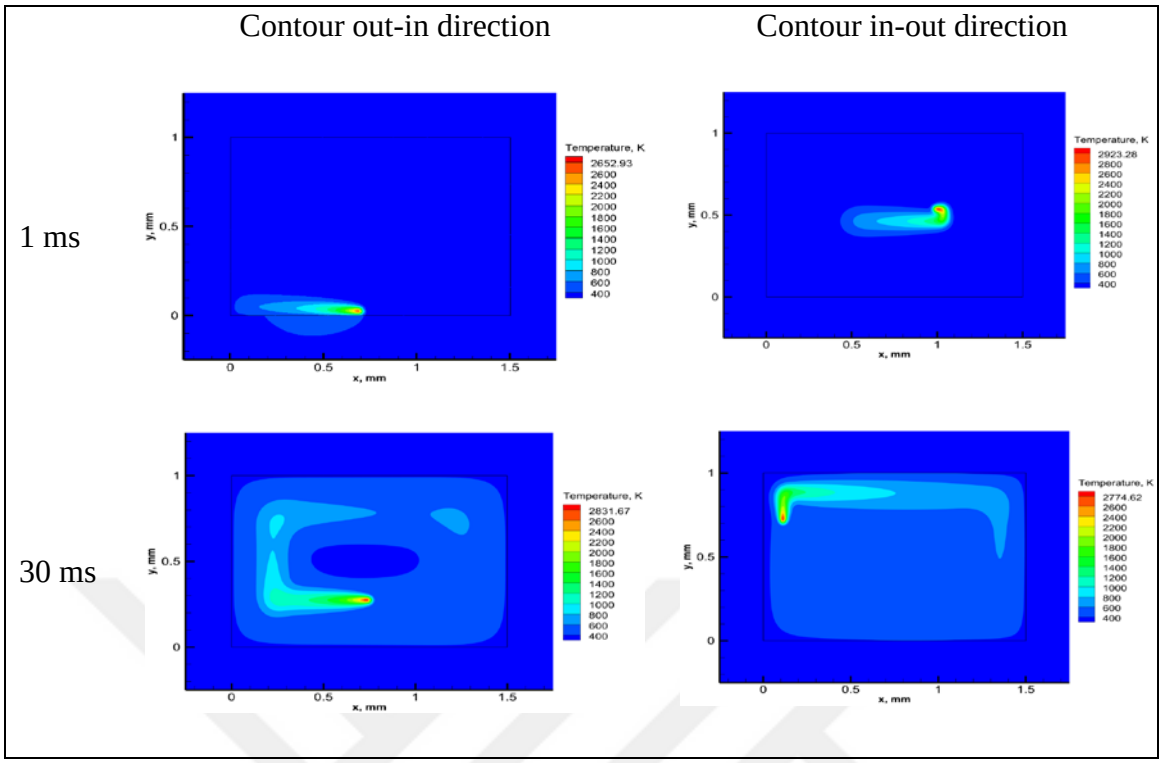

Figure 5.8. The temperature distribution for the concentric scanning strategies at different scanning times.

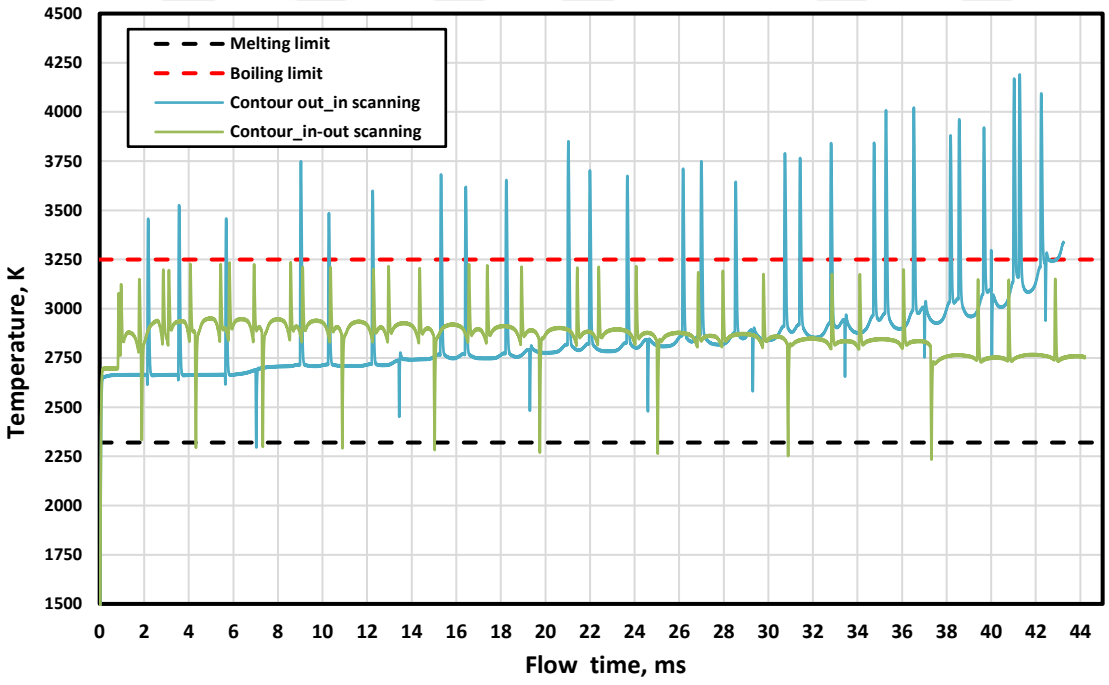

Figure 5.9. The temperature history for the contour scanning strategies.

Newly developed scanning strategies

After examining prior scanning strategies, it is feasible to conclude that peaks-up and peaks-down pose the most significant challenges for these strategies. As illustrated in Figure 5.10, this led to the developing of a novel scanning strategy. In this strategy, the laser beam begins a new path from the end of the preceding path, retaining heat that can be used for preheating and eliminating temperature peaks. Figure 5.11 displays the temperature history variation as a function of scanning time, where the temperature change was roughly within the melting and boiling limits. Thus, the new scanning approach could eliminate temperature peaks during scanning.

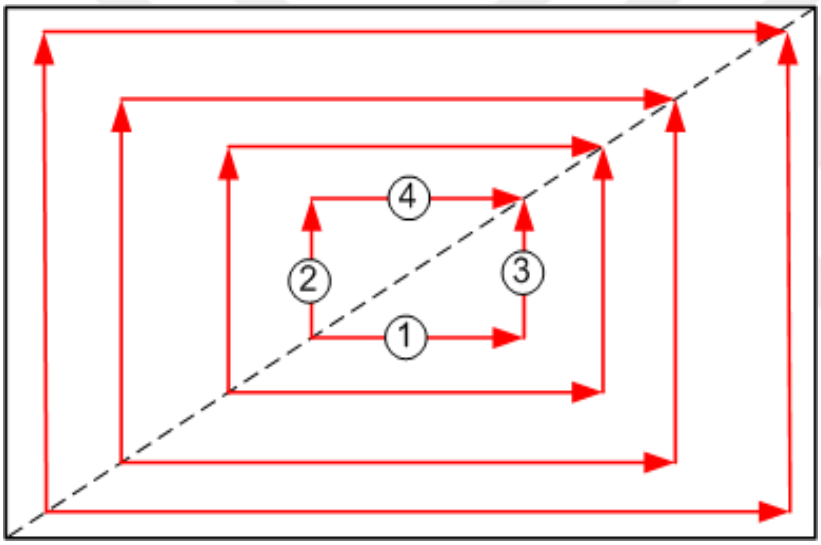

Figure 5.10. New developed scanning strategies (4 direction contour in-out).

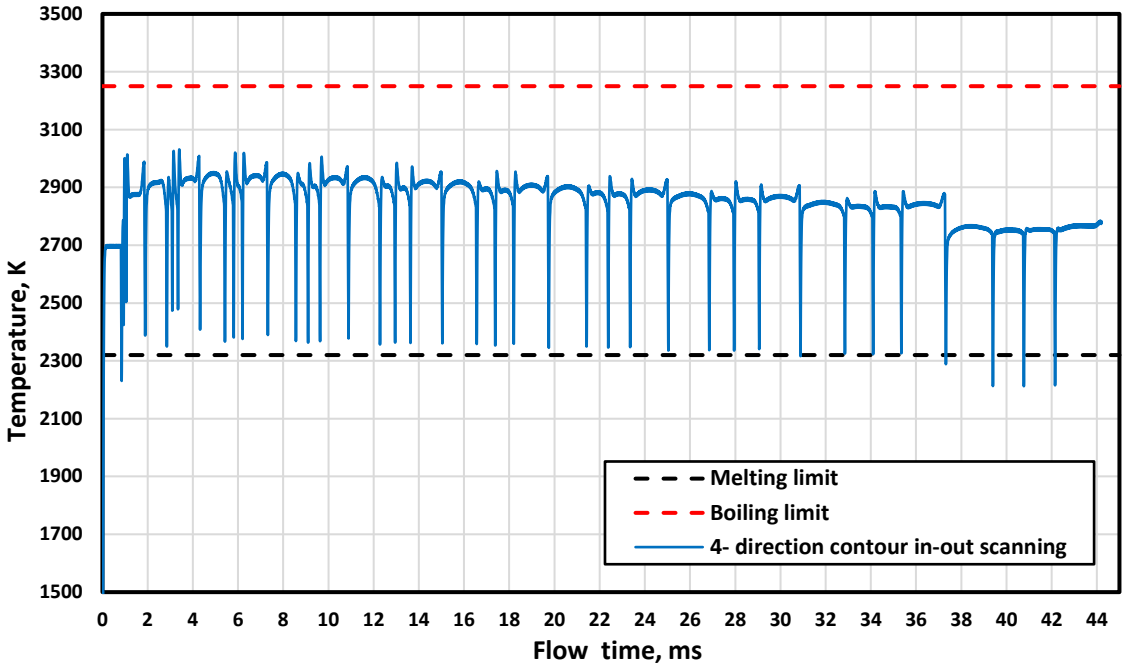

Figure 5.11. The temperature history for the newly developed scanning strategy.

5.1.3. Temperature history: Multi-layer PBSLP of alumina

The process parameters should be selected to investigate the temperature history during the multilayer PBSLP of alumina. Figure 5.2 depicts the process window used for this purpose. Table 5.3 summarises the model dimensions utilized for the multi-layer simulation of the PBSLP of alumina. Notably, the model dimensions considered were relatively small, as the multi-layer model required a substantial amount of time and computed capabilities to solve. In addition, only ten layers were considered for the multi-layer PBSLSP simulation of alumina, which was deemed sufficient to understand the process thoroughly.

Table 5.3. Numerical model geometry dimensions.

Dimension	Base Plate (mm)	Printed Part (mm)
Length	2	1.5
Width	1.5	1
Thickness	0.5	0.5[1]

[1] The printed part contains ten layers; each layer has a thickness of 0.05 mm.

Different laser powers and scanning speeds were investigated, as described in Table 5.4. The laser power of 50W and scanning speed of 1200 mm/s were used to investigate the thermal stresses and distortion during the PBSLP of alumina. All the investigated laser powers and

scanning speeds were able to melt the whole layer thickness and gave a maximum temperature below the evaporation point of alumina to save computational time. Different build orientations were considered, as described in Figure 5.12. The developed numerical model was solved considering these process parameters and the build orientations described in Figure 5.12.

As shown in Table 4.4, various laser powers and scanning speeds were investigated. All of the investigated laser powers and scanning speeds were able to melt the entire layer thickness and obtain a maximum temperature below the evaporation point of the alumina. In order to save computational time and resources, the laser power of 50W and scanning speed of 1200 mm/s were used to investigate the thermal stresses and distortion during the multi-layer PBSLP of alumina. The build orientations should also be considered during multi-layer simulation because they substantially impact the printed part's developed stress and mechanical properties. Figure 5.12 depicts the build orientations that were considered.

Table 5.4. Temperature distribution and melting contour obtained from the numerical model.

Power, W	Scanning speed, mm/s	Top melting contour	Vertical melting contour
30	600	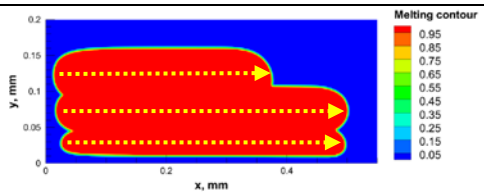	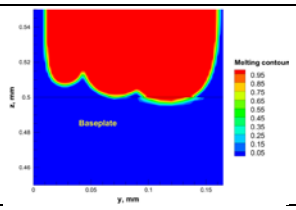
40	900	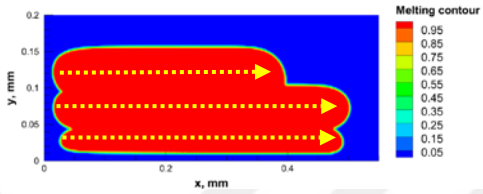	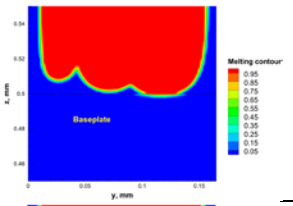
50	1200	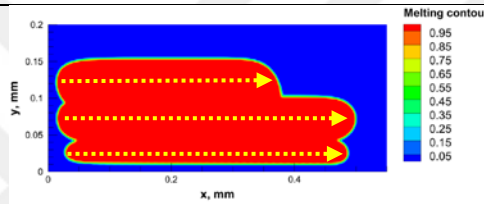	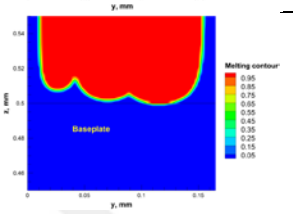
		Temperature distribution	
30	600	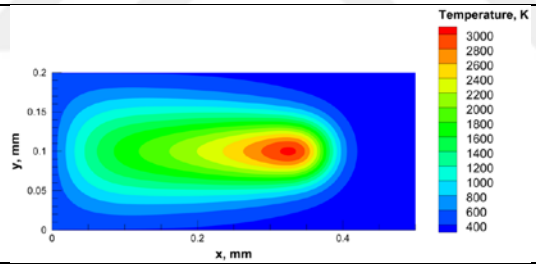	
40	900	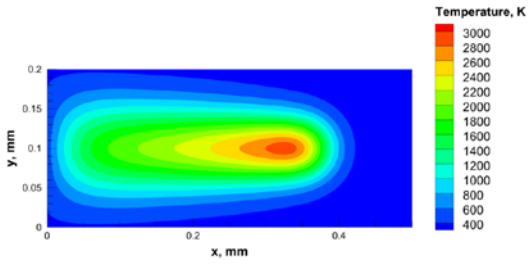	
50	1200	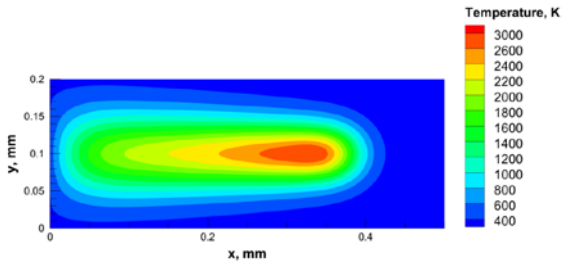	

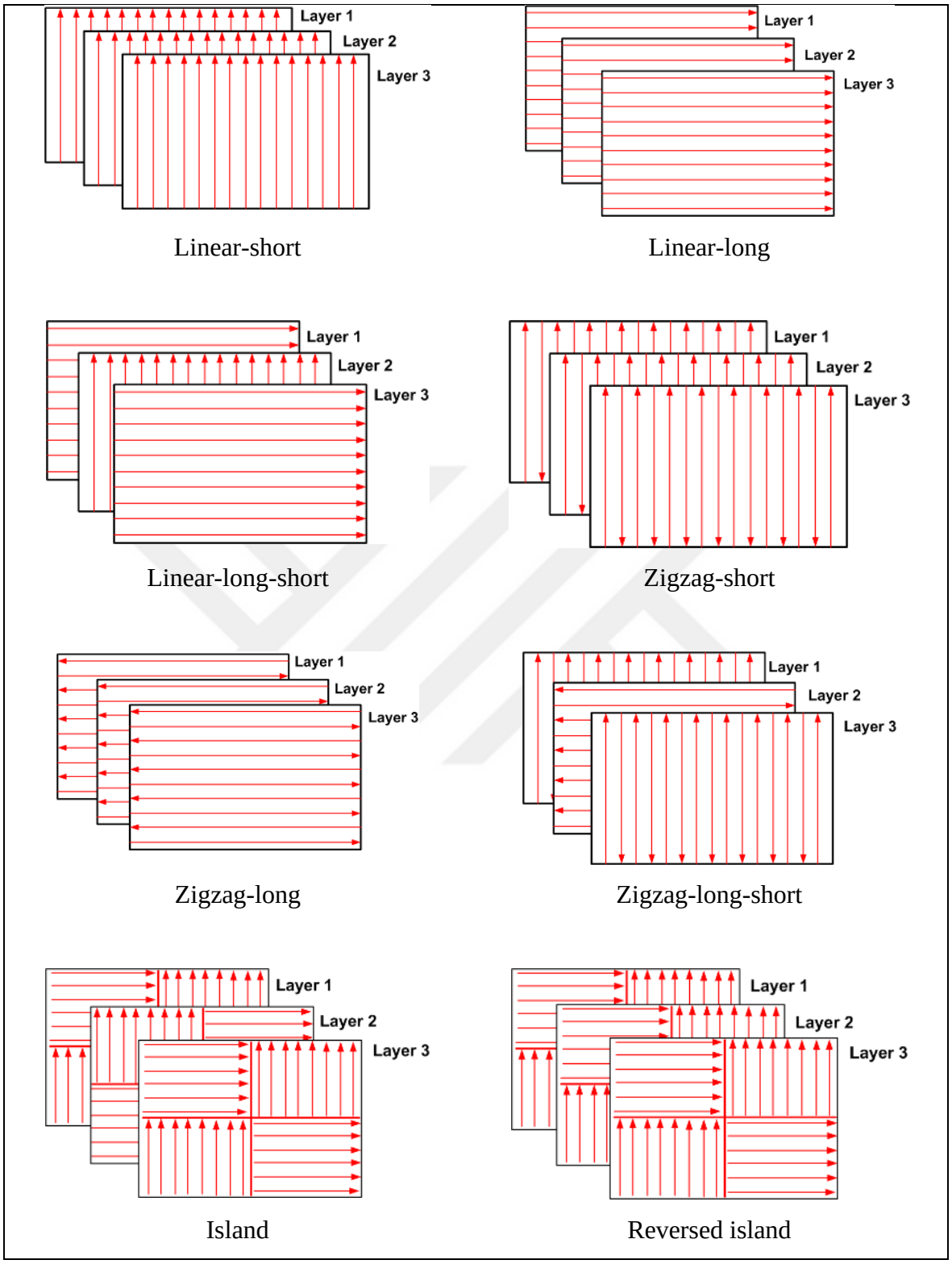

Figure 5.12. The build orientations considered for the PBSLP multilayer simulation of alumina.

Figure 5.13 illustrates the temperature history during the printing process for the whole-part scanning with island scanning build orientation (the part contains 10 layers). It also displays

the temperature history for one-layer scanning derived from the developed multilayer PBSLP model. The curve with the green color illustrates the temperature history for whole-part scanning, whereas the curve with the red color illustrates the temperature history for one-layer scanning. The temperature and scanning time axis for the whole-part scanning is located to the right and bottom, respectively. In contrast, they are located on the left and top of the figure for one-layer scanning.

The laser beam began scanning the first layer at 0s, and it took 0.025s to complete the scanning (The scanning time was minimal as a layer's dimension is small, as described in Table 5.3). During the initial layer scan, the temperature history fluctuated between the boundaries of melting and boiling. After completing the first layer scanning, the laser beam waited for the deposition of the second layer as the component's temperature dropped to above room temperature, indicating that heat had accumulated within the part. As shown in Figure 5.13, the deposition time was set to 10 seconds (it can be modified according to the printer's specifications). Following the deposition of the second layer, the laser beam began to scan. All preceding procedures were repeated until all layers were complete.

By observing the temperature history for the whole-part scanning, it is evident that the temperature history gradually increased with the deposition and scanning of successive layers. This was caused mainly by the gradual heat accumulation inside the printed component. Due to the low thermal conductivity of alumina and the limited time available for heat to evacuate from the component, heat accumulated gradually inside the component. The accumulating heat within the component caused the final four layers to exceed the boiling point (as seen in Figure 5.13). This could cause flaws in the form of pores and cracks. In addition, despite the observed trend in other layers, the temperature history of the last layer was lower than that of the prior layers. This was mostly due to the fact that the last layer had ample time to re-release the heat because no powder had been deposited above it to trap the heat.

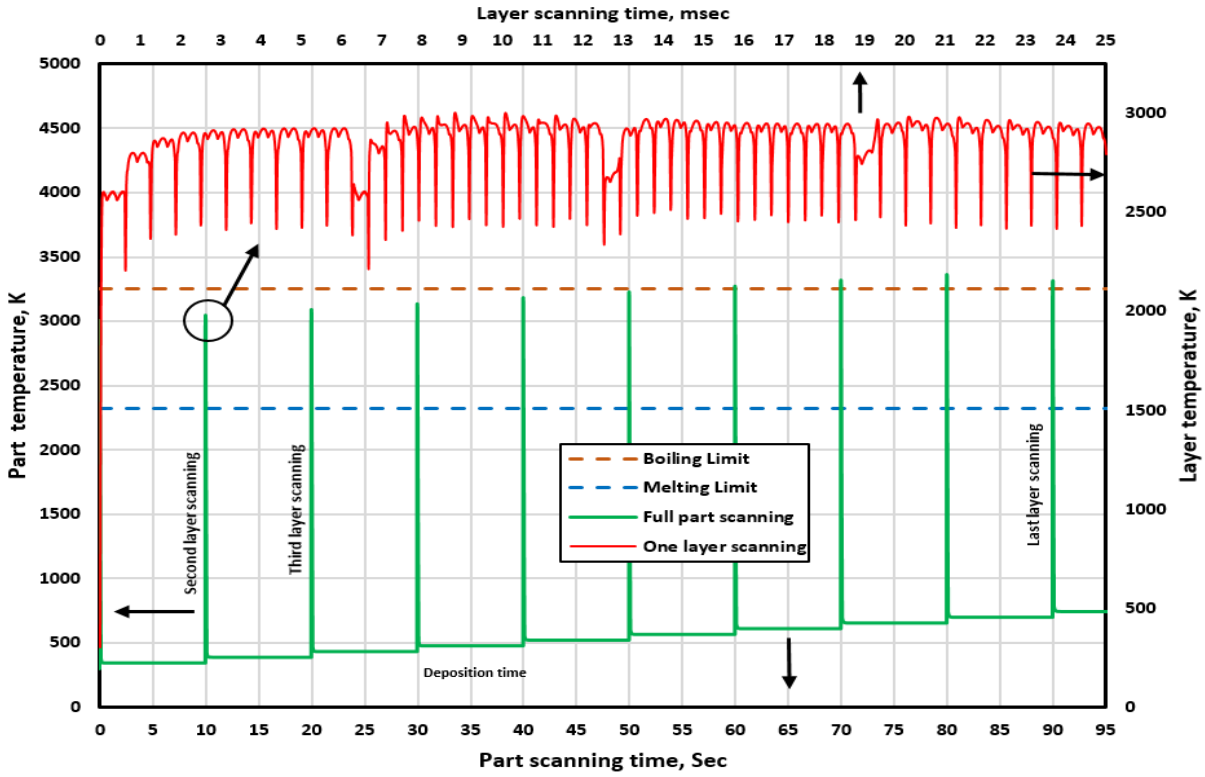

Figure 5.13. The multilayer and one-layer scanning temperature history using the island scanning strategy.

The temperature history for the other build orientations is almost identical to the island scanning build orientation; therefore, the other orientations' temperature histories were not presented. Monitoring the temperature history suggests that PBSLP Printers for ceramic materials should be provided with a temperature controller to maintain the temperature between the melting and boiling limits during the printing process. The laser power or the scanning speed can be modified to adjust the temperature.

5.1.4. Thermal stress and distortion

The residual stress calculation relies heavily on the temperature distribution of the printed object. The temperature distribution was utilized as a thermal load for the coupled thermal-mechanical finite element (FE) model to quantify the thermal stress developed for each build orientation. Figure 5.14 illustrates the temperature distribution obtained from the multilayer PBSLP model for each build orientation immediately following the solidification of the printed item. The temperature distribution reflects the scanning approach employed in each build orientation, which is evident from the most recently scanned layer.

The von-Mises equivalent stress criterion (σe) was utilized to investigate and evaluate the developed residual stress. However, material properties are a function of temperature; hence, the thermal and mechanical properties of the printed item vary accordingly, particularly yield stress (σy). Therefore, the von-Mises equivalent stress criterion for the developed residual stresses cannot be utilized to analyze and investigate the effect of the build orientations. Normalization of the von-Misses equivalent stress could solve this issue by dividing the von-Misses equivalent stress by the yield stress, which changes as a function of temperature at every position in the printed part. Using this normalization, the stress state is unsafe when the normalized von-Misses equivalent stresses are more than or equal to one. In such a situation, there is an excellent likelihood that cracks may emerge. Conversely, the stress state is secure when the normalized von-Misses equivalent stresses are smaller than one.

Figure 5.15 illustrates the normalized von-Mises stress (σe/σy) created in the 3D-printed component at various build orientations. All examples resulted in normalized stresses greater than one, as evidenced by the contours of stress. This signifies that cracks have been present in all build orientations examined. In most cases, thermal stress is caused by a temperature difference and can be reduced by preheating.

Figure 5.16 illustrates the distortion contours for the build orientations evaluated. Due to the small model dimensions, the obtained distortion values are extremely small, on the scale of 0.3 µm. The distortion values at the bottom of the part are very modest, reaching zero, and grow progressively as the height of the part increases. This is because the bottom of the component (bottom layers) has adhered to the base plate, and its temperature is near ambient temperature. The upper layers are deformable and have a higher temperature than the lower levels. The distortion value for each build orientation is relatively close, with the island scanning orientation yielding the highest result.

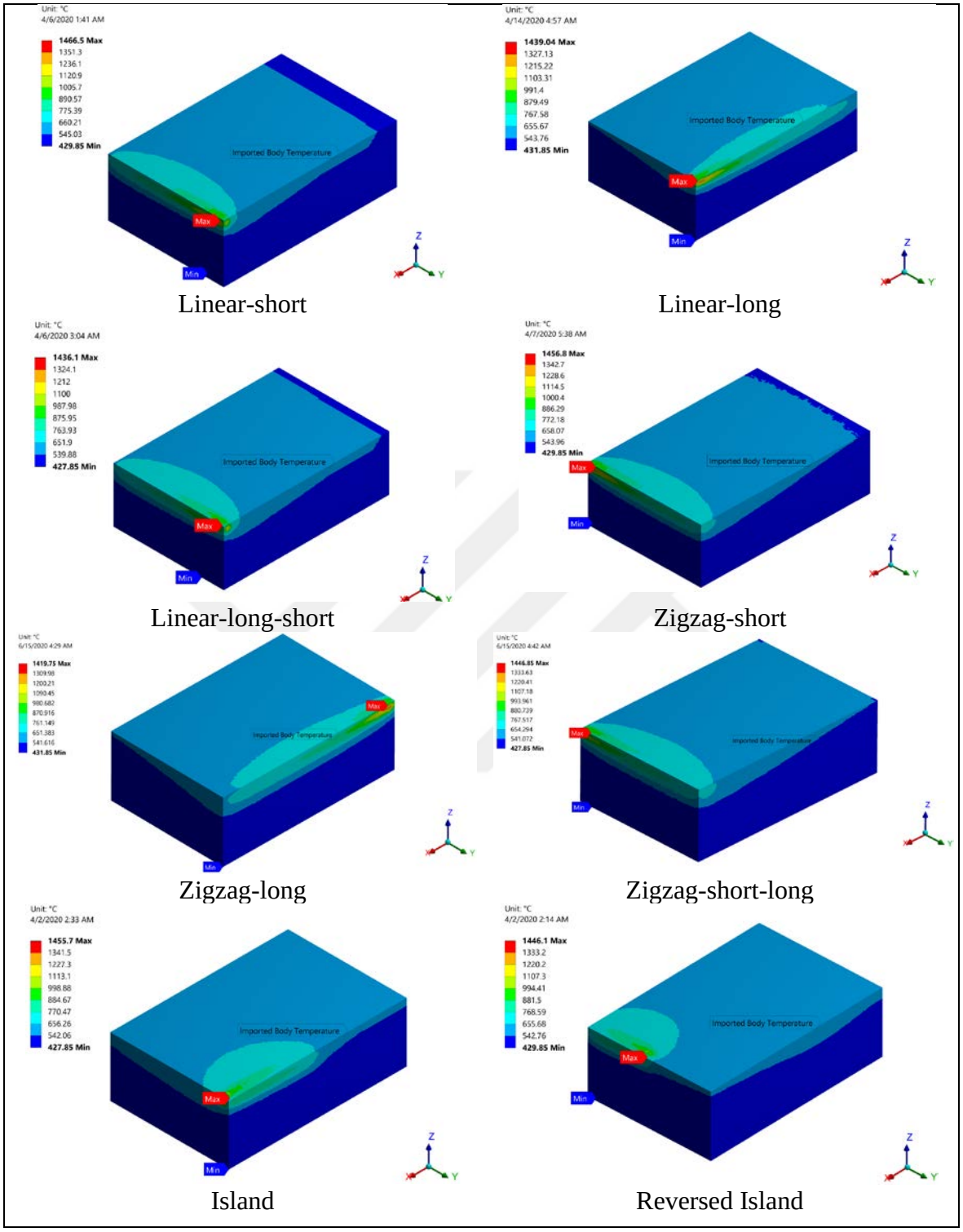

Figure 5.14. Temperature contours for the studied build ordinations just after solidification.

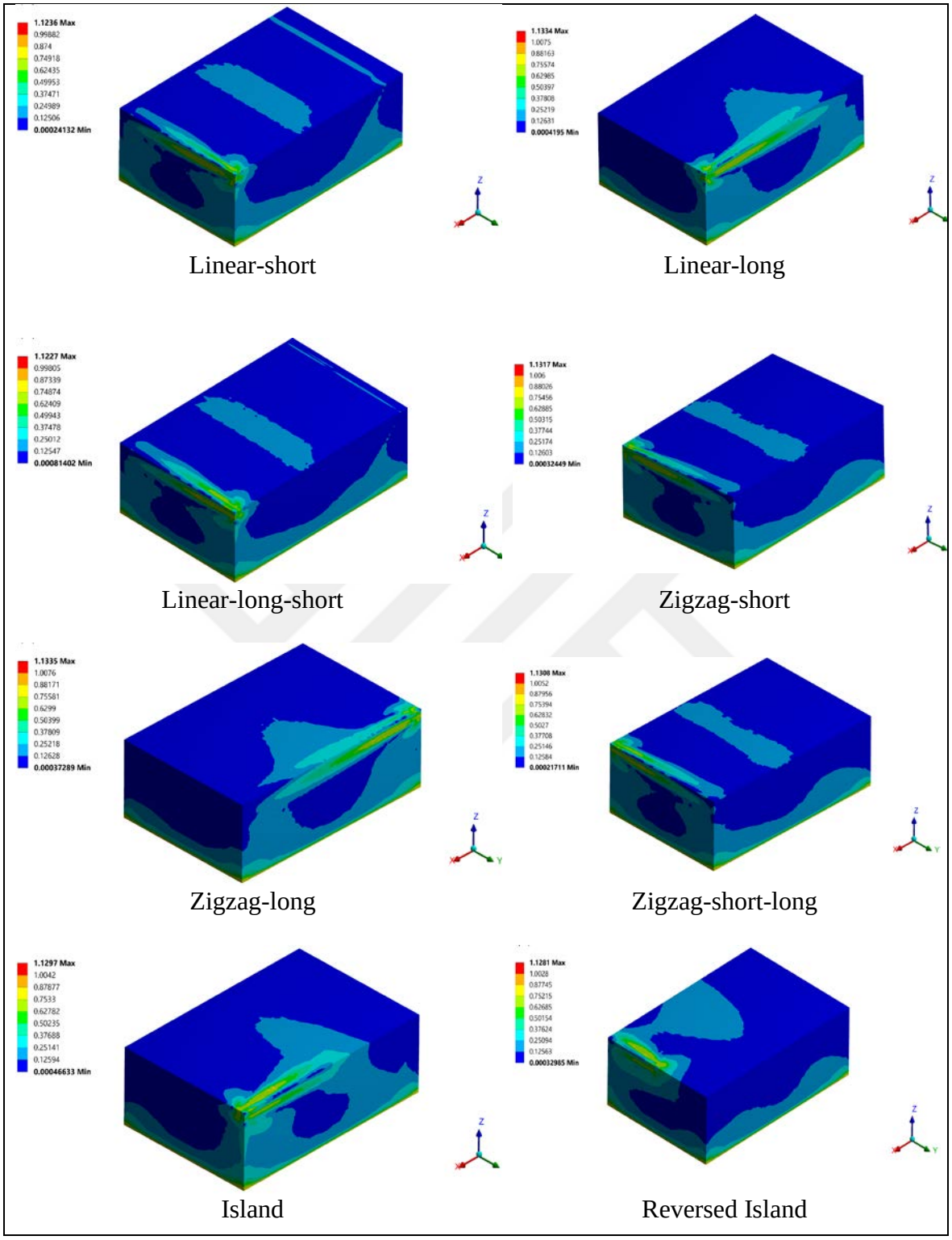

Figure 5.15. Normalized Von-mises stress for the studied build ordinations just after solidification.

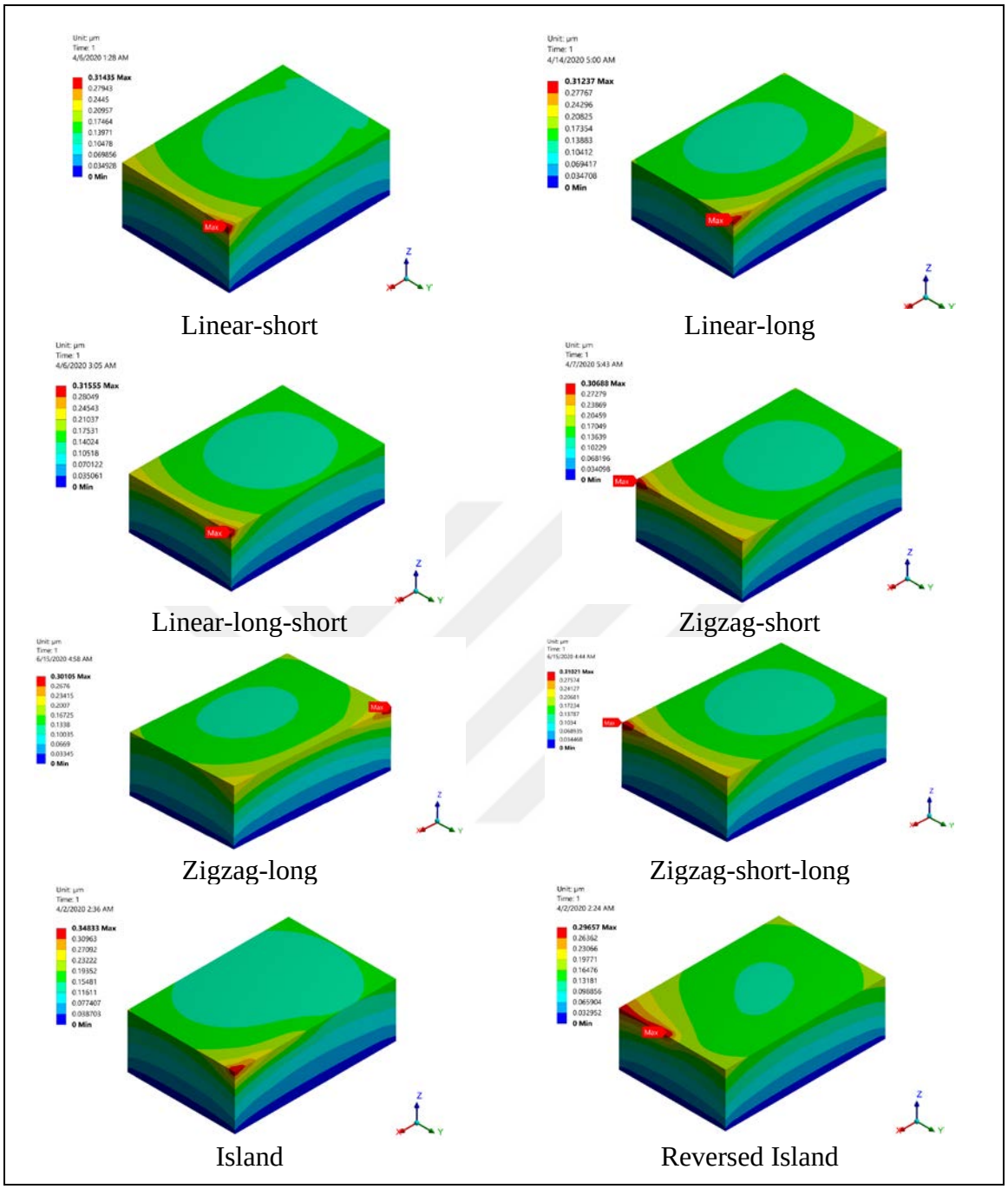

Figure 5.16. Distortion Contours for the studied build ordinations just after solidification.

Figure 5.17 depicts a bar chart for the normalized von Mises stress and distortion for the investigated build orientations. For the linear build orientations, the long-linear orientation had the highest residual stress, i.e., 13.3 % above the yield limit, while the linear-short and linear-long-short orientation had the lowest thermal stress, i.e., 12.2 % above the yield limit. All the linear build orientations produced nearly identical distortion results.

The zigzag build orientations resulted in high thermal stress of 13% above the yield limit and a minor distortion lower than the linear build orientations. The island build orientation generated thermal stress more than 12% higher than the yield. Additionally, the heat accumulation generated by the short scanning paths in a small area caused the island build orientation to have a high distortion value com-pared to the other build orientations. This trend did not appear in the reverse-island orientation, mainly due to the repeated layer scanning orientation changes. Based on residual stress and distortion, it can be concluded that the linear-short and linear-long short build orientations are the most effective.

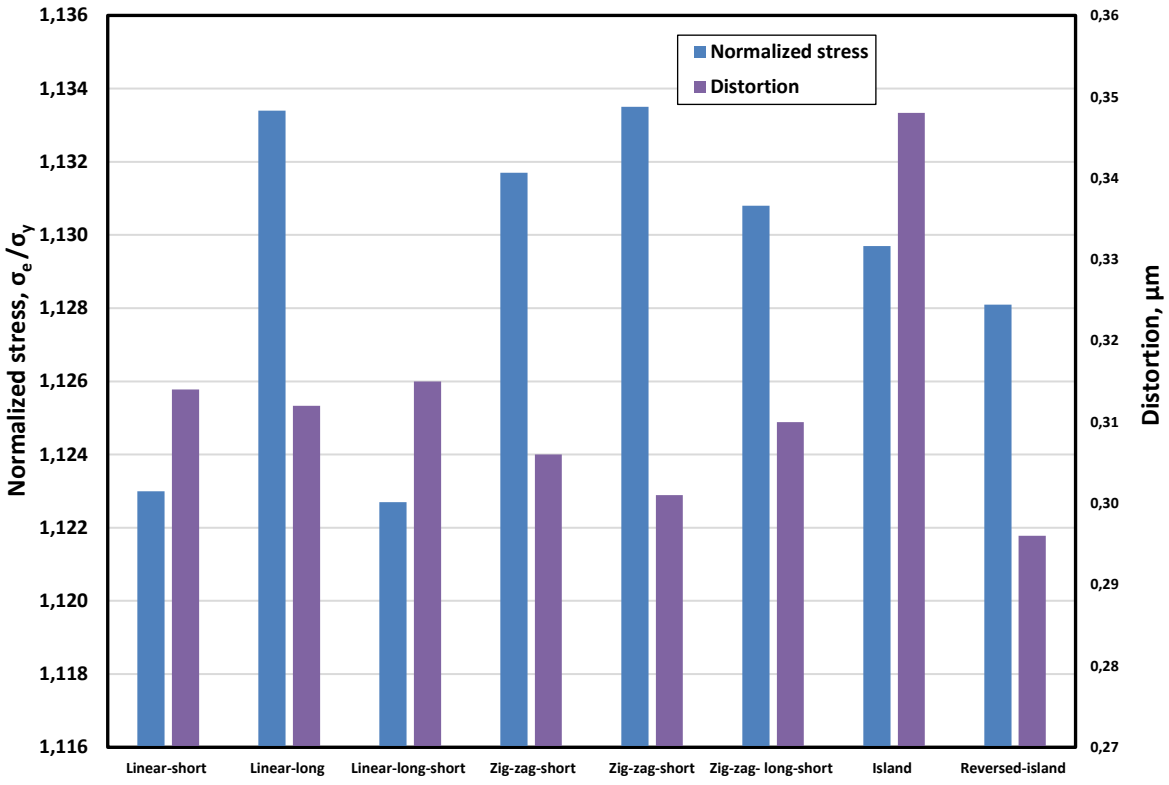

Figure 5.17. Residual stress and distortion for different build orientations.

Preheating 800 K was applied to the model for the linear-long-short build orientation. It can be seen from Figure 5.18 that the normalized von Mises stress decreased by 23% (from 1.22 to 0.947), and the developed distortion decreased by 54%. The reduction in developed stress and distortion is mainly due to the decrease in the temperature difference that the part has undergone. Therefore, it can be concluded that the PBSLP of alumina cannot be prosperous, i.e., free of cracks and defects, without pre-heating, and the available commercial printers

cannot be used effectively for ceramic materials. Special printers equipped with a preheating system for ceramic materials are needed.

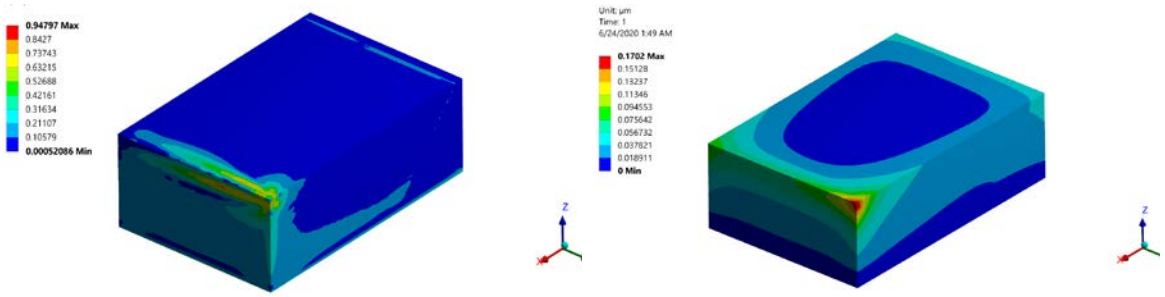

(a) Normalized von-mises stress (b) Distortion

Figure 5.18. Normalized von Mises stress and distortion obtained using a preheating temperature of 800 K (a); distortion obtained using a preheating temperature of 800 K (b).

5.2. Multi-Layer PBSLP Simulation of SiC

Initially, the developed numerical model was used to determine the laser power and sintering speed ranges for multilayer PBSLP of SiC. For the multilayer simulation of SiC, the same technique was used for the multilayer simulation of alumina. Table 4.5 details the laser power and sintering speed range for the 3D Systems-Phenix Pro X200 printer.

Table 5.5. Process parameters used for multilayer PBSLP of SiC

Item	Value
Laser type	Fiber laser
Laser power range (W)	Up to 300 W
Scanning speed range (mm/s)	Up to 1000 mm/s
Laser spot diameter, μm	70
Layer thickness, μm	50
Hatching distance, μm	35

Figure 5.19 displays the maximum temperature attained with different laser powers and sintering speeds. The laser power ranged between 25 and 60 W, while the sintering speed was between 200 and 1,000 mm/s. Figure 4.19 displays the maximum temperature for laser power and sintering speed at various values. SiC's sintering temperature is about 2140 K

[185], and its decomposition temperature is about 2800 K [126]. SiC PBSLP requires that the temperature be maintained within these two limitations. With the SiC PBSLP, all laser powers and sintering speeds that achieve a temperature between the sintering and decomposition limitations can be utilized efficiently.

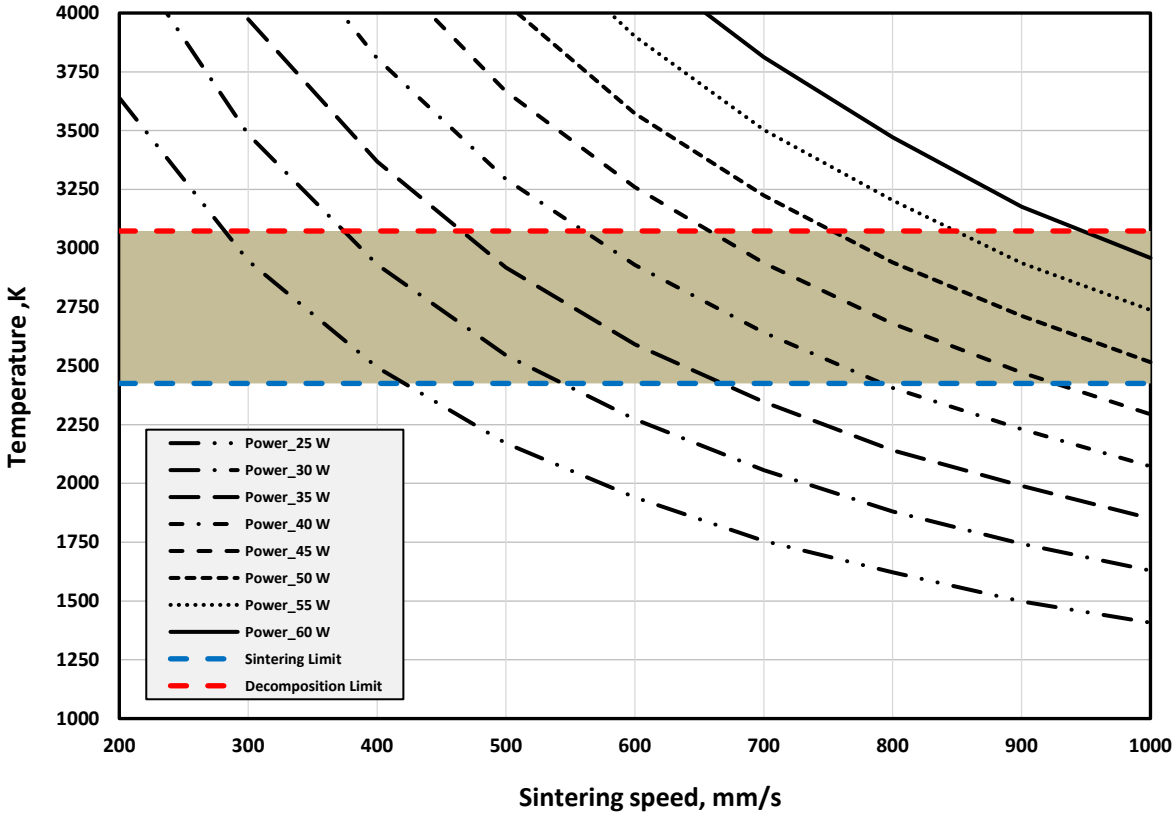

Figure 5.19. The maximum Temperature at different powers and scanning speeds for PBSLP of SiC.

A laser power of 50 W and a sintering speed of 1000 mm/s were selected for the multilayer PBSLP simulation of SiC. Since the long-short linear build orientation yielded the most favourable results in thermal stress and distortion for the PBSLP of alumina compared to the other build orientations, the multi-layer PBSLP of SiC was only investigated with the long-short linear build orientation.

5.2.1. Temperature history: multi-layer PBSLP of SiC

Figure 5.20 depicts the temperature history during the PBSLP of SiC with a long-short scanning orientation. The temperature history for multi-layer (10-layer) scanning is coloured blue, whereas it was coloured red for single-layer scanning. The axes for temperature and

scanning time (in seconds) for multilayer printing are located on the right and bottom of the graph, respectively. They are positioned on the left and top of the one-layer figure. As shown in Figure 5.20, the laser began scanning the first layer at 0s and completed the scan at 0.042s.

The model consumed five seconds (as determined by the 3D Systems-Phenix Pro X200 printer) before depositing the new layer and resuming the scanning process. This procedure was continued until all layers were scanned. The temperature history demonstrates that the heat accumulation within the printed part increased as a new layer was deposited and scanned. This occurred owing to the limited thermal conductivity of SiC, which allowed heat to accumulate within the material, and the short layering time (the amount of time necessary to deposit a new layer), as discussed previously in section 0.

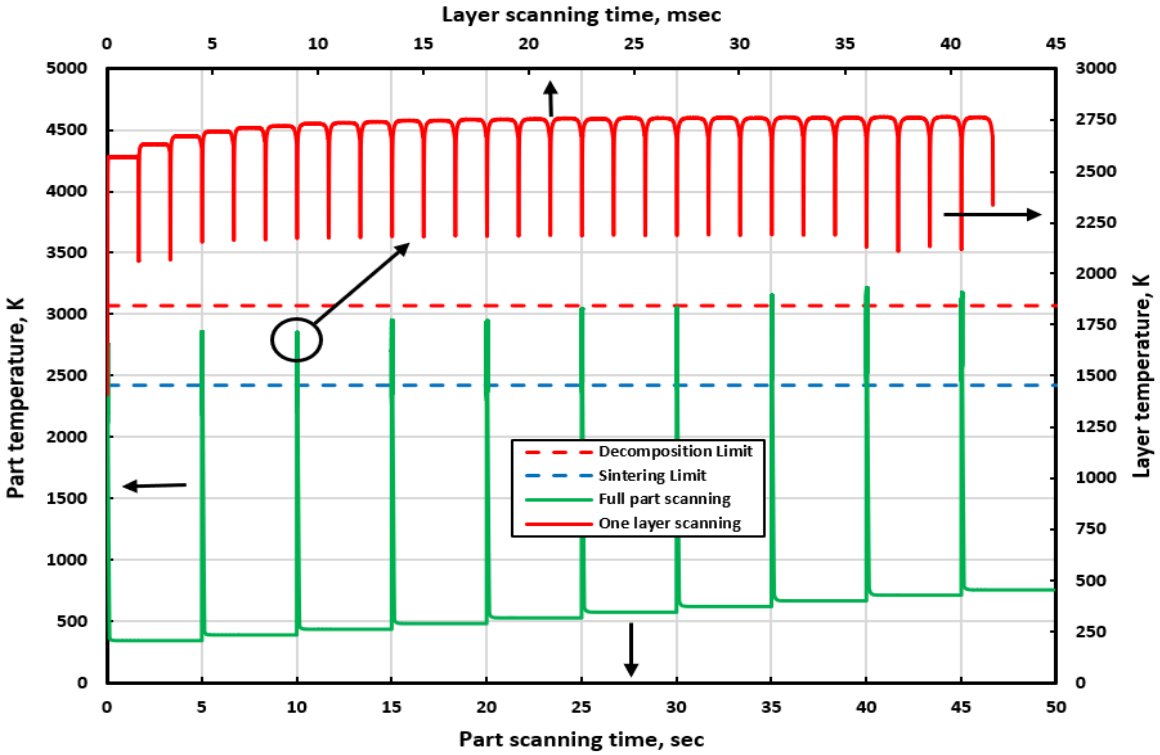

Figure 5.20. The temperature history for the multi-layer PBSLP of SiC.

5.2.2. Thermal stress and distortion

The temperature distribution within the printed component is the primary determinant of the thermal stress developed in part. In the coupled-FE model, the temperature distribution was a thermal load for calculating the thermal strain. Using the numerical model, the temperature

distribution for the multi-layer PBSLP of SiC with the long-short linear build orientation is depicted in Figure 4.21a. Figure 5.22b depicts the computed von-Mises stress, whereas Figure 5.22c depicts the normalized thermal stress. Due to contact with the baseplate, which prevented displacement, the normalized stress contour reveals that the maximum stress was located at the bottom of the part. In addition, certain locations exhibited normalized stresses larger than one, indicating cracks may emerge. Figure 4.21d displays the distortion of the printed part, with the least evident distortion at the base of the part due to contact with the baseplate. As demonstrated in Figure 5.22, preheating can be utilized to lower developed stress. When a 500 K preheating was applied to the model, the normalized von Mises stress reduced from 1.03 to 0.863 (a 16 % decrease) and the distortion decreased to 0.14 µm (a very slight decrease in the distortion value). Consequently, it is essential to employ preheating during ceramic PBSLP.

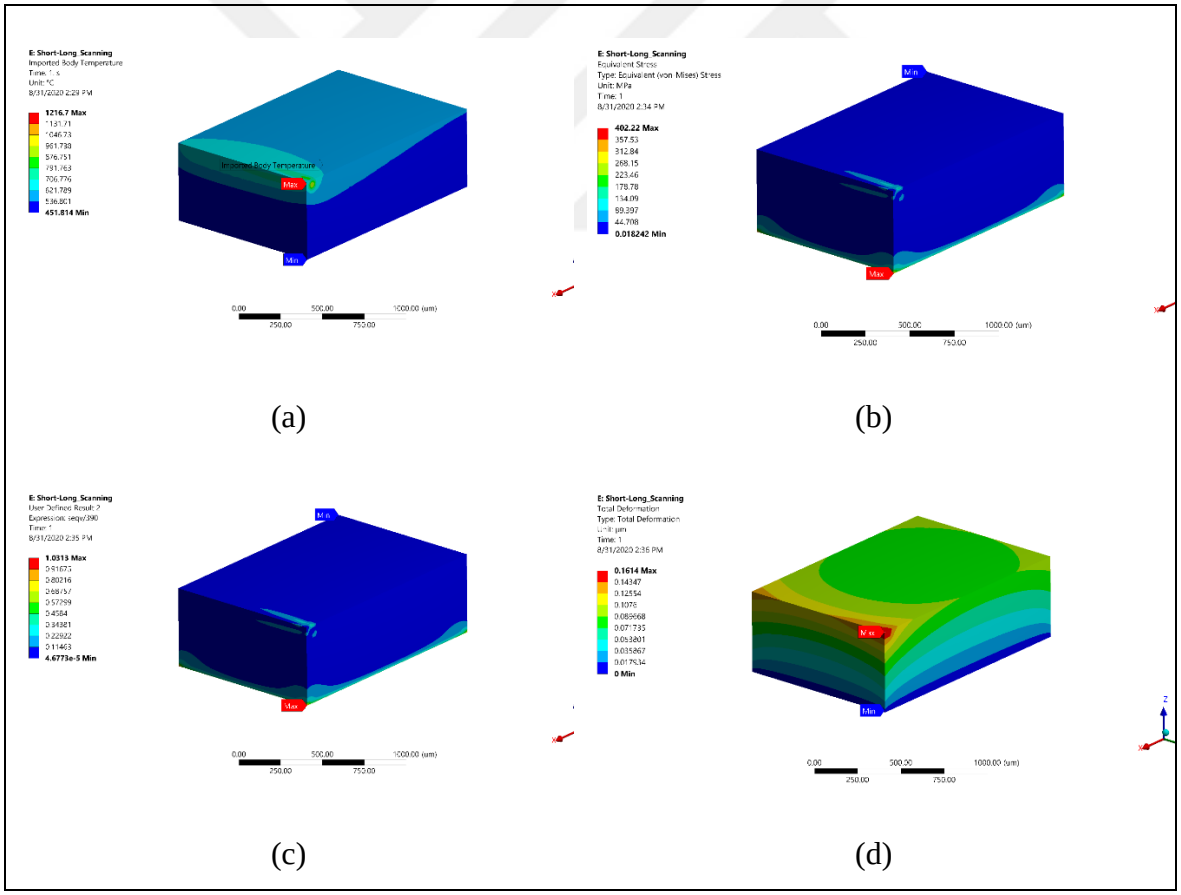

Figure 5.21. Temperature distribution (a); von-Mises stress (b); normalized von Mises stress (c); distortion (d).

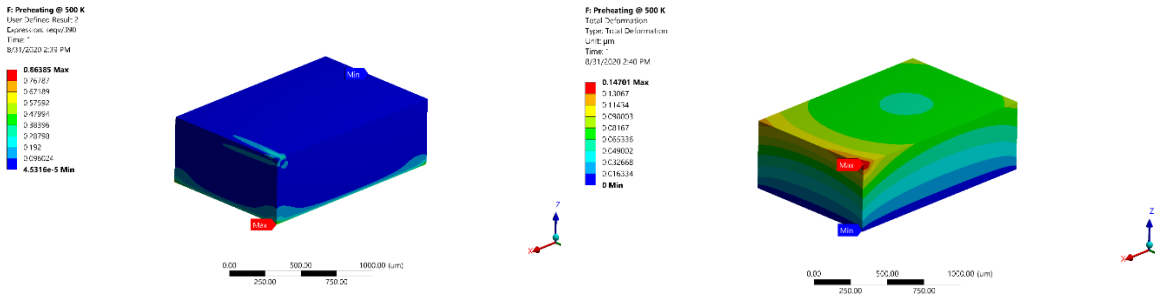

(a) (b)

Figure 5.22. The effect of preheating of multilayer PBSLP simulation of SiC: Normalized von Mises stress (a); distortion (b).

5.3. Conclusion

This chapter concludes that using the appropriate laser for the investigated ceramic materials is essential. The most important factor to consider when selecting a laser is absorptivity, meaning that the ceramic material should have a good absorptivity for the laser. As a result, the PBSLP technique can utilize a low laser power and adequate scanning speed.

Due to the low absorptivity of alumina for the Nd-Yag laser, this laser should be accompanied by high laser power and a low scanning speed. The CO_2 laser, however, requires a low laser power and a high scanning speed. Since alumina has a high absorptivity for the CO_2 laser, it is possible to use low laser power values and a high scanning speed.

In addition, in this section, scanning strategies were investigated using the developed numerical model, and the results indicated that the zigzag strategy showed promising performance for PBSLP of alumina. However, ceramic materials require an entirely new scanning strategy.

Multi-layer PBSLP of alumina was investigated using the developed numerical model employing the previously obtained process parameters and zigzag scanning strategies considering various build orientations. The results demonstrated that heat accumulates as the number of deposited layers increases, affecting the developed thermal stress and distortion. A temperature controller should be used to control the laser power during scanning, and a preheating system should also be utilized to minimize thermal stress and cracks in the printed part.

The conclusion for Multi-layer PBSLP of SiC is identical to that for alumina. The results revealed that there is a heat accumulation during the process, which increases the developed thermal stress and the possibility of cracking. In addition, this heat accumulation increases as the number of deposited layers increases. The development of PBSLP printer for ceramics should consider controlling the temperature and employing preheating, which are crucial factors.

6. D-PBSLP OF ALUMINA

This chapter is divided into four sections and discusses the D-PBSLP for alumina. The characterization of the spray-dried alumina powder is described in Section 6.1. Using the developed numerical model, section 6.2 determines the ideal ranges for laser power, scanning speed, and hatching space based on the available ranges for each parameter in the Renishaw® SLM 125 printer. In addition, section 6.2 studies experimentally and numerically the influence of scanning strategies on the PBSLP of alumina to determine the best scanning strategy. Section 5.3 studies the effect of scanning speed and establishes the best scanning speed range for alumina PBSLP. Using the results of sections 6.2 and 6.3 as a guide, section 6.4 focuses on using the Taguchi optimization methodology to optimize the scanning speed, laser power, and hatching space to obtain a high-quality alumina sample using the D-PBSLP technique. Microhardness and compressive tests are used in section 6.5 to evaluate the mechanical performance of alumina manufactured using the D-PBSLP technique.

6.1. Powder Characterization

Figure 6.5 depicts the PSD for Al-raw powder (as received from Alteo), where it can be observed that the raw powder (Al-raw) has a mean particle size distribution of 390.6 µm and was agglomerated in significant irregular accumulations, which is completely unsuitable for powder bed AM techniques as this high PSD may present difficulties in terms of its uniform spreading on the printer powder bed [68]. This is primarily attributable to the fact that agglomerated particles inhibit the flowability of particles during Powder bed AM techniques [183]. Furthermore, the flowability is affected by the interparticle friction generated by these irregular particles. Therefore, the Al-raw was not considered for the D-PBSLP of alumina also due to its low absorptivity for the printer laser type.

Therefore, as previously explained in section 2.2.1, the spray-dried was used to modify the raw powder to be appropriate for AM powder bed techniques. The spray-dried technique produced two primary powder categories; the main and cyclonic parts are Al-M and Al-C, respectively. In order to investigate the effect of granule size, the powder main part (Al-M) was separated into two batches after sieving at 100 µm, fine and coarse fractions. Al-MF is the fine fraction (powder sizes smaller than 100 µm), while Al-MC is the coarse fraction

(powder sizes greater than 100 µm). Figure 6.5 illustrates the PSD for each powder category, whereas Figure 6.2 depicts each powder category's morphology (SEM images).

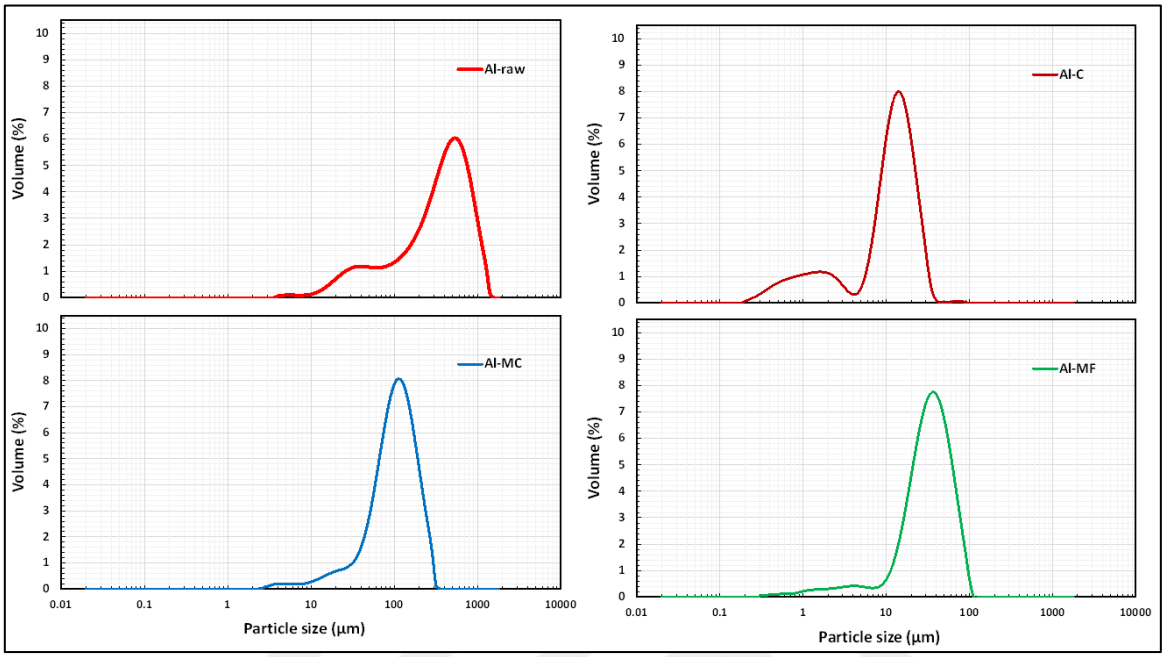

Figure 6.1. PSD for different categories of alumina powder as described in section 3.2.1.

For the cyclonic part of the spray-dried powder (Al-C), it can be noted that it has a narrow distribution with a mean particle size of 12.6 µm, as shown in Figure 6.5, and it contains agglomerated large particles and irregular fine particles, as seen in Figure 6.2, which are vulnerable to significant interparticle friction. In addition, the agglomerated particles were so soft that they could not endure the recoater action during powder layer deposition. Therefore, this powder category was not considered for the D-PBSLP of alumina.

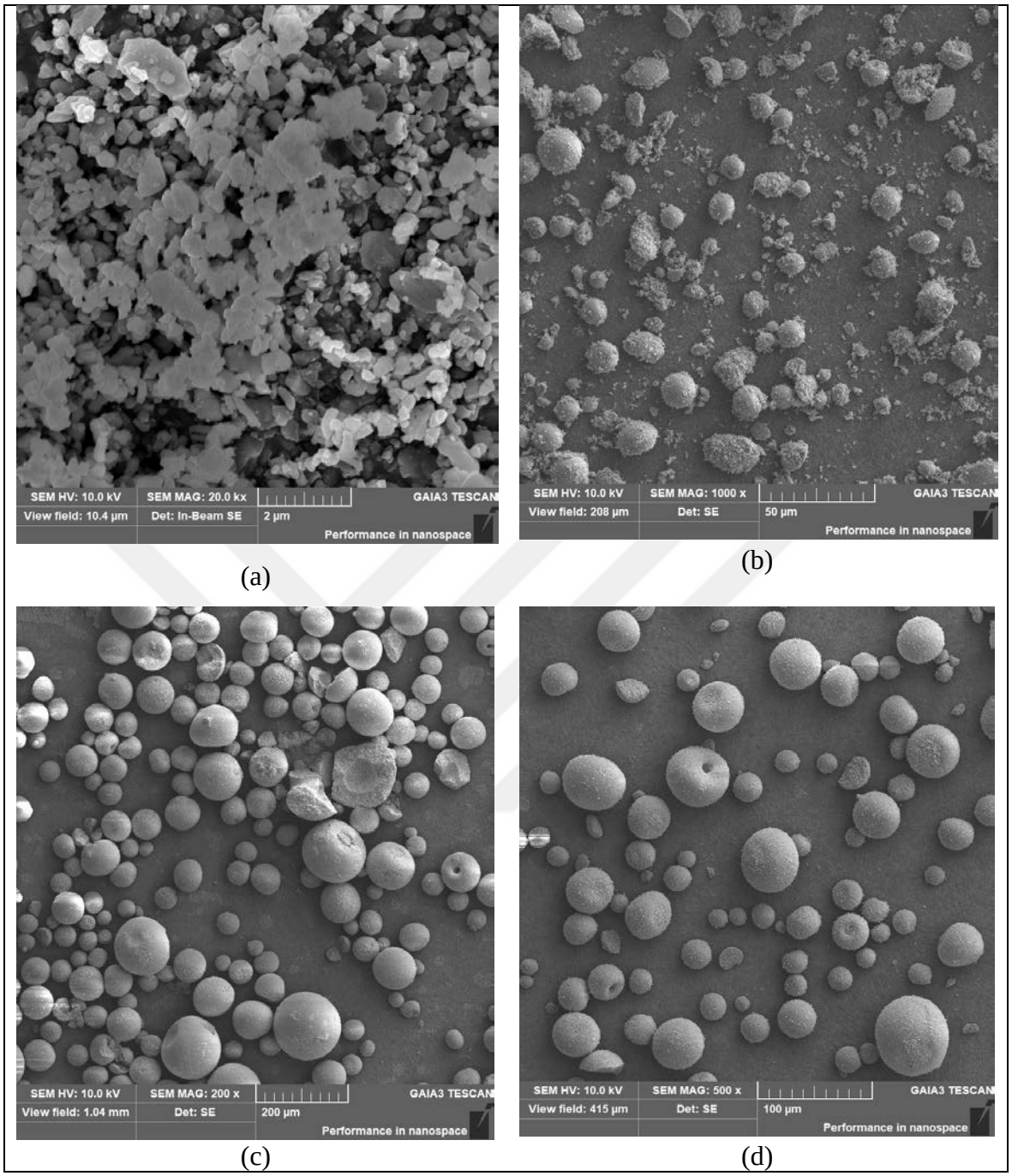

Figure 6.2. Alumina powder morphology: Al-raw (a); Al-MC (b), Al-MF (c); Al-C (d).

In Powder bed AM techniques, it is highly recommended to have a spherical powder shape and a particle size distribution (PSD) within the range of tens of microns to ensure low friction between particles and good flowability during the powder spreading on the powder bed; these conditions can be achieved by spray drying technique utilized in this dissertation [68].

As depicted in Figure 6.2, the major coarse portion of the spray-dried alumina powder (Al-MC) satisfies these requirements as the powder shape seems nearly spherical. However, the Al-MC powder has a PSD distribution of approximately 109.2 µm, which is considered unsuitable for usage with the 100 µm layer thickness employed in this investigation, as most of the powder will be deposited in the printer's surplus tank. Consequently, this powder category also was not utilized in the D-PBSLP of alumina.

The Al-MF powder has a mean PSD of 35 µm, making it an ideal material for powder bed AM methods [68]. In addition, the powder morphology exhibits completely spherical shapes for the powder particles, allowing for more free-flowing behaviours during layer spreading over the powder bed. The Al-MF has therefore deemed the feedstock for the D-PBSLP alumina process.

The powder flowability of Al-MF was evaluated using a Hall Flowmeter. The Hall flow rate (FRH) is defined by ASTM standard (B213-13) as "The time required for a metal powder sample of a particular mass to pass through the orifice of a Hall flowmeter funnel according to a certain procedure" [184]. As a standard technique for characterizing powders, powder metallurgy has embraced the Hall-flowmeter. It calculates the time needed to discharge 50g of powder through a conventional funnel aperture (Figure 6.3) with the top and bottom of the hopper open to the air (so that pressure at these locations is identical). This allows for estimating the average mass flow rate [185, 186]. Hall Flowmeter does not have a criterion that can be used to indicate flowability, but it can be used to compare and evaluate various powders.

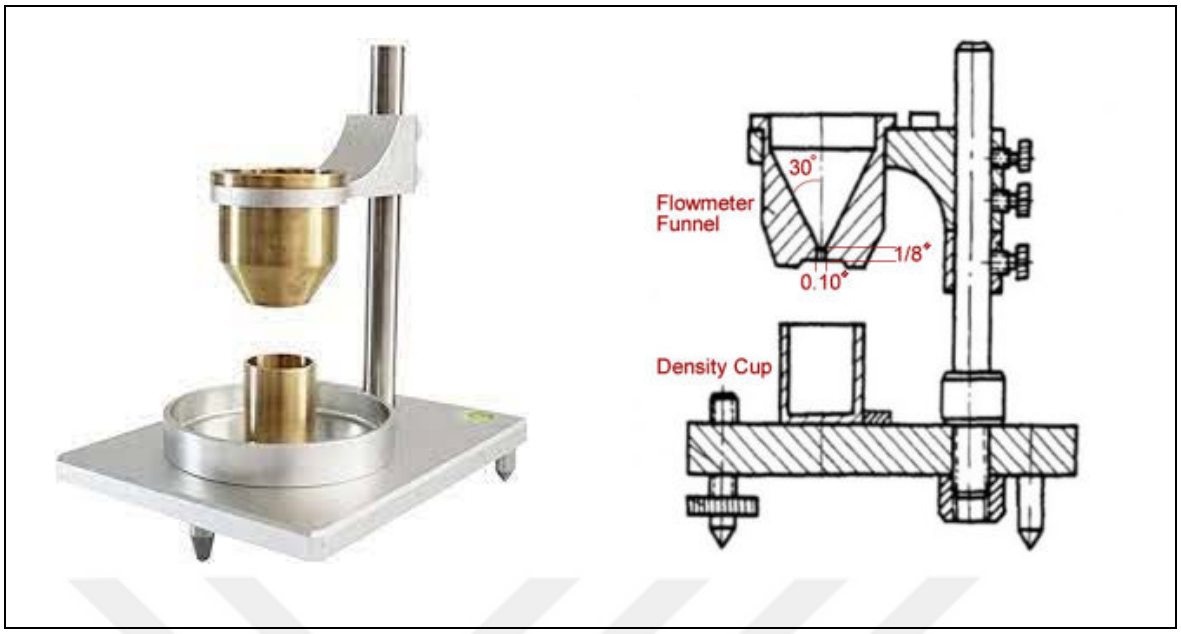

Figure 6.3. Hall flowmeter [187, 188].

To assess Al-MF powder flowability, the time it took for 50g of powder to pass through a conventional Hall flowmeter funnel's orifice was measured and repeated three times. The measured duration of each test is summarized in Table 6.2.

Table 6.1. Elapsed time to discharge a 50g of Al-MF powder through Hall flowmeter orifice.

Test no.	Time, s
1	140
2	140
3	141

It can be observed from Table 5.1 that the time it took for 50g of Al-MF to flow through the orifice is longer than the time it took for a metallic powder to flow through the orifice [184], which may present difficulties when spreading the powder layer on the powder bed.

Therefore, testing the powder deposition on the powder bed was essential. Figure 6.6 demonstrates that the Al-MF powder was successfully and uniformly deposited on the printer bed with no defects.

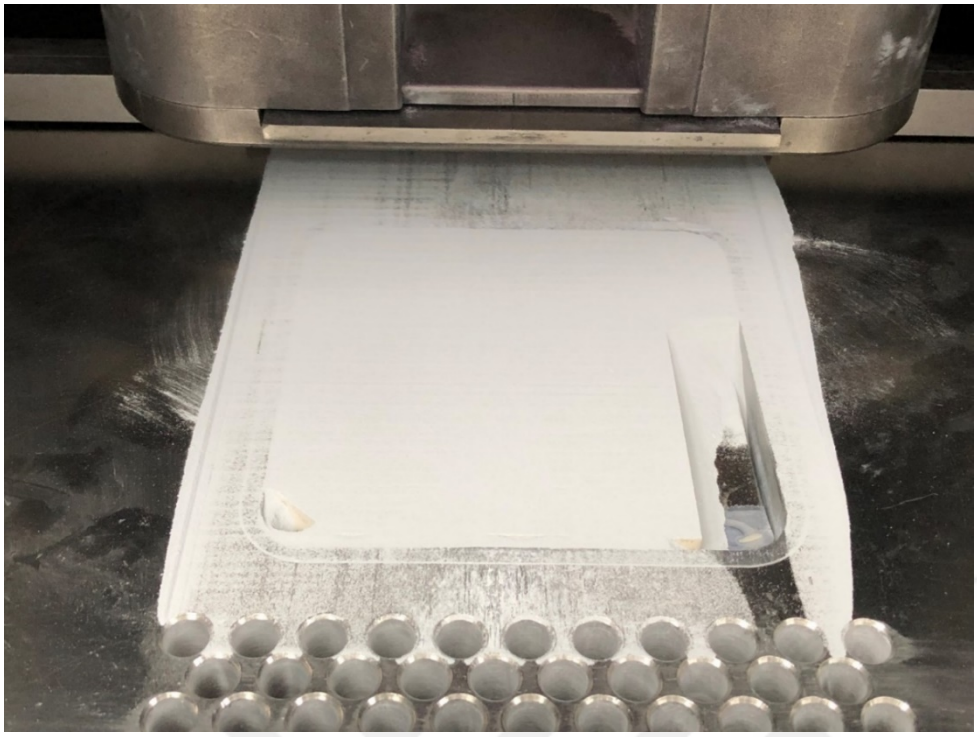

Figure 6.4. Spray-dried alumina (Al-MF) deposition on the printer powder bed.

6.2. Process Parameters Investigation

For PBSLP to be successful on ceramic materials, it is necessary to investigate the process parameters. These parameters include laser power, scanning speed, hatching distance, layer thickness, and scanning strategies. As laser power and scanning speed are interdependent parameters, selecting a laser power and scanning speed eliminates all previous concerns is essential. Laser power describes the transmitted energy to the powder bed. Low laser power results in un-sintered/un-melted regions in the powder bed, whereas high laser power leads to an unstable melt pool and the formation of pores, which impacts the output properties. The scanning speed determines the rate at which energy from the laser source is distributed throughout the powder bed. Low or high scanning speeds will greatly affect the part quality and may result in printing failure.

The hatching spacing is the distance between two adjacent paths, and it is crucial to the mechanical properties of the final printed part because it controls the contact between these adjacent paths. Layer thickness is the distance between successive layers and highly affects the building rate. Using thicker layers decreases the number of times the recoater is required, which substantially affects the processing time. However, the resolution of the component decreases as the layer thickness increases. In addition, excessive layer thickness can lead to

poor adhesion between layers and printing defects. Therefore, the layer thickness should be as high as possible but short enough to ensure adhesion between layers and prevent separation [20]. The scanning strategy refers to how the laser beam scans the entire layer. In addition, it regulates the heat distribution within the layer and, as a result, the thermal stresses and cracks that develop. Therefore, it should be appropriately selected for D-PBSLP of ceramic materials in general, as no previous study has considered its effect.

The developed numerical model was used to initially estimate the appropriate values for these process parameters to be used as a guide throughout the experimental study.

6.2.1. Laser power and scanning speed investigation

The developed numerical model was used to numerically investigate the laser power and scanning speed for the alumina PBSLP. In the Renishaw® SLM 125 printer, the layer thickness was set to 100 µm and could not be changed.

In the Renishaw® SLM 125 printer, the point distance (pd) and the exposure time (exp_t) are used to adjust the scanning speed, as shown in Figure 6.5. To achieve the desired scanning speed, the point distance was fixed at 40 µm, and the exposure time was adjusted.

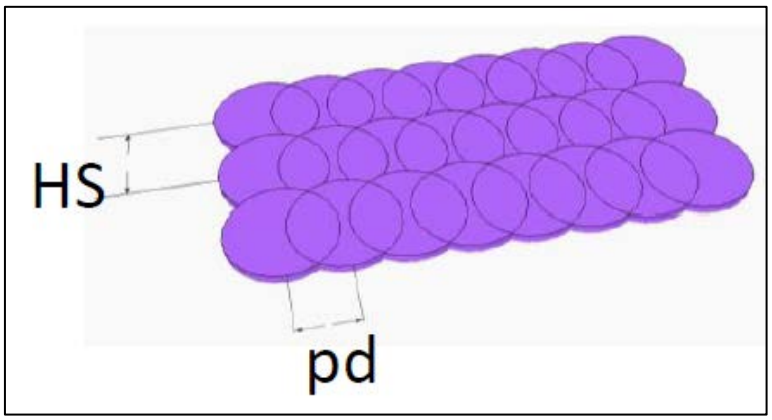

Figure 6.5. Schematic representation of point distance and hatching spacing.

Table 6.2 summarises the point distance and exposure time values per each scanning speed. Relatively low Scanning speeds of 100, 200, 300, and 400 mm/s were considered to reduce the laser beam inertia effect (using high scanning speeds with ceramics, which have low-density values, may result in scattering of powder particles due to high laser beam inertia

due to high scanning speeds). The numerical model was then utilized to determine the optimal laser power range for each scanning speed.

As calculated from the developed numerical model, the appropriate laser power range for each scanning speed was chosen to melt the entire layer thickness, adhere it to the layer below, and provide a maximum temperature lower than Alumina's evaporation limit. As previously stated, the layer thickness employed in PBSLP of alumina was 100 µm.

Table 6.2. Point distance and exposure time used for the PBSLP of Alumina.

No	Scanning speed, mm/s	Point distance, µm	Exposure time, µs
1	100	40	400
2	200	40	200
3	300	40	134
4	400	40	100

The laser power range that met the previously specified requirements for a 100 mm/s scanning speed was determined to be between 50W and 65W, as shown in Table 6.3. This power range could melt the entire layer thickness and adhere it to the layer below. Notably, the obtained temperature was above the alumina's boiling point due to the excessive layer thickness used for alumina (100 µm). Table 6.4, Table 6.5, and Table 6.6 detail the laser power range for scanning speeds of 200, 300, and 400 mm/s, respectively, where each power range determined by the numerical model for each scanning speed could melt the layer thickness and adhere it to the layer beneath.

Table 6.3. Melting contour and temperature distribution at different positions for the scanning speed of 100 mm/s.

Power, W	Top layer melting contour	Cross-sectional melting contour	Temperature contour
50	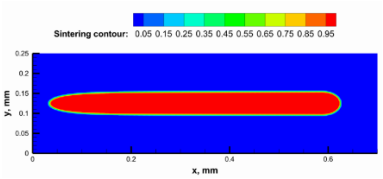	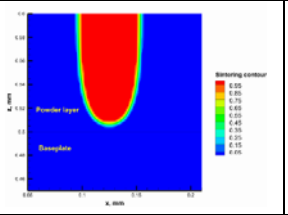	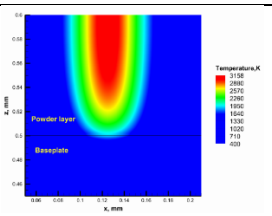
60	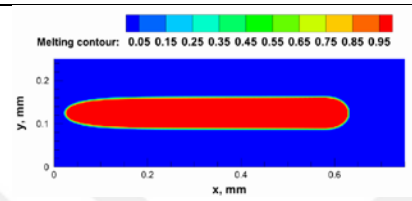	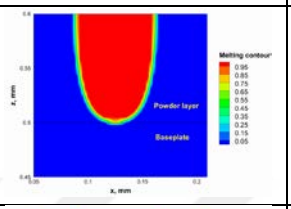	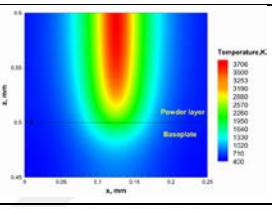
65	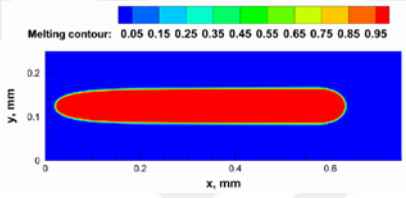	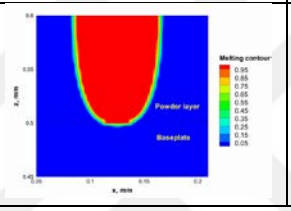	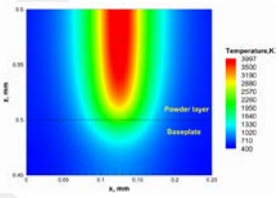

Table 6.4. Melting contour and temperature distribution at different positions for the scanning speed of 200 mm/s.

Power, W	Top melting contour	Cross-sectional melting contour	Temperature contour
95	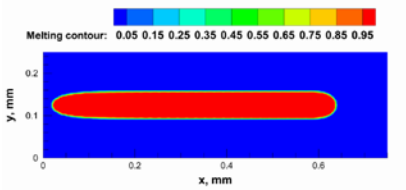	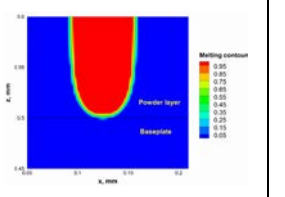	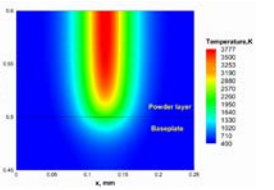
100	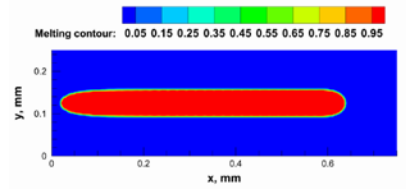	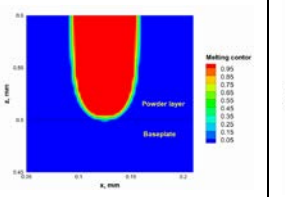	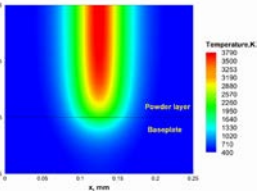
105	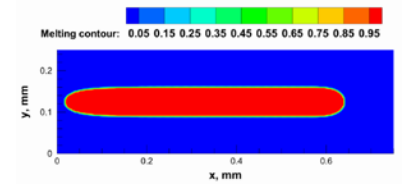	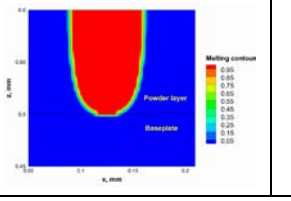	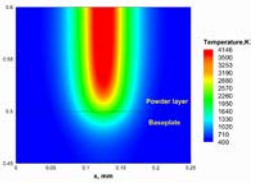

Table 6.5. Melting contour and temperature distribution at different positions for the scanning speed of 300 mm/s.

Power, W	Top melting contour	Cross-sectional melting contour	Temperature contour
120	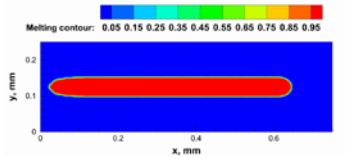	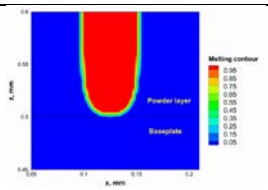	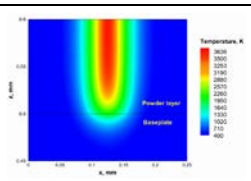
125	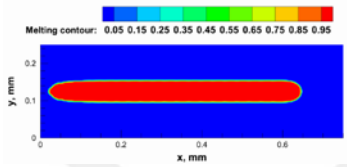	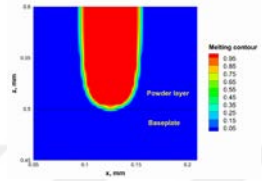	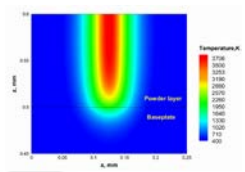
130	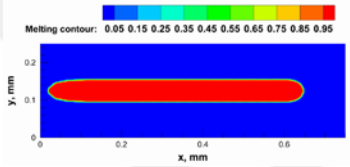	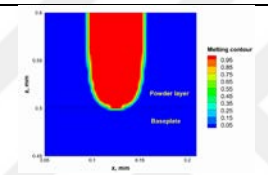	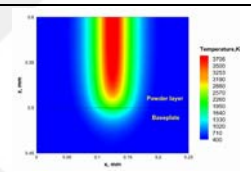

Table 6.6. Melting contour and temperature distribution at different positions for the scanning speed of 400 mm/s.

Power, W	Top melting contour	Cross-sectional melting contour	Temperature contour
150	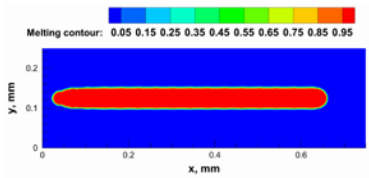	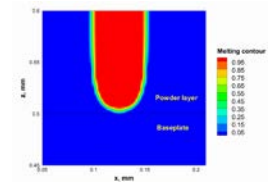	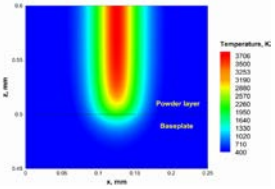
160	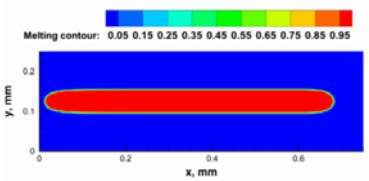	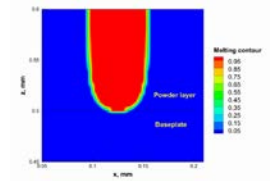	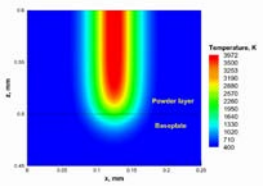
170	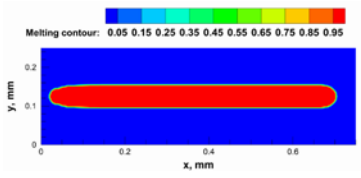	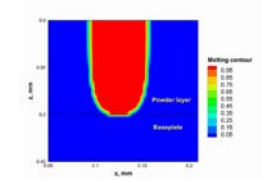	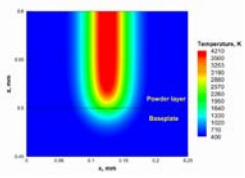

6.2.2. Hatching space investigation

The hatching (distance) space is a crucial parameter because it controls the contact between adjacent paths and, consequently, influences printed samples' mechanical and physical properties. Therefore, it is essential to choose the hatching space with care. The developed numerical model was used to test various hatching spaces, including 100, 75, and 50 µm for each scanning speed, considering the middle value of the laser power range, as previously determined.

Table 6.7 describes the melted path width achieved for each scanning speed. It was discovered that as the scanning speed increased, the width of the melted path decreased. This was primarily because low scanning speed provides more opportunity or time for more particles to melt, as opposed to high scanning speed, in which the powder particles do not have sufficient time to absorb the laser beam's heat. Table 6.7 describes the effect of different hatching space values (as mentioned previously) for each scanning speed. For a 100 µm hatching space, the scanned paths were not connected at all scanning speeds; therefore, it is not recommended to use this value. In addition, using a hatching distance of 75 µm, scanning paths could only be connected with a scanning speed of 100 mm/s, while higher scanning speeds result in no contact. The scanning paths could be connected using a hatching space of 50 µm with all investigated scanning speeds. Therefore, it is recommended that a hatching space of at least 50 µm be used with each of the investigated scanning speeds.

Table 6.7. Hatching distance analysis for different scanning speeds.

speed	One path	100 µm	75 µm	50 µm
100 mm/s	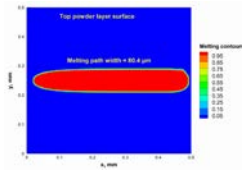	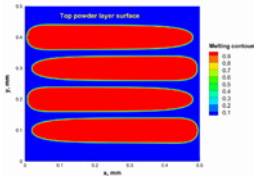	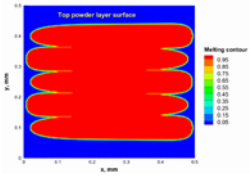	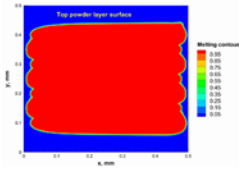
200 mm/s	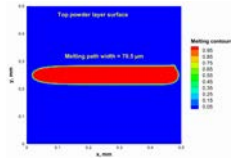	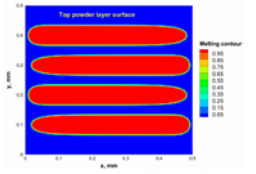	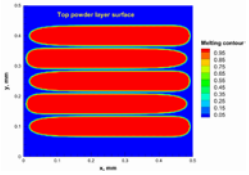	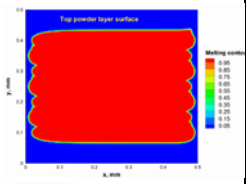
300 mm/s	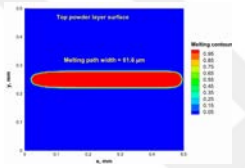	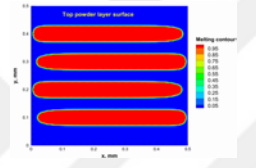	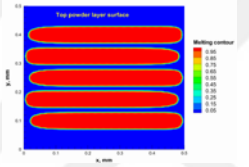	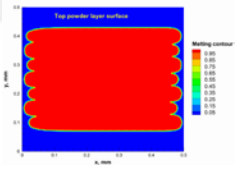
400 mm/s	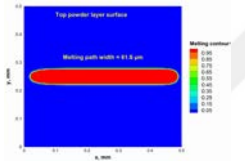	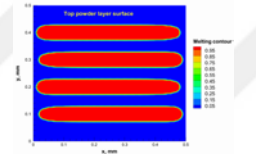	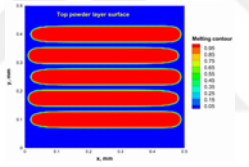	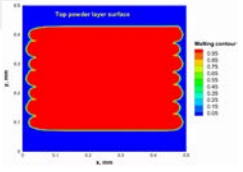

6.2.3. Scanning strategies investigation

PBSLP parameters include, as mentioned previously, laser power, scanning speed, hatching space, layer thickness, and scanning strategies. The laser power, scanning speed, and hatching space have been studied, and their values were initially determined using the developed numerical model; the only remaining parameter to investigate is the scanning strategies.

To investigate the effect of scanning strategies on the D-PBSLP of alumina, a laser power of 95 W, scanning speed of 200 mm/s, hatching distance of 50 µm, and layer thickness of 100 µm were employed. As shown in Figure 6.6, various samples were printed using different scanning strategies, including linear-0°, linear-90°, and linear-45°, concentric out-in, and island, as described in section 0. Except for the island-linear strategy, which failed to print an alumina cubic part due to its short and adjacent scanning paths in a small area, all printed samples have a cubic shape with flat surfaces from all sides. These short scanning

paths accumulated a large amount of heat in a minimal area, which caused the alumina in that region to boil and ultimately caused the building to collapse. Therefore, this strategy cannot be utilized for D-PBSLP of alumina and was excluded from further analysis and investigation.

Figure 6.7 illustrates a 3D microscopic view of the sample's upper surface as captured by a 3D laser scanning microscope (VKX-250, Keyence, Japan). Each sample displayed patterns generated by the employed scanning strategy, precisely the concentric out-in and island strategy. Two crossed lines (X shape) and a central hole were observed in the sample printed using the concentric scanning strategy, whereas the island-concentric strategy produced small holes on the top surface of the sample.

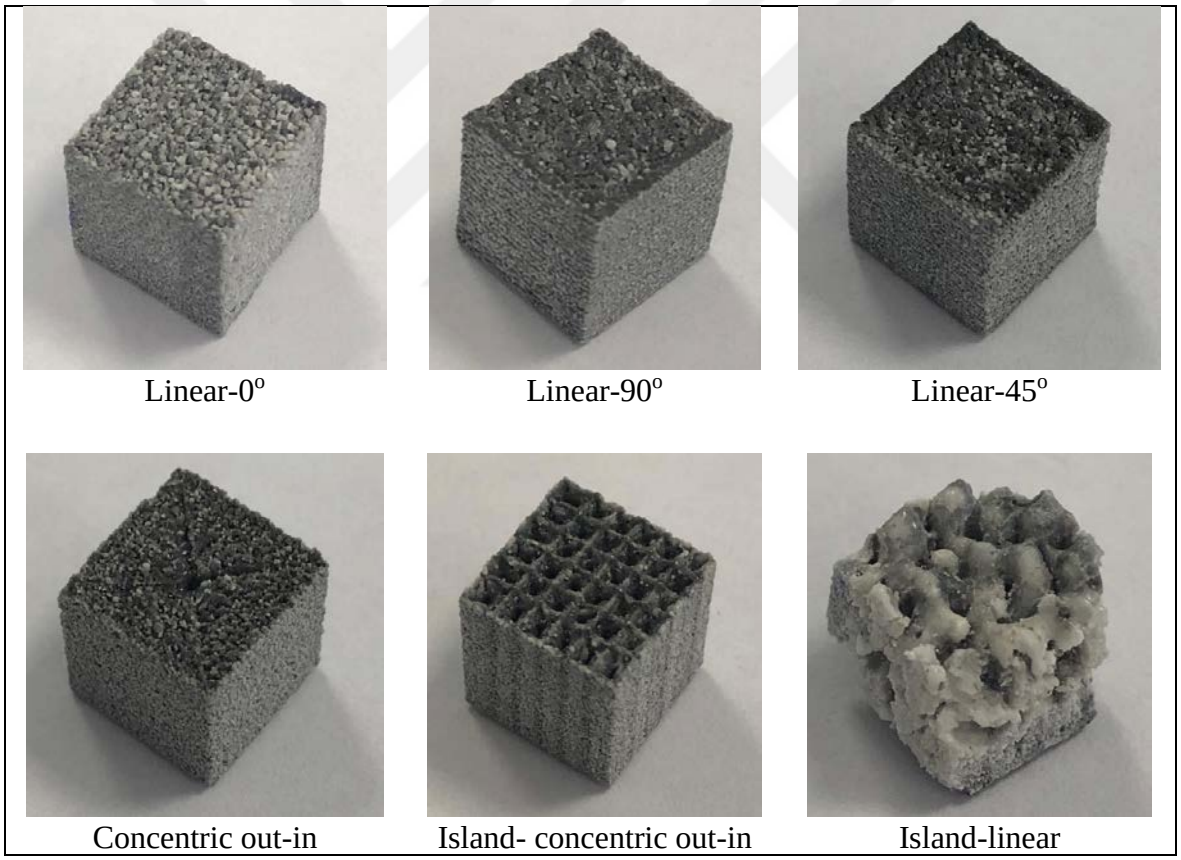

Figure 6.6. Alumina samples printed using different scanning strategies (10×10×10 mm^3).

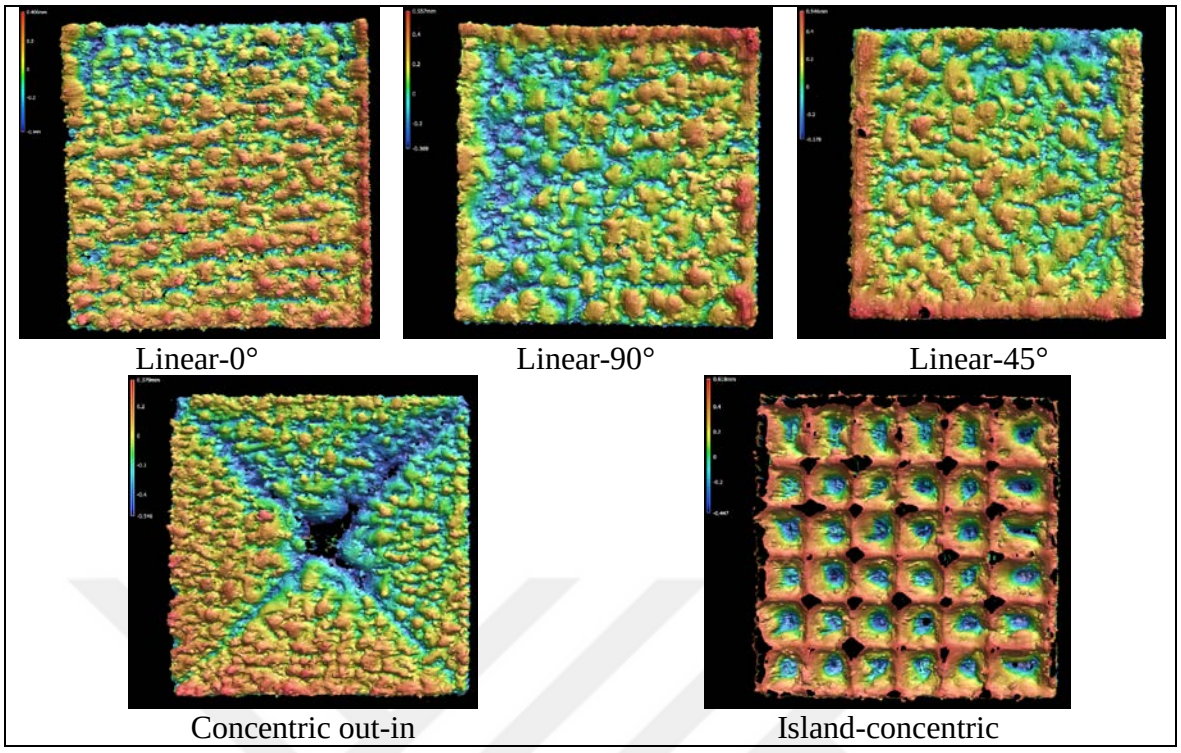

Figure 6.7. 3D microscopic analysis for the alumina samples printed using different scanning strategies.

The developed numerical model was used to interpret the unusual patterns the concentric out-in and island strategies produced. As depicted in Figure 5.8, it was discovered that when the laser began changing its direction, a significant increase in temperature occurred. This abrupt temperature increase was sufficient to evaporate alumina from the center of the rotation. The laser's path changed four times per cycle, resulting in the formation of two diagonal lines. In addition, the small hole that formed in the center of the sample was primarily caused by the short scanning paths that accumulated in a small area at the end of the layer scanning, leading to a high concentration of heat and the removal of sample material from the center.

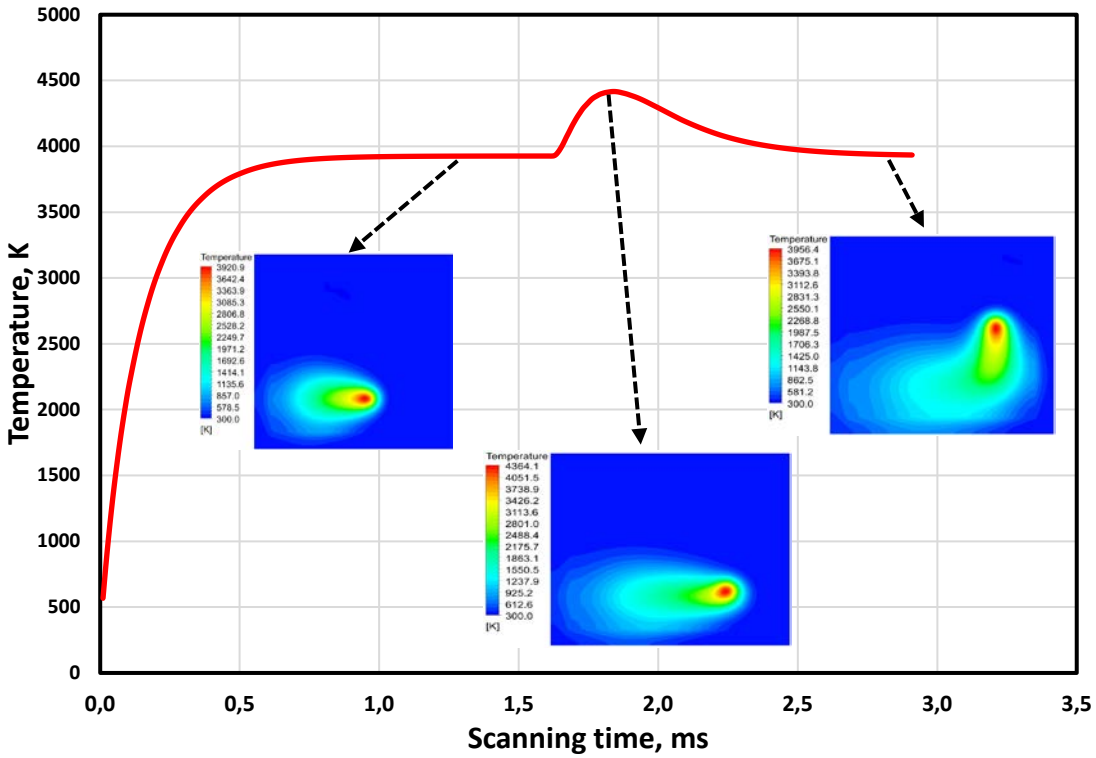

Figure 6.8. Sharp temperature increase due to the laser direction change.

Due to the fact that the island strategy is comprised of a small concentric out-in strategy, small holes formed on the surface of the top layer, primarily as a result of the heat concentration at the minimal area as previously described. Figure 6.9 depicts the melting contour and temperature history for a one-island where the heat concentration resulted in a high-temperature history at the end of the scanning.

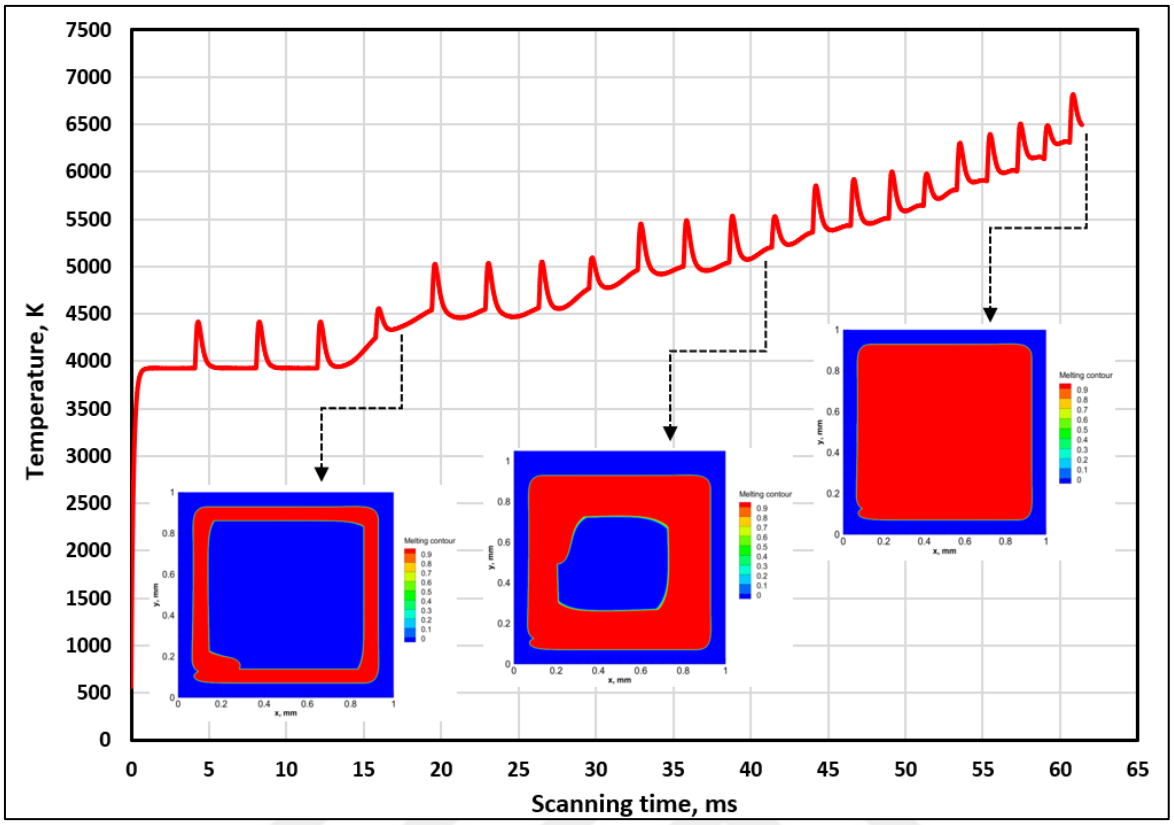

Figure 6.9. The temperature history of small concentric in-out strategy where heat concentration happened at the end of scanning.

The top surface roughness was measured using the 3D laser scanning microscope (VKX-250, Keyence, Japan), and the results are displayed in Figure 6.10. The top surface patterns significantly influenced the surface roughness values for each scanning strategy. Linear strategies exhibited the lowest surface roughness values due to the absence of a distinct pattern on the layer's top surface, whereas concentric in-out and island strategies exhibited high values. The top surface roughness for the concentric in-out strategy was 152 µm, whereas the island strategy produced a surface roughness of 206 µm.

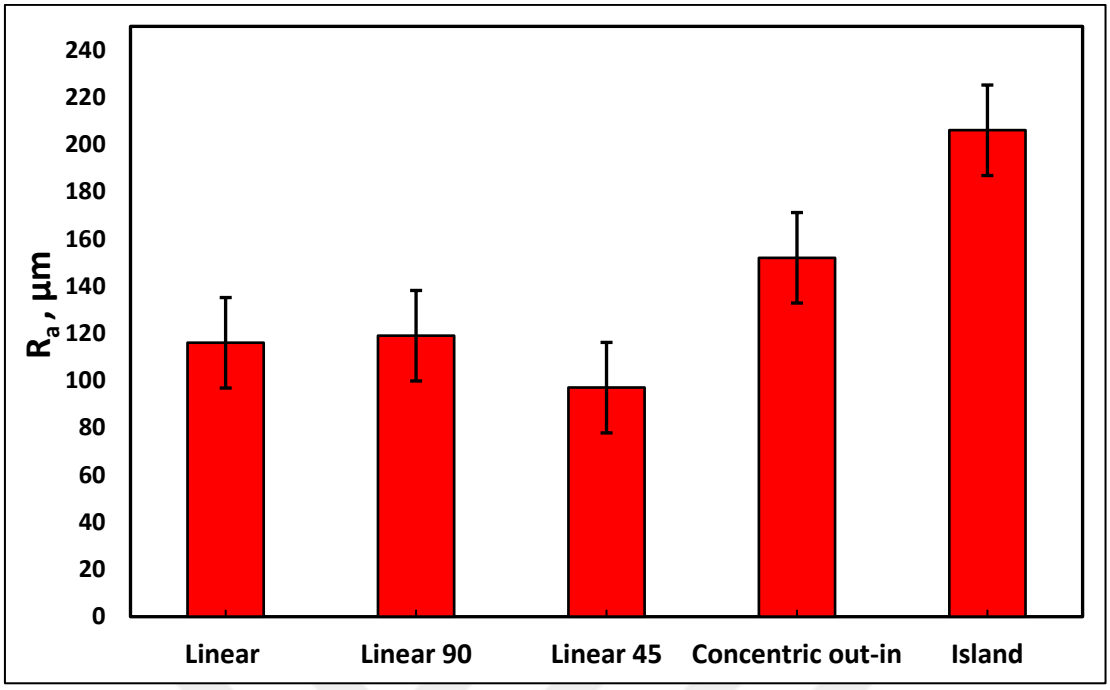

Figure 6.10. Top surface roughness of the printed sample using different scanning strategies.

The relative density of alumina samples was evaluated using Archimedes' method. As illustrated in Figure 6.11, various alumina samples were printed using a scanning speed of 200 mm/s, a layer thickness of 100 µm, a hatching distance of 50 µm, and a laser power range of 95 to 105 W. The black top surface of the alumina samples is primarily attributable to the high oxygen level in the building chamber, which was 5000 ppm and could not be reduced below this value. In addition, the addition of graphite to increase the alumina powder absorptivity was a significant factor. As described in the following sections, XRD analysis was performed to determine the phases within the alumina printed sample.

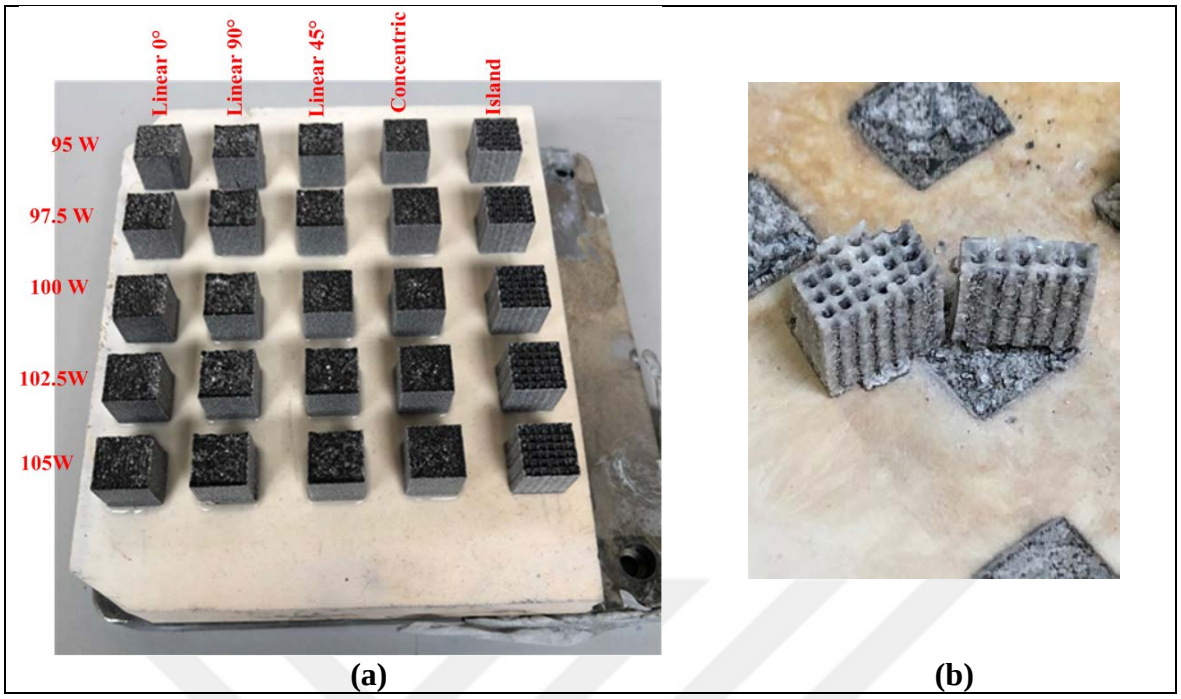

Figure 6.11. Alumina samples were printed using different scanning strategies at different laser power (a); broken alumina samples were printed using the island strategy containing the round passages (b).

Figure 6.12 illustrates the variation in relative density as a function of laser power for various scanning strategies. In general, the relative density increased as the laser power increased. This was primarily since increasing laser power led to more particle densification. At 105 W laser power, the linear-0° strategy had the lowest relative density, reaching 69%, whereas the linear-90° and linear-45° strategies achieved 75% relative density. The unchanging layer orientation during scanning explains why the linear-0° strategy exhibited a lower relative density than the linear-90° and linear-45° strategies, as changing the layer orientation during scanning reduces the sample's porosities. Figure 6.12 also demonstrated that the relative density achieved with the concentric strategy was low, reaching 67%, primarily due to the removal of material caused by the rotation of the laser beam.

Despite the formation of circular passages within the samples, the island strategy successfully achieved a high relative density due to the short scanning paths in tiny areas (islands) that assisted densification. At a laser power of 105 W, 87.8 % relative density was achieved using the island strategy. However, for the island strategy to be effective for D-PBSLP of alumina, the small passages should be overcome, and modifications should be considered. Additionally, the infiltration process can fill these channels and achieve a high densification level.

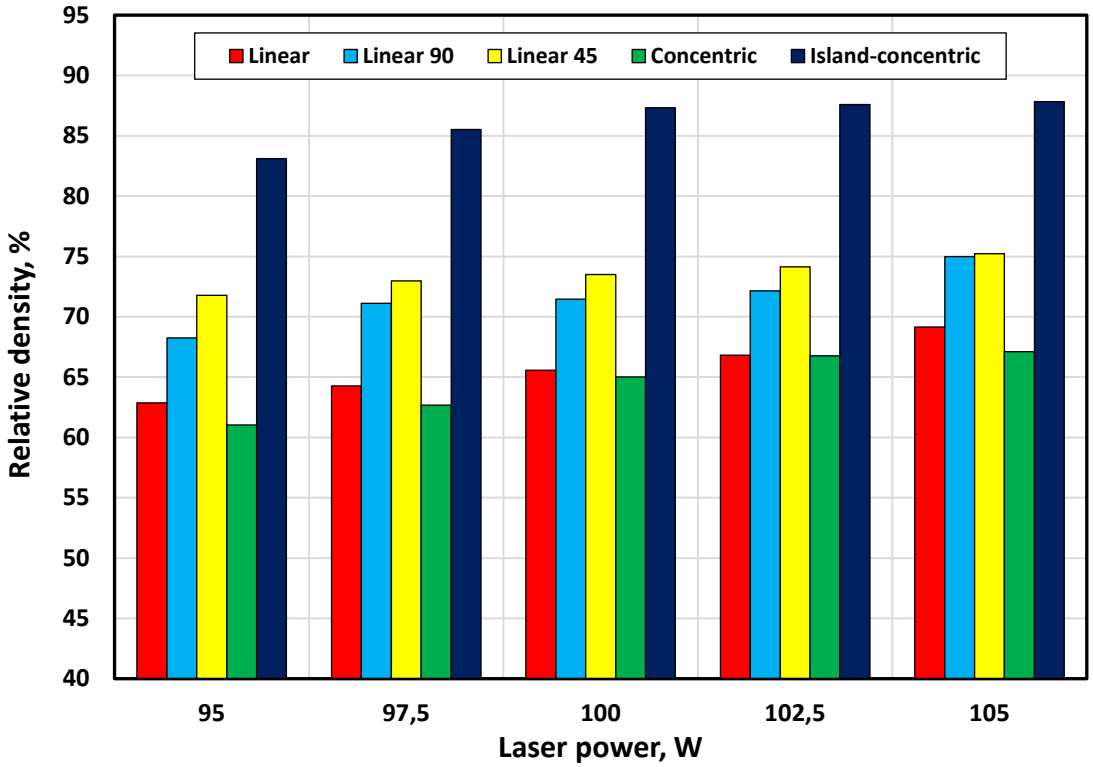

Figure 6.12. Relative density of alumina samples produced with different scanning strategies.

The investigation of scanning strategies revealed that the Linear 45° scanning strategy yielded the most promising results for the D-PBSLP of alumina in terms of printing samples with an acceptable relative density. Moreover, this strategy was capable of providing flat, patternless surfaces with low surface roughness. To accurately define the suitability of the Linear 45° scanning strategy for D-PBSLP of alumina, the internal structure and porosity distribution of an alumina sample printed using this strategy should be investigated. Micro-CT, as described in section 0, was employed for this purpose.

Figure 6.13 illustrates the 3D volume and 3D-voids distribution of the alumina sample printed using the Linear 45° scanning strategy and 102.5 W laser power. The voids percentage reaches 28.5% and is uniformly distributed throughout the sample volume, as shown in Figure 6.13. Additionally, as depicted in Figure 6.12, the voids distribution value corresponds to the 74.5 % relative density value measured using the Archimedes method.

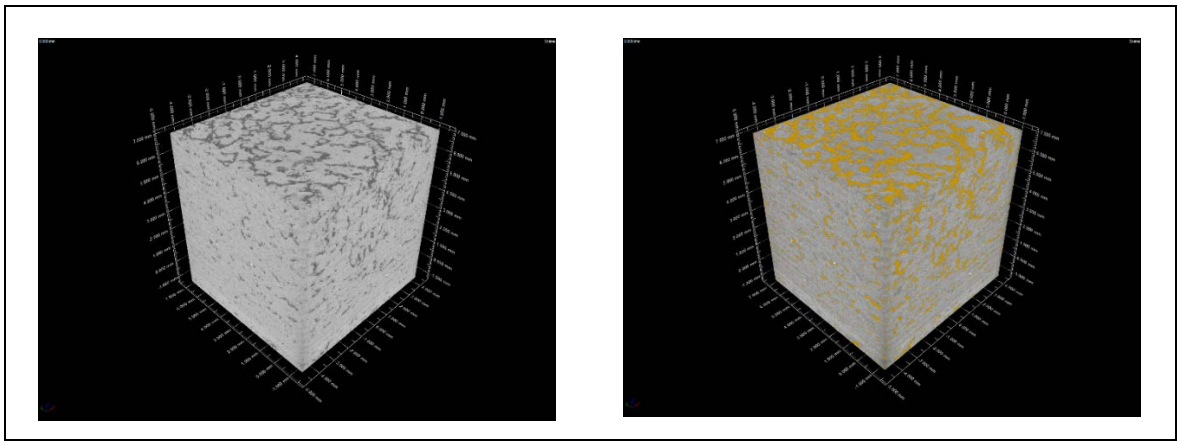

(a) (b)

Figure 6.13. Micro-CT for the Alumina sample printed using Linear 45° scanning strategy: 3D volume of the Alumina sample (a), the 3D volume of the Alumina sample with voids with yellow (b).

Figure 6.14 and Figure 6.15 depict the distribution of voids in various horizontal and vertical planes at the location indicated in the 3D volume representation for each plane. Voids are uniformly distributed throughout the sample's volume, with no discernible pattern. This demonstrates the effectiveness of The Linear 45° scanning strategy, as any increase in density will be uniformly distributed throughout the volume, resulting in the homogeneity of the sample's material. In PBSLP of ceramic materials, separating deposited layers is considered a significant issue, and it is crucial to ensure that the deposited layers adhere to one another. Figure 6.14 demonstrates that, for the PBSLP of alumina, there is no defect at the interface between layers, indicating a relatively strong bond.

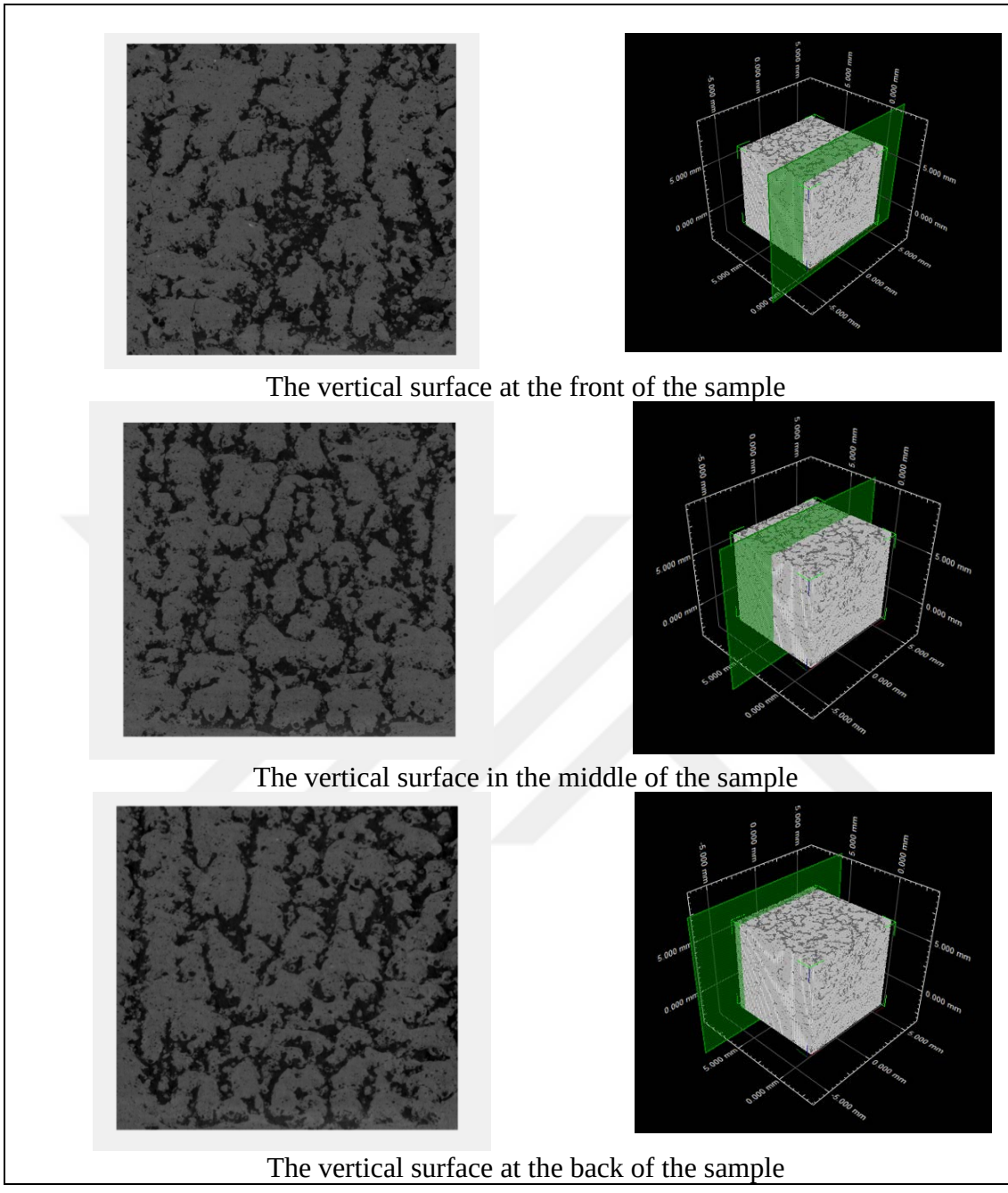

Figure 6.14. Porosity distribution at different vertical planes through the alumina sample (printed using the Linear 45° strategy), as indicated in the 3D volume representation.

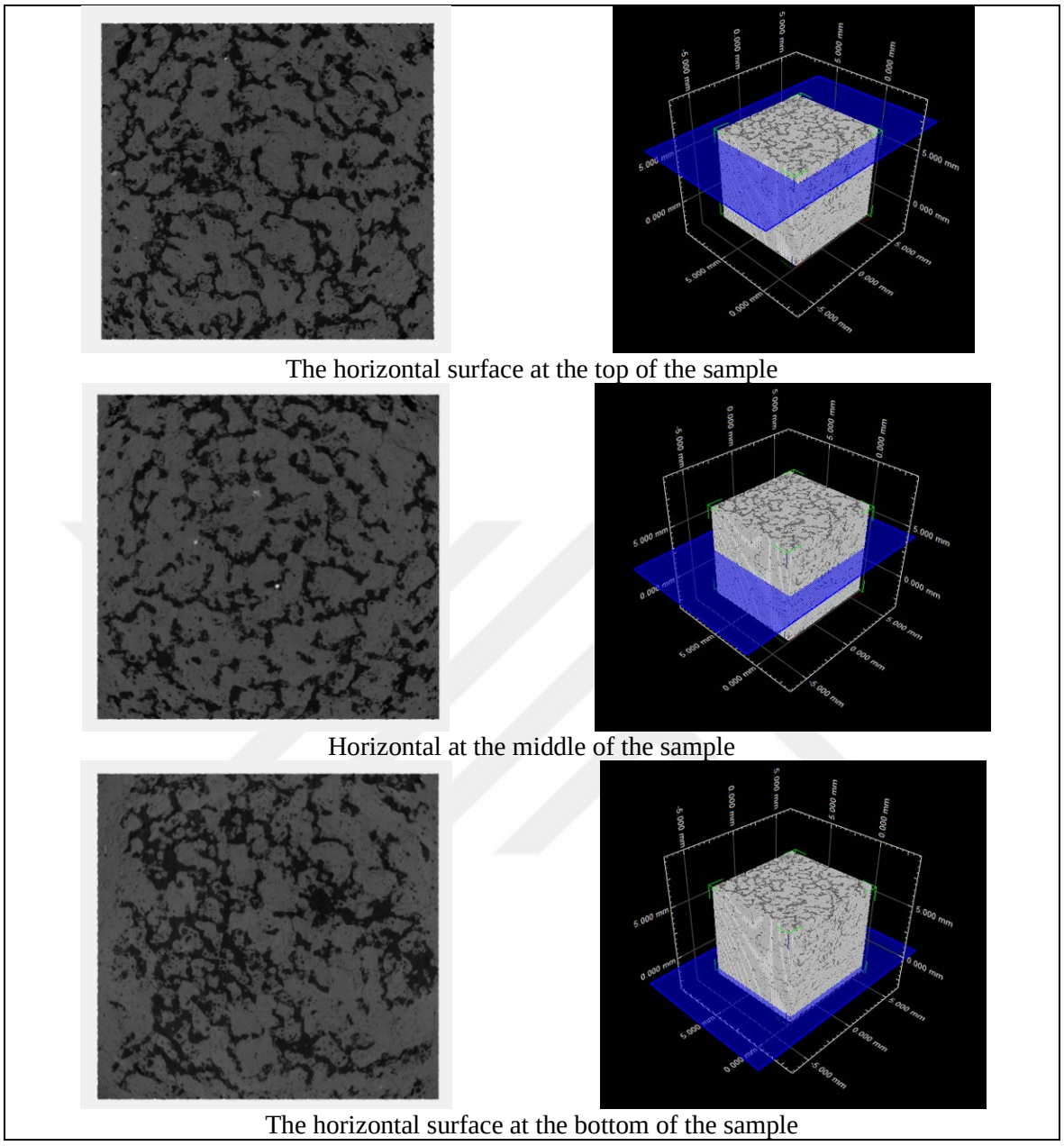

Figure 6.15. Voids distribution at different horizontal planes through the alumina sample (printed using the Linear 45° strategy), as indicated in the 3D volume representation.

In addition, the scanning strategy investigation for D-PBSLP of alumina revealed that the island-concentric strategy yielded the highest relative density compared to all other studied scanning strategies, despite the holes within the sample. Therefore, it is essential to examine the distribution of the voids within the sample and understand the nature of the formed holes within the sample. Figure 6.16 shows the 3D volume of the alumina sample printed using the island-concentric scanning strategy and 102.5 W laser power. It can be found that the voids were uniformly distributed through the sample volume, in the form of holes which

were formed along the sample height, as revealed previously in Figure 6.11. The micro-CT yielded a voids volume percentage of approximately 9 %, almost identical to the relative density obtained for this sample, 87.6 % (as described in Figure 6.12).

Figure 6.17 depicts the distribution of the voids through different vertical planes in different positions, as indicated by the corresponding 3D Volume representation. As seen in Figure 6.17 (at the vertical surface in the middle of the sample), the sample is nearly devoid of porosity (solid material), which explains the high relative density obtained with this scanning technique (island-concentric strategy). In addition, at the location where the section was taken at the center of the formed holes (Vertical surface at the back of the sample in Figure 6.17), it can be observed that the voids volume is exceptionally high as a result of the hole within the sample that began at the sample's base and extended to its top surface.

Figure 6.18 depicts the distribution of the voids in various horizontal planes at various heights above the sample base. The formed holes are barely discernible at the section near the base of the sample. When the section was taken from the middle of the sample, the shape of the formed holes became evident. Finally, the holes are visible in the top horizontal section of the sample. The gradual change in hole shape (from undefined shape to a clear circular section) with increasing sample height, as described in Figure 6.18, can be attributed to the increase in printed sample temperature caused by heat accumulation (as described in chapter 5); as a result, the temperature of the upper layers was high and more material was removed and evaporated from the sample at the center of the formed holes.

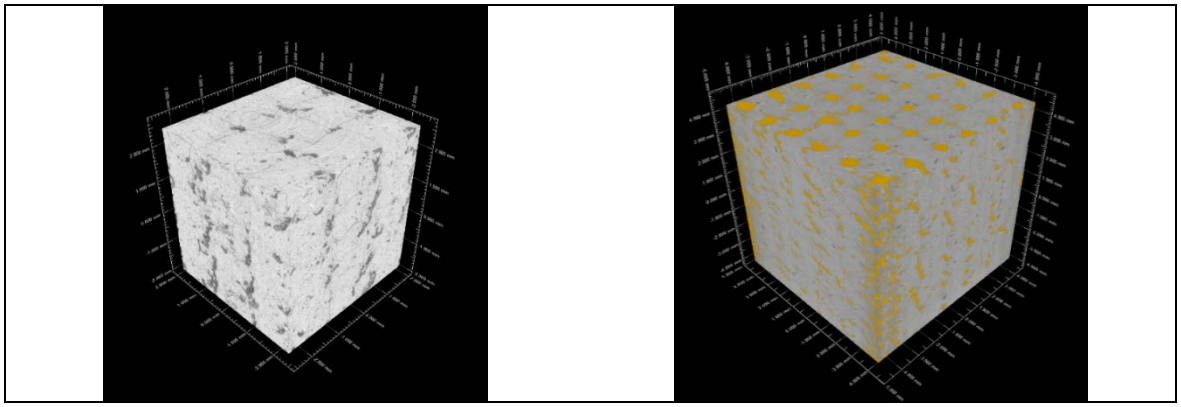

(a) (b)

Figure 6.16. Micro-CT for the alumina sample printed using Island-concentric scanning strategy: 3D volume of the alumina sample (a), the 3D volume of the Alumina sample and the voids with yellow (b).

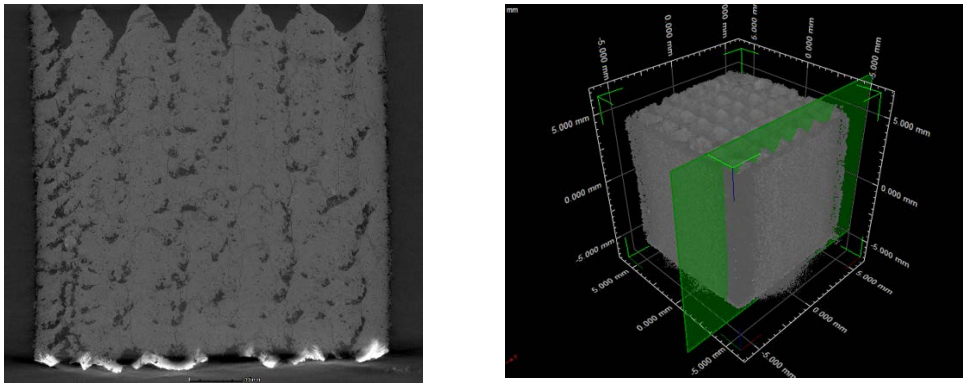

The vertical surface at the front of the sample

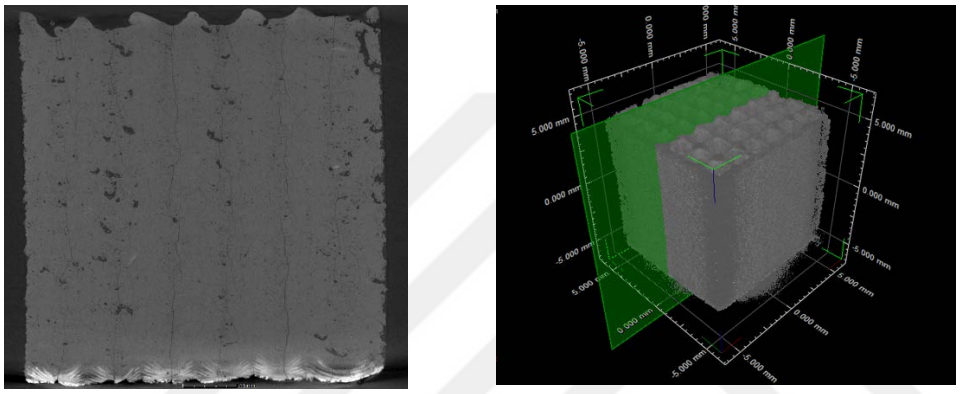

The vertical surface at the middle of the sample

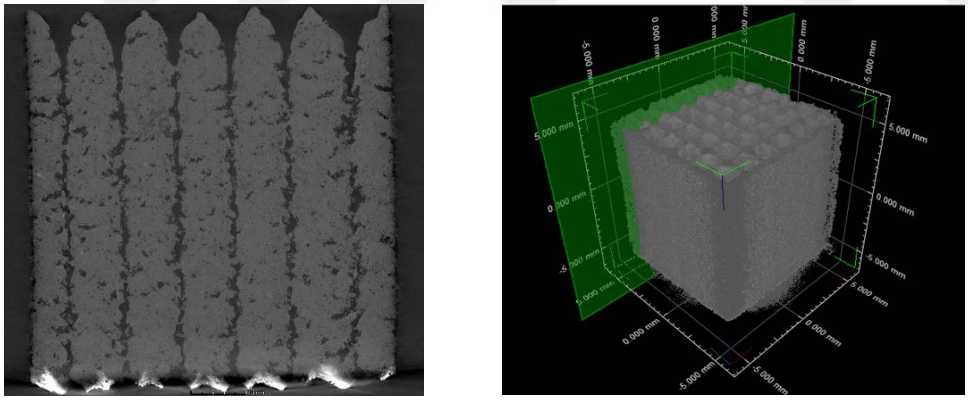

The vertical surface at the back of the sample

Figure 6.17. Porosity distribution at different horizontal planes through the alumina sample (printed using the Island-concentric strategy), as indicated in the 3D volume representation.

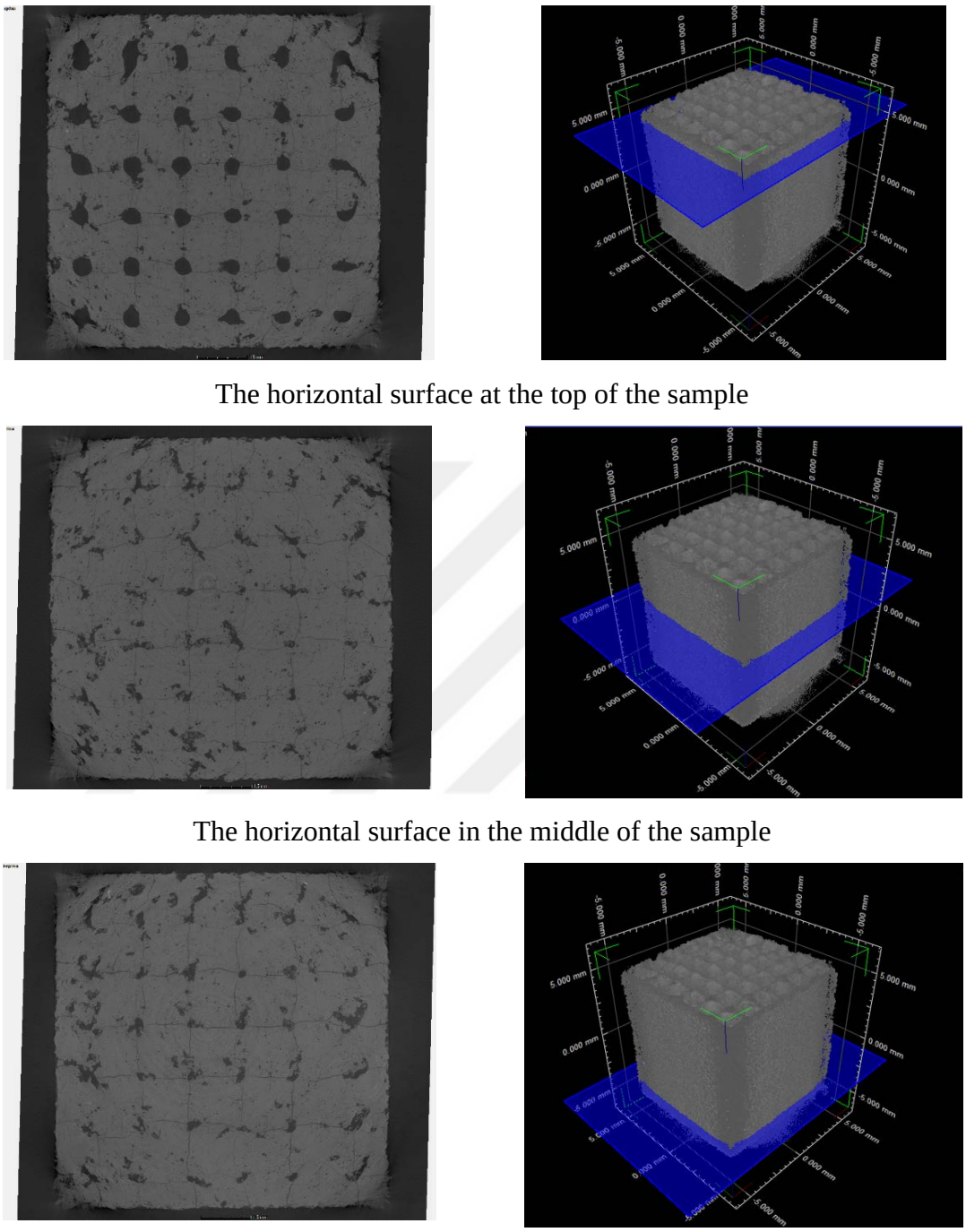

Figure 6.18. Porosity distribution at different horizontal planes through the alumina sample (printed using the Island-concentric strategy), as indicated in the 3D volume representation.

Figure 6.19 depicts SEM images of alumina samples printed with various scanning strategies. For linear strategies, as depicted in Figure 6.19, it can be observed that the samples

experienced a high level of porosity, which explains the low relative density obtained with this scanning strategy. Additionally, numerous cracks formed on the layer's top surface, originating in porous regions. Thermal shocks primarily caused these cracks during scanning. The tiny holes formed in the small island's centre are visible for the island strategy.

Additionally, numerous cracks have formed along the surface of these tiny holes. The concentric strategy's SEM images clearly show the two lines forming the top surface's “X” mark. Focusing on one of these two lines reveals a brittleness, which may separate the sample into four identical shapes, as seen in Figure 6.20.

For side surfaces, all scanning strategies revealed a periodically repeated defect along the building direction, which may be attributable to a lack of adhesion between layers in specific locations along the border (The layer were well-adhered when checked internally by the Micro-CT. However, there is an apparent periodic defect along the sample border). This periodic damage was thoroughly examined and discussed in the following sections.

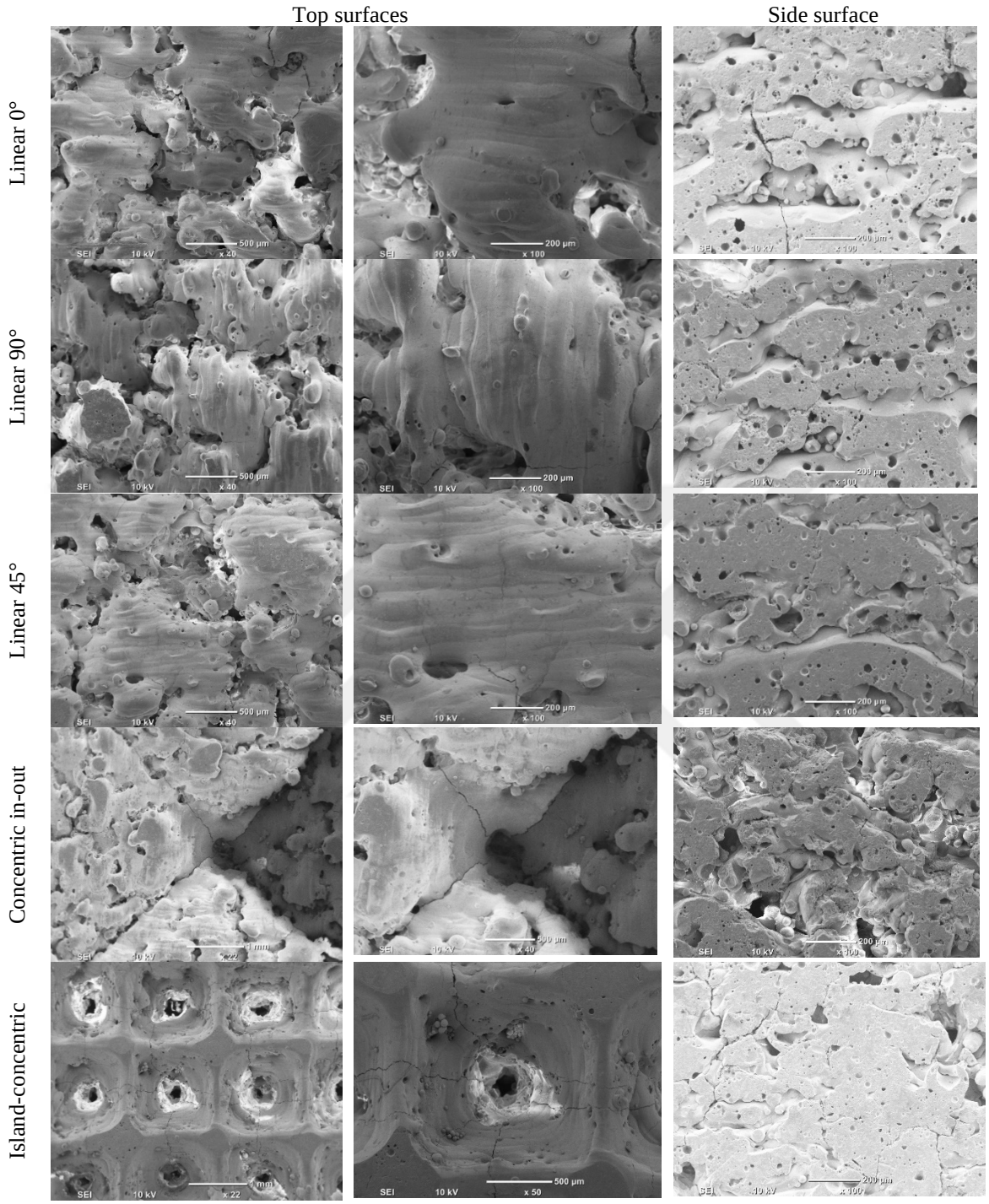

Figure 6.19. SEM images for different scanning strategies at the sample top surface and side surface.

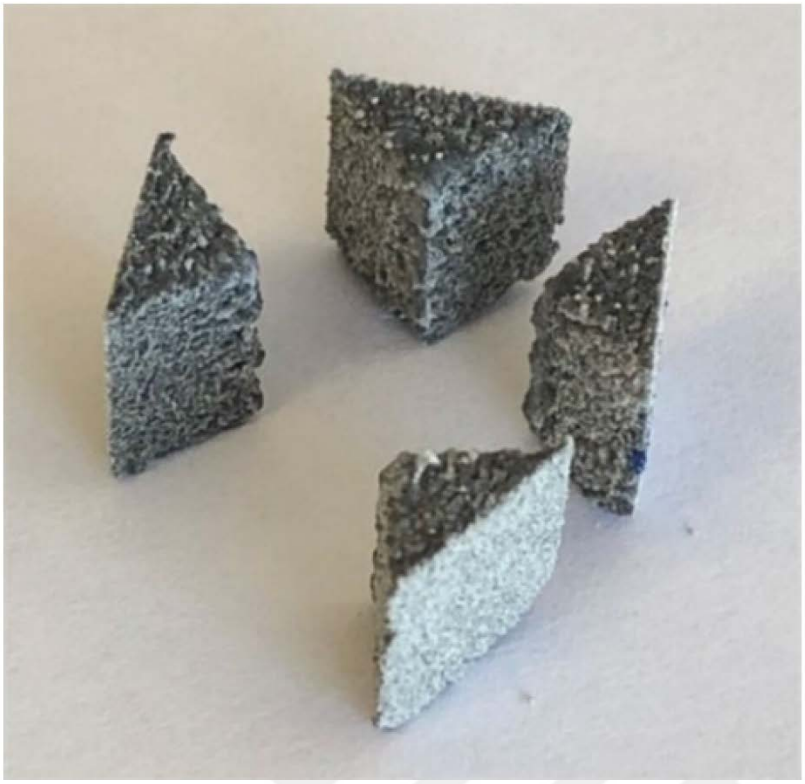

Figure 6.20. Alumina sample was printed using a concentric in-out strategy and separated into four identical parts due to the “X” mark on the sample top surface.

From the investigation of the effect of scanning strategies on the PBSLP of alumina, it can be concluded that Linear-45° is a promising scanning strategy for D-PBSLP of alumina, as it was able to print alumina samples with a flat top surface devoid of distinctive patterns and with an acceptable relative density. Therefore, further investigation into the D-PBSLP of alumina used Linear-45° as the scanning strategy.

6.2.4. Next generation scanning strategy

The island strategy generally employs short scanning paths in a small area (island) to concentrate heat and increase relative density. Based on the investigation of previously described scanning strategies, the island strategy showed auspicious results in terms of the obtained relative density, as it obtained nearly 90% relative density while the other scanning strategies obtained approximately 75% under the same conditions. However, the tiny holes within the sample pose the most difficulty.

Therefore, a new generation of scanning strategies using small scanning paths distributed across the powder layer can be developed to avoid the occurrence of small holes created by

the island strategy. The developed scanning strategy utilizes space-filling mathematical curves to control the movement of the laser beam on the powder bed. The space-filling curve is formed from the 2-D unit square, as shown in Figure 6.21(a), and the scanning strategy is formed by repeating this 2-D rectangular unit, as depicted in Figure 6.21(b) and (c) (c). Due to the difficulty of modifying the built-in scanning strategies of commercial SLM printers, the study has recommended this new strategy for future work. The melting contour for the newly proposed scanning strategy is depicted in Figure 6.21(d). To avoid the concentration of heat in a small area, as is the case with the island strategy, the laser scans over a broad area along a short path. In addition, the length of the long and short rectangular sides could be adjusted to cover some unscanned areas.

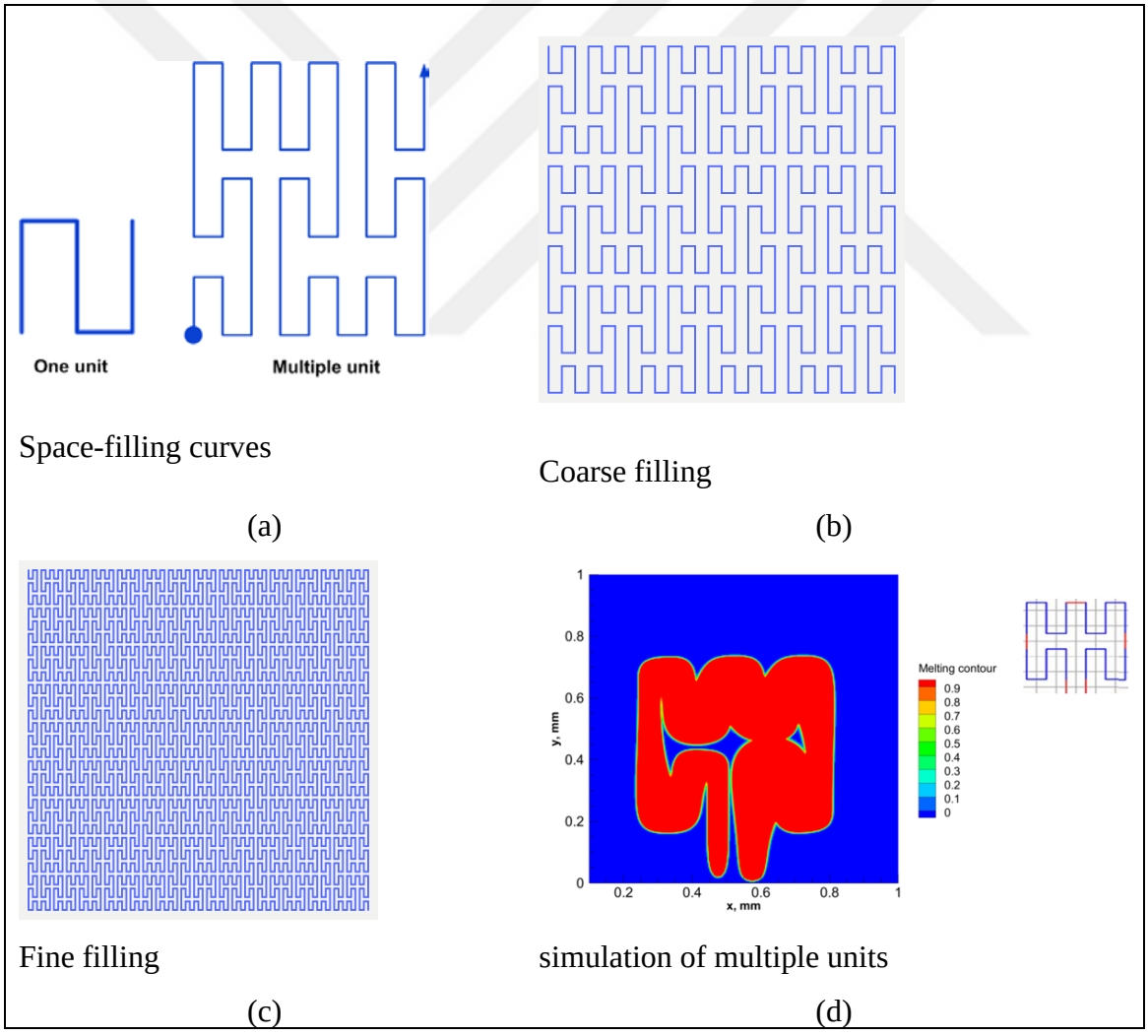

Figure 6.21. Space-filling curves: one and multiple units (a); coarse filling of the new proposed scanning strategy (b); fine filling of the new proposed scanning strategy (c); melting contour of space filling considering one unit (d).

6.3. The Influence of Scanning Speeds on the D-PBSLP of Alumina

After evaluating the influence of various process parameters and determining the appropriate values for each parameter using the developed numerical model, it became necessary to conduct an experimental investigation for the D-PBSLP of alumina to evaluate each parameter's efficiency value, especially the scanning speeds. The scanning speed and associated laser power are essential for the successful D-PBSLP of alumina; consequently, their effects should be investigated experimentally to determine the optimal scanning speed for D-PBSLP of alumina. Various scanning speeds, including 100, 200, 300, and 400 mm/s, as specified in section 5.2, were investigated, and alumina samples were printed using the obtained results from the numerical model with the Linear 45° scanning strategy, as specified in section 5.2.3.

Figure 6.22 demonstrates that alumina cubes (10 ×10 ×10 mm3) were successfully printed using different scanning speeds and laser powers, as determined by the numerical model. This demonstrates the ability of the numerical model to predict the appropriate process parameters. Two samples were printed at each laser power level to evaluate the printability and repeatability. The samples have a clearly defined cube shape with no discernible printing defects.

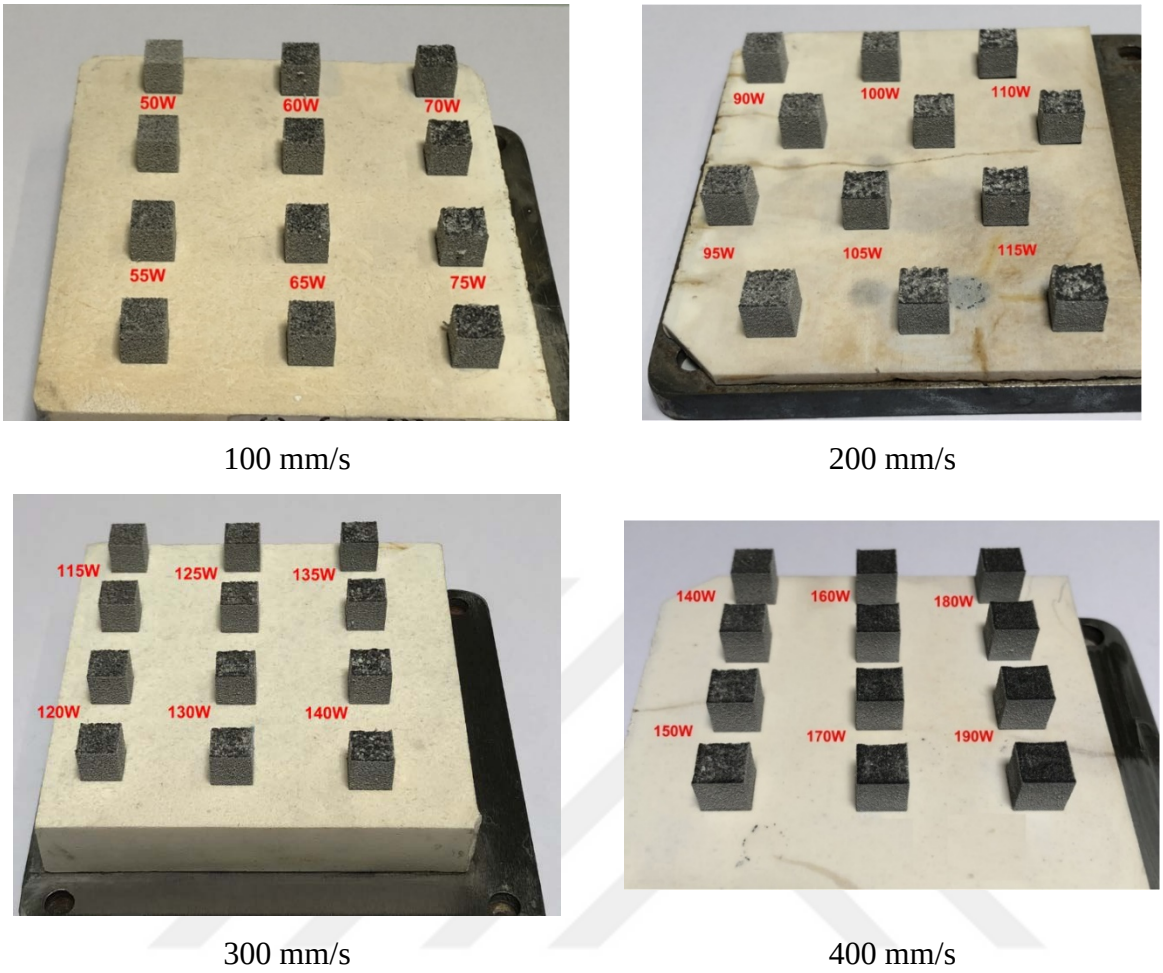

100 mm/s 200 mm/s

300 mm/s 400 mm/s

Figure 6.22. Alumina samples printed using different scanning speeds.

The relative density measurement was considered to evaluate the quality of the printed samples at different scanning speeds and laser powers. The Archimedes method was used to predict the density of the samples, and two readings were taken for each sample, with the average being considered and the results are shown in Figure 6.23. For all scanning speeds, it can be observed that the relative density increased as the laser power increased; this was primarily due to the increase in laser energy density ($\mathrm{LED} = \mathrm{P}/(\mathrm{v} \times \mathrm{L} \times \mathrm{h})$, where P is the laser power, v is the scanning speed, L is the layer thickness, and h is the hatching space), which led to higher densification.

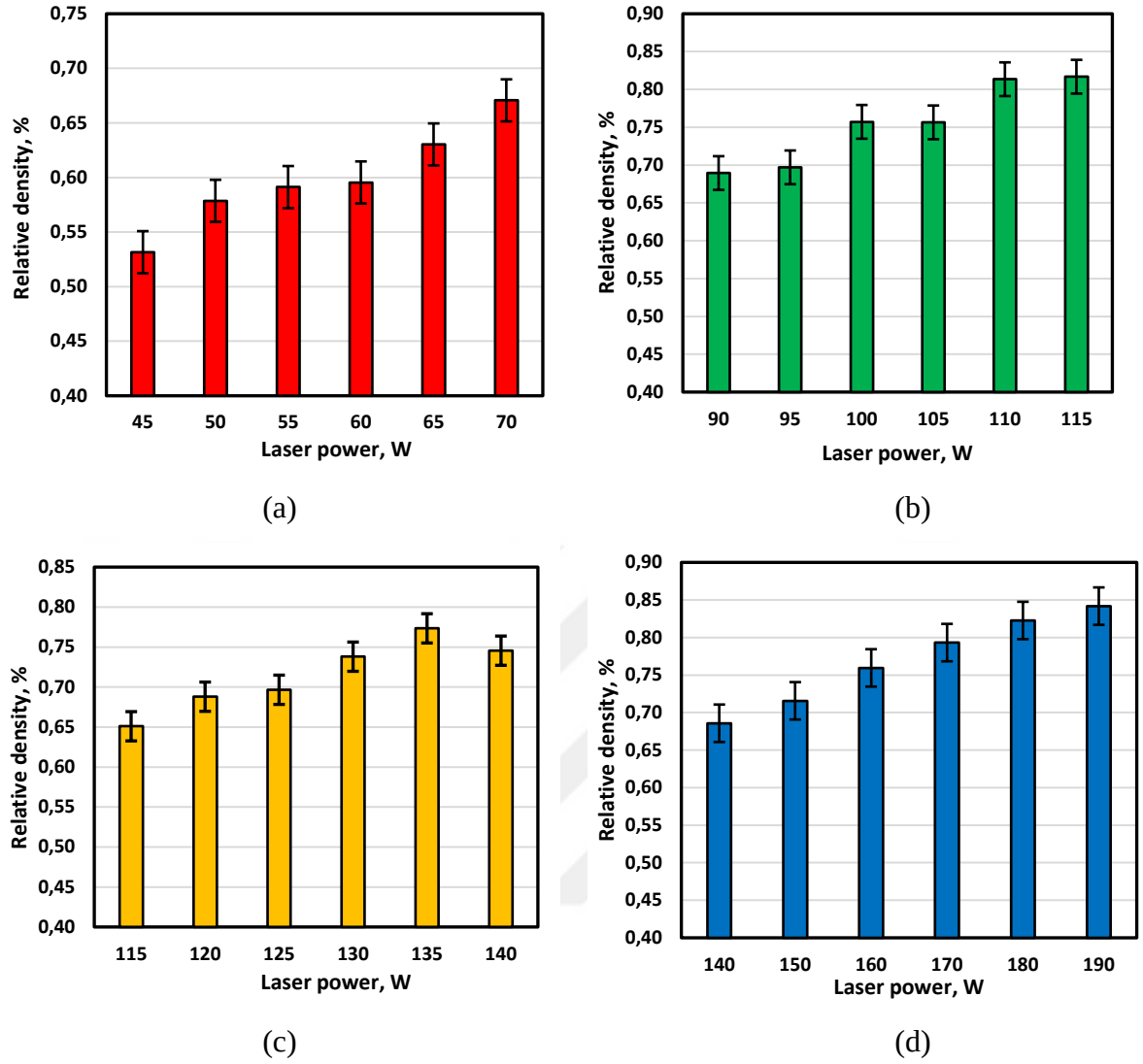

Figure 6.23. Relative density of alumina samples at different scanning speeds; 100 mm/s (a), 200 mm/s (b), 300 mm/s (c), 400 mm/s (d).

The maximum relative density obtained at scanning speeds of 100, 200, 300, and 400 mm/s is 69.5 %, 81.6%, 77.3 %, and 84.2%, respectively. It can be observed that increasing the scanning speed led to an increase in the relative density of the printed samples, even though the applied laser energy density did not change significantly.

To gain a clear understanding of the effect of the scanning speeds on the relative density, various alumina samples (Figure 6.25) were printed at scanning speeds of 100, 200, 300, and 400 mm/s, and the laser powers were adjusted to maintain a constant laser energy density at each scanning speed; laser energy densities of 90 and 100 J/mm3 were considered.

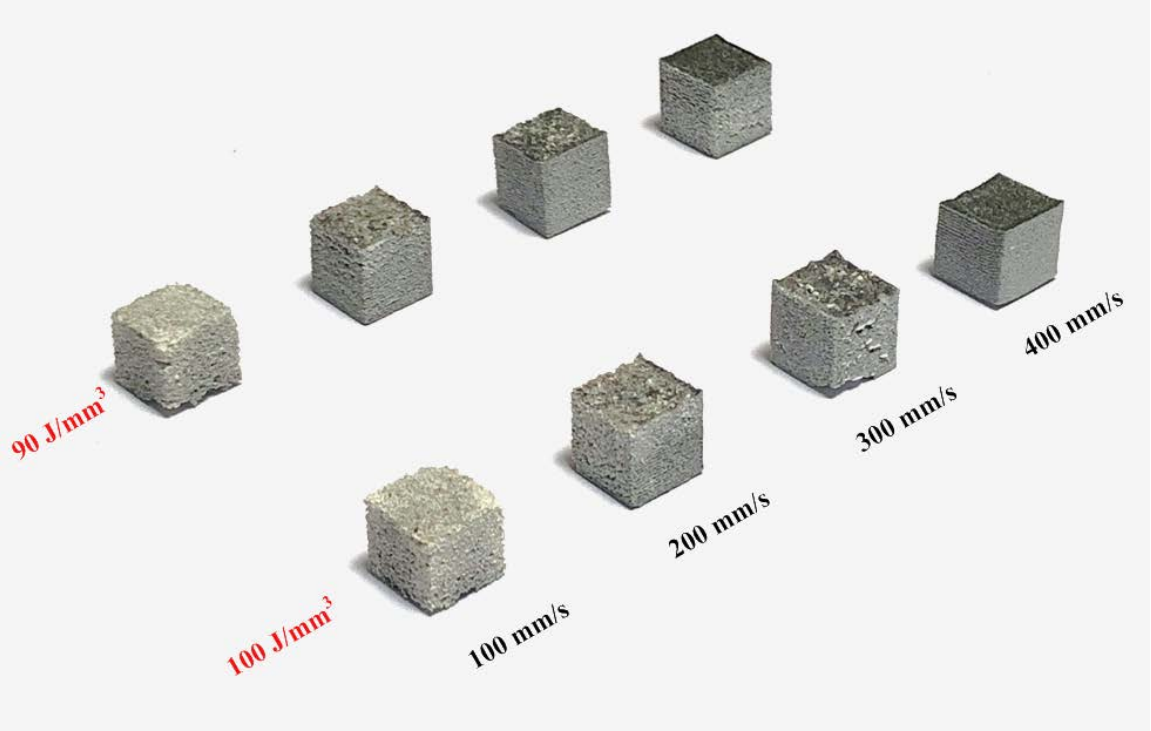

Figure 6.24. Alumina samples printed at different scanning speeds with fixed laser energy densities of 90 and 100 J/mm3.

When the laser energy density was held constant at each scanning speed, the relative density increased as the scanning speed increased, and the highest relative density was achieved at a scanning speed of 400 mm/s, as seen in Figure 6.25. Juste et al. [189] also observed this behaviour when studying the selective laser melting of spray-dried alumina. However, many previous studies on metallic materials reported that the relative density increased as the scanning speed decreased [190, 191], which is entirely at odds with this study and the study of Juste et al.[189] observed. In order to determine why the relative density of alumina increased as the scanning speed increased, it is necessary to observe the powder bed closely as the laser scans the powder to investigate this finding further.

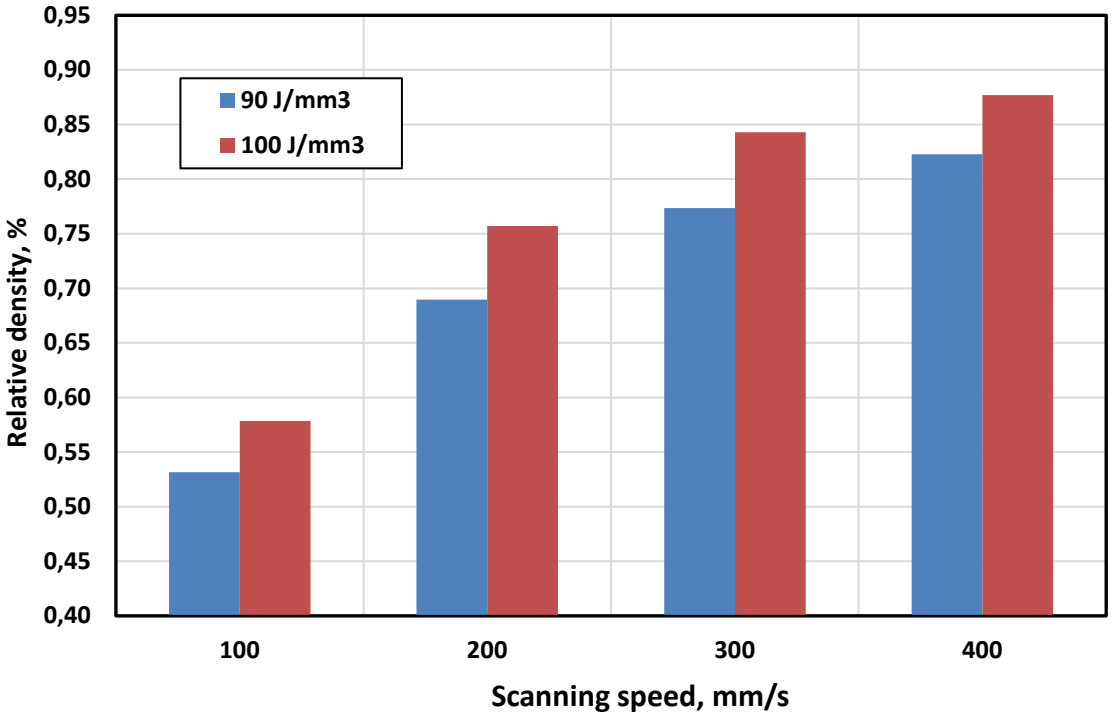

Figure 6.25. Relative density of Alumina samples at different scanning speeds and laser energy densities.

Figure 6.26 shows the powder bed after scanning the first layer (the printer was paused and opened to see the powder bed closely). It was found that high scanning speed (400 mm/s) dragged spray-dried alumina particles surrounding the scanning area toward the laser spot achieving a high level of densification, which is the leading cause of the high relative density obtained at high scanning speed. No dragging was observed for low scanning speed (100 mm/s); therefore, low relative density was obtained at low scanning speed. This finding agreed well with the study of Bidare et al.[192] when they used a high-speed camera to investigate the behaviour of powder particles during scanning with different scanning speeds, they found that at high scanning speed, powder particles were pulled to the laser spot due to the aerodynamic drag achieving high densification. Therefore, it can be concluded that increasing or decreasing the relative density with scanning speed is not a general case or rule and varies according to the material used.

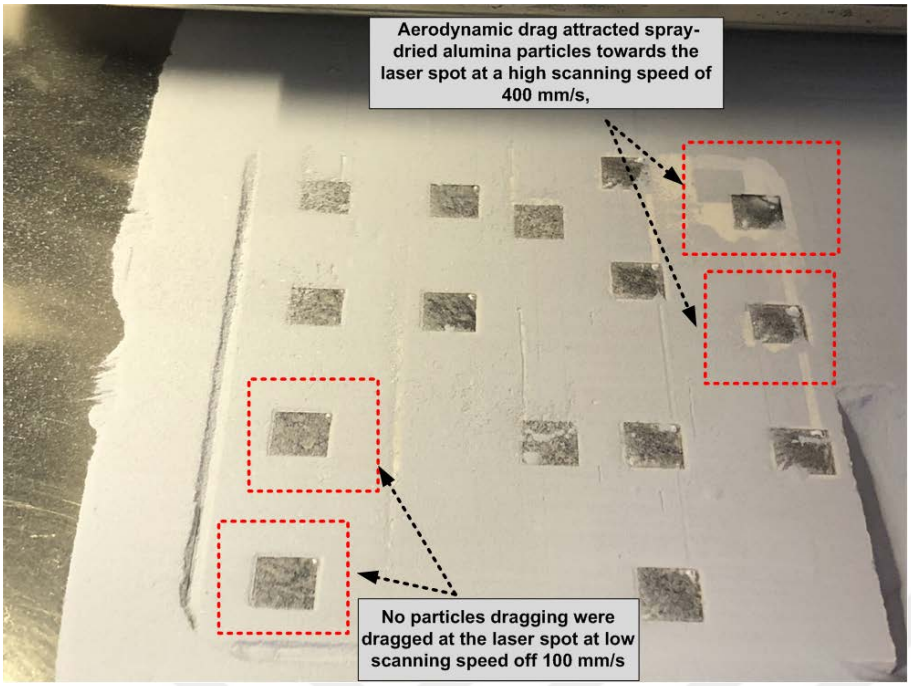

Figure 6.26. Spray-dried alumina powder bed behaviour at different scanning speeds.

Figure 6.27 depicts the alumina samples printed with a laser energy density of 90 J/mm3 at different scanning speeds. In addition, a detailed view of the sample's top surface 3D height is also captured with a 3D laser scanning microscope (VKX-250, Keyence, Japan). Due to the 100 µm layer thickness, the sample's build direction resolution is shallow. The top surface is not flat for scanning speeds of 100, 200, and 300 mm/s; the phenomenon of balling described by Qiu et al. [73] is evident. As described in section 0, the balling phenomenon is caused by molten ceramic materials' high viscosity and surface tension. However, the 400 mm/s/ scanning speed did not highly show this phenomenon because, as described previously, high scanning speeds pull alumina powder particles surrounding the scanning area to the laser spot due to aerodynamic drag. As a result, the alumina sample printed at 400 mm/s had more molten alumina material than samples printed at slower speeds. The large quantity of molten material permeated the surface and highly reduced the balling phenomenon.

Consequently, the surface of the alumina sample printed with a scanning speed of 400 was nearly flat and devoid of defects that appeared with other scanning speeds. Figure 6.27 reveals an additional significant observation: as the scanning speed increases, the sample colour changes. The sample printed at 100 mm/s has an off-white colour, whereas the sample of alumina printed at 200 mm/s is slightly darker. The darkness of the sample increased as

the scanning speed increased to 300 mm/s, and the sample became completely dark at 400 mm/s. As shown in Figure 6.28, a 3D laser scanning microscope (VKX-250, Keyence, Japan) was used to obtain a fine and accurate view of the top surfaces of alumina samples printed using various scanning strategies at a fixed laser energy density of 90 and 100 J/mm3. It is evident that as the scanning speed increased, the darkness of the samples increased despite the laser energy density remaining unchanged.

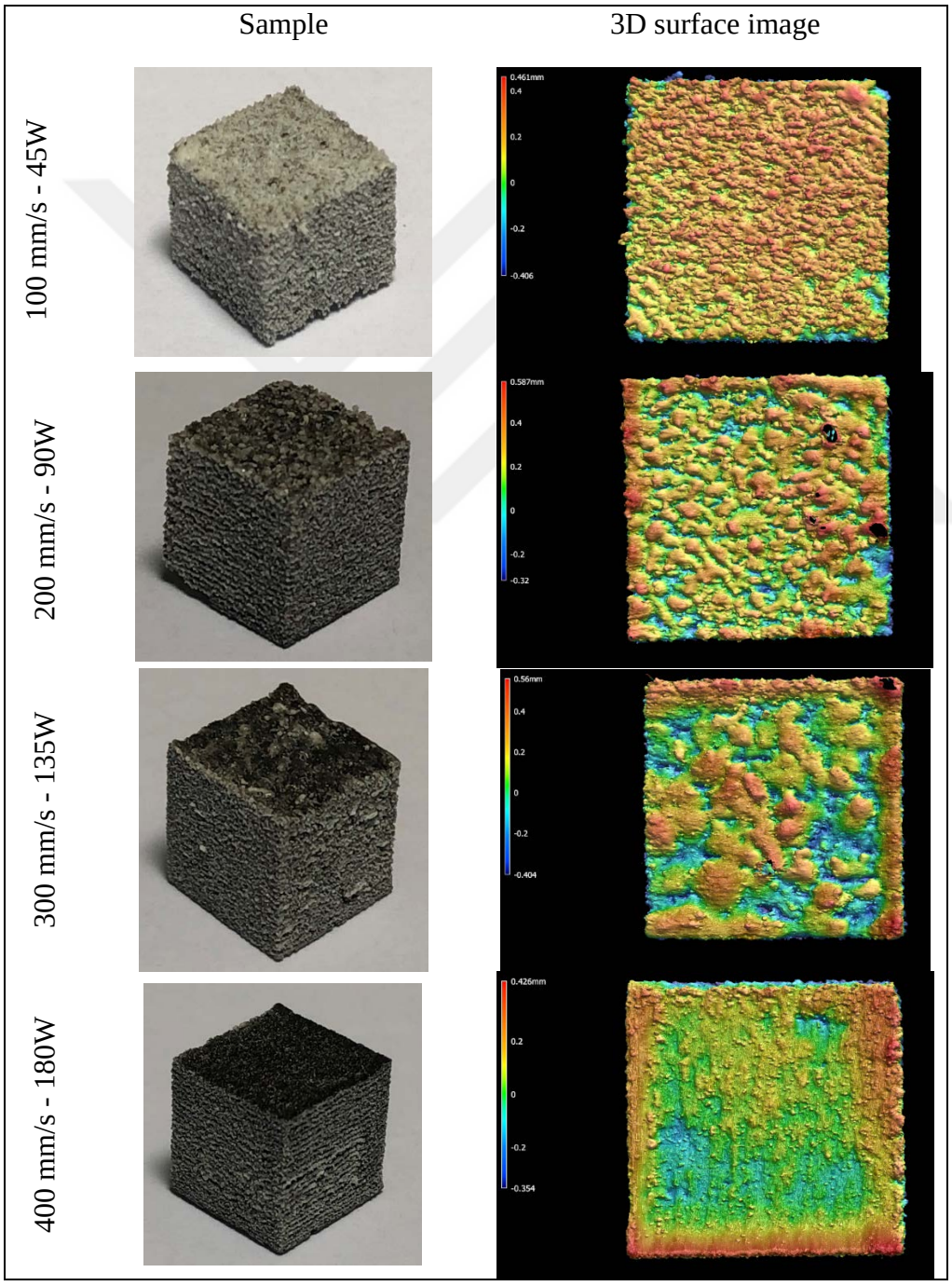

Figure 6.27. Alumina samples and the corresponding 3D surface height at different scanning speeds with a fixed laser energy density of 90 J/mm^3.

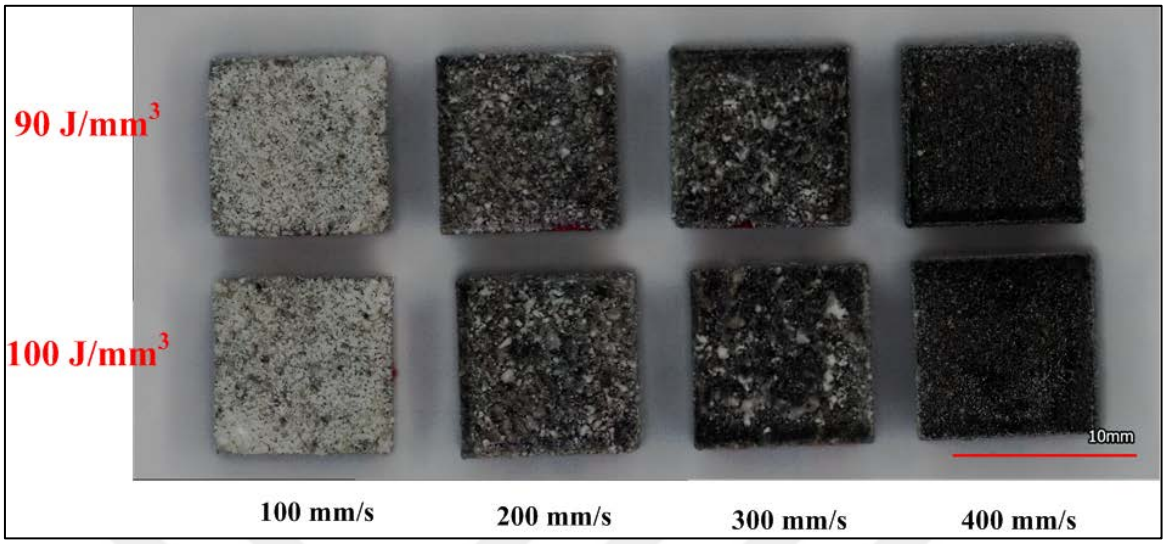

Figure 6.28. Optical microscopic top surface of alumina samples printed at different scanning speeds at a fixed laser energy density of 90 and 100 J/mm^3.

Typically, the laser energy density is utilized in PBSLP as a comparison and design parameter because it combines the laser power, scanning speed, layer thickness, and hatching space into a single parameter that is easily correlated to the PBSLP process output (relative density, porosity, surface roughness, and defects) [193]. Numerous previous metallic PBSLP studies have demonstrated a significant relationship between laser energy density and PBSLP processes output, such as density, porosity, surface roughness, defect formation, and sample colour [194, 195]. Bertoli et al. [196] reported that due to the complex physics of the melt pool in PBSLP technique, including Marangoni flow, hydrodynamic effect, and recoil pressure, the applicability of laser energy density as a design parameter for describing the PBSLP process accurately is limited. This is what was typically observed in this study with alumina PBSLP, where laser energy density could not effectively describe the output of the process and a new parameter should be developed to overcome this shortcoming. However, based on the previous result, the alumina samples relative density, surface texture, and sample color changed while the laser energy density remained unchanged.

Figure 6.29 depicts SEM images of alumina samples scanned at various speeds while maintaining a constant laser energy density of 90 J/mm3. As the melted particles were fragile and did not connect strongly to one another, it was not easy to polish the surfaces of samples printed at 100 and 200 mm/s scanning speed for SEM imaging. Only samples printed at

speeds between 300 and 400 mm/s were polished. In the case of 100, 200, and 300 mm/s scanning speeds, it is evident from the SEM images that the balling of particles is highly visible. Additionally, high porosity and cracks are prevalent. For scanning speeds of 400 mm/s, the microstructure is superior to other scanning speeds, and the samples do not exhibit balling. In addition, the cracks are visible, as is the case with the other scanning speeds. The thermal shock during the PBSLP process resulted in the development of these cracks, which can be controlled using the preheating systems described in Chapter 5.

Figure 6.30 displays SEM images for the side surface of the alumina sample printed at a scanning speed of 400 mm/s. There is no discernible separation between the layers, as they have firmly adhered together. However, there is cyclical damage along the building direction of the layers. This cyclic damage resembles a brick wall with approximately 500 µm. This cyclic damage occurred after every five layers were printed. The movement mechanism of the building's baseplate is likely responsible for this cyclical damage (the system responsible for lower the baseplate after printing each layer to allow the deposition of a new layer).

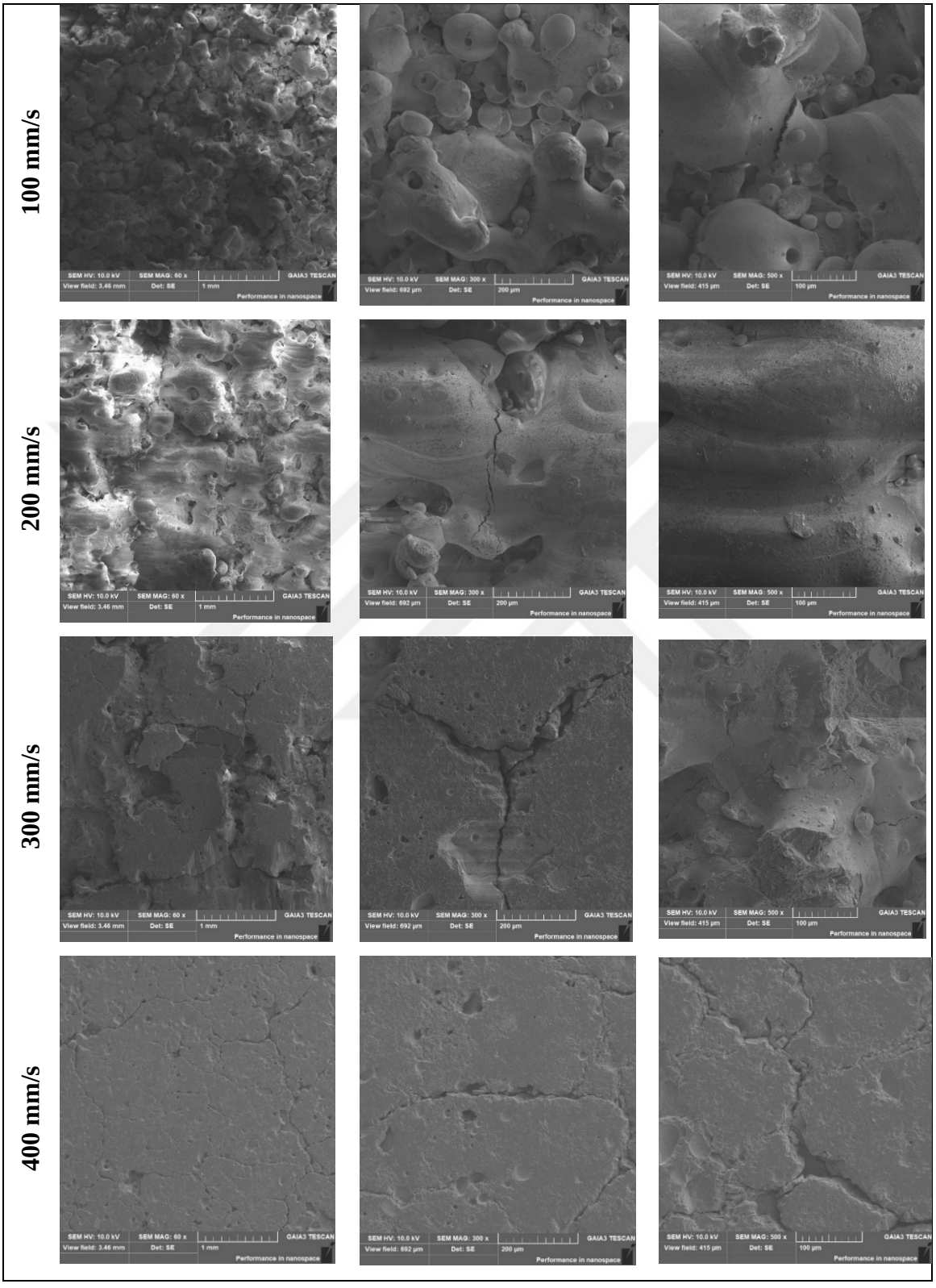

Figure 6.29. SEM images for the top surface of alumina samples printed at different scanning speeds at a fixed laser energy density of 90 J/mm3.

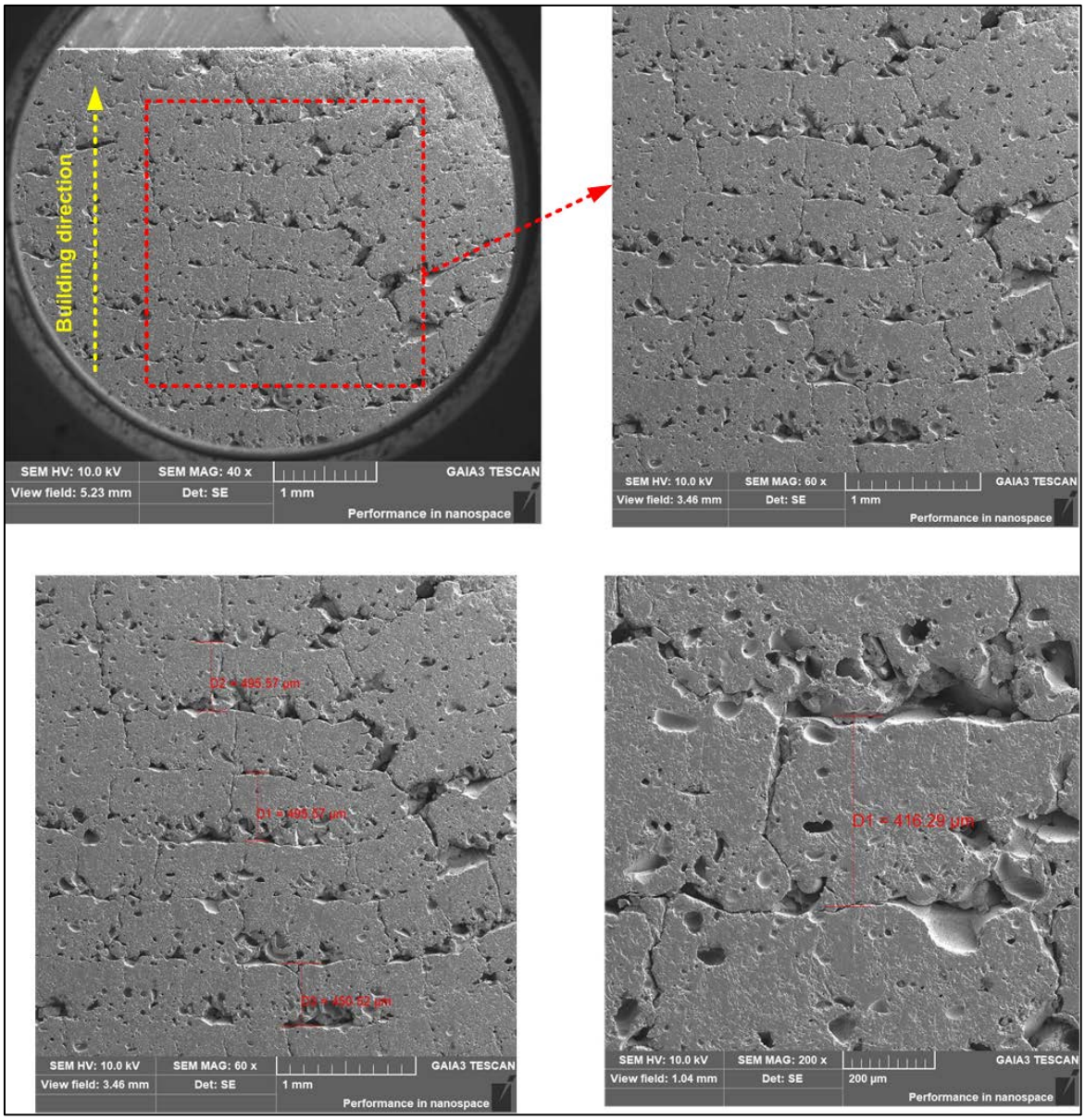

Figure 6.30. SEM images for the side surface of alumina sample (along the build direction) printed with 400 mm/s scanning speed at a fixed laser energy density of 90 J/mm^3.

To investigate the influence of the graphite addition on the spray-dried process, XRD analysis was utilized to identify the phases inside the alumina-printed sample, and Rietveld analysis was used to quantify these phases. Figure 5.31 depicts the XRD spectra for alumina raw powder, alumina spray-dried powder, and an alumina sample printed using the D-PBSLP (400 mm/s, 180W, and 50 µm). Neither the spray-drying approach nor the D-PBSLP methodology changes the XRD spectra due to the production of additional phases. Rietveld analysis was performed to determine the amount of each phase inside each case by refining the XRD spectra for each case, as detailed in section 3.3.6. Table 6.8 summarizes the results

of the Rietveld analysis, which utilized alpha-alumina and graphite phases for the refining. In all situations (alumina raw powder, spray-dried alumina powder, and alumina printed sample), only the alumina phase was present, and this explains why the XRD spectra in Figure 6.31 remained unchanged. Therefore, the dark colour of the D-PBSLP-printed alumina sample is primarily attributable to the chamber's high oxygen content, scanning speed (400 mm/s), and laser power (180 W).

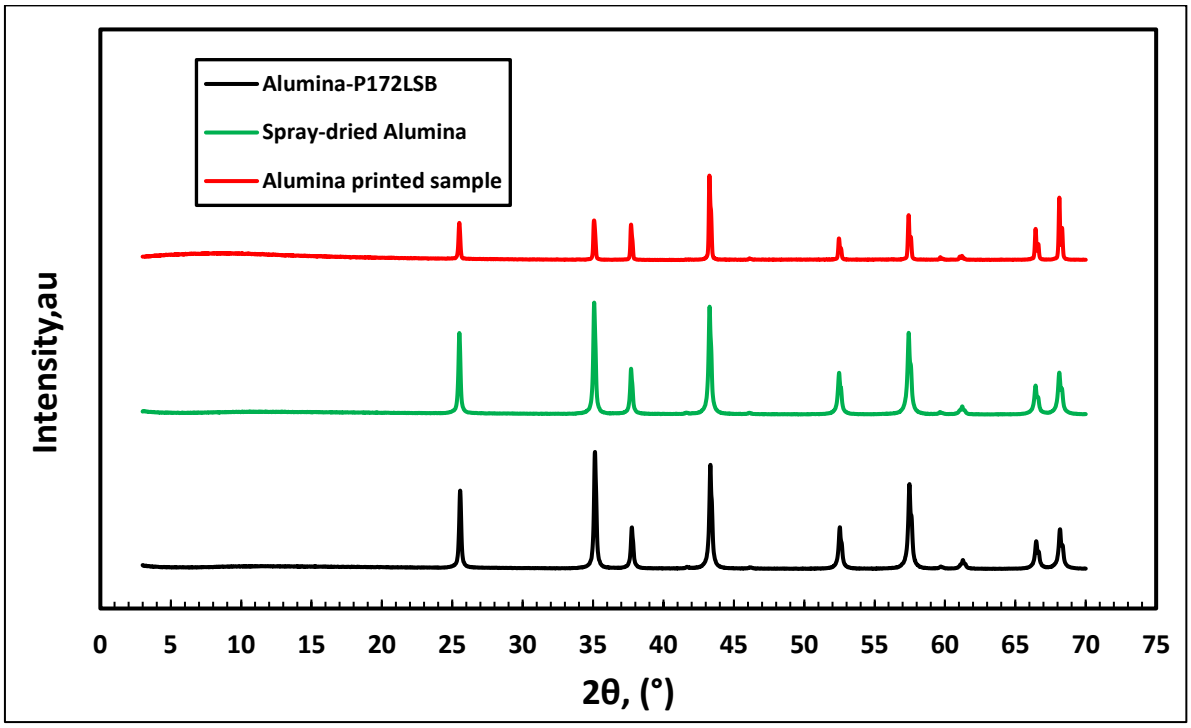

Figure 6.31. XRD spectra for alumina raw powder, alumina spray dried powder, and alumina sample printed using D-PBSLP.

Table 6.8. Alumina quantitative phase analysis.

Item	Alpha- Al_2O_3	Carbon	Rwp (%)	Rexp (%)
Alumina-P172LSB	100% ± 0.0	0.0 ± 0.0	10.99	4.62
Spray-dried Alumina	100%±5.68e-8	0.0 ± 0.0	26.33	4.59
Alumina printed sample	100 ±8.14e-8	0.0 ± 0.0	30.37	6.04

From the scanning speed investigation, it can be concluded that the 400 mm/s scanning speed was able to overcome all of the difficulties encountered with the other investigated scanning speeds and that employing the 400 mm/s scanning speed for the D-PBSLP of alumina can result in a higher building rate. Therefore, the scanning speed of 400 mm/s was considered for the next alumina D-PBSLP investigation.

6.4. Process Parameters Optimization

After thoroughly understanding the effect of the process parameters, such as laser power, scanning speed, scanning strategies, and hatching distance, it is essential to optimize these process parameters to obtain the optimal values for achieving the desired properties, such as high relative density. Using a scanning speed of 400 mm/s, a Linear 45° scanning strategy, laser power calculated from the numerical model, and hatching space of 50 µm or less are promising process parameter values for obtaining good-quality alumina samples using the D-PBSLP technique.

As described previously in Section 2.6, the Taguchi optimization technique can provide an effective and efficient procedure for determining the optimal parameters for D-PBSLP of alumina to attain the highest relative density and good surface quality.

The Taguchi optimization technique consists of three distinct stages. The first stage is the design phase, which entails executing the system within which the experiments will be conducted, identifying all the factors (process parameters) that influence the process, determining the range of each factor (levels) included in the experiments, and identifying the response factors.

The second stage is the excitation stage, which consists of two steps. In the first step, the orthogonal array (OA) was constructed based on the factors and level of each factor. The design of the OA should incorporate all feasible treatments that address all factors and levels under consideration. The second step involves conducting experiments in accordance with the OA and determining the response factors for each treatment. The second stage is the most crucial and should be executed with care. All possible factors should be considered during the design phase, as this greatly aids in the early identification of ineffective factors.

The final stage is the analysis and optimization phase, which consists of response factor analysis (data analysis), determining the optimal factors value, and conducting a confirmation test using the optimal factors value.

6.4.1. Taguchi optimization-first stage

For the alumina PBSLP treatments, the commercial Renishaw® SLM 125 printer was employed. The factors that influence the PBSLP of alumina have been identified and their levels based on the previous numerical and experimental investigation for the D-PBSLP of alumina, as obtained in Sections 5.2 and 5.3. These factors include laser power and hatching space. In addition, the hatching space, as recommended by the numerical model, should be 50 µm. Since the scanning speed of 400 mm/s yielded promising results for PBSLP of alumina, it was considered during the optimization treatments. The levels for each factor are shown in Table 6.9, where three levels were considered for each factor.

Table 6.9. Factors and levels used in the D-PBSLP optimization of alumina.

Factor	Symbol	Level 1	Level 2	Level 3
Laser power, W	A	180	190	200
Hatching distance, µm	B	50	60	70

This optimization aims to successfully print alumina samples with the highest possible relative density and good surface conditions. Consequently, the relative density and the top surface roughness were considered as response functions (response factors) during the optimization of Alumina PBSLP.

6.4.2. Taguchi optimization-second stage

Using a full factorial design of experiments resulted in 27 treatments, which is a time and cost-intensive process, whereas the Tauchi optimization method can reduce the number of treatments in a way that guarantees to capture the optimal level for each factor. The standard orthogonal array (OA) L9 (33) was used to construct the treatments in this study. This array consists of 9 treatments (instead of 27 treatments if the full factorial was used), including the two factors at different levels as described in Table 6.9. Table 6.10 shows the nine treatments included in this optimization, combining different level conditions for each factor (E1–E9). The treatments considered different levels of laser energy density; high energy density (E1, E4, E7), medium energy density (E2, E5, E8), and low energy density (E3, E6, E9).

Table 6.10. Factor levels for each treatment in PBSLP of Alumina.

Treatment	A	B
E1	1	1
E2	1	2
E3	1	3
E4	2	1
E5	2	2
E6	2	3
E7	3	1
E8	3	2
E9	3	3

After obtaining the orthogonal array, the second stage consisted of conducting the experiments (treatments) outlined in Table 6.10. The treatments were performed using the commercial Renishaw® SLM 125 printer, and Figure 6.32 depicts the printed alumina samples. Two samples were printed for each treatment to obtain more accurate measurements and check the printability and repeatability.

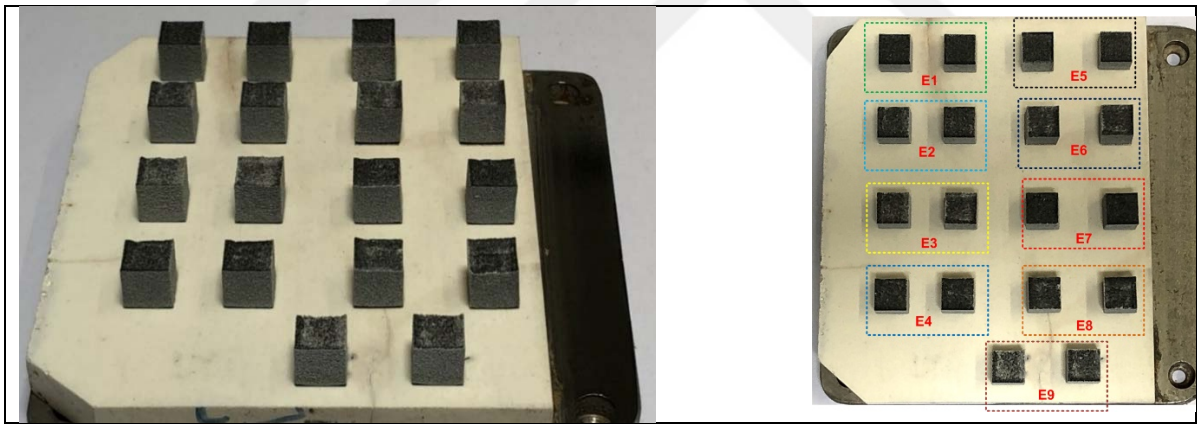

Figure 6.32. Alumina samples printed according to the treatments described in Table 6.10.

It can be observed that relative density increases as the laser power increases and hatching space decreases. For each treatment, the relative density was measured using Archimedes' method (the density was measured three times, and the average was considered), and the top surface texture and roughness were evaluated using the 3D laser scanning microscope (VKX-250, Keyence, Japan). Since the 3D laser scanning microscope employed accurate surface roughness detection via multiple line measurements and the average value was calculated and considered, as shown in Figure 6.33, only one measurement was considered for the surface roughness of each treatment. The 3D surface height for each treatment is

shown in Figure 6.34. Table 6.11 summarises the relative density and surface roughness for every treatment.

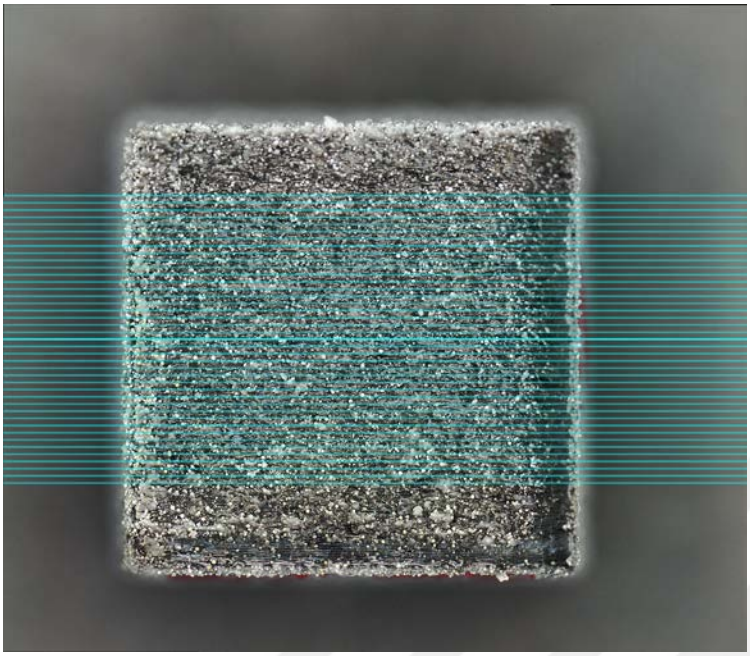

Figure 6.33. Surface roughness measurement through multiple lines used in the optical microscope (VKX-250, Keyence, Japan).

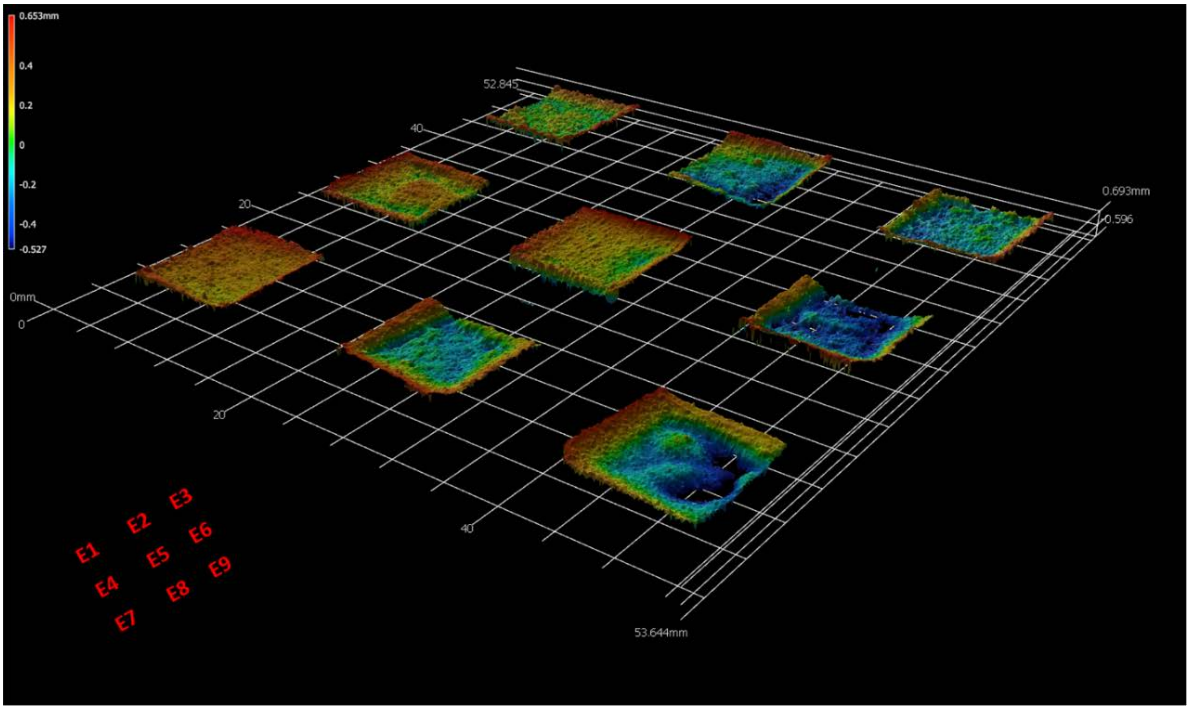

Figure 6.34. 3D top surface height of alumina sample at each treatment.

Table 6.11. Relative density and surface roughness of alumina sample at each treatment.

Treatment	Levels of input factors		Measured response factor				
	A	B	Relative density				Surface roughness (R_a), µm
			First reading	Second reading	Third reading	Average	Average
E1	1	1	0.87	0.86	0.87	0.87	54
E2	1	2	0.85	0.83	0.85	0.84	108
E3	1	3	0.77	0.75	0.78	0.77	112
E4	2	1	0.90	0.89	0.90	0.90	151
E5	2	2	0.84	0.85	0.85	0.85	146
E6	2	3	0.81	0.81	0.81	0.81	145
E7	3	1	0.87	0.92	0.92	0.92	132
E8	3	2	0.87	0.86	0.87	0.87	171
E9	3	3	0.79	0.79	0.79	0.79	180

6.4.3. Taguchi optimization-Final stage

The final phase in the Taguchi optimization is devoted to response factor analysis (data analysis), determining the optimal factor value, and conducting a confirmation test using the optimal factor value.

In order to analyze the obtained data, the Taguchi optimization technique uses the Signal to Noise (S/N) response analysis to evaluate the quality of each treatment instead of the standard deviation. This is mainly because the standard deviation decreases or increases according to the mean. The S/N ratio mainly focuses on measuring the response factor's variation to the nominal or target value under different noise conditions (uncontrollable factors). There are four categories for the S/N ratio calculation based on the desired output quality: smaller is the better, larger is the better, nominal is the better, and nominal is the best. For the D-PBSLP of alumina, the larger is, the better was used for the relative density, as described by equation (5.1), while for surface roughness smaller is, the better was used, as described by equation (5.2) [177].

$$S/N = -10 \times \log\frac{1}{n}\left(\sum \frac{1}{{Y_i}^2}\right) \quad (5.1)$$

$$S/N = -10 \times \log\frac{1}{n}\left(\sum {Y_i}^2\right) \quad (5.2)$$

Where, Y_i represents the individual measured relative density (first, second and third reading for the relative density and the calculated surface roughness, as described in Table 6.11, while n represents the number of the reading (n =3 for relative density and n=1 for surface roughness). Table 6.12 summarizes the S/N ratio for each treatment's relative density and SiC percentage.

Table 6.12. Calculated S/N ratio for each treatment used in alumina-PBSLP optimization.

Treatment	Levels of input factors		Calculated S/N ratio	
	A	B	Density	Surface roughness
E1	1	1	-1.25404	-34.6479
E2	1	2	-1.48772	-40.6685
E3	1	3	-2.36043	-40.9844
E4	2	1	-0.97368	-43.5795
E5	2	2	-1.45583	-43.2871
E6	2	3	-1.84450	-43.2274
E7	3	1	-0.76754	-42.4115
E8	3	2	-1.28461	-44.6599
E9	3	3	-2.06087	-45.1055

In the Taguchi optimization technique, the largest S/N ratio would represent the optimal response for the desired output (maximum relative density and low surface roughness). As described earlier, the S/N category used in this study for relative density is “the larger is, the better”, and for surface roughness is “the smaller is, the better”, which means that the largest relative density content and the smallest surface roughness value are desired. The S/N ratio response graphs for the relative density and surface roughness are shown in Figure 6.35. The optimal combination of the process parameters can be determined from these graphs. It can

be seen that the hatching space (factor B) is the most significant parameter, followed by the laser power (factor A), and to achieve the maximum relative density, the smallest hatching space value of 50 µm (B1) and the highest laser power (A3) should be used, i.e., treatment E7 should be used.

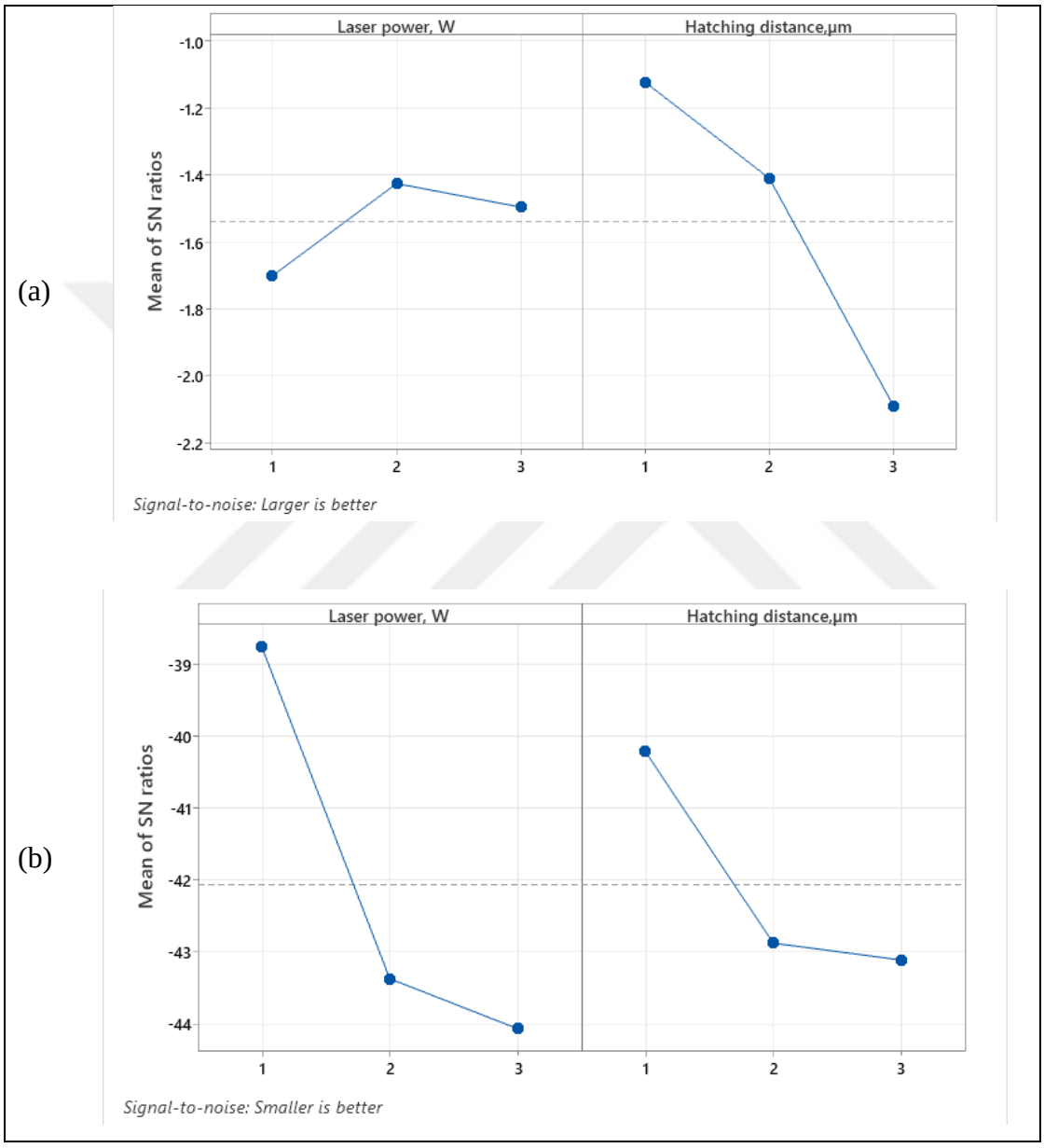

Figure 6.35. S/N ratio response graph of relative density (a) and surface roughness (b)- PBLSP optimization of alumina.

The optimal combination of the process parameters values can be determined from Figure 5.35(b) for achieving an excellent top surface roughness. It can be seen that the laser power (factor A) is the most significant parameter, followed by the hatching space (factor B) and

the optimal process parameters values to achieve good surface conditions are a laser power of 180W (A1) and hatching space of 50 µm (B1), i.e., treatment E1 should be used.

6.4.4. Pareto ANOVA: an alternative technique

As previously stated in Chapter 3, Pareto ANOVA is a technique used to analyze data for process parameters optimization, and it can also provide the percentage contribution of each parameter to the response functions straightforwardly [81,82]. The S/N response data for each response function is used to construct the Pareto ANOVA analysis. The S/N response data can be calculated by taking the sum of all S/N ratio values (as described in Table 6.12) at the same level as the input parameter. Table 6.13 summarizes the S/N response data values for relative density and surface roughness.

Table 6.13. S/N response data of alumina's relative density and surface roughness-PBLSP optimization.

Relative density %			Surface roughness		
Levels	A	B	Levels	A	B
1	-5.10	-3.36	1	-116.30	-120.64
2	-4.27	-4.22	2	-130.09	-128.62
3	-4.48	-6.26	3	-132.18	-129.32

After calculating the S/N response data for each input parameter, the summation of squares of differences was calculated for each input parameter using the following equation:

$$S_d^A = (A_1 - A_2)^2 + (A_1 - A_3)^2 + (A_2 - A_3)^2 \quad (5.3)$$

Where S_d^A represents the squares of difference for the input parameter (laser power) A; similarly, the square of differences can be calculated for the hatching space. The percentage contribution for each input parameter was calculated by considering the percentage summation of the squares of differences to the total summation of the squares of differences for all input parameters. The input parameters were organized in Pareto diagram in a way that the parameter with highest contribution comes first and then followed by other parameters based on their contributions. The Pareto diagram was plotted considering the

obtained percentage for each input parameter. Table 6.14 and Table 6.15 summarize the Pareto ANOVA analysis for relative density and surface roughness, respectively.

According to Table 6.14, for relative density, the hatching space is the most influential parameter, contributing 90.64 %. The laser power's contribution is then 9.36 %. The optimal combination of input process parameters to achieve the maximum relative density is A3-B1. This is primarily since decreasing the hatching distance and increasing the laser power allow more alumina powder particles to be well consolidated and densified.

For surface roughness, as described in Table 6.15, the laser power contributed the most, 76.21%, followed by the hatching space, which contributed 23.79%. A1-B3 is the optimal combination of input process parameters for producing a surface with favourable characteristics. A low laser energy density was required to achieve desirable surface conditions (high hatching space and low laser power).

Table 6.14. Paetro ANOVA analysis for relative density of alumina samples -D-PBSLP optimization

Input parameters		Laser power (A)	Hatching space (B)
Summation at input parameter level.	1	-5.10	-3.95
	2	-4.27	-5.08
	3	-4.11	-4.93
Total summation at the input parameter level		-13.48	-13.96
Summation of the squares of the differences.		$S_d^A = 1.6946$	$S_d^B = 2.2598$
Total Summation of the squares of the differences.		$S_{total} = S_d^A + S_d^B = 3.9544$	
Input parameter contribution ratio %		$\frac{S_d^A}{S_{total}} = 42.85$	$\frac{S_d^B}{S_{total}} = 57.15$
Paetro ANOVA diagram			
Cumulative contribution %		90.64	100
Remarks		The most significant input parameter is the hatching space and the laser power.	
Optimum input parameters combination		A3	B1

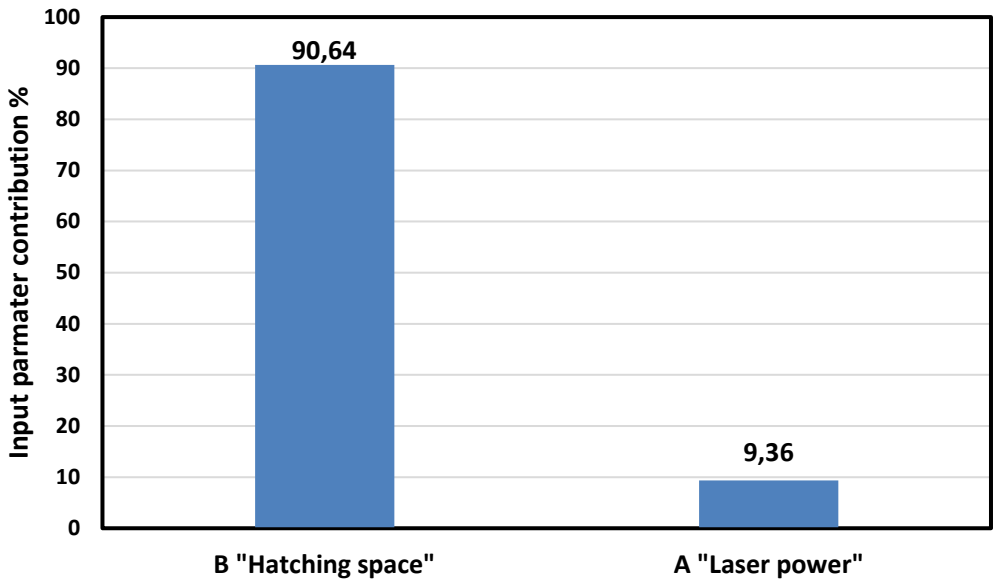

Table 6.15. Paetro ANOVA analysis for the surface roughness of alumina samples printed by PBSLP.

Input parameters		A	B
Summation at input parameter level.	1	-116.30	-120.64
	2	-130.09	-128.62
	3	-132.18	-129.32
Total summation at the input parameter level		-13.48	-378.57
Summation of the squares of the differences.		$S_d^A = 446.64$	$S_d^B = 139.43$
Total Summation of the squares of the differences.		$S_{total} = S_d^A + S_d^B + S_d^C = 586.07$	
Input parameter contribution ratio %		$\frac{S_d^A}{S_{total}} = 76.21$	$\frac{S_d^B}{S_{total}} = 23.79$
Paetro ANOVA diagram			
Cumulative contribution %		76.21	100
Remarks		The most significant input parameter is the laser power and hatching space.	
Optimum input parameters combination		A1	B1

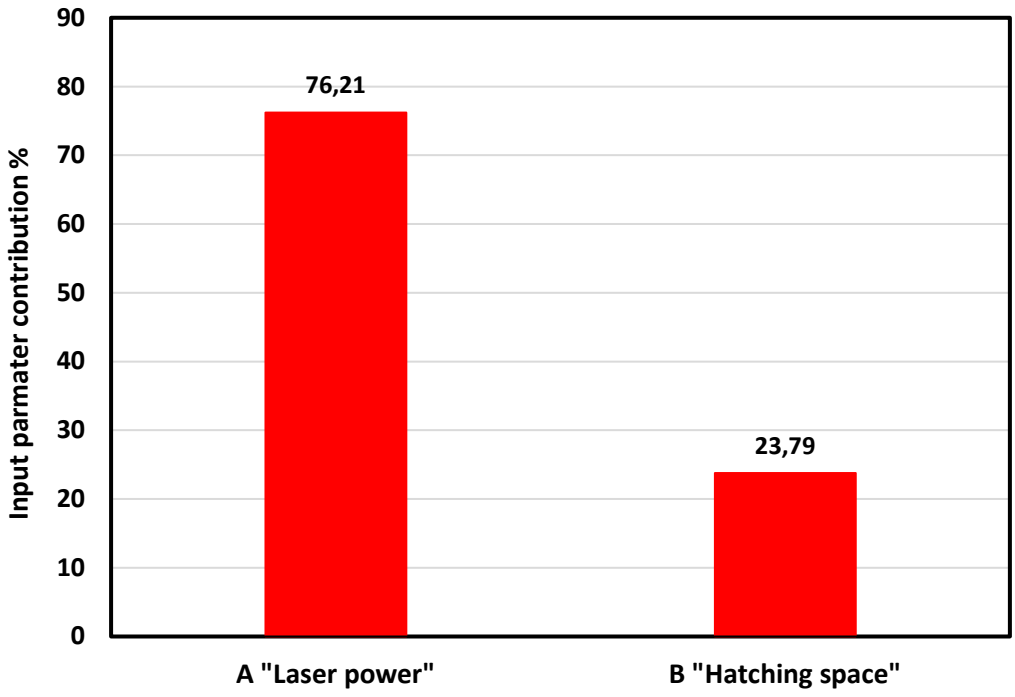

From the optimization of the process parameters for PBSLP of alumina, it is evident that achieving a high relative density value will harm the sample surface quality. Consequently, the effectiveness of the process parameters to achieve higher density values and good surface

roughness is limited, and alternative solutions should be considered. Powder improvement can play a significant role in achieving this objective. As described in section 5.1, the spray-dried alumina powder has a porous structure (the powder particle is hollow and not completely solid), which may be the primary cause of the poor surface conditions obtained with a high laser energy density used to maximize the density. When melted by the laser, this porous structure causes a large drop in layer level in specific locations, increasing surface roughness. This can be compensated by using solid-spherical alumina powder produced by high-temperature plasma technology [68]. In addition, some PBSLP printers are equipped with a compaction cylinder integrated with the recoater (as available in the Phenix printer used for D-PBSLP of SiC). This compaction cylinder can compensate for the porous structure of spray-dried powder, thereby allowing the falling of the layering level at specific locations to be significantly mitigated and the surface quality greatly enhanced. This is an important research topic that should be addressed in future investigations.

6.4.5. Confirmation test

Since the recommended optimal values of the process parameters, as determined by the Taguchi optimization method and Pareto ANOVA analysis, have already been taken into account, it is unnecessary to conduct a confirmation test for both the relative density and the surface roughness. However, as shown by the optimization of process parameters, the relative density increased with increased laser power and decreased hatching space. Therefore, examining the impact of increasing the laser power and decreasing the hatching space on the relative density is worthwhile. As depicted in Figure 6.36, Alumina samples were printed with varying laser power, including 200 and 210 W (the laser power cannot be increased above 210 W, as this is the highest value permitted by the printer) and hatching space, including 50, 40, and 30 µm. The alumina samples were successfully printed but with a wavy top surface.

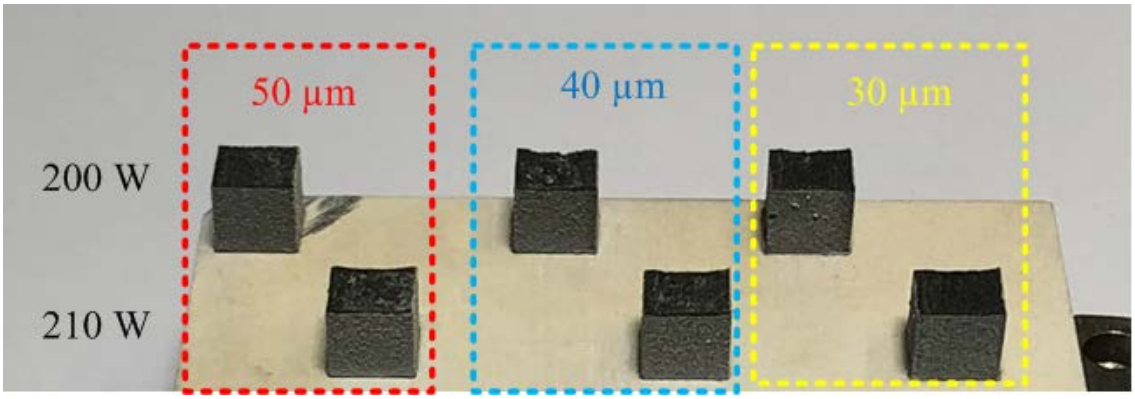

Figure 6.36. Alumina samples printed with different laser power and hatching space, as instructed by the optimization of the process parameters.

Table 6.16 shows the printed alumina samples, their top surface under an optical microscope, 3D top surface height, and surface roughness value measured by optical microscope (VKX-250, Keyence, Japan) at 210 W and various hatching spaces. The top surfaces were unlevel, wavy, and filled with defects. In addition, it can be observed that the surface roughness value dropped as the hatching space decreased, which corresponded to the conclusion provided in section 6.4.3.

Table 6.16. Alumina samples, top surface view, 3D surface height, and surface roughness value at a laser power of 210 W and different hatching spaces.

Sample		Top surface image	3D image	Ra, µm
Hatching space 50 µm		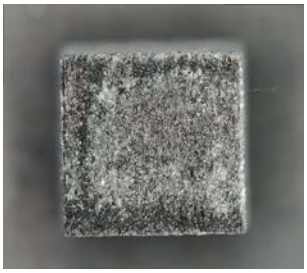	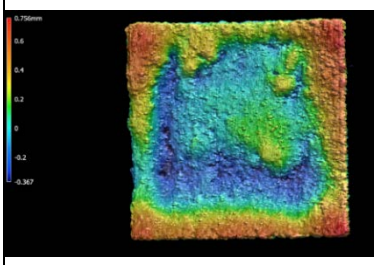	163
Hatching space 40 µm	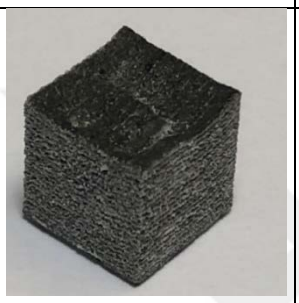	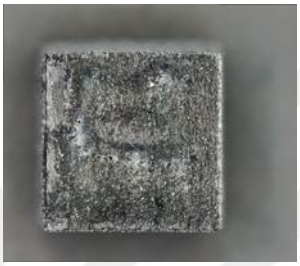	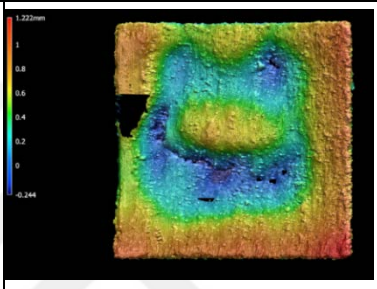	147
Hatching space 30 µm	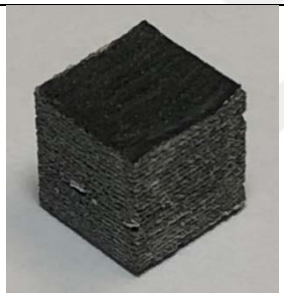	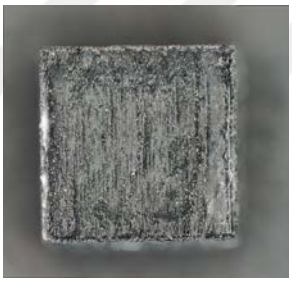	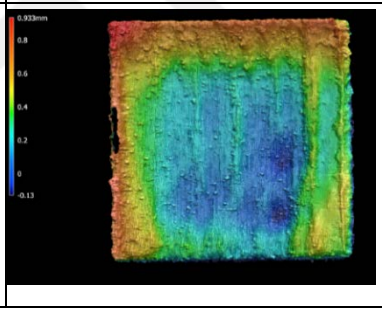	131

Figure 6.37 depicts the variation in relative density concerning laser power and hatching spacing for the alumina samples depicted in Figure 6.36. The relative density increased with an increase in laser power and a decrease in the hatching space, with a maximum relative density of 94.7 % attained using 210 W of laser power and a hatching spacing of 30 µm.

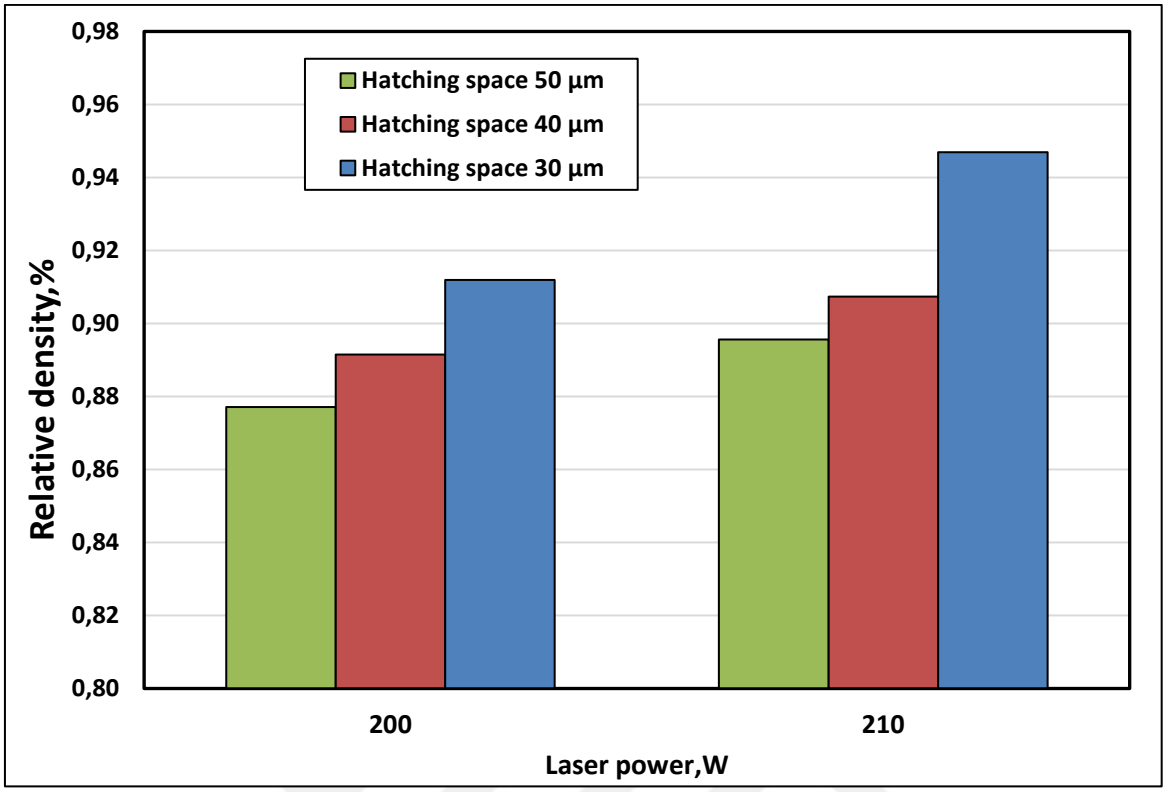

Figure 6.37. Alumina samples printed with varying laser power and hatching space, as the process parameters optimization instructed.

Figure 6.38 shows SEM images of alumina samples printed with 210 W of laser power and 50, 40, and 30 m hatching space. The samples contain defects in the form of small holes and notches. In addition, there are numerous cracks dispersed over the surface as a result of the thermal shock experienced during D-PBSLP. As previously explained, these cracks can be eliminated by preheating the powder layer before scanning.

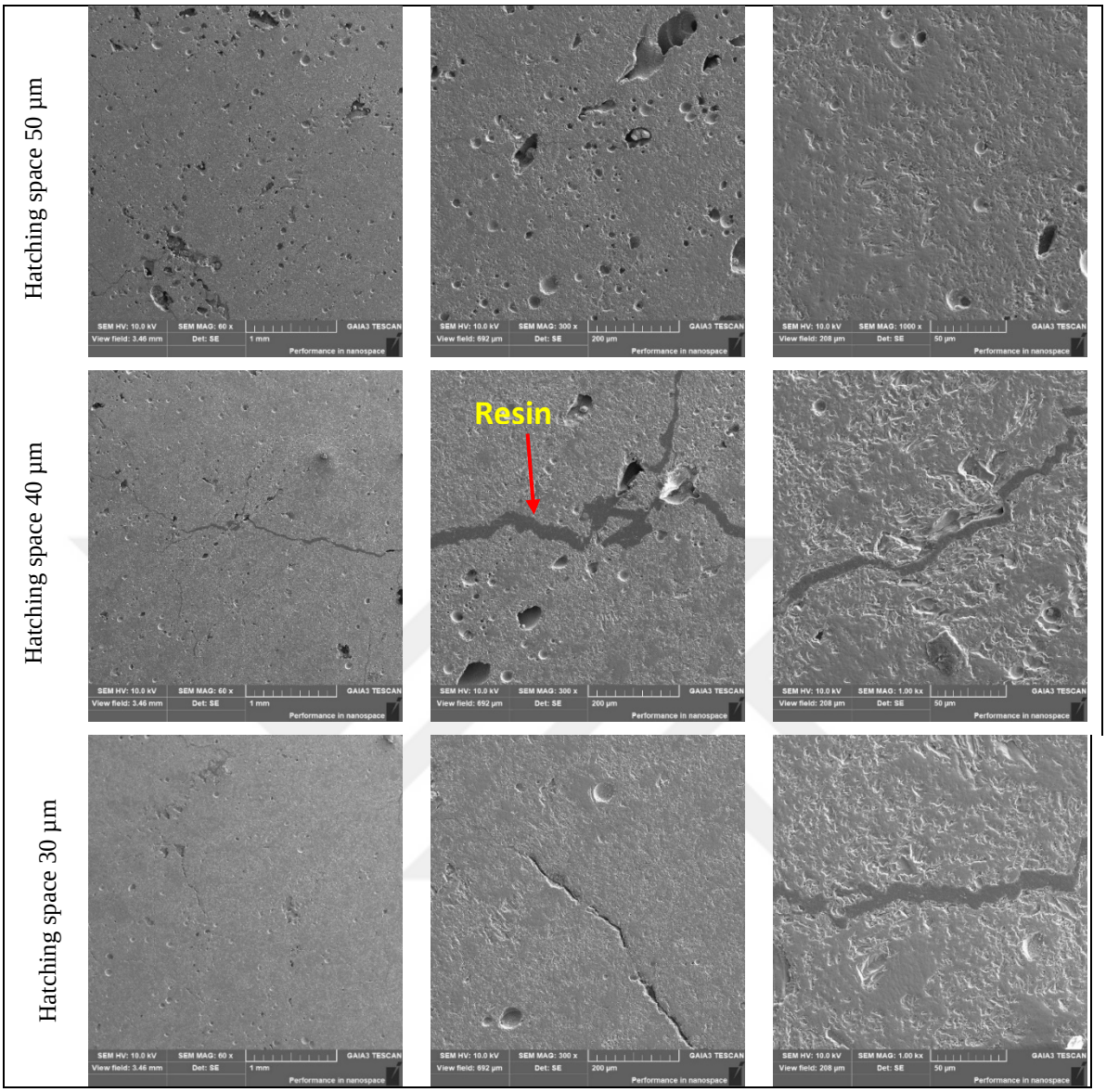

Figure 6.38. SEM images of alumina samples' top surface at a laser power of 210 W and different hatching spaces.

Different alumina lattice structures, including gyroid, diamond, and primitive, were printed to demonstrate the capabilities of the D-PBSLP technology to print extremely complicated geometries, as shown in Figure 6.39. The removal of the lattice from the baseplate led to the appearance of some defects in the sample base. In addition, the layers are visible along the building direction, primarily due to the 100 µm layer thickness used.

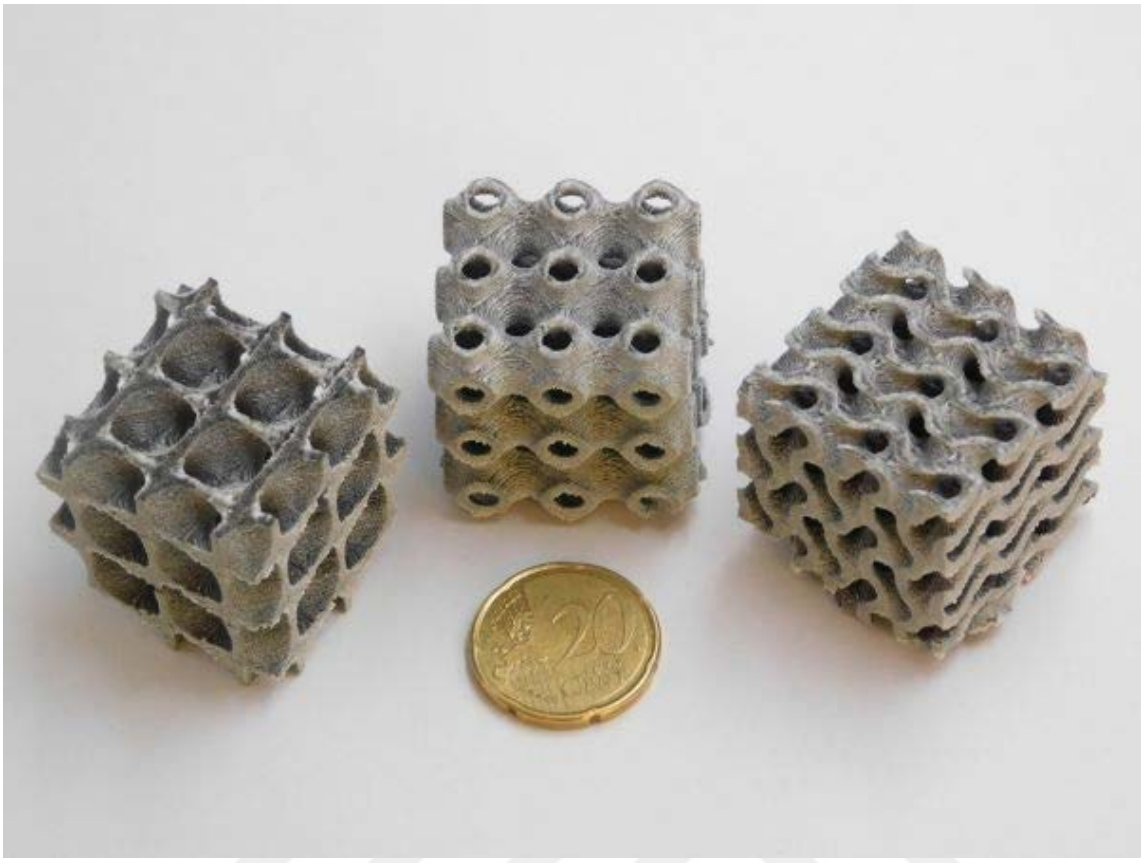

Figure 6.39. Alumina lattice structures printed for demonstration purposes.

6.5. Mechanical Performance Evaluation

The mechanical performance of alumina samples printed using the PBSLP process was evaluated utilizing microhardness and compression tests. Section 0 describes the methods employed for each test. The findings of each test were compared to those that had previously been reported in the literature.

6.5.1. Microhardness testing

The Vickers microhardness test was utilized to analyze the PBSLP-printed alumina sample. To observe the load's influence on the material's hardness, 100, 200, and 300 g indentation loads were applied. Each load was tested three times, with each reading being recorded and the average value being considered. Figure 6.40 illustrates the results of the test. The achieved microhardness was 2180 HV with a 100g load and grew to 2370 HV with a 300g load, as observed. The literature reports that the microhardness of alumina is roughly 2000 HV [196, 197], which is virtually identical to the hardness determined using the PBSLP

approach in this investigation. In conclusion, the hardness of the alumina samples obtained using the D-PBSLP is comparable to that described in the literature.

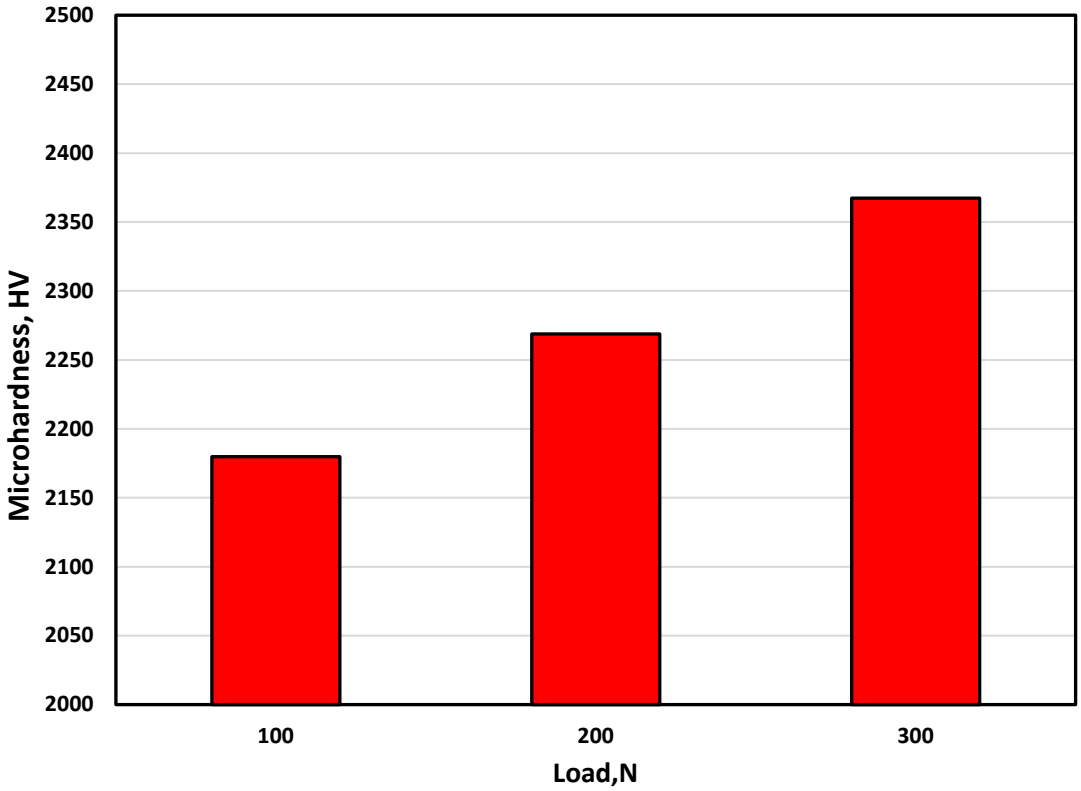

Figure 6.40. Variation of the microhardness of alumina printed using the D-PBSLP technique with different loads.

6.5.2. Compressive test

As ceramic materials are renowned for their high compressive strength, it became necessary to investigate the compressive strength of alumina samples printed using the D-PBSLP technique with the previously determined optimal process parameter. For this purpose, cylindrical alumina samples (10 mm in diameter and 25 mm in length) were printed with optimized process parameters (210 W of laser power, 400 mm/s of scanning speed, 30 µm of hatching distance, and 100 µm of layer thickness).

Figure 6.41(a) depicts the printed compressive samples before being unloaded from the printer baseplate. To prepare the alumina samples for the compressive test, the two opposite cross-sectional areas were hand-polished until they became flat and parallel, as shown in Figure 6.41(b). The length of the samples was adjusted to 20 mm (L=2D, where L is the

length of the sample and D is its diameter). Compressive strength was calculated according to equation (2.16), as described in Section 3.5.

(a)

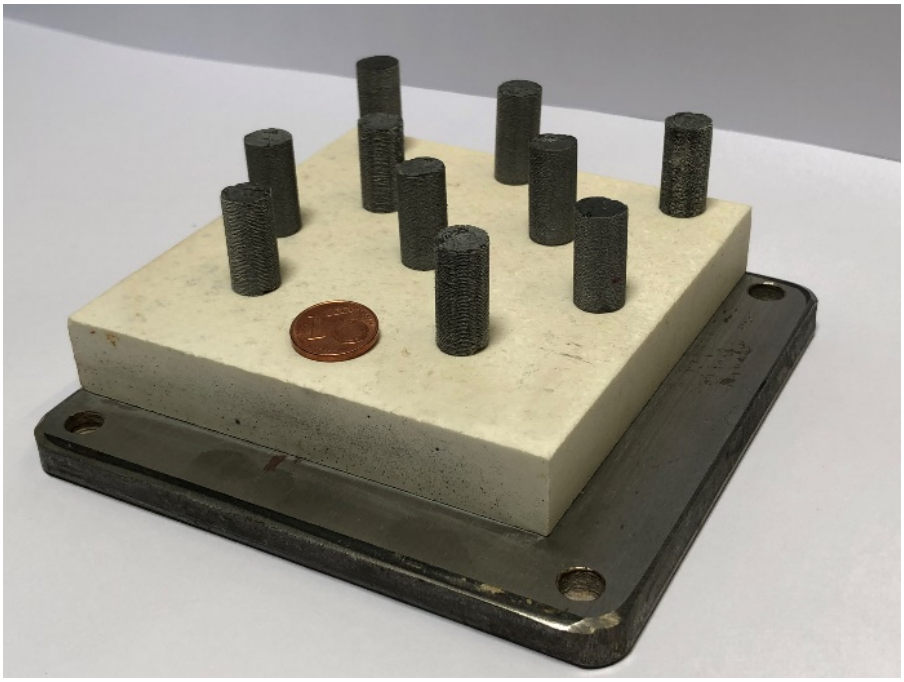

(b)

Figure 6.41. Alumina compressive test samples: before de-powdering (a); after the preparation for the compressive test.

The compressive tests were conducted using a Z100 Universal testing machine (Zwick, Germany) equipped with a 100 kN cell force, and the machine's upper head was lowered at a rate of 1 mm/min until failure occurred.

Tests were conducted on ten samples, and the mean of all measurements was calculated. The obtained compressive strength was 140.8 ± 11.6 MPa, which is considered low compared to the compressive strength of alumina manufactured with conventional techniques, reaching 3000 MPa [198]. This is primarily due to the cyclic damage experienced along the printing direction, as described in Figure 6.30. Generally, the maximum compressive strength reported for ceramic materials processed by AM techniques is 1000 MPa.

Figure 6.42 shows the stress-strain curve for one of the alumina printed samples, and Figure 6.43 depicts alumina samples that have been crushed after reaching their compressive strength limit.

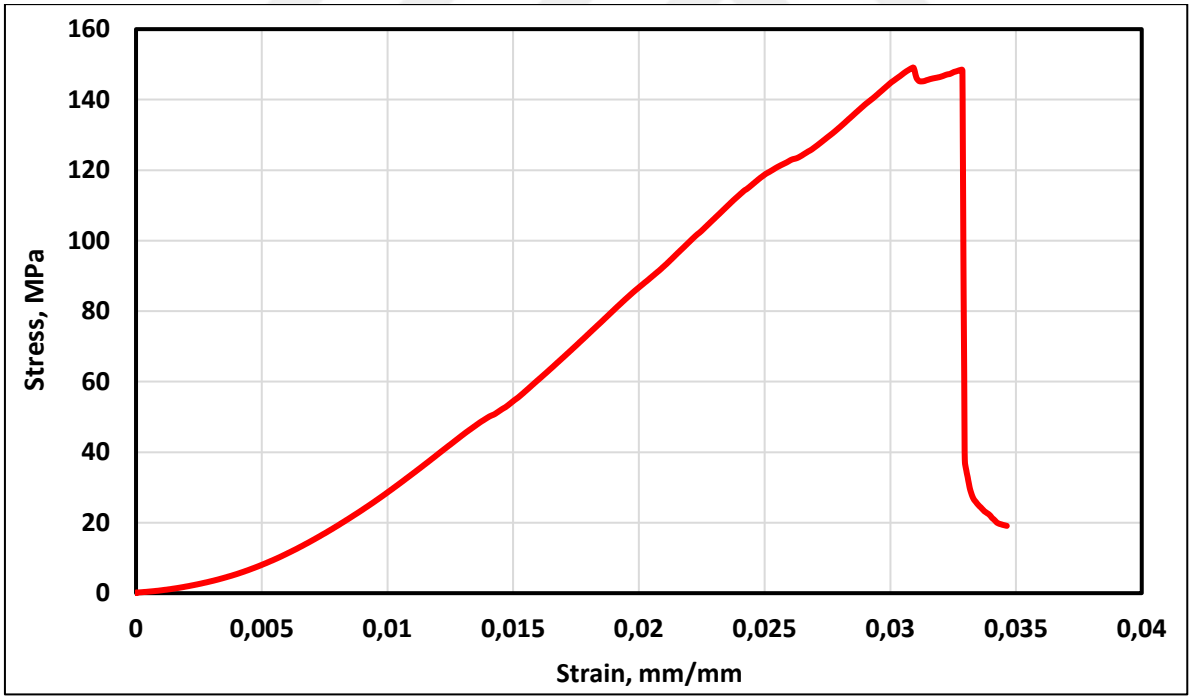

Figure 6.42. Stress-strain curve for alumina sample under compression test.

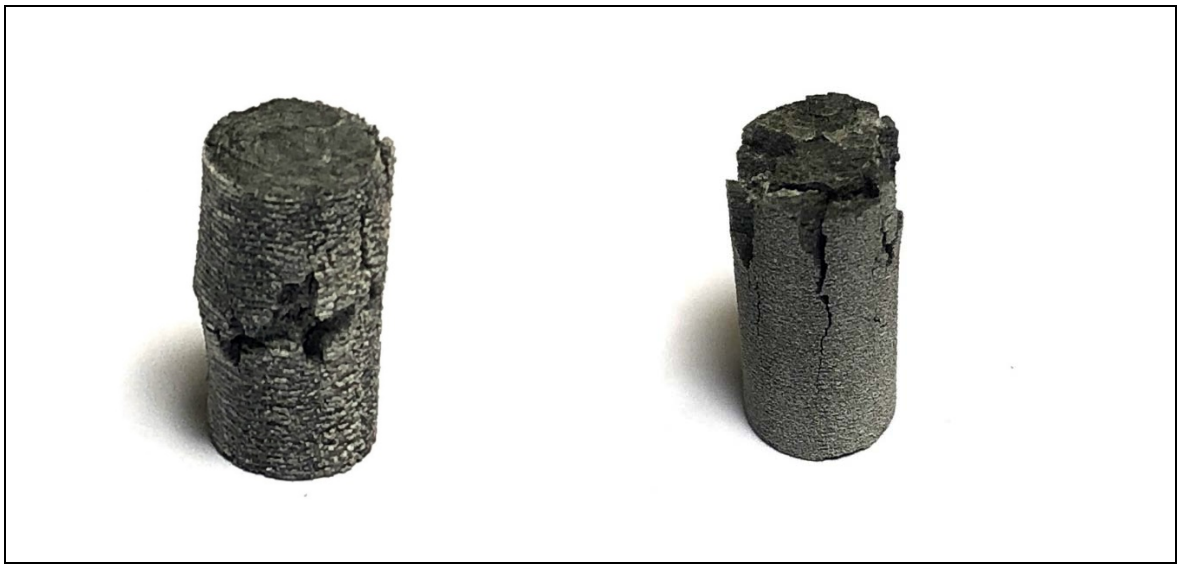

Figure 6.43. Stress-strain curve for alumina sample under compression test.

6.6. Conclusion

This chapter investigates experimentally and numerically the PBSLP of alumina. First. The alumina powder was modified using the spray-drying technique to obtain an appropriate powder for the PBSLP technique. The developed model was then utilized to predict the initial values of the process parameters, such as the laser power, scanning speed, hatching space, and scanning strategies. The PBSLP printer (SLM 125, Renishaw®, UK) provides different scanning strategies, including linear with varying orientations, concentric, and island.

In comparison to the other scanning strategies, the linear 45° yielded promising results in terms of the obtained relative density and surface quality and was considered for the other PBSLP investigation of alumina. Concerning the effects of scanning speeds, the results demonstrated that increasing the scanning speed positively impacted the quality of the printed samples. Using a scanning speed of 400 mm/s, 85 % relative density alumina samples were obtained.

The process parameters were then optimized using the Taguchi optimization technique, with laser power, scanning speed, and hatching space. The optimization identified the optimal parameters for PBSLP of alumina, which enabled the printing of alumina with a relative density of 94.5%.

Compressive and microhardness tests were used to evaluate the mechanical performance of the printed samples. As depicted in the SEM images, the low performance obtained during the compressive test was due to cyclic damage along the building direction of the sample. For the microhardness test, the printed samples exhibited a hardness value comparable to that of alumina processed using conventional techniques, whereas for the compressive test, the printed samples demonstrated a low compressive strength in comparison to conventional techniques.

7. D-PBSLP of SiC

This chapter has six sections and discusses the D-PBSLP of SiC. Section 7.1 focuses on the characterization of used SiC powder. Section 7.2 presents the preliminary investigation of SiC to estimate the possibility of D-PBSLP SiC and provides an overview of the factors that should be prioritized to print SiC using the D-PBSLP method successfully. Section 6.3 determines the optimal ranges for the process parameters available in the commercial Phenix printer (ProX® DMP 200) to be appropriately used for the D-PBSLP of SiC using the developed model and experimental study. In addition, section 7.3 examines the impact of scanning strategies on the D-PBSLP of SiC to determine the optimal scanning strategy. Section 7.4 examines the impact of scanning speed and determines the optimal scanning speed range for D-PBSLP of SiC. Using the results of sections 7.3 and 7.4 as a guide, section 7.5 focuses on using the Taguchi optimization technique and Pareto ANOVA analysis to optimize the scanning speed, laser power, and hatching space in order to print high-quality SiC samples using the D-PBSLP technique. Section 7.6 evaluates the mechanical performance of SiC parts processed using the D-PBSLP technique.

7.1. Powder Characterization

As described in section 3.2.2, the SiC powder used in this study was supplied by Mersen Boostec®. The powder is an alpha-SiC powder with a purity of 98.5%. The particle size distribution (PSD) is shown in Figure 7.1, where it can be seen that the mean particle diameter (d50) is about 20 µm which is considered appropriate for powder bed AM application [68].

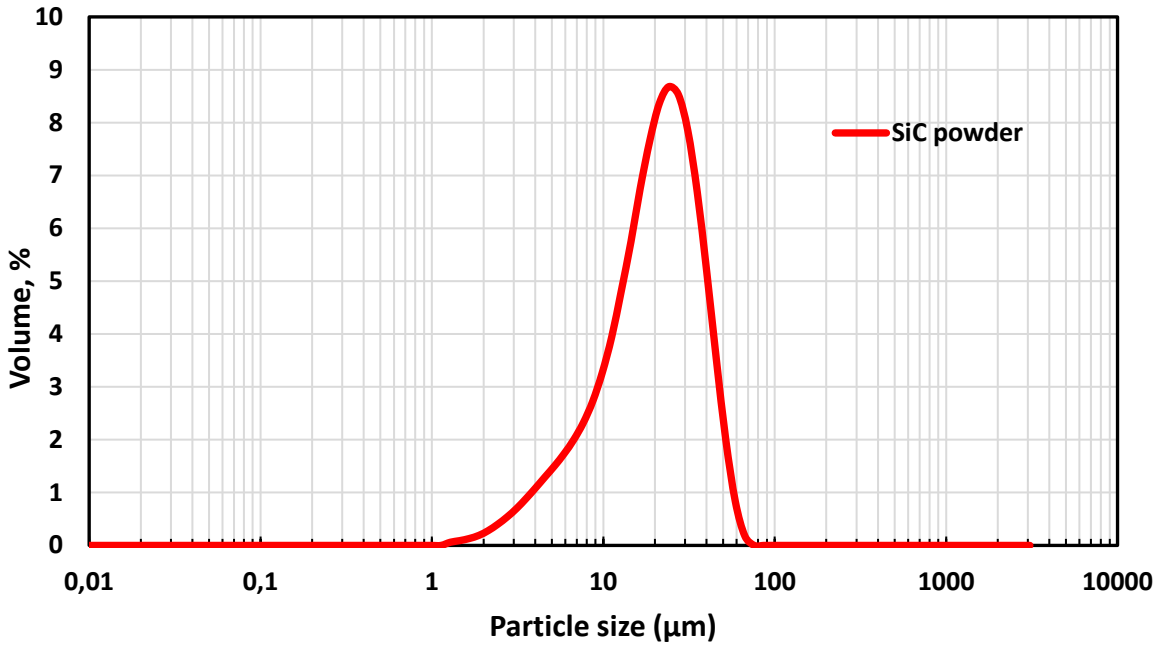

Figure 7.1. The particle size distribution of SiC powder.

As described in chapter 6, the powder's morphology is crucial and should be evaluated to ensure a uniform powder bed deposition. The SEM images in Figure 7.2 demonstrate that the SiC powder has an irregular shape, not a spherical shape, as is usually the case with PBSLP techniques. Due to the friction developed between the particles and the baseplate and the particles themselves, the irregular shapes of the powder may cause issues during the deposition of the layer on the powder bed. Therefore, it was essential to evaluate the flowability of the powder.

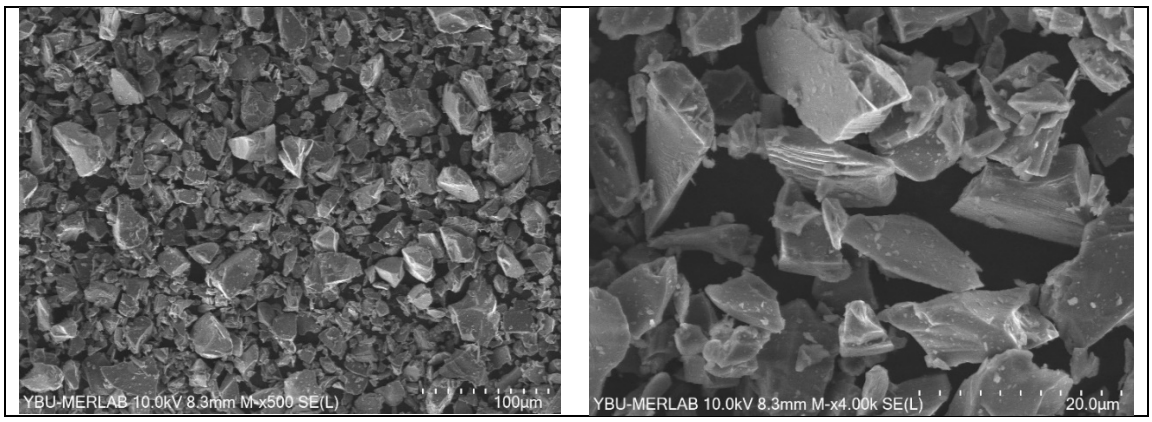

Figure 7.2. SiC powder morphology.

The powder flowability was evaluated using the dynamic angle of repose technique. ASTM recommends this technique as a characterization way to quantify the flowability of powders for AM applications [199]. Different ways can obtain the angle of repose, and in this study, it was measured using the angle of repose [200]. The powder Characteristics Tester (PT-S, Hosokawa Micron Ltd, UK) was used to measure the angle of repose. The average angle of repose obtained from this test was 41°, as described in Figure 7.3, which is considered acceptable for the powder bed AM techniques [201,202].

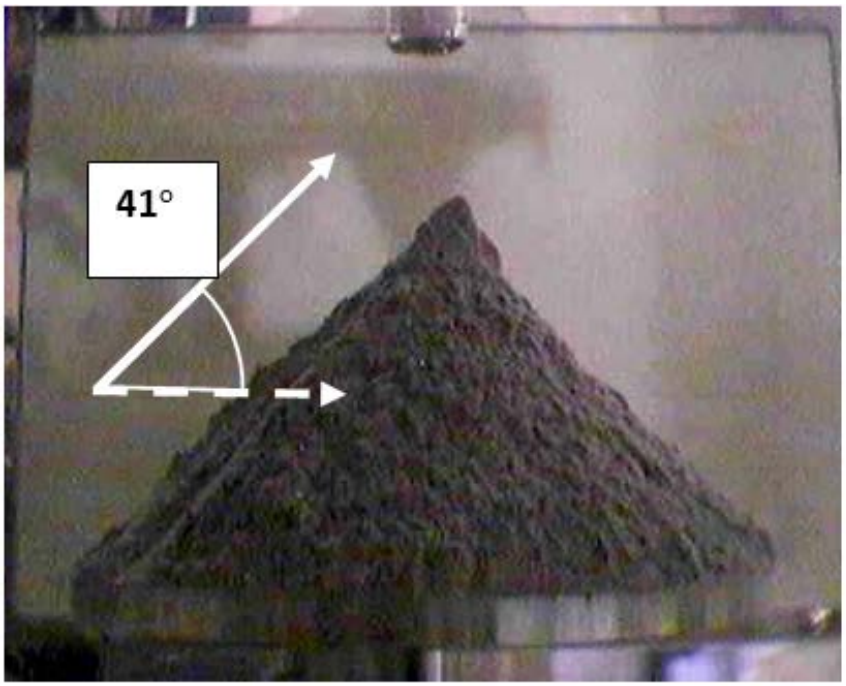

Figure 7.3. Angle of repose for SiC powder.

Initial testing was performed to check the powder's deposition on the printer baseplate and SiC powder. It was discovered that the powder was successfully and smoothly deposited on the powder bed, as can be seen in Figure 7.4. This was done in order to confirm that the flowability of the powder was adequate. Lastly, it is essential to examine the SiC phases present in the powder. Figure 7.5 depicts the results of the XRD analysis, which revealed two primary SiC phases: hexagonal SiC (SiC 6H) and cubic SiC (SiC 3C).

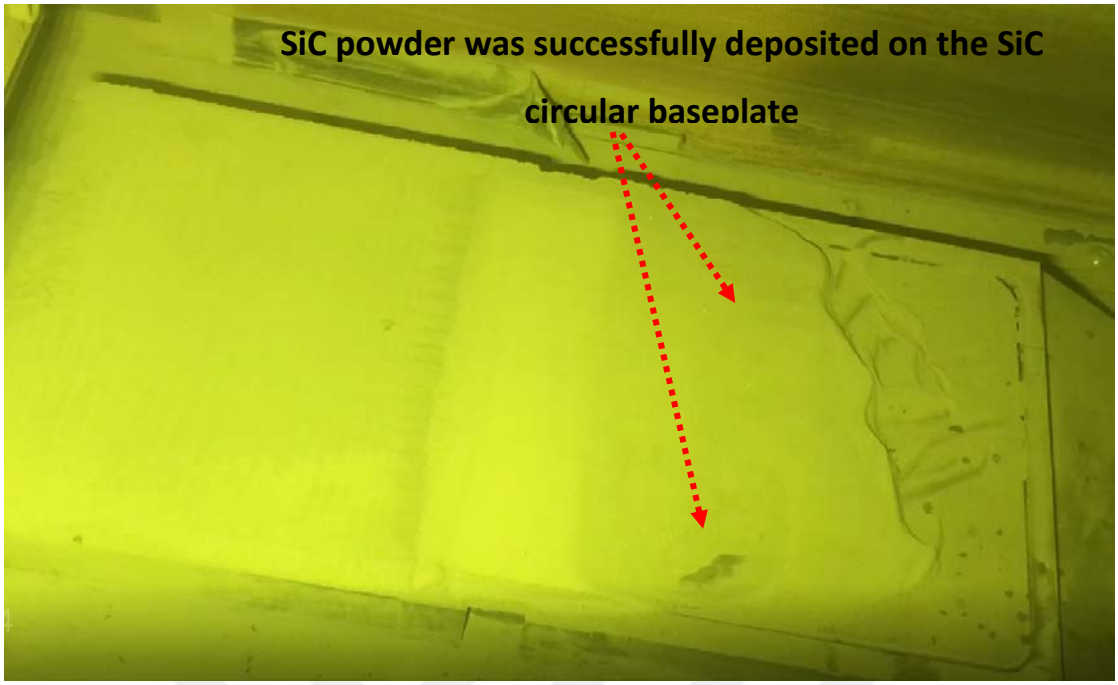

Figure 7.4. SiC powder was deposited smoothly on the SiC circular baseplate.

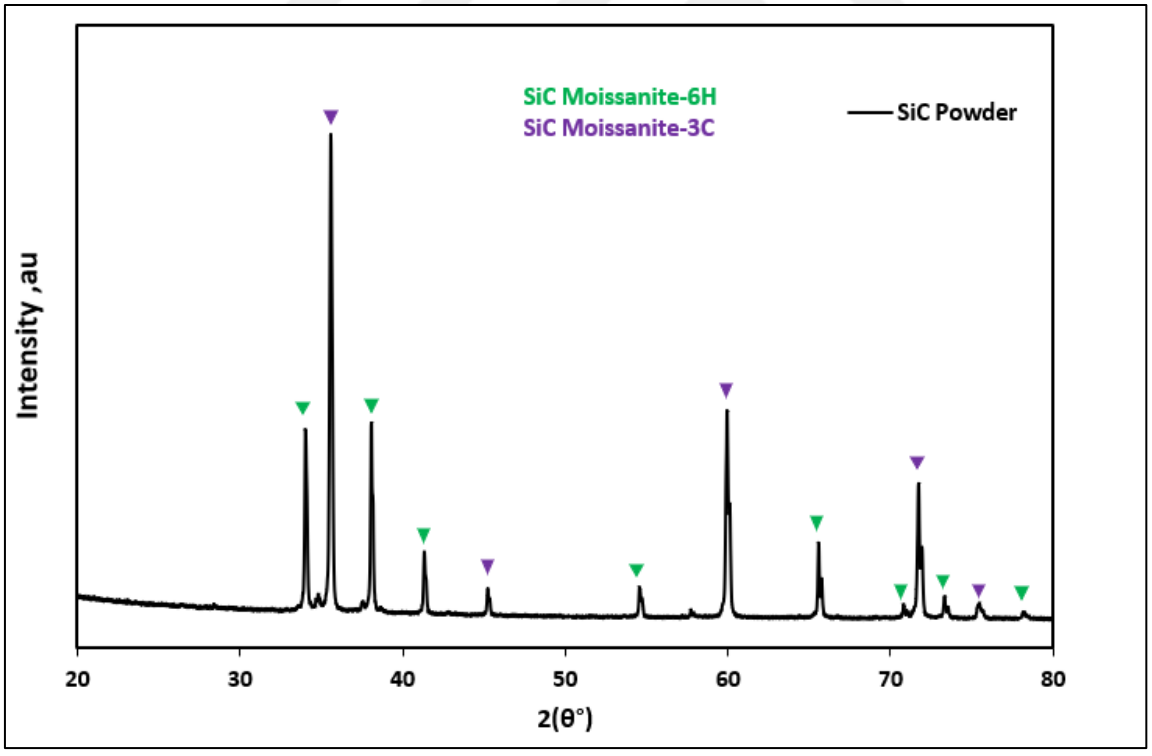

Figure 7.5. XRD spectra of SiC powder.

7.2. Process Parameters Investigation

As described in Chapter 2, the process parameters, such as laser power, scanning speed, hatching distance, layer thickness, and scanning strategies, should be thoroughly

investigated to achieve the D-PBSLP of SiC. Therefore, as dependent parameters, the laser power and scanning speed were investigated simultaneously, and the appropriate values were estimated using the developed numerical model for various layer thickness values. The hatching space (distance) was then analyzed based on the laser power and scanning speed values, and the appropriate values were obtained using the developed numerical model. Finally, the scanning strategies were investigated, and the most effective scanning strategy was used for the D-PBSLP of SiC.

7.2.1. Laser power and scanning speed investigation

For successful D-PBSLP of SiC, it is crucial to employ the appropriate laser power and sintering speed. The laser power and sintering rate are two crucial parameters for the D-PBSLP of SiC. Low laser power with high sintering speed may result in un-sintered powder particles, whereas using high laser power with low sintering speed may result in SiC decomposition and building failure. The developed numerical model was used to predict the appropriate laser power range for varied sintering speeds of 100, 250, and 500 mm/s with layer thicknesses of 22, 30, and 40 µm. The appropriate laser power range was determined by sintering the layer thickness and adhering it to the layer beneath.

Moreover, the predicted laser power should result in a maximum temperature below the SiC decomposition limit. SiC decomposes at temperatures above 2800 K, yielding silicon liquid and carbon [141]. Therefore, it is recommended that the highest temperature during PBSLP be maintained below the SiC decomposition limit.

Table 7.1 demonstrates that with a layer thickness of 22 µm and a sintering speed of 100 mm/s, a laser power range of 20 to 30 W generated a temperature value almost below the decomposition point of SiC; however, this power range was insufficient to achieve complete sintering and adhesion with the layer below or the baseplate. According to the Phoenix 3D printer's specifications, the minimal amount of power it can output is 30W. (10 per cent of the maximum available power). In order to satisfy this criterion, the laser power range has been increased from 30 W to 40 W. As shown in Table 7.2, this laser power range of 30 to 40 W nearly matched all of the requirements listed. However, the generated temperature surpassed the SiC's decomposition limit. Due to the rapid nature of the laser scanning process (on the order of microseconds), this high temperature may not be sufficient to decompose

SiC. The XRD analysis discussed in the following sections should be used to confirm this conclusion.

As indicated in Table 7.3 and 6.4, for sintering speeds of 250 mm/s and 500 mm/s, the laser power range satisfying the abovementioned requirements is between 40 W and 50 W and 65 W and 75 W, respectively. In addition, it should be noted that the laser power range calculated for both 250 mm/s and 500 mm/s sintering speeds could not achieve good adhesion between the current scanned layer and the layer beneath (as seen in Table 7.3 and Table 7.4), which may have an effect on the success of the printing process. Therefore, it is not advisable to use a high sintering speed with the D-PBSLP of SiC. To validate this numerical simulation-based result, additional experimental investigations were conducted and described in the following sections

Table 7.1. Sintering contour and temperature distribution at different positions for the layer thickness of 22 µm and scanning speed of 100 mm/s.

Power, W	Top sintering contour	Cross-sectional sintering contour	Temperature contour
20	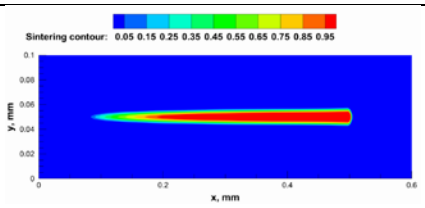	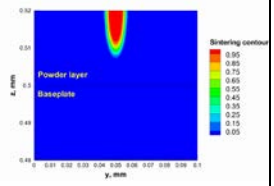	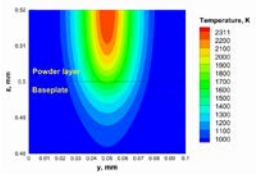
25	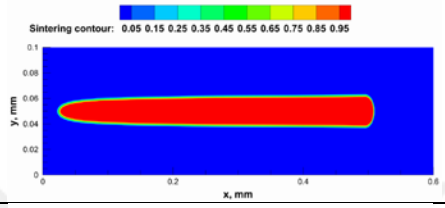	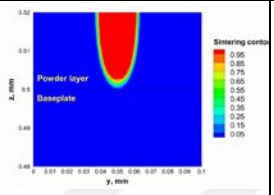	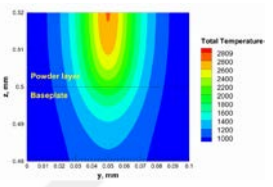
30	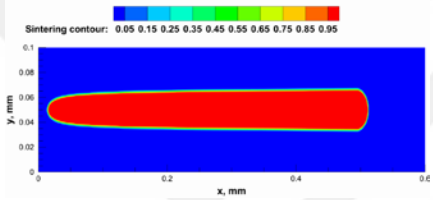	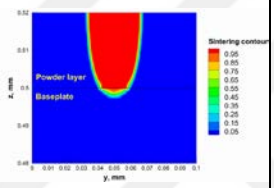	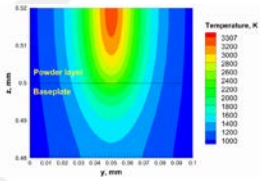

Table 7.2. Sintering contour and temperature distribution at different positions for the layer thickness of 22 µm and scanning speed of 100 mm/s using minimum power range as available in the commercial Phoenix 3D printer.

Power, W	Top sintering contour	Cross-sectional sintering contour	Temperature contour
30	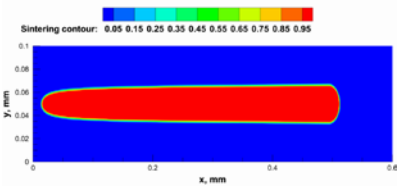	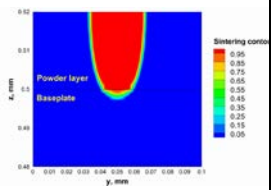	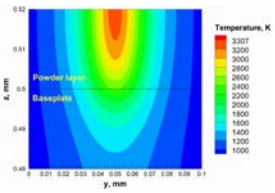
35	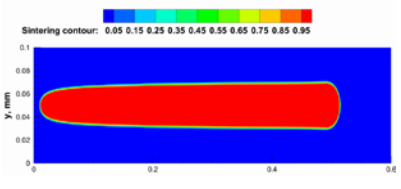	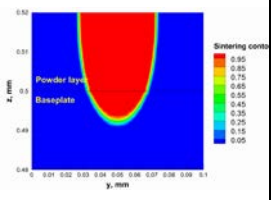	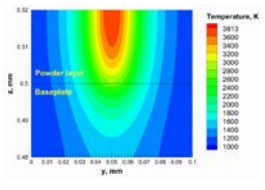
40	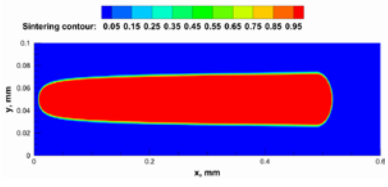	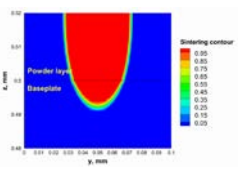	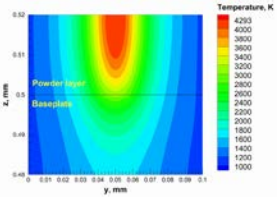

Table 7.3. Sintering contour and temperature distribution at different positions for the layer thickness of 22 µm and scanning speed of 250 mm/s.

Power, W	Top sintering contour	Cross-sectional sintering contour	Temperature contour
40	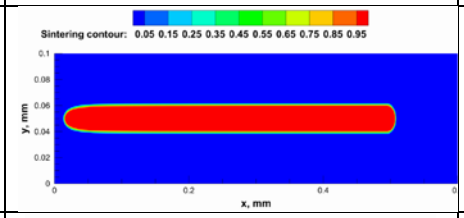	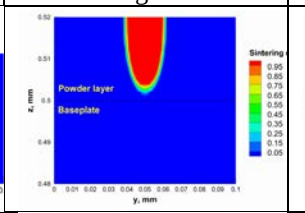	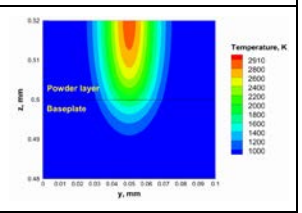
45	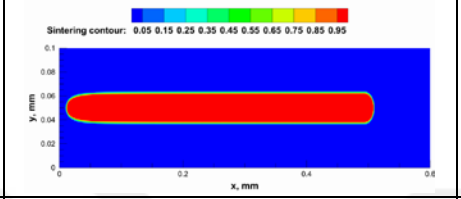	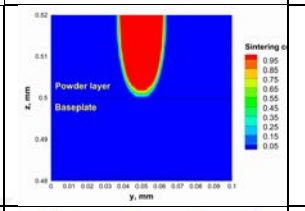	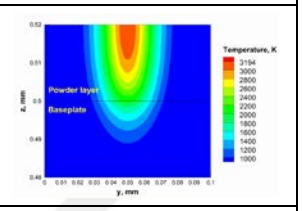
50	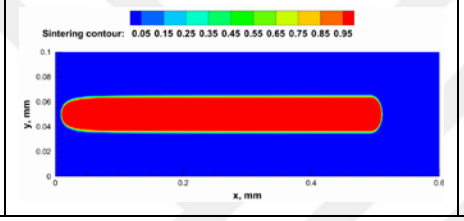	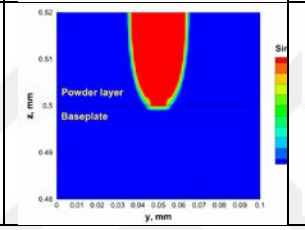	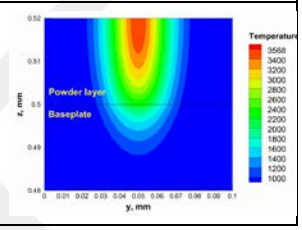

Table 7.4. Sintering contour and temperature distribution at different positions for the layer thickness of 22 µm and scanning speed of 500 mm/s.

Power, W	Top sintering contour	Cross-sectional sintering contour	Temperature contour
65	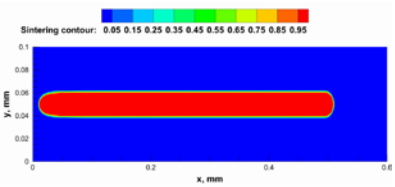	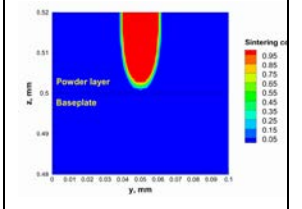	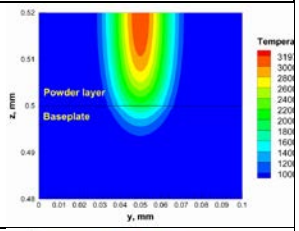
	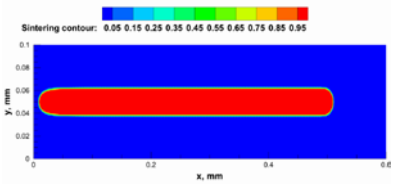	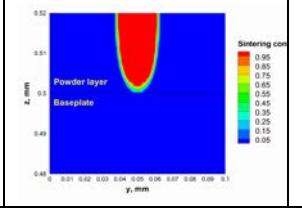	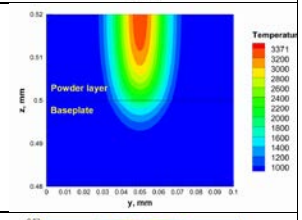
75	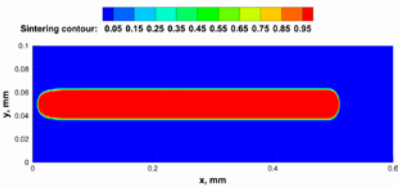	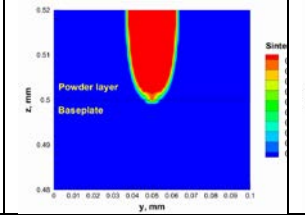	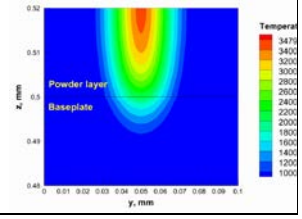

For a layer thickness of 30 µm, the same approach as for a layer thickness of 22 µm was followed, where the developed numerical model was employed to test various laser power ranges until a range that satisfied the previously mentioned conditions was identified. Notably, with a scanning speed of 100 mm/s, the laser power range had to be lower than the lowest value the printer could deliver. However, as stated in Table 7.5, the laser power range has been increased to be between 30 and 40 W, above the minimum value of 30 W. In addition, it was found that this laser power range generated a temperature value that exceeded the decomposition point of SiC, as was the case with a layer thickness of 22 µm. This could cause SiC to decompose, but as laser scanning is a highly rapid process, there may not be enough time for this to occur. XRD analysis was used to analyze this issue in the following subsections.

For a scanning speed of 250 mm/s, as indicated in Table 6.7, the appropriate laser power range was found to be 45 to 55W, and this power range also generated a maximum temperature above the SiC decomposition point. However, the region that experienced temperatures beyond SiC's decomposition point is deemed small and did not represent a substantial surface defect. Moreover, as shown in Table 7.6, the calculated laser power range could barely penetrate the layer beneath to create a good adhesion between layers. This suggests that increasing the sintering speed may negatively affect the printing process's success. Lastly, for a scanning speed of 500 mm/s, a laser power range of 65 to 85 W was established, as given in Table 7.7, resulting in a maximum temperature above the SiC decomposition limit. In addition, with a sintering speed of 250 mm/s, the laser power range could barely adhere to the current layer beneath the layer. Based on the simulation results shown, it can be concluded that increasing the speed and lower is not recommended due to the defects outlined previously.

Almost the same behaviour observed with a layer thickness of 30 µm was also observed with a layer thickness of 40, where the numerical mode was used to test different laser power ranges with scanning speeds of 100, 250, and 500 mm/s until the previously described conditions were met. Table 7.8 through Table 7.10 summarize the contour obtained at various positions for each scanning speed. With a scanning speed of 100 mm/s, it is clear that the laser power range was able to sinter the entire layer thickness and adhere to the layer below, but the issue of the high temperature exceeding the decomposition of SiC remains a challenge. The laser power range could barely achieve layer adhesion at scanning speeds of

250 and 500 mm/s. An experimental investigation was carried out to test the obtained parameters from the numerical model to obtain the optimal values for the process parameters, which were covered in the coming sections.

Table 7.5. Sintering contour and temperature distribution at different positions for the layer thickness of 30µm and scanning speed of 100 mm/s.

Power, W	Top sintering contour	Cross-sectional sintering contour	Temperature contour
30	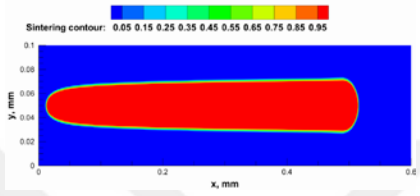	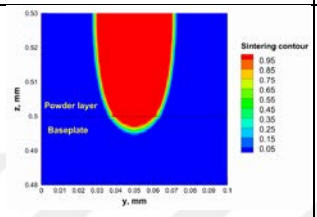	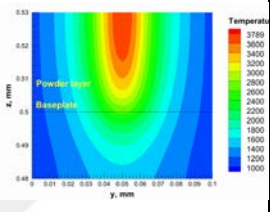
35	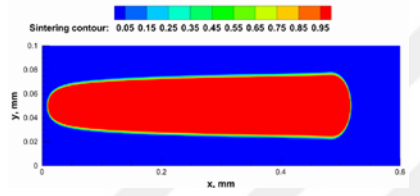	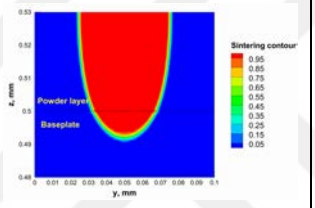	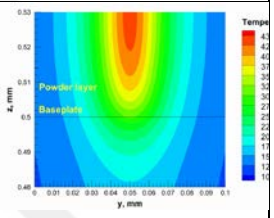
40	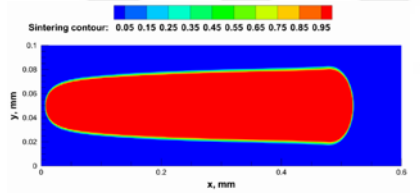	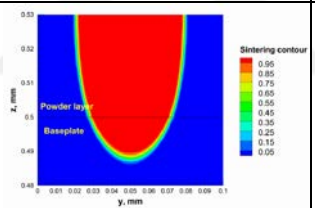	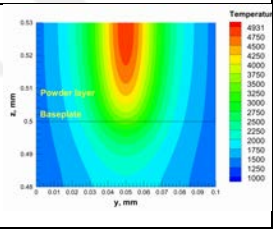

Table 7.6. Sintering contour and temperature distribution at different positions for the layer thickness of 30µm and scanning speed of 250 mm/s.

Power, W	Top sintering contour	Cross-sectional sintering contour	Temperature contour
45	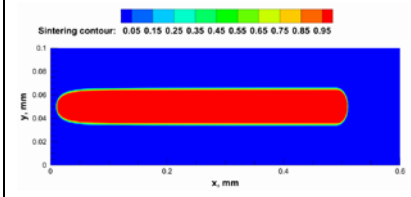	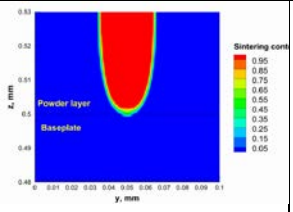	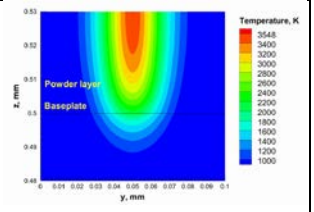
50	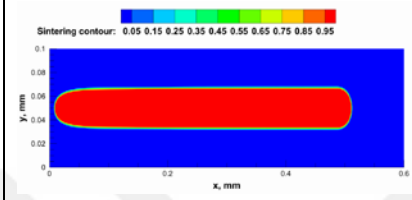	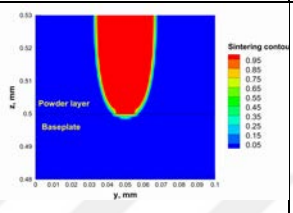	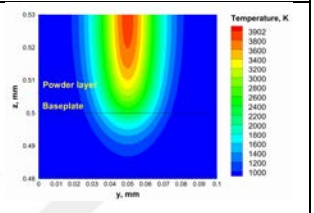
55	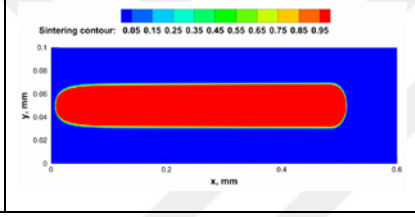	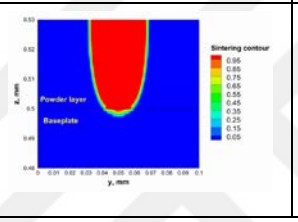	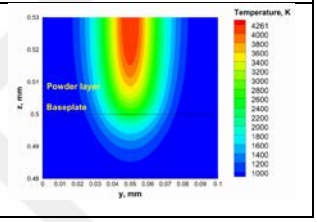

Table 7.7. Sintering contour and temperature distribution at different positions for the layer thickness of 30µm and scanning speed of 500 mm/s.

Power, W	Top sintering contour	Cross-sectional sintering contour	Temperature contour
65	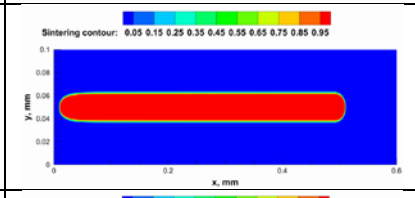	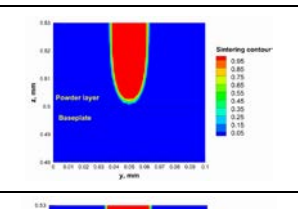	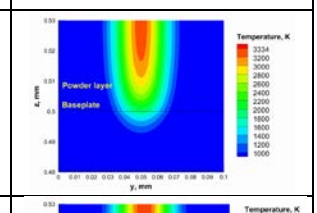
75	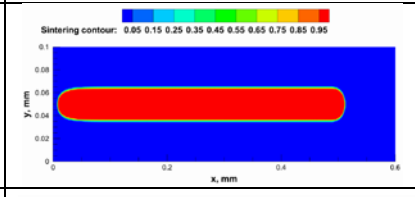	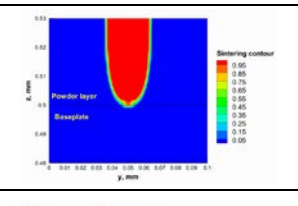	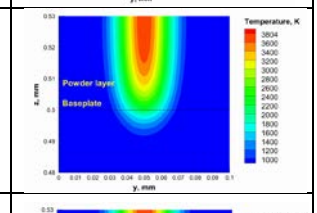
85	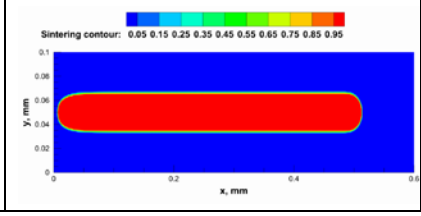	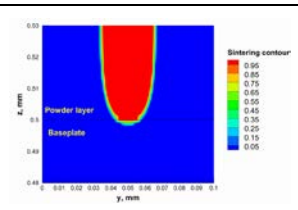	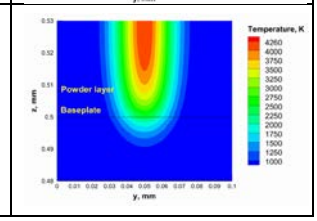

Table 7.8. Sintering contour and temperature distribution at different positions for the layer thickness of 40µm and scanning speed of 100 mm/s.

Power, W	Top sintering contour	Cross-sectional sintering contour	Temperature contour
35	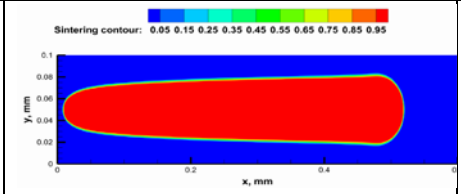	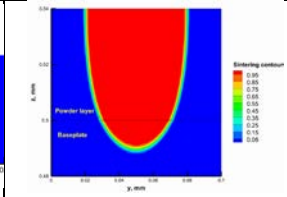	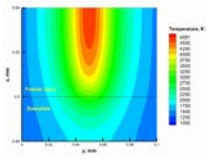
40	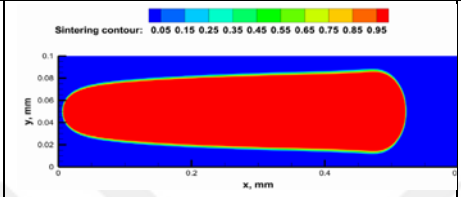	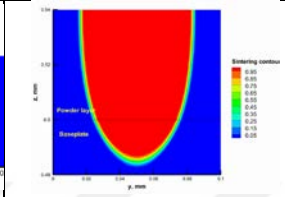	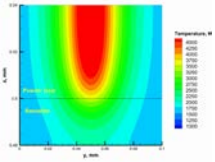
45	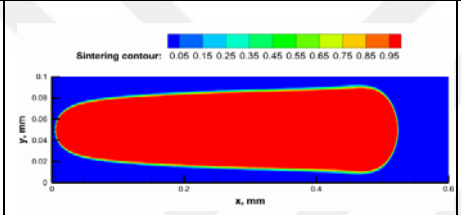	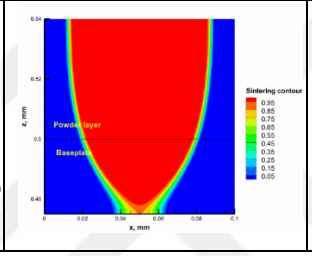	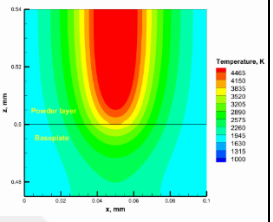

Table 7.9. Sintering contour and temperature distribution at different positions for the layer thickness of 40µm and scanning speed of 250 mm/s.

Power, W	Top sintering contour	Cross-sectional sintering contour	Temperature contour
50	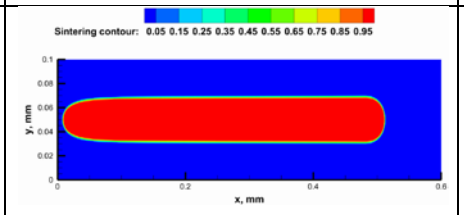	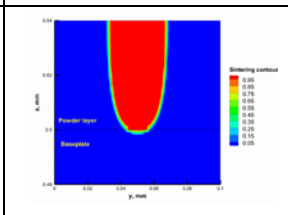	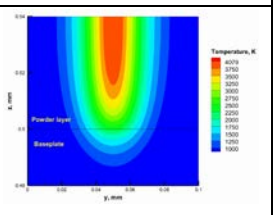
55	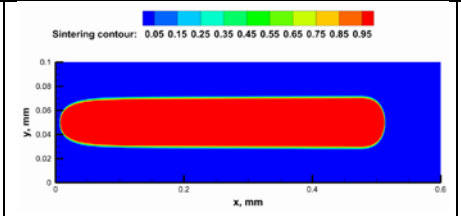	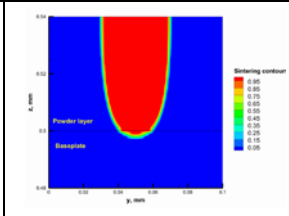	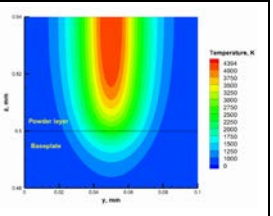
60	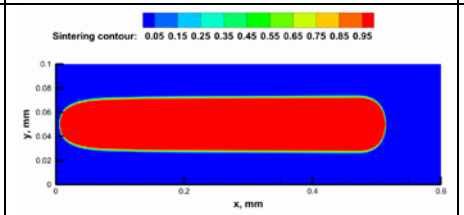	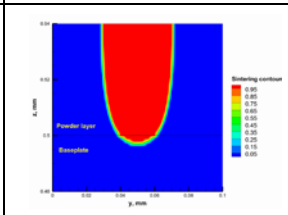	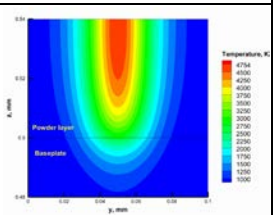

Table 7.10. Sintering contour and temperature distribution at different positions for the layer thickness of 40µm and scanning speed of 500 mm/s.

Power, W	Top sintering contour	Cross-sectional sintering contour	Temperature contour
90	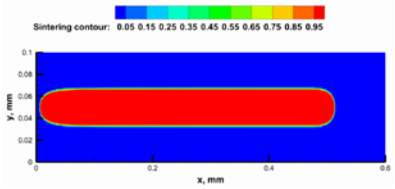	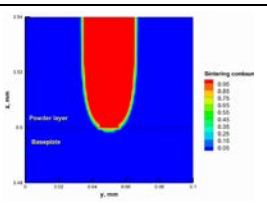	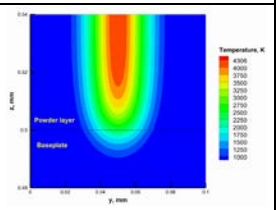
100	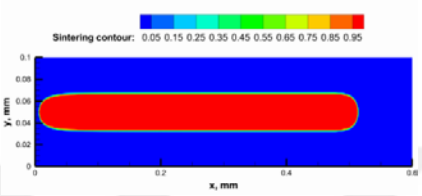	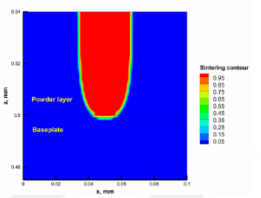	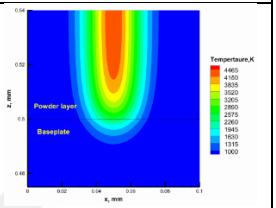
110	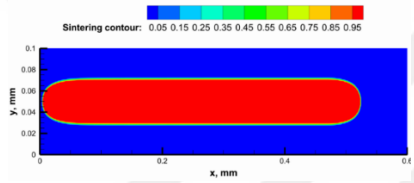	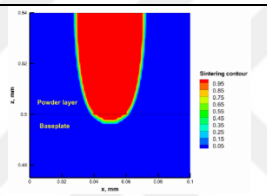	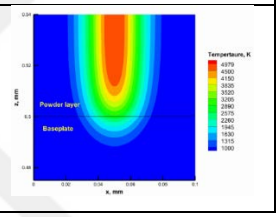

7.2.2. Hatching spacing investigation

Hatching space is another critical parameter that governs the contact between adjacent paths using a large hatching distance value results in unconnected scanning paths, affecting the printed part's mechanical properties. Furthermore, using small hatching distance values increases the building time and heat accumulated inside the part during construction. As a result, selecting the proper hatching distance value is critical.

The developed model was used to predict the appropriate hatching space value by simulating multiple scanning paths with the laser power calculated from the numerical model, as described in the previous sections for each scanning speed. The hatching space value should be selected to connect the adjacent paths. Different hatching space values were considered, including 100, 75, 50, and 35 µm.

Table 7.11 and Table 7.12 show the sintering contour for multiple scanning paths on the layer top surface at different temperatures of 100, 250, and 500 mm/s with different hatching space values.

It can be seen that when hatching spaces of 100, 75, and 50 µm were used, the adjacent paths were not connected, whereas when hatching space of 35 µm was used, the adjacent paths were almost connected with all investigated scanning speeds. As a result, a hatching space of 35 µm is recommended for D-PBSLP of SiC, and this value was considered in all subsequent investigations on D-PBSLP of SiC in this dissertation.

Table 7.11. Sintering contour for multiple scanning paths using 100 and 75 µm hatching space for D-PBSLP of SiC using 30 µm layer thickness and different scanning speeds.

Hatching space, µm	Scanning speed, mm/s		
	100	250	500
100	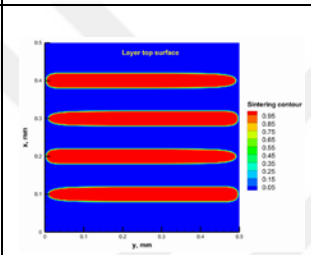	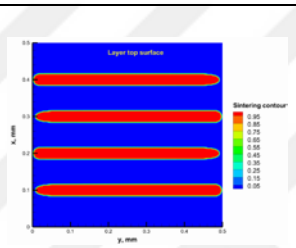	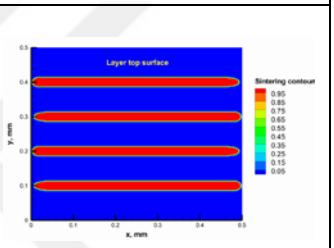
75	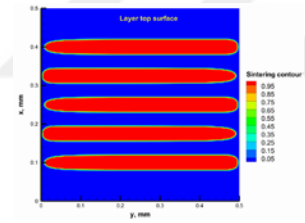	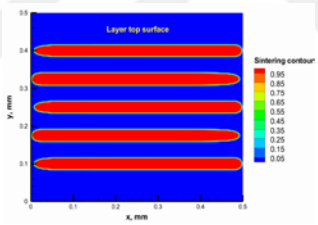	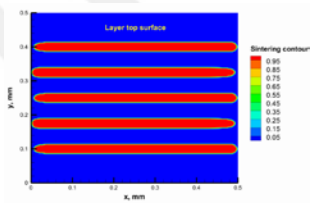

Table 7.12. Sintering contour for multiple scanning paths using 50 and 35 µm hatching space for D-PBSLP of SiC using 30 µm layer thickness and different scanning speed.

Hatching space, µm	Scanning speed, mm/s		
	100	250	500
50	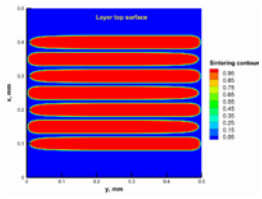	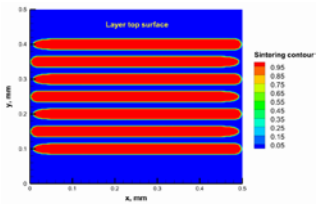	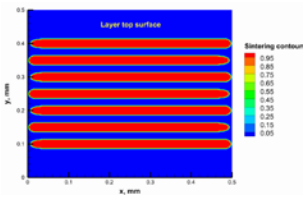
35	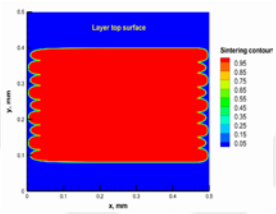	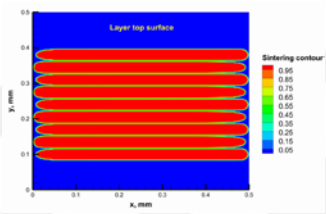	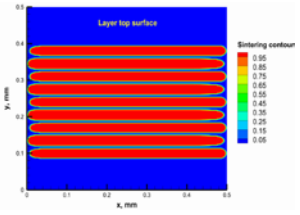

7.2.3. Scanning strategies investigation

For the D-PBSLP of SiC to be successful, it is crucial to choose the appropriate scanning strategy. The scanning strategy is regarded as one of the most crucial parameters in the PBSLP technique, as it controls the laser movement on the layer surface, heat distribution within the layer, thermal stress development, and the obtained mechanical and physical properties. As described in section 5.2, an improper scanning strategy can result in printing failure.

This section analyzed the effect of scanning strategies on SiC's D-PBSLP and determined the optimal scanning strategy. Various scanning strategies, as described previously in chapter 2, such as linear, zigzag, concentric in-out, and hexagonal, were evaluated. Four SiC samples (10×10×8 mm3) were 3D-printed using a numerical model's parameters. These parameters are 100 mm/s scanning speed, 32 W of laser power, a hatching distance of 35 µm, and a layer thickness of 22 µm. Figure 7.6 demonstrates the printed samples. The samples were successfully printed using the parameters obtained from the numerical model, demonstrating the power of the numerical model to predict the appropriate process parameters even for difficult-to-print materials, such as SiC, using the D-PBSLP technique.

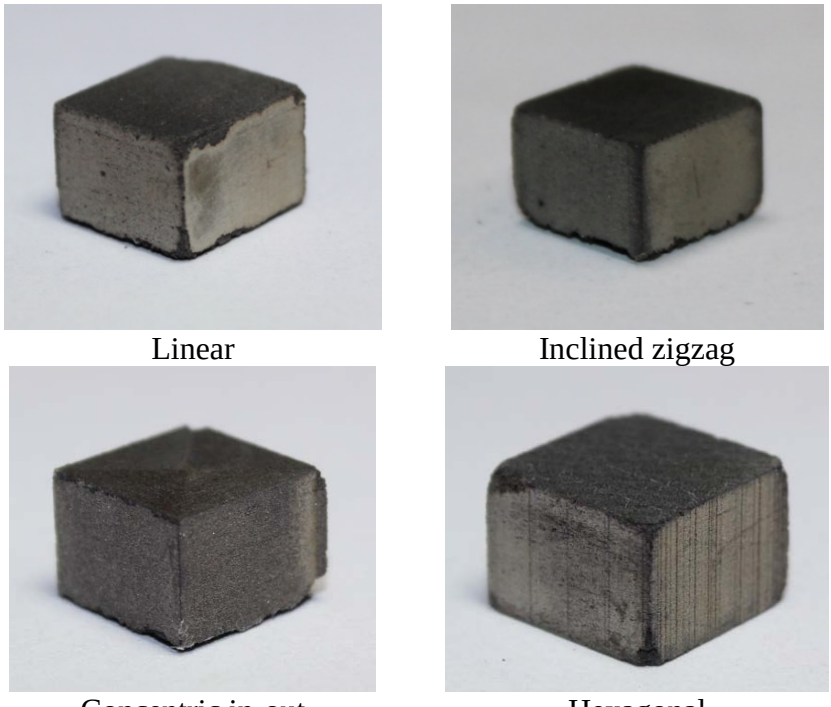

Figure 7.6. SiC samples printed using the process parameters obtained from the numerical model with different scanning strategies.

Figure 7.7 illustrates the outcomes of the optical microscopy (VKX-250, Keyence, Japan) examination of the top surface of samples. These high-quality optical microscopy images make it simple to discern the laser tracks that follow the employed scanning strategy. In addition, numerous flaws on the layer top surface of the samples can be readily identified.

On the top surface of the concentric in-out strategy, two intersecting lines form an "X" and a minor defect in the form of a small hole in the center of the "X.", as the case with the concentric out-in strategy when used for the D-PBSLP of alumina. This result can be interpreted by simulating the scanning strategy with the developed numerical model to determine what happened during the scanning procedure.

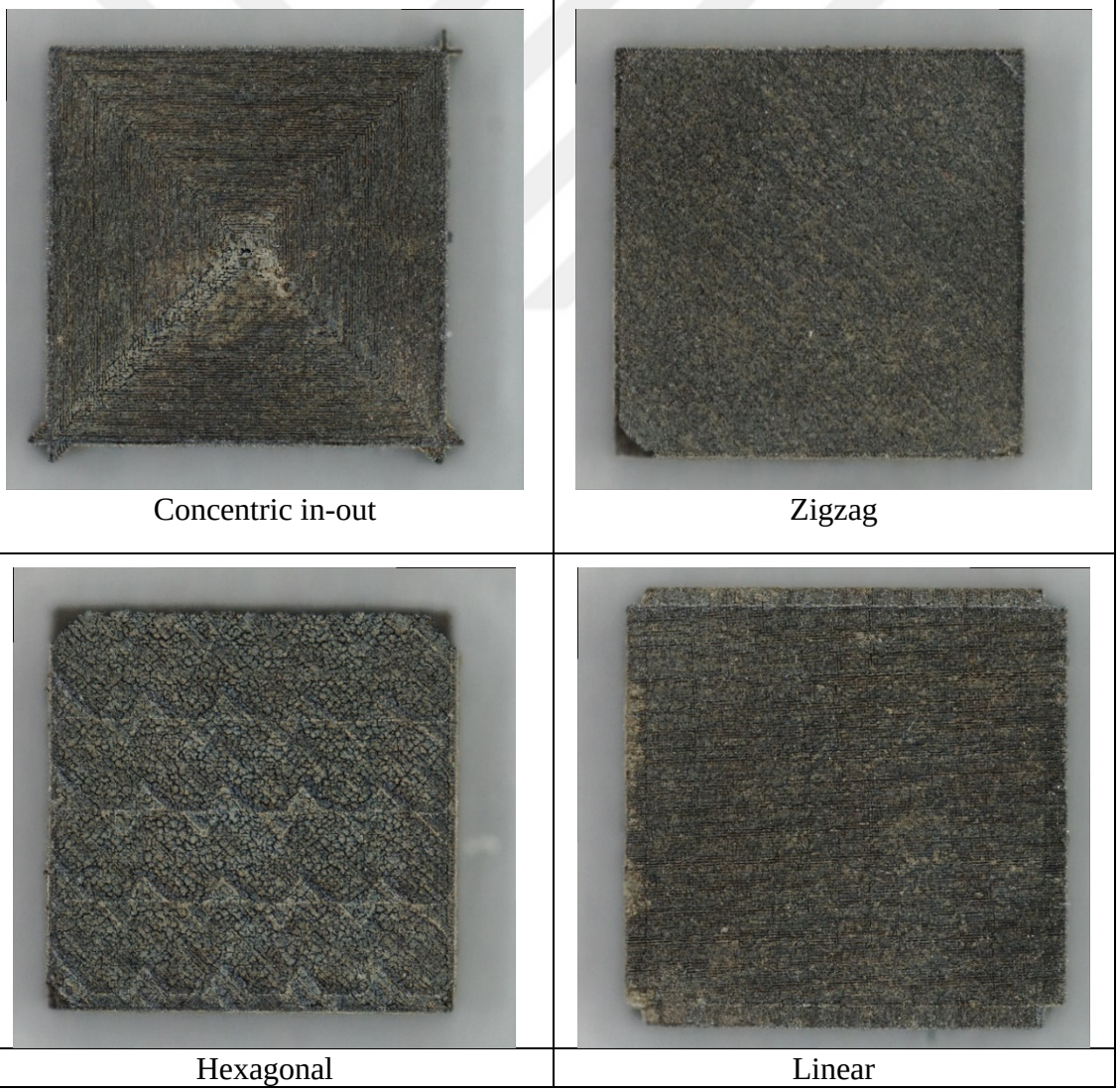

Figure 7.7. 3D microscope images for SiC samples top surface printed using different scanning strategies.

At the beginning of the scanning, high-temperature peaks were observed in the temperature history. These peaks result from the initial short scanning paths that led to the formation of the sample center hole (the dashed red circle). In addition, the temperature peaks were repeated regularly along the temperature history due to the rotation of the laser beam when changing its direction, leading to the formation of the "X" mark on the top surface of the sample. Figure 6.8 illustrates the maximum temperature history during scanning with a concentric in-out strategy for only approximately 70 ms.

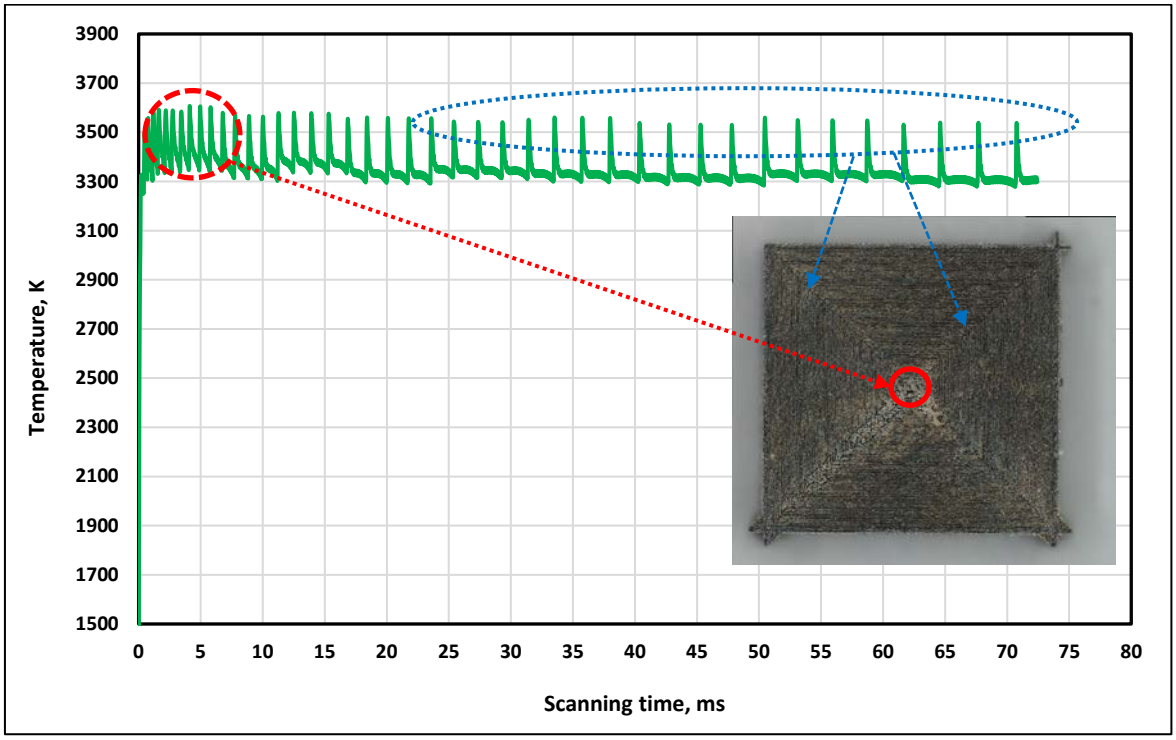

Figure 7.8. The maximum temperature history for the concentric in-out strategy.

For the zigzag scanning strategy, as seen in Figure 6.7, the sample was printed with acceptable geometric forms, a smooth flat surface, and straight dimensions, indicating that it is very promising for D-PBSLP of SiC parts. In addition, the specimen has a flat surface without any particular pattern, as with the concentric in-out strategy. Based on visual inspection, the surface porosity level is low relative to the concentric in-out scanning strategy. Initially, the zigzag strategy appears to be superior to the concentric in-out scanning strategy, but it is evident that the corners of the specimens are imperfect. The defects at the specimen's corners are visible as small material removal or dull corners.

The numerical model was used to simulate this scanning strategy to determine what was happening and causing the corner defects. Figure 7.9 depicts the inclined zigzag technique's temperature history (limited paths to conserve computational time). When the laser completed a path and was repositioned to scan a new path, the temperature rose dramatically (peaks-up). As for the zigzag strategy, the new position of the laser beam was very close to the end of the previously scanned path, which maintains some heat and causes a sharp temperature rise. The temperature began to drop as the laser beam moved along the new route. In addition, the path scanning time increased gradually as the scanning path length grew longer due to the scanning inclination.

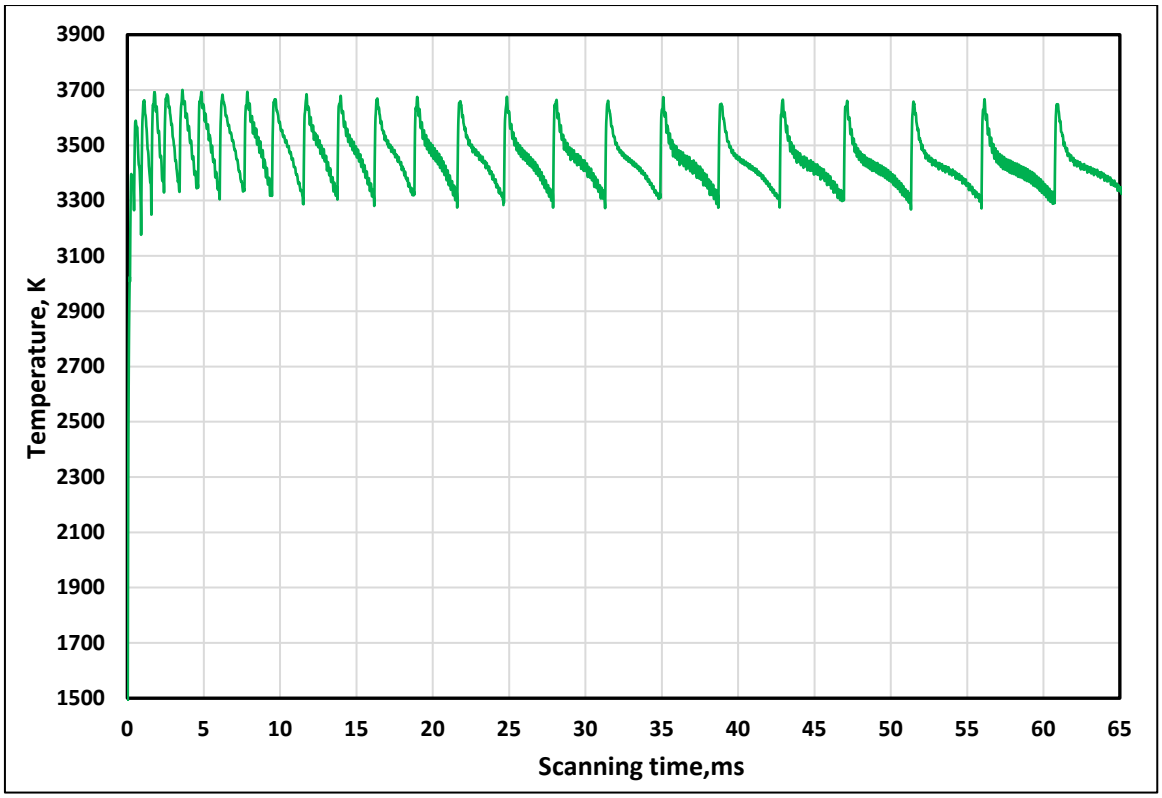

Figure 7.9. The maximum temperature history for the inclined zigzag scanning strategy (only 25 paths are considered to make the figure clear).

Regarding the hexagonal scanning strategy, the specimen has a well-defined square shape, except for small hexagonal patterns visible on the surface of the top layer (Figure 7.7). In addition, porosities appear as small holes dispersed across the top surface.

The numerical model was used to simulate the hexagonal scanning strategy, and the obtained temperature history is depicted in Figure 7.10. After scanning the hexagon's interior (using

the zigzag strategy) began scanning its perimeter. In this scanning strategy, the sharp increase in temperature when the laser starts a new path is also a concern. The border scanning temperature history is significantly lower than the zigzag scanning within the hexagon. This is primarily due to the long and continuous paths of border scanning compared to the shorter paths of zigzag scanning. The increase in temperature caused by the zigzag effect occurred within the sample surface and did not affect the edges, as was the case with other scanning strategies, including zigzag.

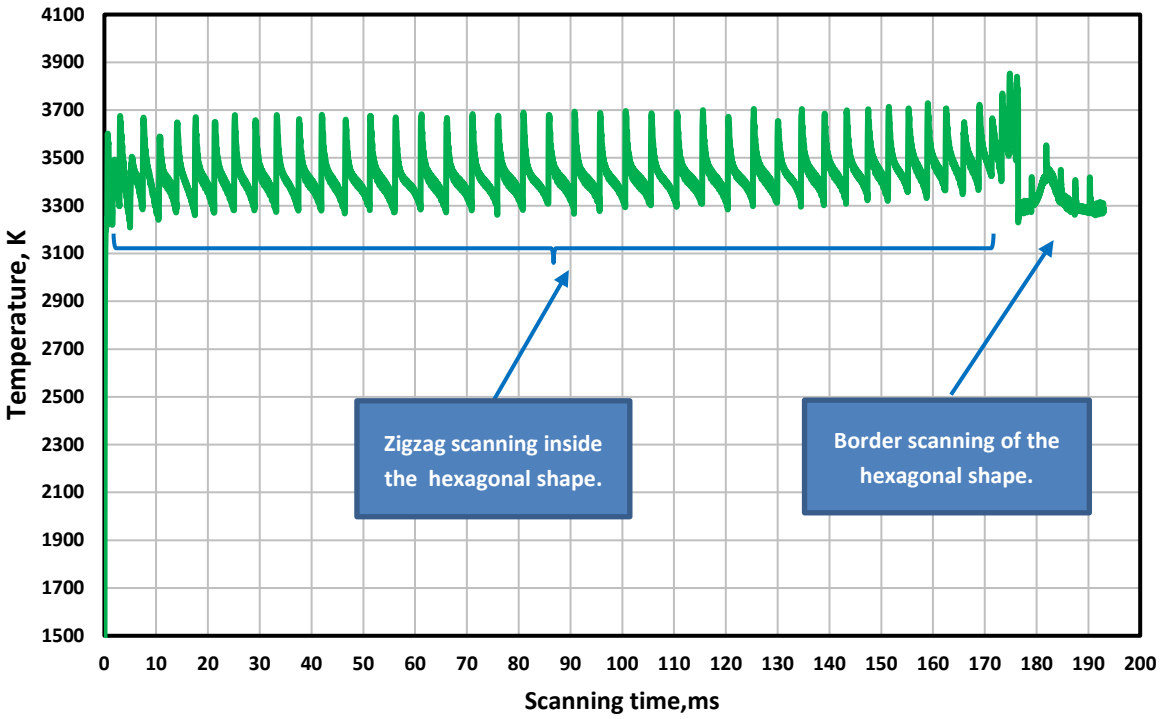

Figure 7.10. Maximum temperature history obtained with the hexagonal scanning strategy.

For the linear scanning strategy, a large number of defects exhibited as destroyed edges and pores. Also, as is evident in Figure 7.7, shifting between layers occurred, which is considered a serious issue as it will significantly impact the obtained mechanical performance and the dimensional accuracy of the printed part. Figure 7.11 depicts a magnified image of the sample corners where the shifting is highly noticeable.

Figure 7.11. Shifting at the linear scanning strategy at; the top-left corner (a), and bottom-right corner (b).

By analysing the maximum temperature history obtained using the numerical model depicted in Figure 7.12, it is possible to determine that temperature peaks are down at the beginning of each scanning path. This is primarily due to the laser-driven-off time (the time it takes to reach the next scanning position while it is turned off) and the time it takes for the laser to raise the powder's temperature to the sintering point.

Primarily, shifting can occur when successive layers are not correctly adhered to one another; therefore, the force generated by the recoater when depositing a new layer can be sufficient to cause shifting. Focusing on the temperature history for this scanning strategy, where the temperature during scanning is approximately 3200 K, makes this evident. This temperature is merely adequate to sinter the employed layer thickness (22 µm) with weak adhesion to the layer beneath. This shifting did not occur with previous scanning strategies due to the temperature peaks-up during scanning, which helped the current scanned layer adhere to the layer beneath and provide sufficient support to withstand the force exerted by the recoater. In the linear strategy, no temperature peaks-up were formed during scanning, so this did not occur. It is not advisable to increase the laser power to eliminate this shift in the linear strategy, as this will place the laser temperature well above the SiC decomposition point.

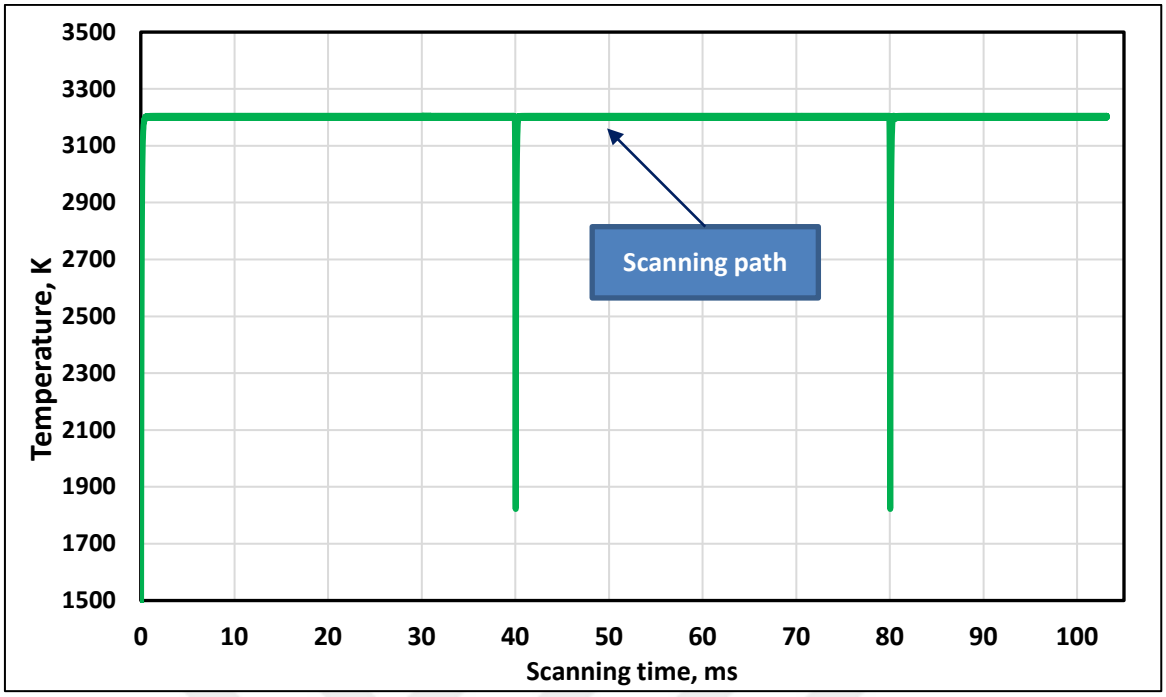

Figure 7.12. The maximum temperature history during the linear scanning strategy.

The developed numerical model was also used to interpret this finding by simulating the scanning strategies and obtaining the sintering contour at various positions, as depicted in Figure 7.13, which shows the sintering contour for the concentric, inclined zigzag, and linear strategies at the layer top surface at cross-section planes to check the sintering depth. For linear strategy, as seen from the cross-section at x = 0.1 mm plane, the adhering between the current scanned layer and the layer below did not happen (or was very weak), and this is another interpretation for the shifting between layers that happened in this scanning strategy. The adhering between the layer and the layer below is evident for the other scanning strategies, so no shifting was noticed in these strategies. Also, regarding the adhering depth, the zigzag strategy achieved higher adhering depth than other scanning strategies.

Figure 7.14 illustrates the 3D surface morphology obtained by an optical microscope (KEYENCE VR-3000). The concentric in-out strategy has a distinctive "X"-shaped pattern on the top surface of the layer, as described previously. Both the zigzag and linear strategies have a surface that is flat and devoid of any specific pattern. Due to the small hexagons formed by the scanning strategy, the hexagonal scanning strategy produced a surface that was not flat.

Figure 7.15 depicts the results of measuring the surface roughness with the optical microscope (VKX-250, Keyence, Japan) to determine the effect of scanning strategies on the top surface roughness. It can be seen that linear and zigzag scanning strategies achieved the lowest surface roughness. In contrast, concentric and hexagonal scanning strategies obtained high surface roughness values due to the characteristic patterns presented on the layer's top surface for each, as previously described.

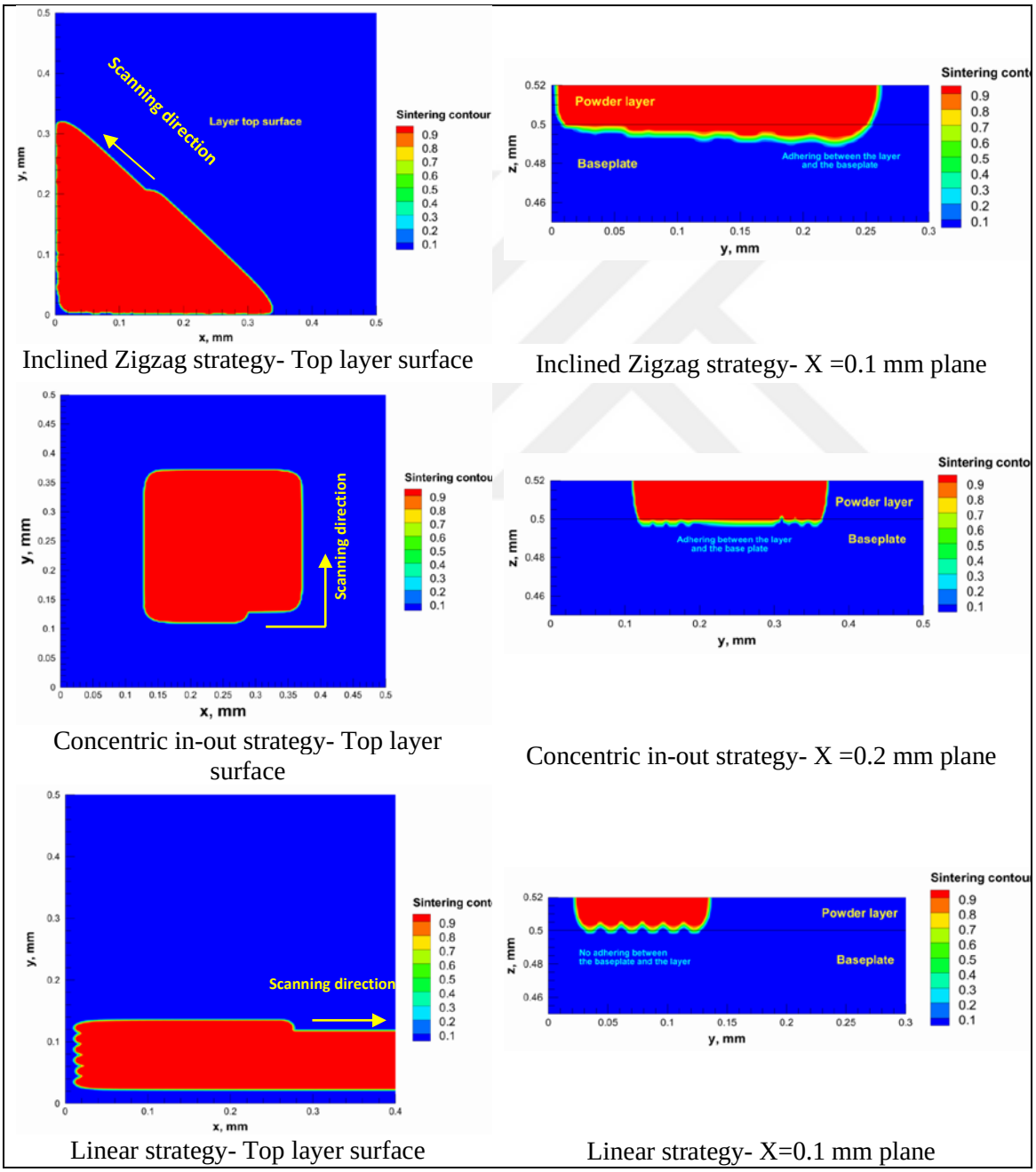

Inclined Zigzag strategy- Top layer surface

Inclined Zigzag strategy- X =0.1 mm plane

Concentric in-out strategy- Top layer surface

Concentric in-out strategy- X =0.2 mm plane

Linear strategy- Top layer surface

Linear strategy- X=0.1 mm plane

Figure 7.13. The progress of the sintering contour with different scanning strategies at the top layer surface and vertical cross-section (as specified below each contour).

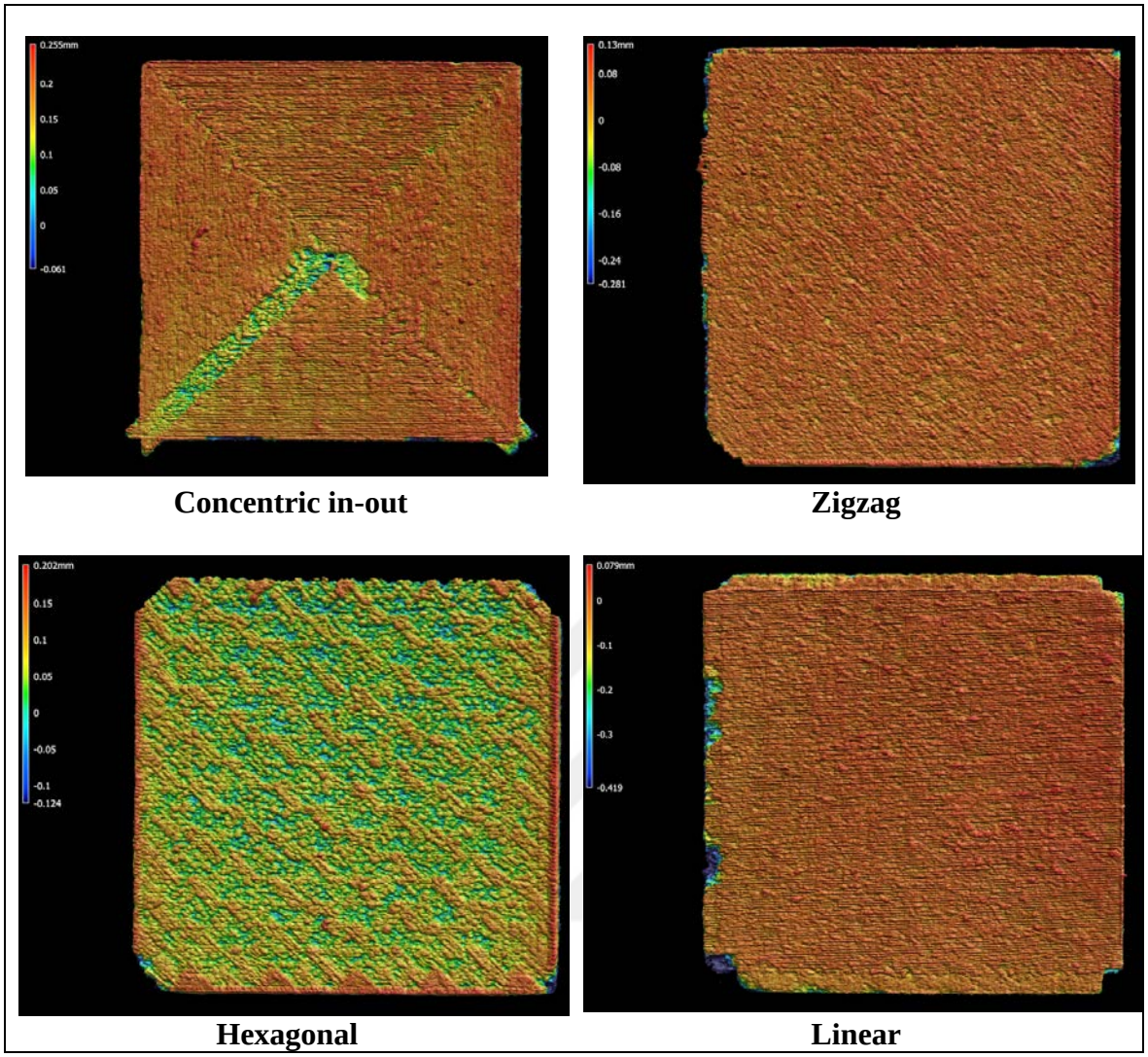

Figure 7.14. 3D Surface morphology for the SiC samples produced using different scanning strategies.

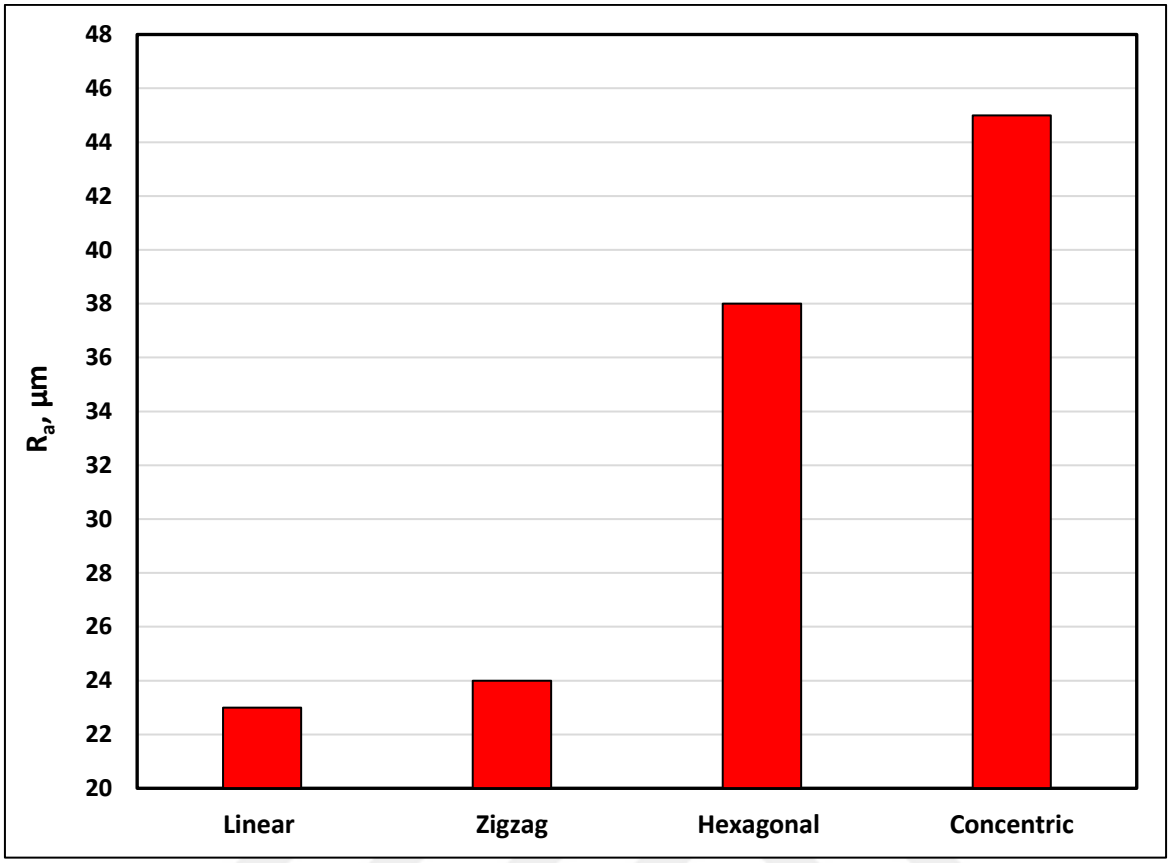

Figure 7.15. Surface roughness measured at the top layer surface for different scanning strategies.

The effect of scanning strategies on the obtained relative density of SiC was analyzed, and the outcomes are depicted in Figure 7.16. All scanning strategies gave a relative density value that was nearly identical. The relative density achieved by the zigzag and hexagonal strategies was 81.5 and 82.5%, respectively. The linear and concentric strategies successfully achieve relative density values of 76.5 and 80 %, respectively.

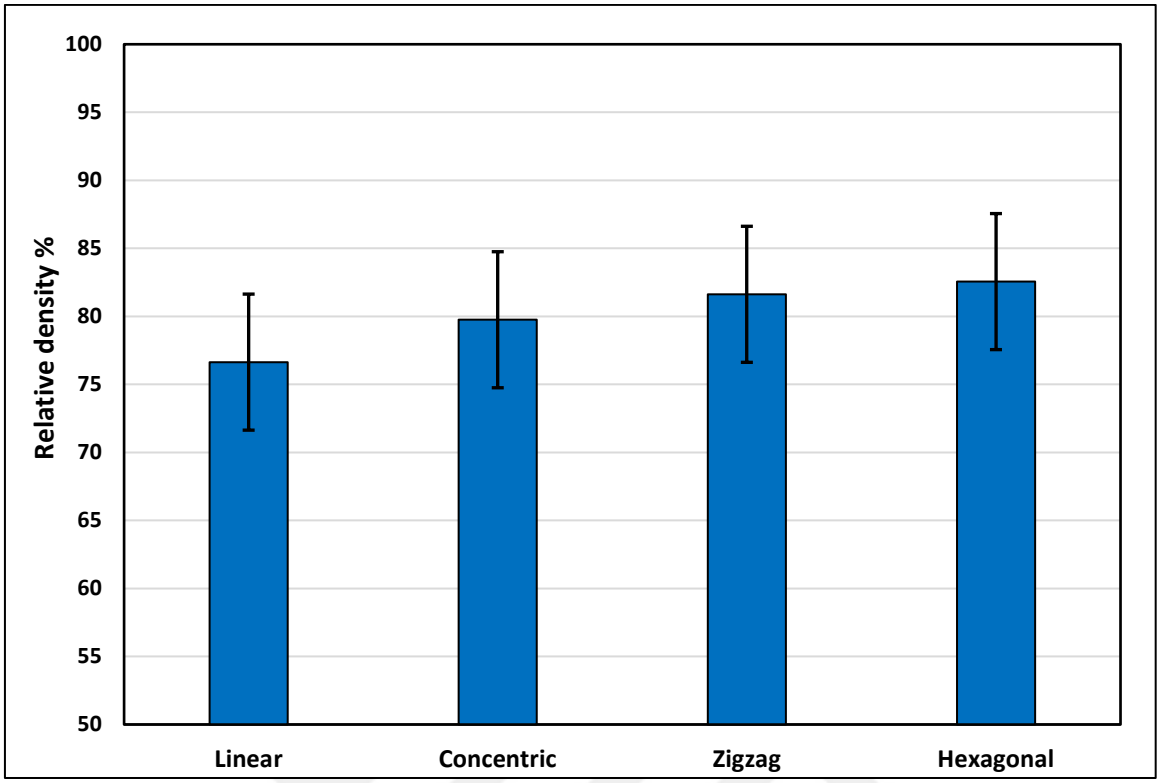

Figure 7.16. Relative density for SiC samples printed with different scanning strategies.

The morphology of SiC samples' top surfaces printed using hexagonal, zigzag, and concentric in-out scanning strategies was evaluated using SEM images, as seen in Figure 7.17. The SEM images revealed that the SiC particles were sintered in all the scanning strategies, and the laser sintering paths were visible. In addition, the porosity distribution on the top surface can be seen. There was no discernible pattern on the surface of sintered hexagonal and zigzag strategies. In the case of a concentric in-out strategy, the laser tracks on the top surface of the layer and the position of the laser's rotation are obvious. There are no cracks in any strategy.

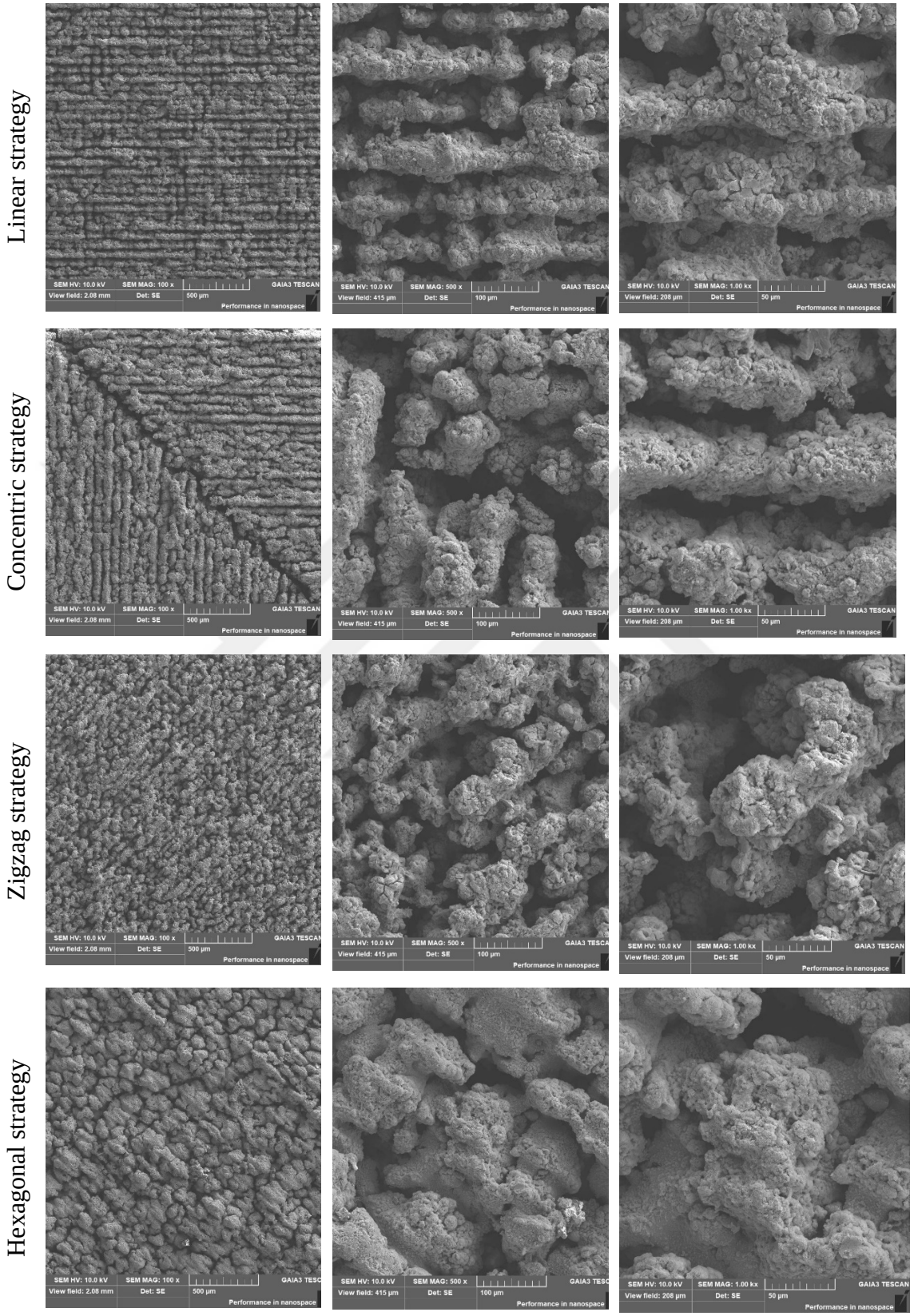

Figure 7.17. SEM images for SiC samples printed using different scanning strategies.

Since the previously presented physical characterizations and SEM images confirm that a certain amount of porosity is still present within the samples, it is essential to examine the internal structure and porosity distribution inside the SiC samples using Micro-CT. SiC samples printed with the hexagonal and zigzag scanning strategies were the only ones considered for The Micro-CT analysis because their relative density was superior to that of the other scanning strategies.

Figure 7.18 demonstrates that the Mico-CT images of a SiC sample printed with a zigzag scanning strategy reveal a uniform structure and low porosity distribution throughout the sample. In addition, the sample's internal structure was examined from various vertical and horizontal planes (Figure 7.19 and Figure 7.20), which revealed a well-distributed material within the sample. There is no visible defect at the interface between layers, indicating that the adhesion is quite strong.

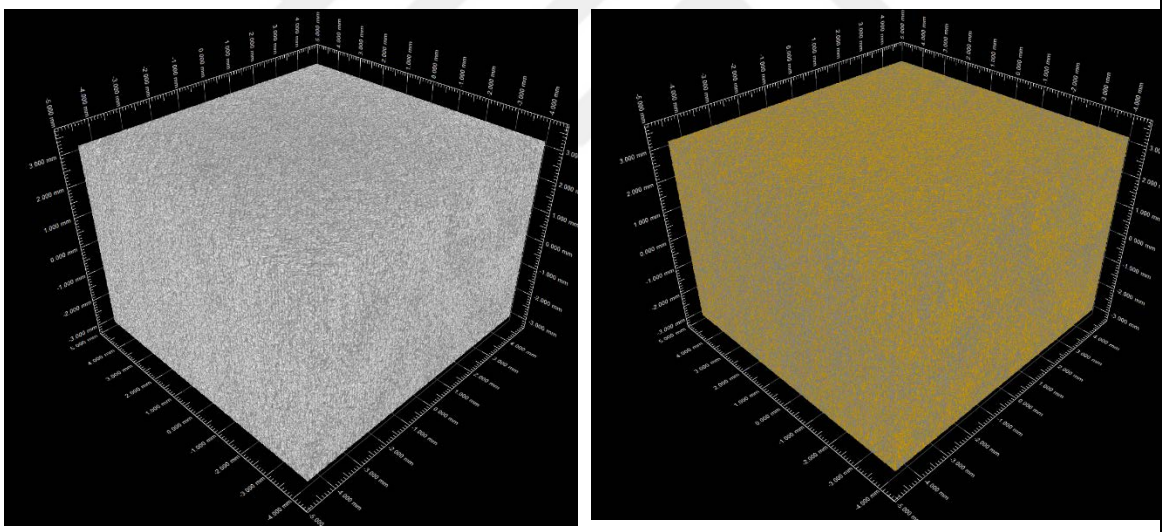

(a) (b)

Figure 7.18. Micro-CT for the SiC sample printed using Zigzag scanning strategy: 3D volume of the Alumina sample (a), the 3D volume of the Alumina sample and the porosity filled with yellow (b).

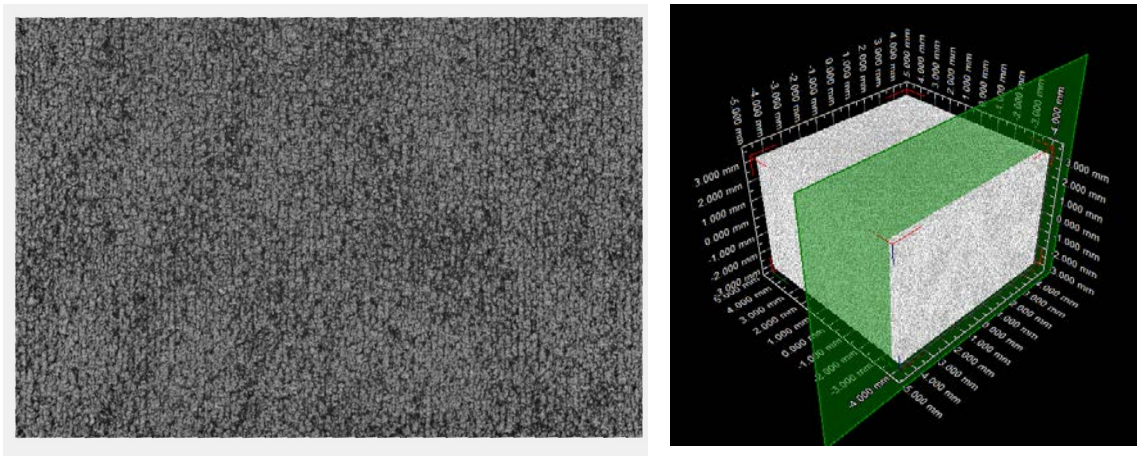

The vertical surface at the front of the sample

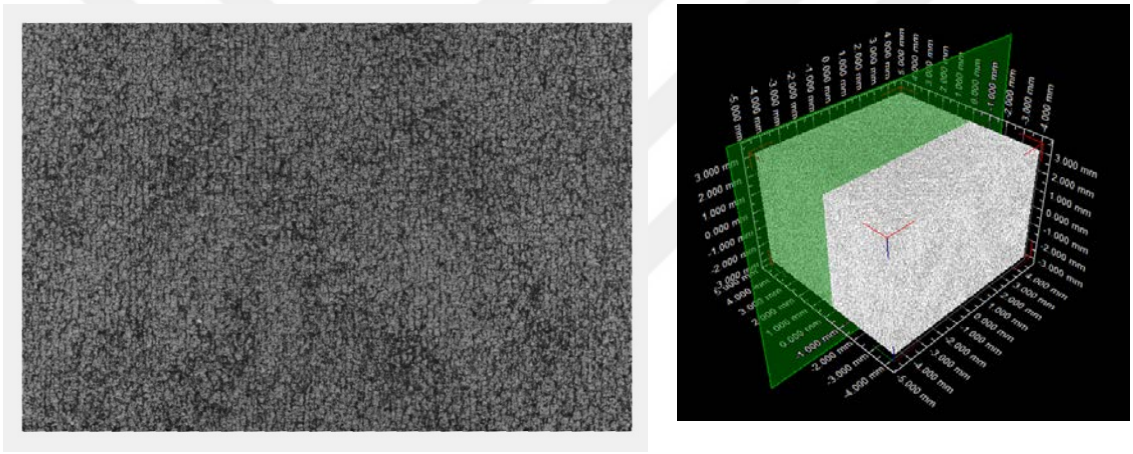

The vertical surface in the middle of the sample

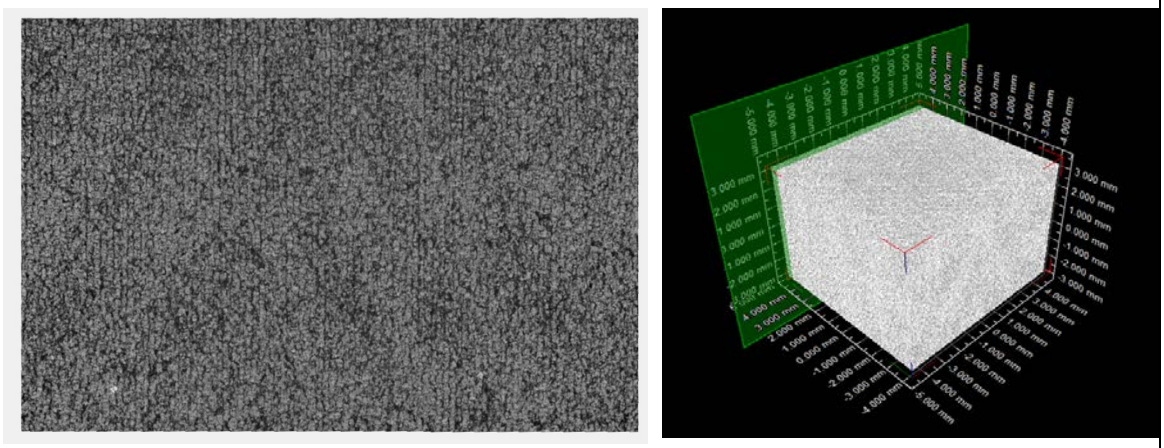

The vertical surface at the back of the sample

Figure 7.19. Porosity distribution at different vertical planes through the SiC sample (printed using the Zigzag strategy), as indicated in the 3D volume representation.

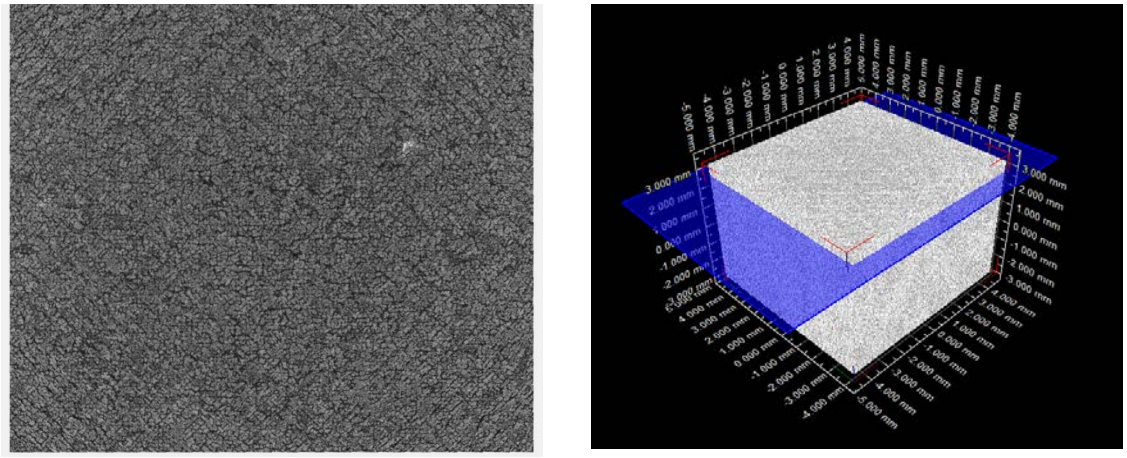

The horizontal surface at the top of the sample

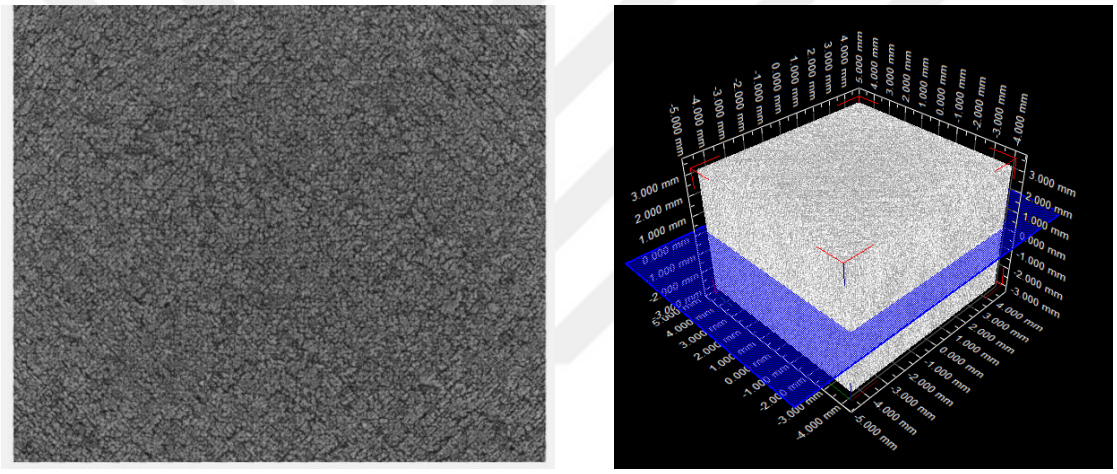

Horizontal in the middle of the sample

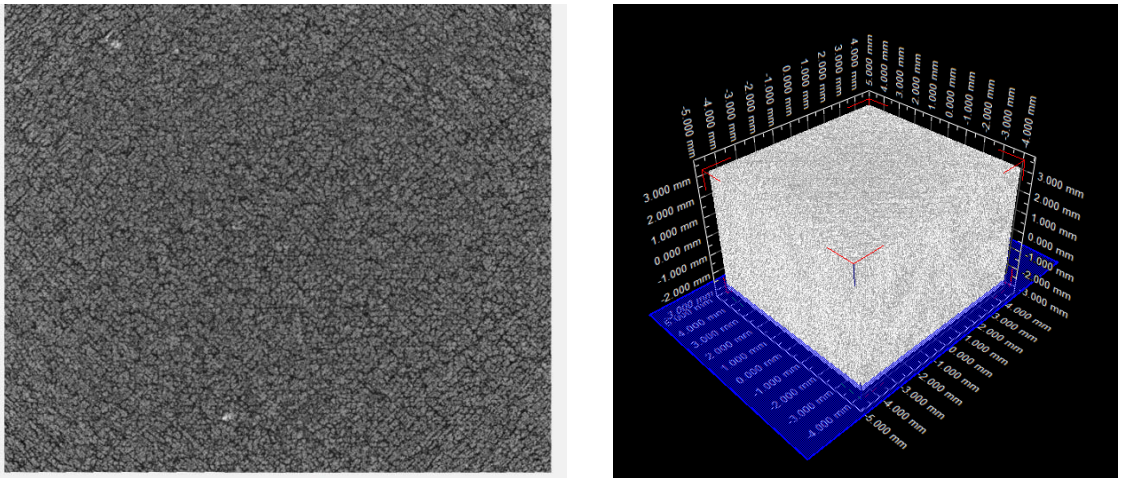

The horizontal surface at the bottom of the sample

Figure 7.20. Porosity distribution at different horizontal planes through the SiC sample (printed using the Zigzag strategy), as indicated in the 3D volume representation.

Figure 7.21 demonstrates that there is no significant difference between the micro-CT analysis of a SiC sample printed with a hexagonal scanning strategy and a SiC sample printed with a zigzag scanning strategy, only a lower porosity level. The Micro-CT for the hexagonal scanning strategy reveals that the SiC sample printed with a hexagonal scanning strategy has a uniform structure and low porosity distribution throughout the sample. In addition, the sample's internal structure was examined from various vertical and horizontal planes, as depicted in Figure 7.22 and Figure 7.29, revealing a material evenly distributed within the sample. There is no visible defect at the layer interface, indicating that the adhesion is quite robust.

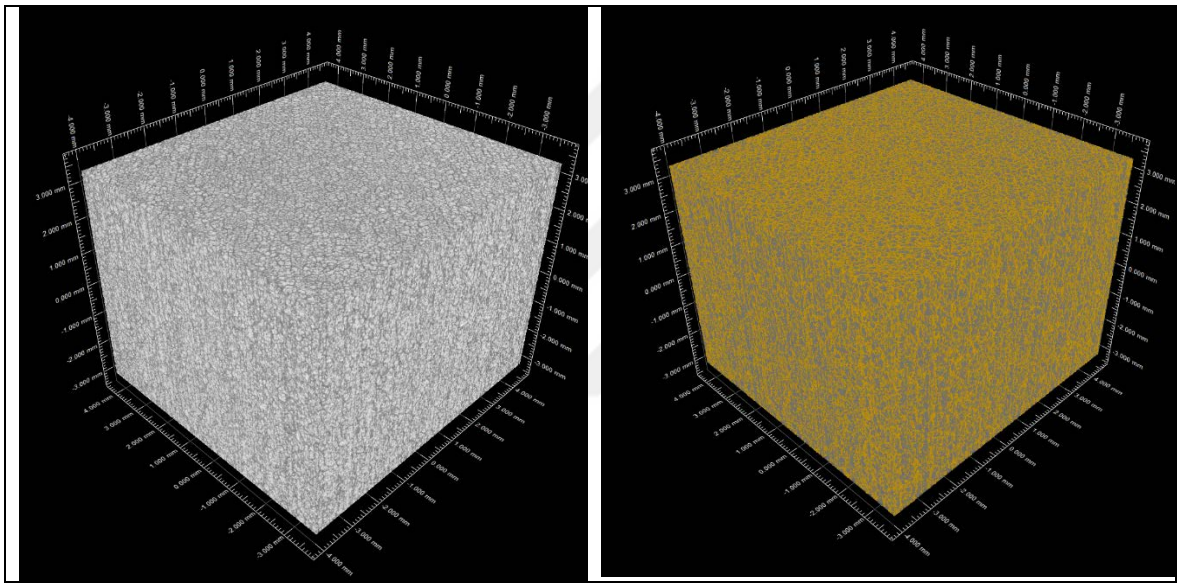

(a) (b)

Figure 7.21. Micro-CT for the SiC sample printed using hexagonal scanning strategy: 3D volume of the Alumina sample (a), the 3D volume of the Alumina sample and the porosity filled with yellow (b).

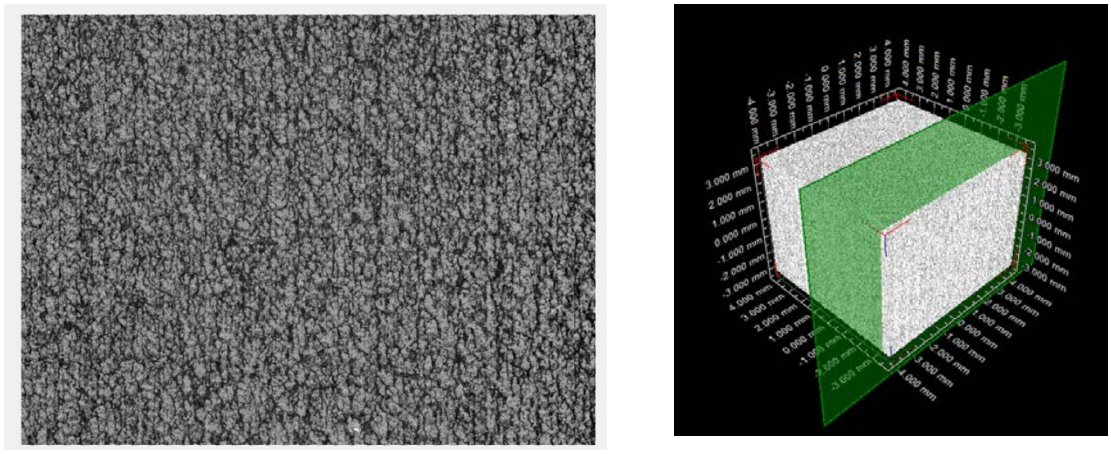

The vertical surface at the front of the sample

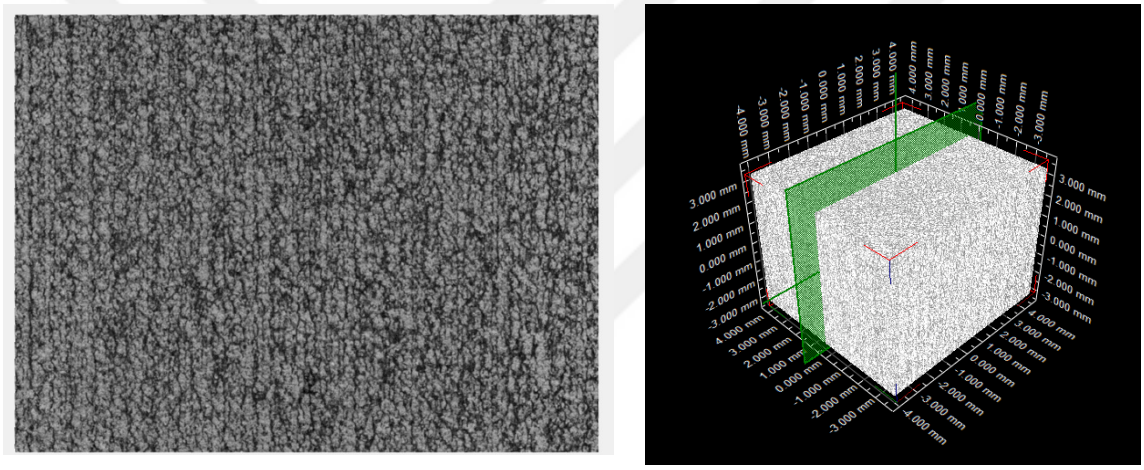

The vertical surface in the middle of the sample

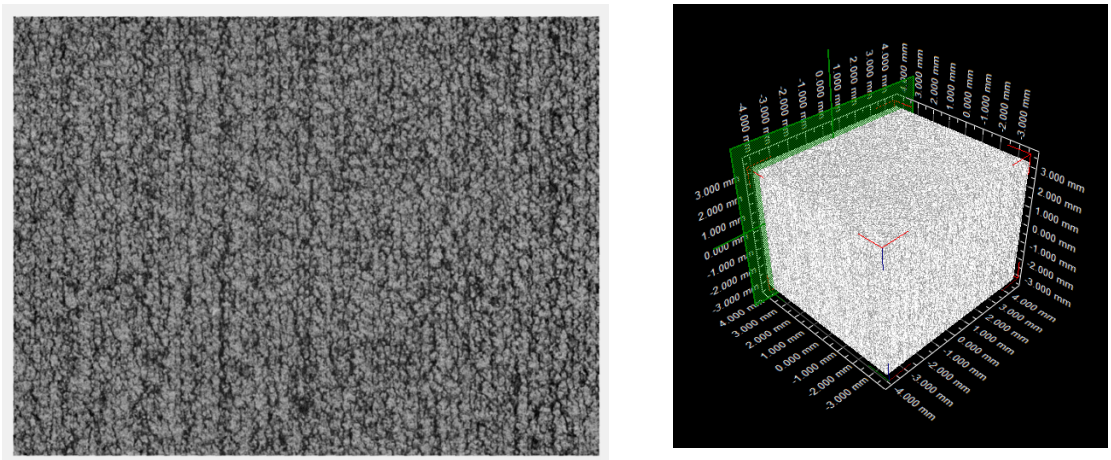

The vertical surface at the back of the sample

Figure 7.22. Porosity distribution at different vertical planes through the SiC sample (printed using the Zigzag strategy), as indicated in the 3D volume representation.

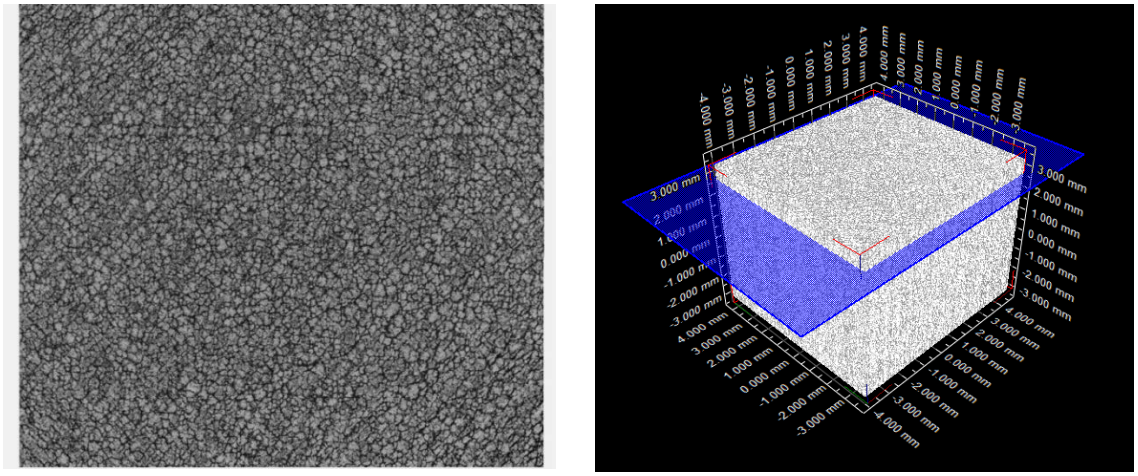

The horizontal surface at the top of the sample

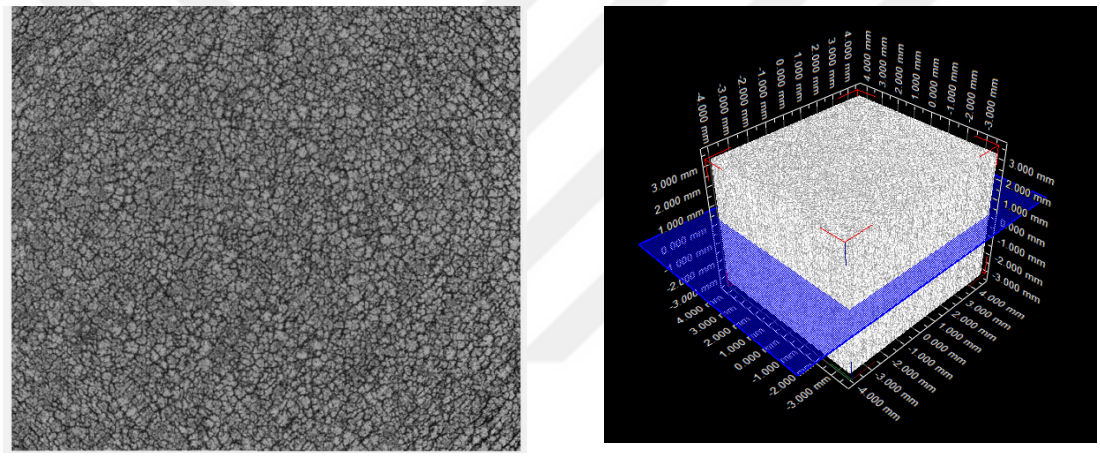

The horizontal in the middle of the sample

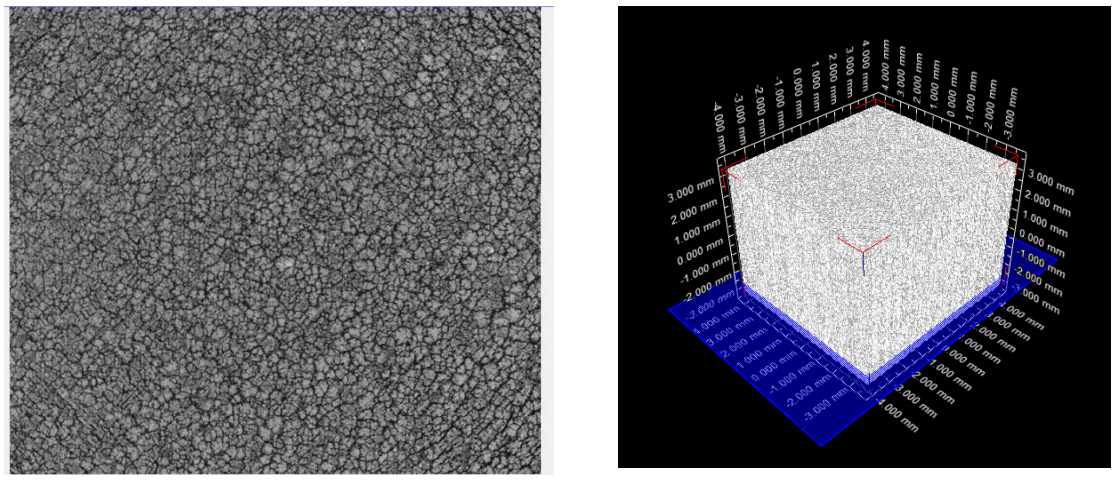

The horizontal surface at the bottom of the sample

Figure 7.23. Porosity distribution at different horizontal planes through the SiC sample (printed using the Zigzag strategy), as indicated in the 3D volume representation.

Since the temperature history for SiC samples printed using different scanning strategies demonstrated that there were temperature peaks during the scanning process, it is important to check the phases inside the SiC printed sample. Figure 7.24 depicts the X-ray diffraction spectrum of the initial SiC powder used in this study and the SiC sample produced by D-PBSLP using a zigzag strategy. SiC powder's XRD spectrum reveals that only SiC Moissanite 6H and 3C exist, whereas the D-PBSLP SiC sample contains SiC phases, silicon, and carbon. This indicates a partial decomposition, which was anticipated due to the peaks of high temperature during scanning at the beginning of a new path, as shown in Figure 7.9.

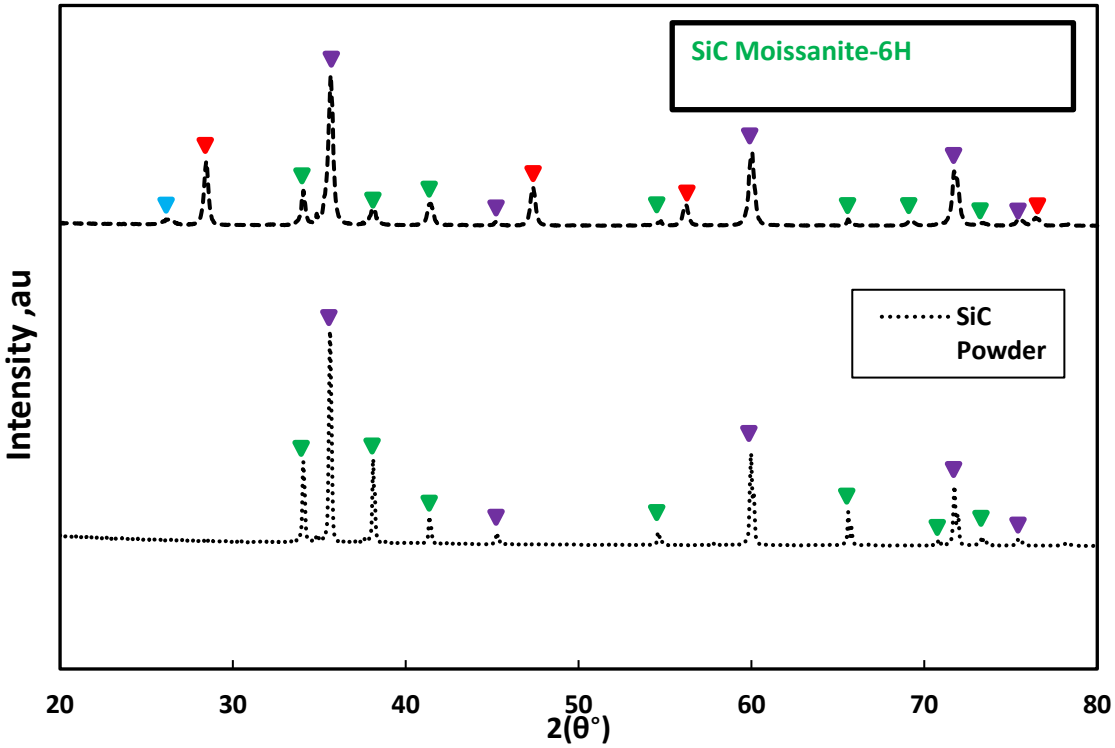

Figure 7.24. XRD spectra of the SiC powder and SiC manufactured part by D-PBSLP using zigzag scanning strategy.

It is important to evaluate the effect of scanning strategies on SiC decomposition. Because nearly all of the employed scanning strategies exhibited high-temperature peaks and the used laser energy density gave a maximum temperature that was above the SiC decomposition point, it is expected that all SiC samples contain regions where SiC decomposed. The effect of scanning strategies on the percentage of SiC decomposition was evaluated using XRD-Rietveld analysis, in which the XRD spectra of the samples were refined using Maud software. Figure 7.25 depicts an example of XRD spectra refinement for a SiC sample

printed using a zigzag scanning strategy, and Table 7.13 depicts the Rietveld analysis results for the used scanning strategies.

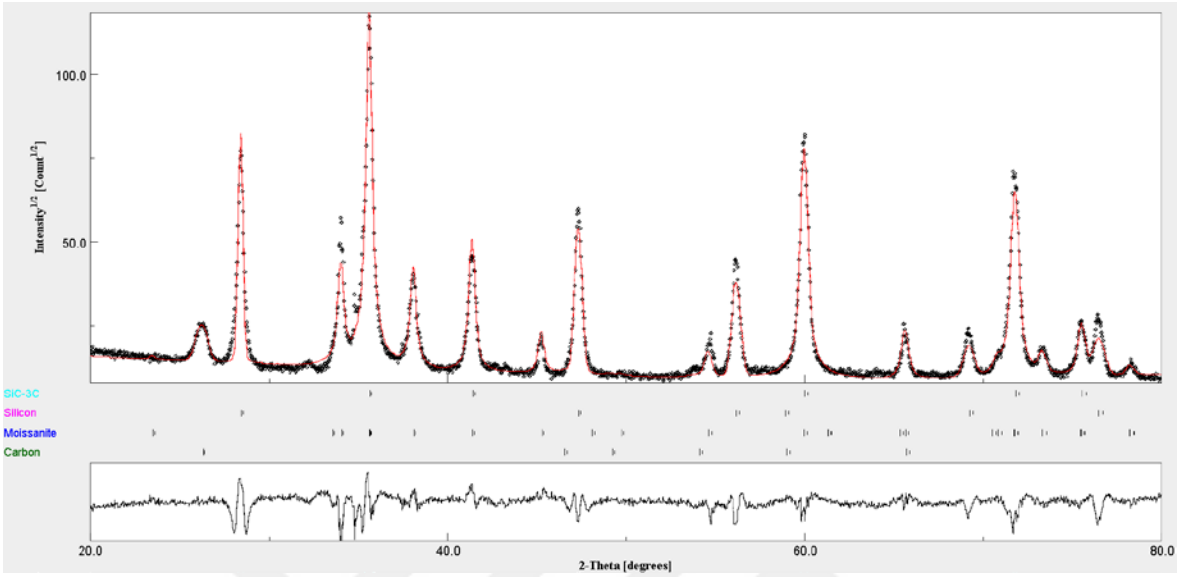

Figure 7.25. Refinement of the XRD spectra for SiC sample printed with the zigzag scanning strategy.

As shown in Table 7.13, hexagonal, concentric in-out, and linear scanning strategies resulted in a high decomposition of samples with 75.5, 78.6, and 79.42 % SiC, respectively. The decomposition in the hexagonal and concentric in-out strategies is primarily caused by the high laser power and high-temperature peaks-up experienced on the layer top surface during scanning with these strategies, as previously described.

Because the linear scanning strategy did not experience any temperature peaks, as shown in Figure 7.12, the decomposition was caused primarily by the high laser power used during scanning, and there are some regions at the start of each path that were not fully sintered because the laser beam took a while to reach the sintering point of SiC. As there were any temperature peaks happened on the layer top surface, and all temperature peaks happened at the sample border, which was consumed to reach the sintering point of SiC at the start of each scanning path, the zigzag scanning strategy succeeded in giving the lowest decomposition (or the highest SiC content).

Table 7.13. Phase composition, determined by Rietveld method, SiC powder and SiC 3D part samples prepared by PBSLP at different scanning strategies.

Item	SiC Polytypes (%)	Silicon (%)	Carbon (%)	R_{wp} (%)	R_{exp} (%)
SiC Powder "As received"	100	0	0	15.66	4.18
Concentric In-out	78.61 ± 2	15.06 ± 0.82	6.09 ± 0	14.74	4.14
Zigzag	83.95 ± 2.68	12.55 ± 1.18	3.47 ± 0	16.72	4.57
Hexagonal	75.53 ± 2.49	19.18 ± 1.26	5.27 ± 0	15.39	4.18
Linear	79.42 ± 2.13	13.46 ± 0.67	7.01 ± 0	15.38	4.14

Figure 7.26 depicts the processing time required to print a SiC cube with dimensions of 10×10×10 mm3 using various scanning strategies. It can be seen that the hexagonal scanning strategy consumed more time than the other scanning strategies, reaching 11.75 hours, whereas the other scanning strategies took about 4 hours to finish the printing.

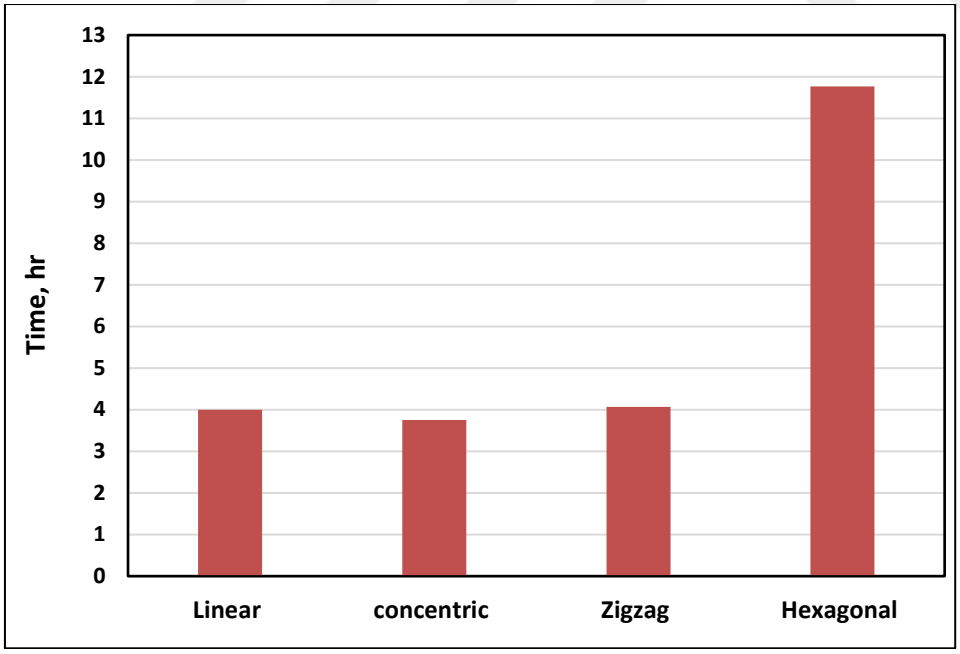

Figure 7.26. Processing time required to print a SiC cube (10×10×10 mm3) using a scanning speed of 100 mm/s with different scanning strategies.

Based on the scanning strategy investigation for D-PBSLP of SiC, it can be concluded that the zigzag scanning strategy is the appropriate scanning strategy because it could print SiC sample with a flat top surface and without any characteristic pattern as experienced with the

other scanning strategies, provided a good relative density, did not experience any layer shifting as happened with the linear strategy, and provided excellent s roughness at the top surface compared to the other scanning strategies. Therefore, all subsequent studies used the zigzag scanning strategy for SiC D-PBSLP.

7.3. The Influence of Scanning Speed on the PBSLP of SiC

In the previous sections, process parameters such as laser power, scanning speed, and hatching distance were numerically investigated, and the developed numerical model was used to predict the appropriate values for each parameter. In addition, the scanning strategies were investigated numerically and experimentally, and the optimal strategy for D-PBSLP of SiC was determined. To fully cover the D-PBSLP of SiC, it became necessary to verify the obtained process parameters from the numerical model using an experimental investigation to find the optimal value for each parameter. Therefore, in this section, low-level (100 mm/s), medium-level (250 mm/s), and high-level (500 mm/s) sintering speeds were investigated, together with layer thicknesses of 22, 30, and 40 µm. Based on section 6.2's findings, the laser power value and hatching distance were selected.

7.3.1. Layer thickness 40 µm

Cubic SiC samples (10×10×5 mm3) were printed at various sintering speeds, including 100 mm/s, 250 mm/s, and 500 mm/s, with the corresponding laser powers calculated from the numerical model (Section 6.2). In other instances, the laser power was increased or lowered beyond the range specified by the numerical model to understand the influence of the laser power at each scanning speed employed.

For low sintering speed level (100 mm/s), laser powers ranging from 40 to 45W were utilized, as calculated by the numerical model; Figure 7.27 depicts the printed samples. The samples were successfully printed with a definite cube shape; however, they were softer than anticipated and could be broken. As shown in Figure 7.27, increasing the laser power above the limit of the numerical model (48, 55, and 60W) resulted in very porous and quickly damaged samples. In addition, a layer of adherent SiC powder surrounded the samples, caused mainly by the slow sintering speed (100 mm/s), which allowed heat to seep through the powder surrounding the printed layer and cause it to adhere to the layer boundary.

Archimedes' method was used to evaluate the sample density, around 2.5 g/cm3 (78% R.D.), for samples printed with 40 to 48 W laser power. Increasing the laser power to 55 and 60W increased the density to 2.7 g/cm3 (84% R.D.); however, this increase was anticipated to be a result of SiC decomposition into Si and Carbon (not real density). In addition, the samples contained more defects than had been previously identified.

The numerical model calculated that the laser power range (50 to 60 W) was utilized to print SiC samples at the medium sintering speed level (250 mm/s). As depicted in Figure 7.27 (b), the samples' top surfaces exhibited numerous flaws in the form of deterioration. When the laser power was decreased below the limit determined by the numerical model (laser power was reduced to 45 W to determine if the defects were a result of using a high laser energy density), it was discovered that the defects were still present. In addition, when the laser power was increased beyond the numerical model's limit (65 and 70 W), the described flaws were retained in the samples.

The effect of a high-level sintering speed (500 mm/s) with a layer thickness of 40 µm was studied using the numerical model's recommended laser power. As depicted in Figure 7.27(c), the building failed due to improper adhesion of the first layers to the baseplate. Increasing the laser power beyond the limit of the numerical model led to deterioration between the deposited layers and defects on the layer's top surface (laser tracks can be easily seen). In addition, due to the high inertia of the laser beam, powder particles ejected from the powder bed, as depicted in Figure 7.27(d), notably in the laser scanning region. This affects the layering quality because when the recoater deposits a new layer, a portion of the recoated powder is used to fill these areas in the previous layer, leaving insufficient powder to fill the current layer efficiently.

It can be concluded that the layer thickness of 40 µm is not recommended for D-PBSLP of SiC due to challenges such as layer degradation, surface flaws, and poor adhesion with the baseplate. The issues encountered with a layer thickness of 40 µm could be overcome by reducing the layer thickness, as will be discussed in the following sections.

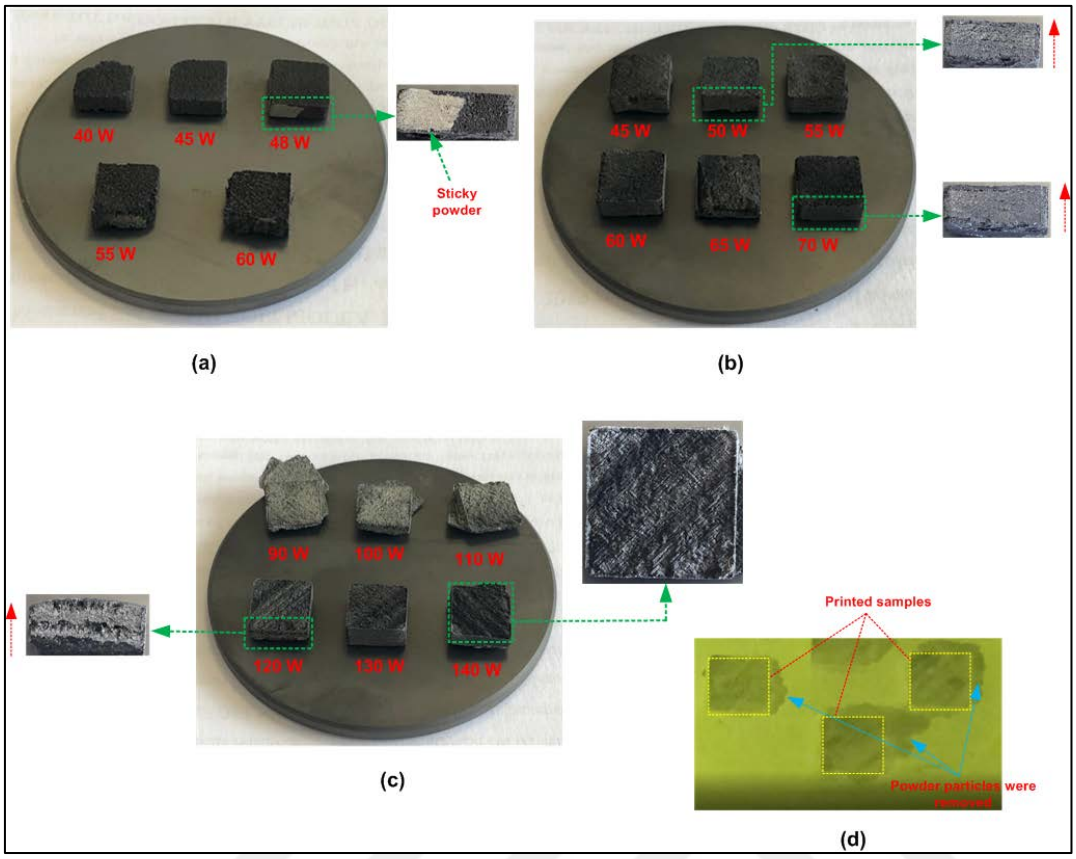

Figure 7.27. SiC samples printed using 40µm layer thickness and sintering speed of 100 mm/s (a), 250 mm/s (b), and 500 mm/s (c); powder particles were removed due to the high laser beam inertia (d).

7.3.2. Layer thickness 30 µm

D-PBSLP of SiC was investigated with a layer thickness of 30 µm and the same sintering speed levels as previously employed with a layer thickness of 40 m. The laser powers and hatching space were chosen according to section 6.2. Figure 7.28(a) demonstrates that using the sintering speed of 100 mm/s, entirely well-defined cubic samples with no defects (except for the sticky powder layer on the sample side surfaces) were printed using the numerical model's recommended laser power (35 and 40W). The samples' density was determined using the Archimedes method and was found to be 2.65 g/cm3 (82.5 % R.D.). As demonstrated in Figure 7.28(a), increasing the laser power beyond the limit suggested by the computational model (45, 50, 55, and 60 W) resulted in weak and porous SiC samples.

Using medium and high sintering speeds (250 and 500 mm/s) resulted in several defects on the printed samples, including layer degradation and a destroyed top surface (Figure 7.28 (b) and (c)), particularly when the laser power surpassed the limit of the numerical model.

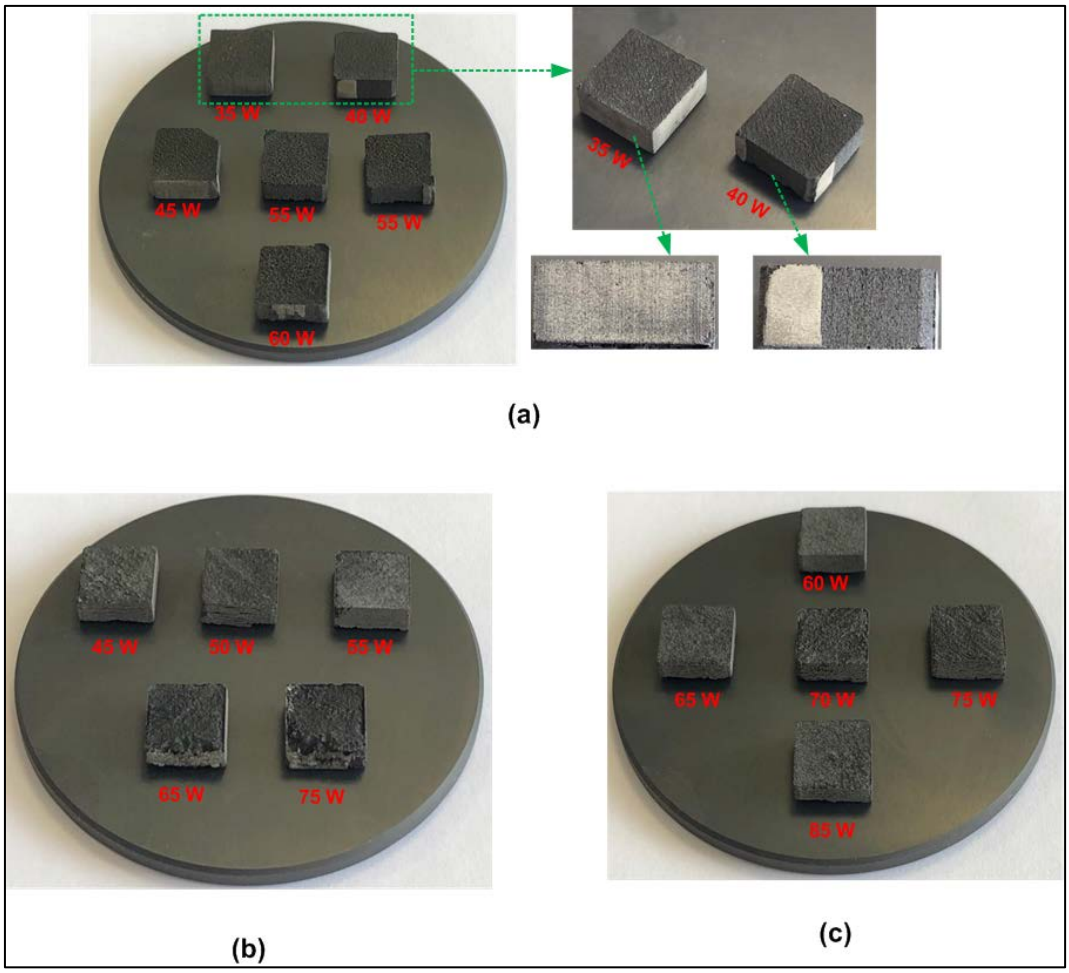

Figure 7.28. SiC samples printed using 30 µm layer thickness sintering speed of: 100 mm/s (a), 250 mm/s (b), and 500 mm/s (c).

7.3.3. Layer thickness 22 µm

D-PBSLP of SiC was investigated with a layer thickness of 22 µm and the previously employed scanning speeds. Figure 7.28(a) demonstrates that the numerical model estimated that SiC samples were successfully printed at 100 mm/s sintering speed with laser powers of 30, 35, and 40W. The samples exhibited a well-defined cubic shape and were devoid of the flaws associated with 40 µm layer thicknesses, except for the sticky powder on the surfaces of the sample sides. The density of the samples was evaluated to be 2.64 g/cm3 (83% R.D.), which was greater than the value obtained with a 40 µm layer thickness. As illustrated in Figure 7.28(a), increasing the laser power above the limit of the computational model (45, 50, and 55 W samples) produced very porous and quickly destroyed samples.

SiC samples were successfully printed when the medium sintering speed level (250 mm/s) was investigated utilizing the laser power values specified by the numerical model (40 to 50W). In addition, it was discovered that decreasing the laser intensity to 35W caused layers to degrade, as seen in Figure 7.28(a). The maximum density achieved was around 2.62 g/cm3 (82% R.D.). When the sintering speed of 500 mm/s was investigated, several defects appeared on the SiC samples, particularly layer degradation, as seen in Figure 7.28(c).

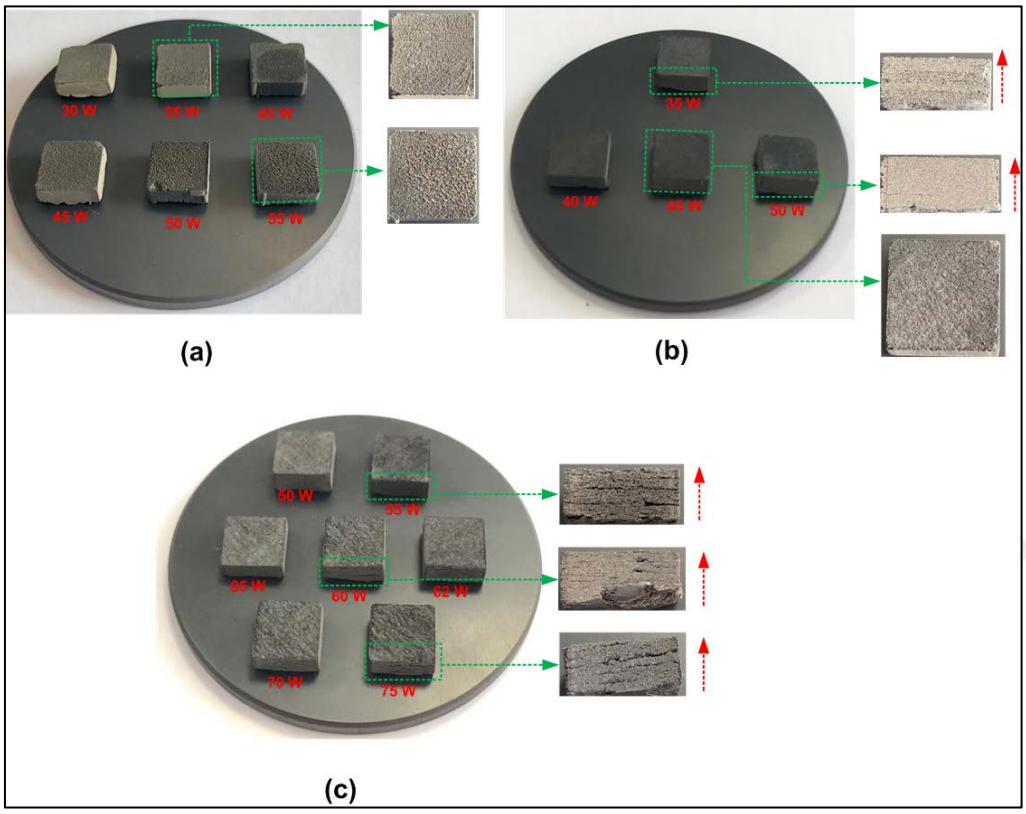

Figure 7.29. SiC samples printed using 22 µm layer thickness sintering speed of :100 mm/s (a), 250 mm/s (b), and 500 mm/s (c).

Based on the investigation of the effect of scanning speed on D-PBSLP of SiC, it can be concluded that layer thicknesses of 22 and 30 µm can be employed efficiently with low (100 mm/s) and medium (250 mm/s) sintering speed levels. The layer thickness of 30 µm is regarded as the optimal layer thickness for D-PBSLP of SiC to accomplish a high manufacturing rate and outstanding building resolution. It was considered for the process parameter optimization and mechanical performance evaluation of D-PBSLP of SiC. D-PBSLP od SiC is not advised to be sintered at a high rate (500 mm/s).

7.3.4. Compaction effect

Increasing the packing density of the powder bed by compacting the layer powder prior to scanning can significantly affect the part's final density. The commercial Phenix™ Systems (ProX® DMP 200 3D printer) has a compaction cylinder (described in section 2.2) that compacts the layer thickness, increasing the packing and final sample density. The influence of different compaction levels (such as 100, 200, and 300 %) on the final density was investigated. SiC Samples were printed using 22 µm layer thicknesses, 100 mm/s sintering speeds, and laser power of 35 and 40W, as seen in Figure 7.30(b). Figure 7.30(c) demonstrates the effect of compaction on the relative density of the part, where an increase in compaction considerably led to an increase in density to roughly 86.5% at the compaction level of 300%.

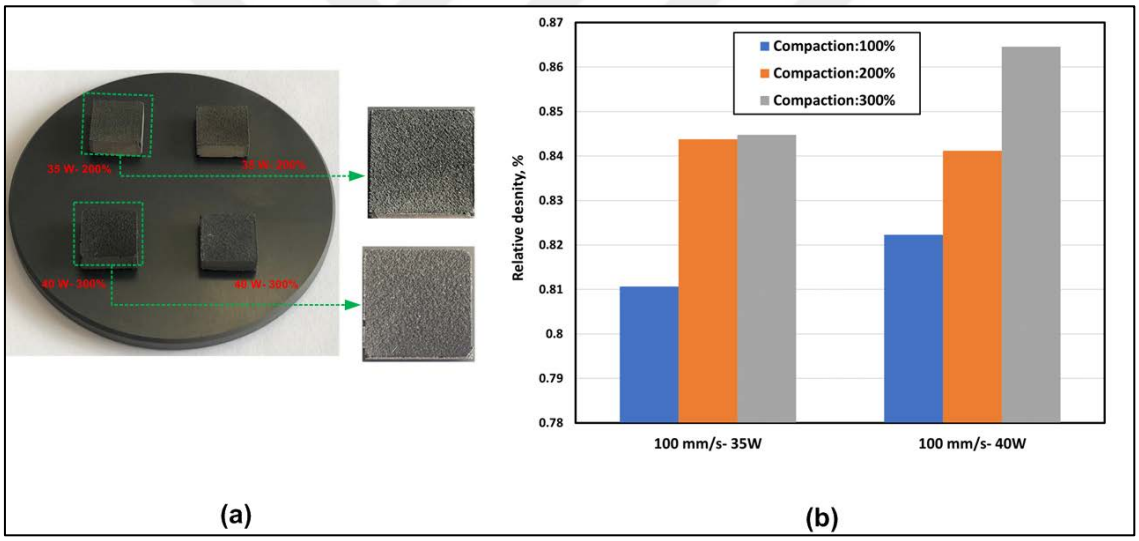

Figure 7.30. Recoater and compaction cylinder available in 3D SYSTEM-PRO200 printer (a), SiC samples printed using layer thickness of 22 µm and sintering speed 100 mm/s.

7.4. Process Parameters Optimization

Studying the layer thicknesses, sintering speed levels, and compaction effect on D-PBSLP of SiC led to the conclusion that 30 µm layer thickness, 300% compaction, and low and medium sintering speed are promising process parameter values for manufacturing high-quality and denser SiC components by D-PBSLP. At this stage, it is essential to optimize the process parameters in order to reach the most efficient and optimal values for the process parameters. As previously described in section 2.5, the Taguchi optimization technique can

be used to determine the optimal parameters for D-PBSLP of SiC to achieve the highest relative density and the least amount of decomposition for SiC.

The Taguchi optimization technique utilizes three stages to optimize the D-PBSLP of SiC, as described in the following sections.

7.4.1. Taguchi optimization-first stage

The commercial Phoenix 3D printer manufactured by 3D Systems® was utilized to perform the SiC PBSLP treatments. The factors influencing the PBSLP of SiC have been identified, and their levels. These factors include laser power, scanning speed, and hatching space. As shown in Table 7.14, three levels were considered for each factor, and these levels were determined based on the results and recommendations for each factor obtained in sections 6.2 and 6.3.

Table 7.14. Factors and levels used in the optimization of D-PBSLP of SiC.

Factor	Symbol	Level 1	Level 2	Level 3
Laser power, W	A	35	40	45
Sintering speed, mm/s	B	100	200	300
Hatching distance, µm	C	30	35	40

The objective of the D-PBSLP for SiC is to print SiC samples successfully with the highest possible relative density and the least amount of SiC decomposition. Consequently, the sample's relative density and per cent SiC content were considered response functions (response factors) during the optimization of the D-PBSLP of SiC.

7.4.2. Taguchi optimization-second stage

The full factorial design of experiments yields 27 treatments, which is a time- and cost-intensive process, whereas the Tauchi optimization method can reduce the number of treatments while ensuring that the optimal level for each factor is captured. Therefore, the standard orthogonal array (OA) L9 (33) was used to construct the treatments in this study. This array consists of 9 treatments, including the three factors at different levels as described in Table 7.14. The treatments considered the different level of laser energy density (as used

with alumina D-PBSLP optimization); high energy density (E1, E4, E7), medium energy density (E2, E5, E8), and low energy density (E3, E6, E9). Table 6.15 shows the nine treatments included in this study with the combination of different levels conditions for each factor (E1–E9).

Table 7.15. Factor levels for each treatment in PBSLP of SiC.

Treatment	A	B	C
E1	1	1	1
E2	1	2	2
E3	1	3	3
E4	2	1	2
E5	2	2	3
E6	2	3	1
E7	3	1	3
E8	3	2	1
E9	3	3	2

After obtaining the orthogonal array, the next step in the second stage was carrying out the experiments (treatments) described in Table 7.15. Two samples for each treatment were printed to get more flexible measurements. The treatment was carried out using the commercial Phoenix 3D printer manufactured by 3D Systems®, and the printed SiC samples are shown in Figure 6.31.

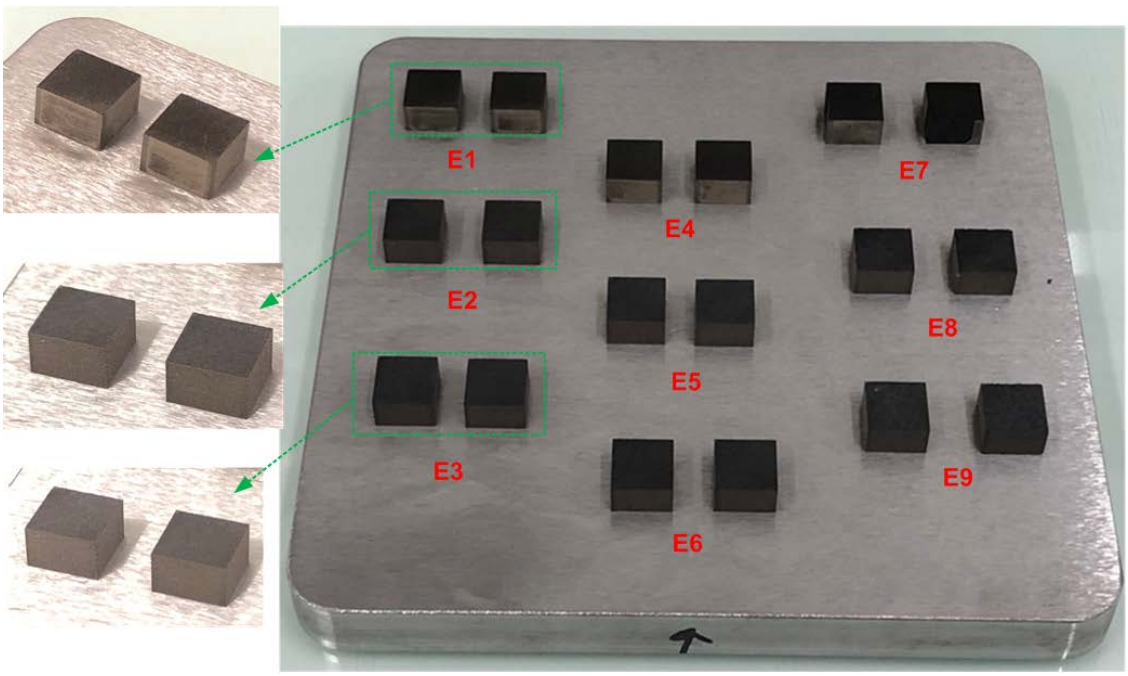

Figure 7.31. SiC samples printed according to the treatments described in Table 7.15.

Furthermore, it can be seen that the SiC Samples were successfully printed using a metallic baseplate rather than a SiC baseplate, which is considered an excellent achievement for the PBSLP of Sic and ceramic in general because it demonstrates that there is no need for expensive ceramic baseplate by using the appropriate process parameters.

The sample top surface was evaluated using SEM images for each laser energy density level (low, medium, and high), with E7 corresponding to the high energy density level, E8 to the medium energy density level, and E9 to the low energy density level.

Figure 7.32 illustrates the SEM images in which It is clear that the scanning paths followed the scanning strategy (zigzag inclined with 45°) and are easily discernible). The surface is smooth and devoid of any distinct pattern. The porosity level within the samples is easily detectable and does not appear low. In addition, the sintered particles are visible, confirming the possibility of direct sintering of SiC and other ceramic materials without a melting face.

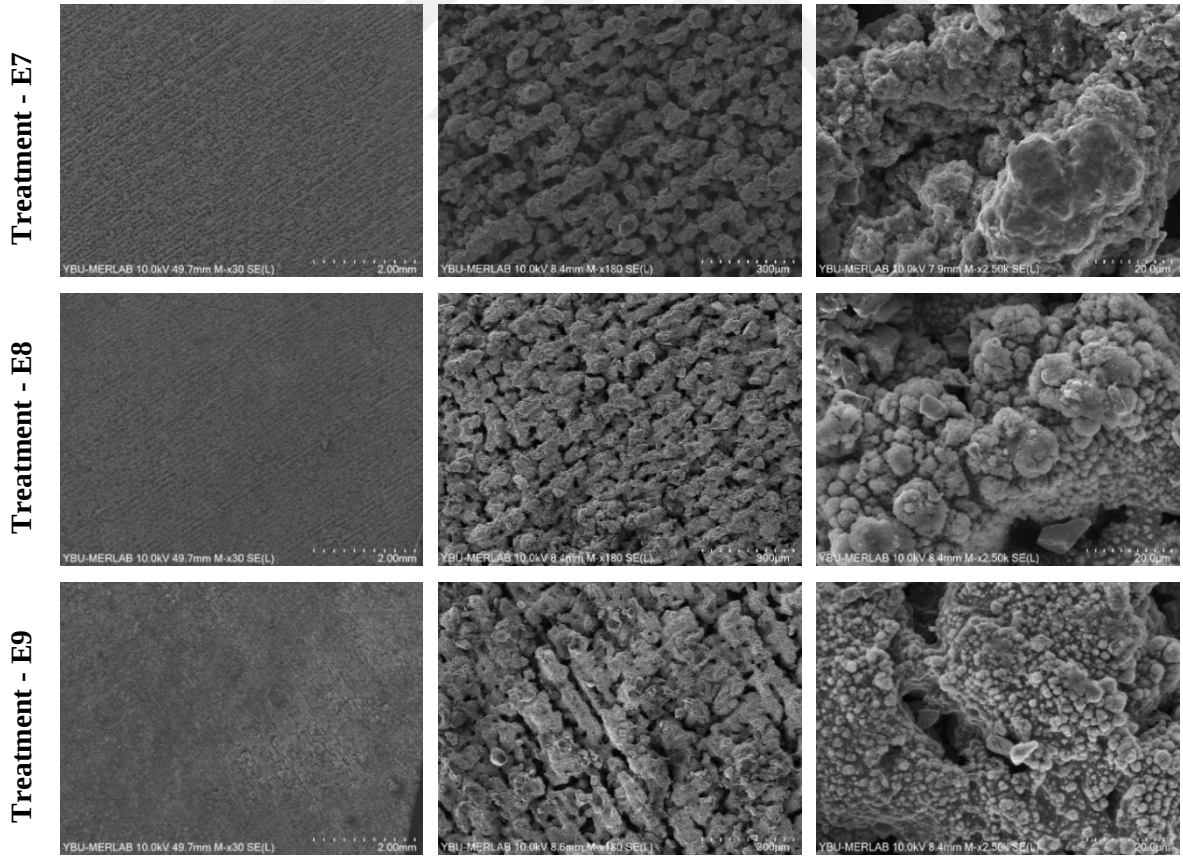

Figure 7.32. SEM images for SiC samples printed with different laser energy density treatments (E7, E8, and E9).

For each treatment, the relative density was measured using Archimedes' method (the average of three measurements was considered), and the decomposition was evaluated using XRD Rietveld analysis. Table 7.16 summarizes the obtained results for each treatment.

Table 7.16. Relative density and SiC% content for each treatment.

Treatment	Levels of input factors				Measured response factor			
	A	B	C	Energy density	Relative density			
				J/mm^3	First	Second	Third	Average
					reading	reading	reading	
E1	1	1	1	388.89	0.852	0.857	0.859	0.856
E2	1	2	2	166.67	0.818	0.836	0.817	0.824
E3	1	3	3	97.22	0.834	0.834	0.830	0.832
E4	2	1	2	380.95	0.852	0.859	0.863	0.858
E5	2	2	3	166.67	0.816	0.832	0.829	0.826
E6	2	3	1	148.15	0.829	0.804	0.810	0.814
E7	3	1	3	375.00	0.864	0.858	0.870	0.864
E8	3	2	1	250.00	0.823	0.831	0.803	0.819
E9	3	3	2	142.86	0.838	0.830	0.841	0.836
Treatment	A	B	C	Decomposition				
				SiC %	Si %	C %	Rwp (%)	Rexp (%)
	1	1	1	84.37	13.85	1.74	18.01	4.44
E2	1	2	2	13.93	8.08	20.58	4.07	4.07
E3	1	3	3	11.54	6.70	21.03	4.08	4.08
E4	2	1	2	16.58	4.41	18.39	4.11	4.11
E5	2	2	3	13.39	7.87	19.38	4.10	4.09
E6	2	3	1	8.0	3.01	22.04	4.24	4.24
E7	3	1	3	21.16	2.59	19.93	4.14	4.14
E8	3	2	1	16.61	5.35	20.68	4.35	4.35
E9	3	3	2	14.45	6.03	23.04	4.18	4.18

There is no apparent relationship between the relative density or SiC % and the laser energy density because many parameters changed during each treatment, making it difficult to derive such a relationship and promote the previous conclusion about developing a new design parameter for the accurate description of the PBSLP process instead of the laser energy density parameter.

7.4.3. Taguchi optimization-final stage

The final phase in the Taguchi optimization is devoted to response factor analysis (data analysis), determining the optimal factor value, and conducting a confirmation test using the optimal factor value.

In order to analyze the obtained data, the Taguchi optimization technique uses the Signal to Noise (S/N) response analysis to evaluate the quality of each. There are four categories for the S/N ratio calculation based on the desired output quality, as described previously in chapter 6, and for relative density and SiC%, the larger, the better is used, and the equation for calculating the S/N ratio is as follows [177].

$$S/N = -10 \times \log \frac{1}{n}\left(\sum \frac{1}{Y_i^2}\right) \quad (7.1)$$

Where, Y_i represents the individual measured relative density (first, second and third reading for the relative density and the calculated SiC percentage, while n represents the number of the reading (n =3 for relative density and n=1 for SiC%). Table 7.17 summarize the S/N ratio for the relative density and SiC percentage.

Table 7.17. Calculated S/N ratio for each treatment.

Treatment	Levels of input factors			Calculated S/N ratio	
	A	B	C	Density	SiC %
E1	1	1	1	-1.351	38.5238
E2	1	2	2	-1.685	37.8397
E3	1	3	3	-1.593	38.2487
E4	2	1	2	-1.332	37.9503
E5	2	2	3	-1.664	37.9217
E6	2	3	1	-1.788	38.9849
E7	3	1	3	-1.272	37.6425
E8	3	2	1	-1.735	37.8441
E9	3	3	2	-1.551	38.3291

The S/N category used in this study is the larger, the better, which means that the largest relative density and SiC% content are desired, and the largest S/N ratio would represent the optimal response that gives the lowest noise. This is the criteria used in this study to determine the optimal process parameters (laser power, scanning speed and hatching distance). The S/N ratio response graphs for the relative density and SiC% are shown in Figure 7.33. The optimal combination of the process parameters can be determined from these graphs. For relative density, the scanning speed (factor B) is the most significant parameter, followed by the hatching distance (factor C) and the laser power (factor A) and to achieve the maximum relative density, a laser power of 45W (A3), scanning speed of 100 mm/s (B1) and hatching distance of 40 µm (C3), i.e., treatment E7 should be used.

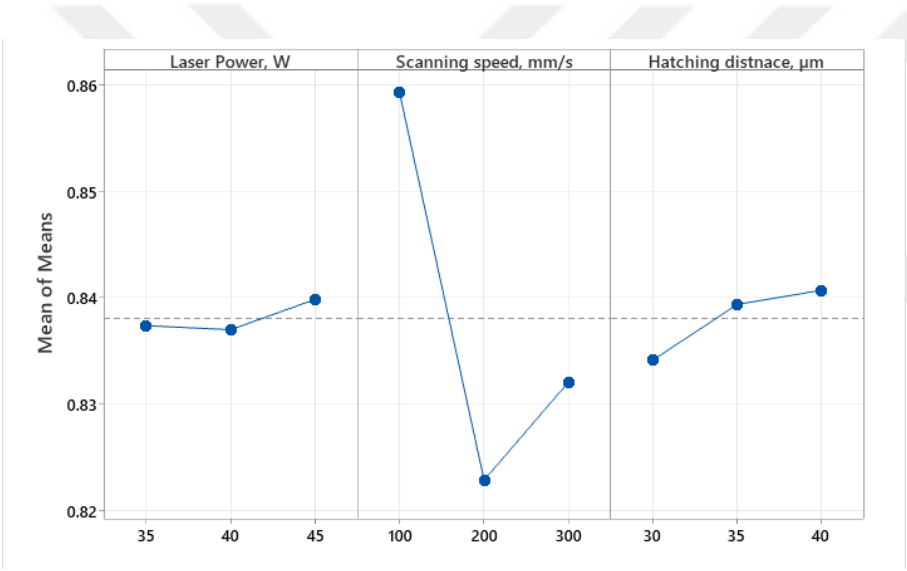

(a)

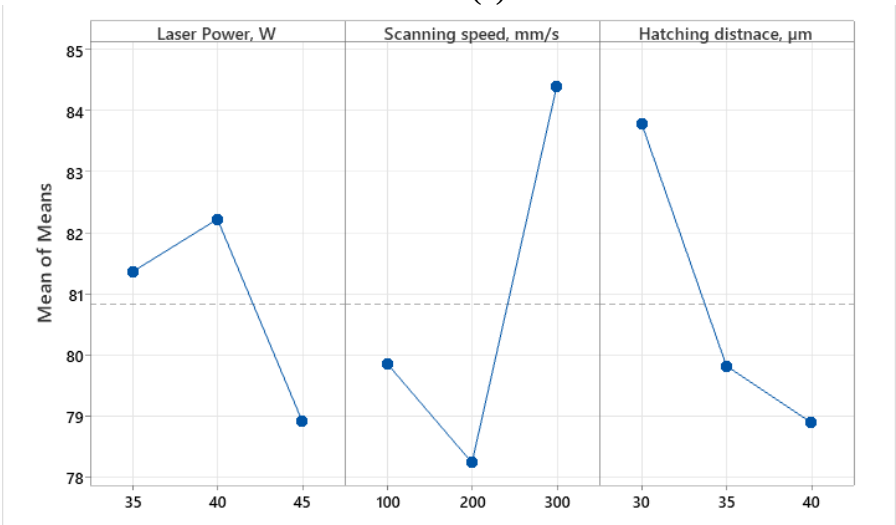

(b)

Figure 7.33. S/N ratio response graph of relative density (a) and SiC percentage content (b).

For SiC percentage content in the sample, the optimal combination of the process parameter values can be determined from Figure 7.33(b). it can be seen that the scanning speed (factor B) is also the most significant parameter, followed by the hatching distance (factor C) and the laser power (factor A), and the optimal process parameters values to be used to reduce the decomposition inside the SiC sample are a laser power of 40W (A2), scanning speed of 300 mm/s (B3) and hatching distance of 30 µm (C1), i.e., treatment E6 should be used.

7.4.4. Pareto ANOVA: an alternative technique

As previously stated in Chapter 3, Pareto ANOVA is a technique used to analyze data for process optimization, and it can also provide the percentage contribution of each parameter to the response functions straightforwardly [81,82]. The S/N response data for each response function is used to construct the Pareto ANOVA analysis. The S/N response data can be calculated by taking the sum of all S/N ratio values (as described in Table 7.16) at the same level as the input parameter. Table 7.18 summarizes the samples' S/N response data values for relative density and SiC percentage content.

Table 7.18. S/N response data of the relative density and SiC%.

Relative density				SiC%			
Levels	A	B	C	Levels	A	B	C
1	-4.628	-3.951	-4.874	1	114.6	114.1	115.4
2	-4.782	-5.088	-4.570	2	114.9	113.6	114.1
3	-4.560	-4.930	-4.526	3	113.8	115.6	113.8

After calculating the S/N response data for each input parameter, the summation of squares of differences is calculated for each input parameter using the following equation:

$$S_d^A = (A_1 - A_2)^2 + (A_1 - A_3)^2 + (A_2 - A_3)^2 \quad (7.2)$$

Where S_d^A The input parameter is organized in the Pareto diagram so that the parameter with the highest contribution comes first and then is followed by other parameters based on their contributions. represents the squares of difference for the input parameter (laser power) A, and similarly, the square of differences can be calculated for the other input parameters (scanning speed) B and (hatching distance) C. The percentage contribution for each input

parameter is calculated by considering the percentage summation of the squares of differences to the total summation of the squares of differences for all input parameters. The Pareto diagram is plotted considering the obtained percentage for each input parameter. Table 7.19 and Table 7.20 summarize the Pareto ANOVA analysis for relative density and SiC%, respectively.

Table 7.19. Paetro ANOVA analysis for relative density of SiC samples produced by D-PBSLP technique.

Input parameters		A	B	C
Summation at input parameter level.	1	-4.628	-3.95	-4.87
	2	-4.782	-5.08	-4.57
	3	-4.560	-4.93	-4.52
Total summation at the input parameter level		-13.97	-4.627	-3.951
Summation of the squares of the differences.		$S_d^A = 0.0776$	$S_d^B = 2.276$	$S_d^C = 0.2154$
Total Summation of the squares of the differences.		$S_{total} = S_d^A + S_d^B + S_d^C = 2.569$		
Input parameter contribution ratio %		$\frac{S_d^A}{S_{total}} = 3.02$	$\frac{S_d^B}{S_{total}} = 88.59$	$\frac{S_d^C}{S_{total}} = 8.38$
Paetro ANOVA diagram		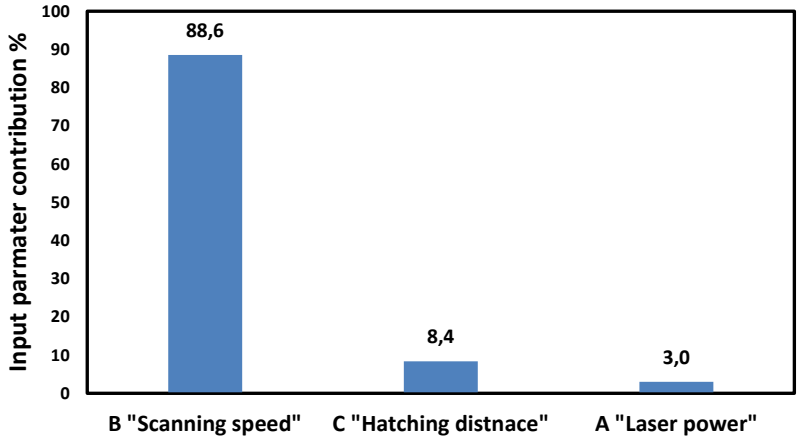		
Cumulative contribution %		88.6	96.98	100
Remarks		The most significant input parameter is the sintering speed, hatching distance and laser power.		
Optimum input parameters combination		A3	B1	C3

It was found that the scanning speed is the most significant parameter among all parameters, with an 88.6 % contribution. Therefore, higher relative density can be obtained using low scanning speed, but, unfortunately, using low scanning speed requires less than 30 W (laser power cannot be lowered than 10% of the maximum printer power, 300 W), and this could not be achieved. The hatching distance had the second contribution, while the laser power had the lowest contribution concerning the obtained relative density. The optimal combination of the input process parameters to achieve the maximum relative density is A3-B1-C3.

As with relative density, it was discovered that the scanning speed is the most significant parameter among all parameters for obtaining less SiC decomposition inside the samples, with a 52 % contribution, followed by the hatching distance with a 33 % contribution. Finally, laser power contributed the least, accounting for 15% of the total. The optimal combination of the input process parameters to achieve the minimum SiC% decomposition is A2-B3-C1.

Table 7.20. Paetro ANOVA analysis for SiC percentage content in SiC samples produced by D-PBSLP technique.

Input parameters		A	B	C
Summation at input parameter level.	1	114.6	114.1	115.4
	2	114.9	113.6	114.1
	3	113.8	115.6	113.8
Total summation at the input parameter level		343.3	343.3	343.3
Summation of the squares of the differences.		$S_d^A = 1.8$	$S_d^B = 6.2$	$S_d^C = 4.0$
Total Summation of the squares of the differences.		$S_{total} = S_d^A + S_d^B + S_d^C = 11.9$		
Input parameter contribution ratio %		$\frac{S_d^A}{S_{total}} = 15$	$\frac{S_d^B}{S_{total}} = 52$	$\frac{S_d^C}{S_{total}} = 33$
Paetro ANOVA diagram		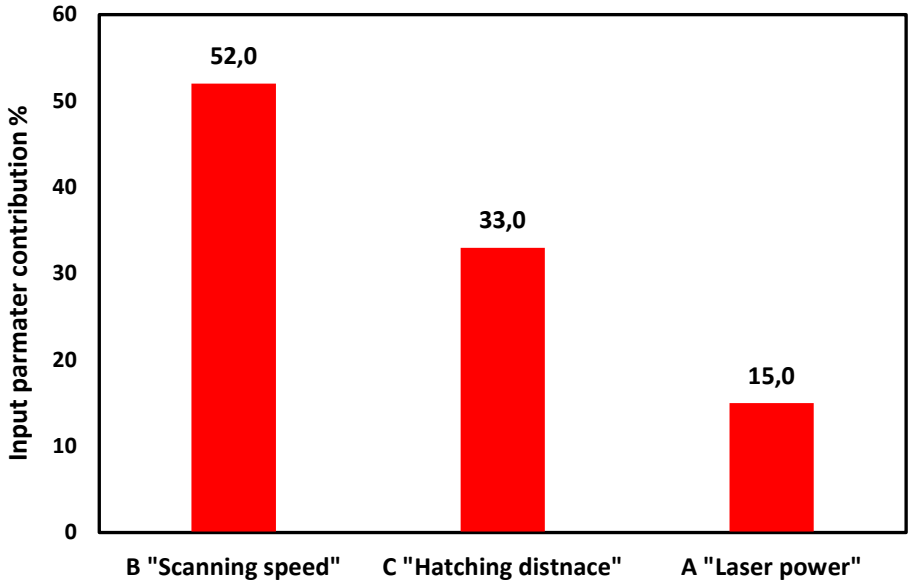		
Cumulative contribution %		52	85	100
Remarks		The most significant input parameter is the sintering speed, hatching distance and laser power.		
Optimum input parameters combination		A2	B3	C1

7.4.5. Confirmation test

There is no need to perform a confirmation test because the recommended optimal parameter combination was already considered in the treatments. To summarize the optimization

results, the parameter combination A3-B1-C3 should be used to achieve high relative density, whereas, to achieve less SiC decomposition, the parameter combination A2-B3-C1 should be used. However, because there is no significant difference in the relative density obtained using the parameter combinations A3-B1-C3 and A2-B3-C1, the parameter combination A2-B3-C1 can be considered the optimal combination for achieving high relative density with minimal decomposition. In order to confirm that optimal parameters were superior regarding the D-PBSLP of SiC, different lattice structures and gyroid and primitive were printed to demonstrate the capabilities of the D-PBSLP technique to print extremely complicated geometries. Figure 6.39 the printed lattice structures (10×10×10 mm3), which seem to be successful without any defects and with highly smooth surfaces.

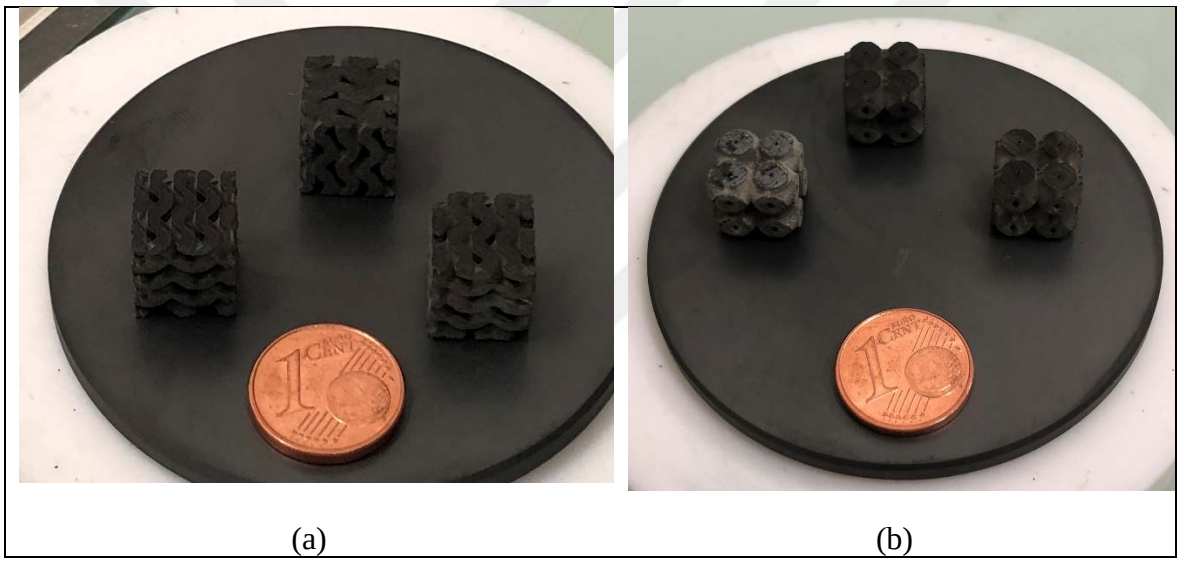

(a) (b)

Figure 7.34. SiC lattice structures printed for demonstration purposes; (a) gyroid, (b) primitive

Additionally, the optimization study revealed that the scanning speed is the most significant parameter and that to increase the relative density, the scanning speed should be decreased below 100 mm/s. However, this is impossible as decreasing the speed should be accompanied by a reduction in power utilization to less than 10 % of the printer's maximum power, and the power cannot be reduced below 10 %. In addition, the scanning speed should be increased to reduce decomposition. Due to the high inertia of the laser beam and powder particles, increasing the scanning speed will cause powder particles to be ejected away from the powder bed, as depicted in Figure 7.27(d). Consequently, the scanning speed cannot be altered in either scenario.

The second significant parameter obtained from the optimization is the hatching space, and it was determined that increasing the hatching space increases the relative density and decreases the SiC per cent content within the samples. Consequently, it is essential to determine how increasing the hatching space affects the obtained relative density and the SiC per cent content. Different SiC samples were printed with the same laser power and scanning speed used in E6 and E7 but with different hatching space values, including 45, 50, 55, 60, 65, and 70 µm, as can be seen in Figure 7.35 and Figure 7.36.

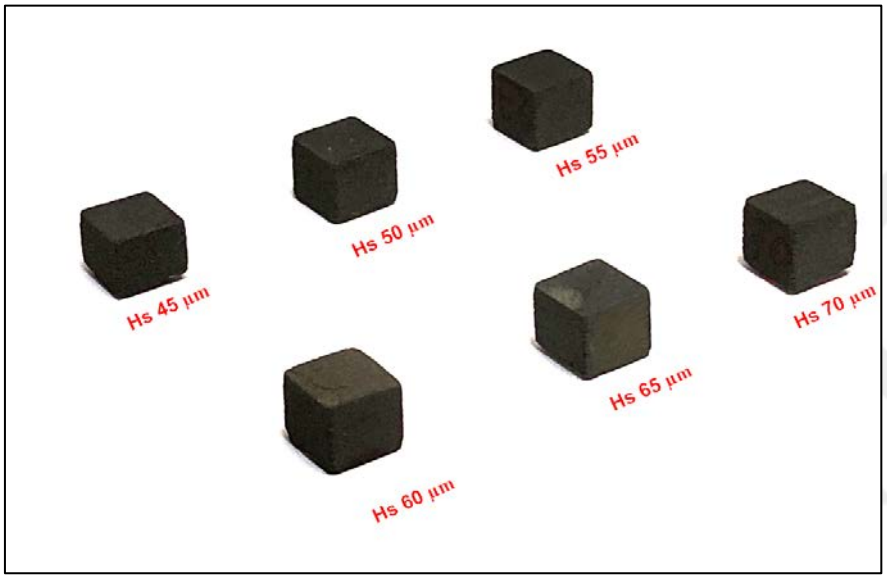

Figure 7.35. SiC samples printed with the laser power and scanning speed used in the treatment E6 with different hatching spaces.

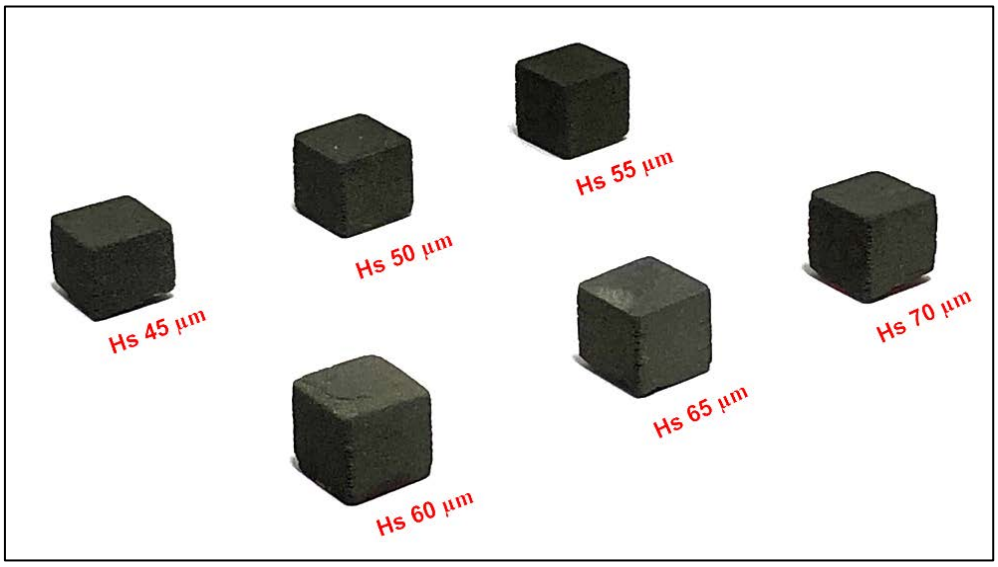

Figure 7.36. SiC samples printed with the laser power and scanning speed used in the treatment E7 with different hatching spaces.

Figure 7.37 depicts the relative density of SiC samples printed with the laser power and scanning speed used in treatments E6 and E7 with different hatching spaces and with the same hatching space used during the optimization study, labelled as "Old". For E6, increasing the hatching distance to 45µm increased the density from 81 % to 84 %, while E7 decreased from 86.5 % to 83.5 %. Any further increase of the hatching space nearly resulted in a relative density reduction. Therefore, it can be concluded that the maximum hatching space to be used with D-PBSLP of SiC is 45µm, consistent with the results obtained from the previous numerical model.

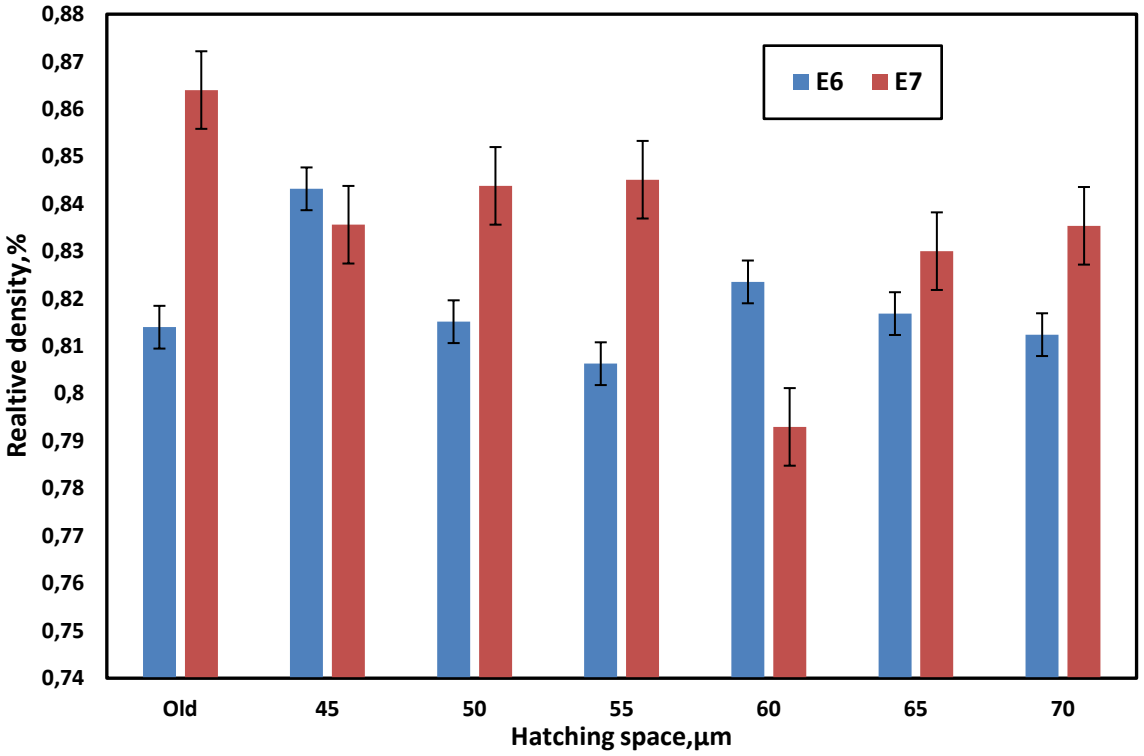

Figure 7.37. Relative density for SiC samples printed with the laser power and scanning speed used in the treatment E6 and E7 with different hatching spaces.

Figure 7.38 depicts the SEM images of SiC samples printed with the laser power and scanning speed used in treatment E6 and with varying hatching spaces. Using a 45 µm hatching space, it is evident that the sample's top surface is extremely dense and has a low level of porosity, which explains the case's high relative density. Any increase in hatching space beyond 50, 60, and 70 µm increased porosity, as seen in SEM images for hatching spaces of 50, 60, and 70 µm. Due to the high energy density of the E7 treatment, the laser tracks are readily visible in the SEM images as narrow paths, as depicted in Figure 7.39, and increasing the hatching space led to an increase in the porosity level observed on the layer's

top surface. Therefore, it is recommended to comply with the process parameter values derived from the numerical model.

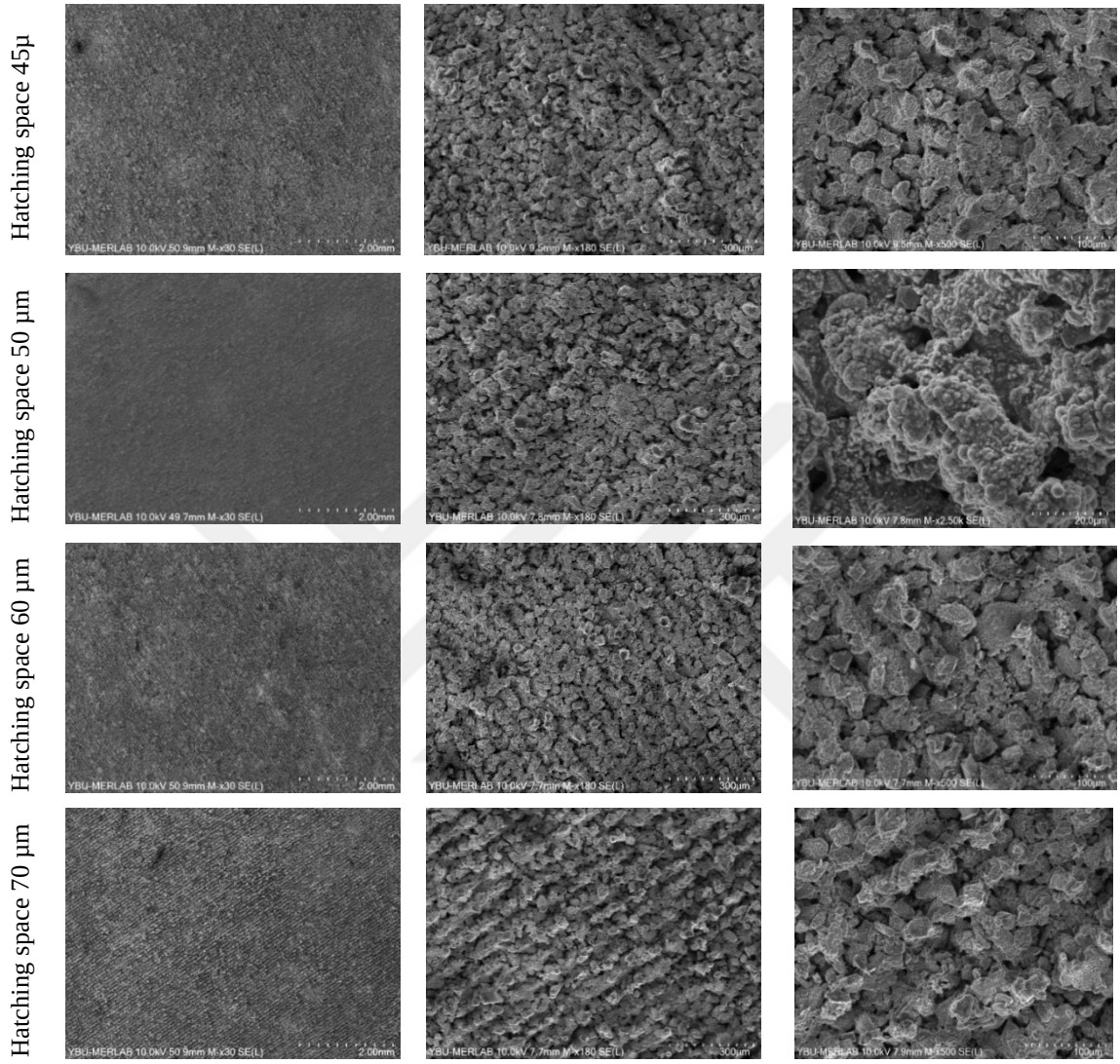

Figure 7.38. SEM images for SiC samples top surface printed with the laser power and scanning speed used in the treatment E6 with different hatching spaces.

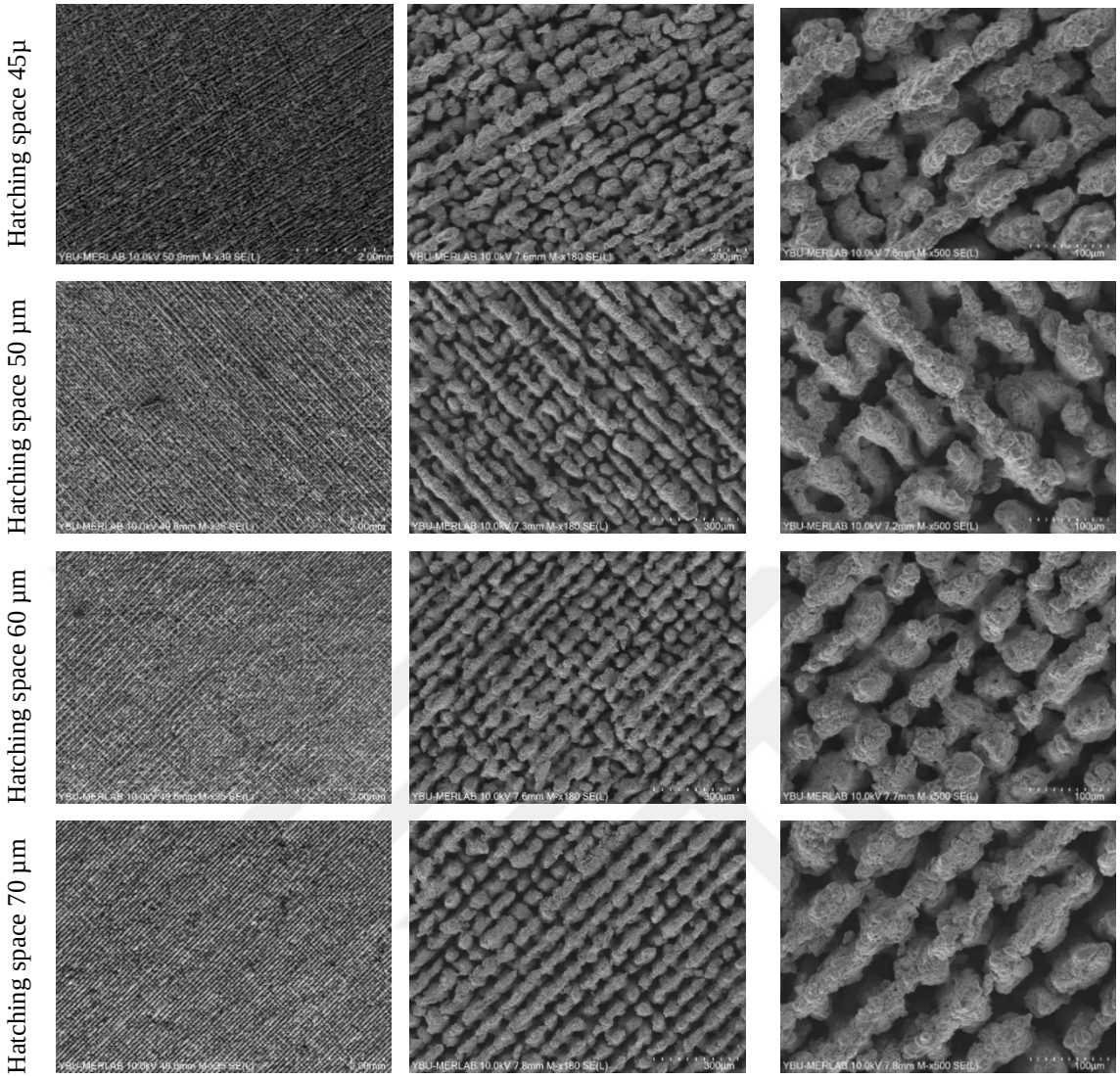

Figure 7.39. SEM images for SiC samples top surface printed with the laser power and scanning speed used in the treatment E7 with different hatching spaces.

Using the Rietveld method, quantitative phase analysis was performed to determine the effect of increasing the hatching space on the SiC decomposition resulting from D-PBLSP. Table 7.21 displays the phase content of SiC samples printed with E6 treatment and 35 and 60 m spacing between nozzles. It can be observed that increasing the hatching space decreases the decomposition of SiC samples printed using the D-PBSLP method. This is primarily because increasing the hatching space decreases the laser energy density used to print SiC.

Table 7.21. Effect of increasing the hatching space on the SiC % content inside the SiC samples printed using the D-PBSLP technique.

Hatching space, µm	SiC %	Si %	C %	Rwp (%)	Rexp (%)
35	88.97	8.0	3.01	22.04	4.24
60	91.46	6.79	1.733	22.47	5.63

7.5. Mechanical Performance Evaluation

It is crucial to evaluate the mechanical performance of SiC samples prepared by D-PBSLP to understand the obtained mechanical performance comprehensively. Therefore, the compressive test was conducted on SiC samples to evaluate their compressive strength and compare it with the compressive strength of SiC material reported in the literature.

SiC cylindrical samples (10 mm in diameter and 25 mm in length), as shown in Figure 7.40, were printed with the optimized process parameters (E7 treatment). To prepare the SiC samples for the compressive test, the two opposite cross-sectional areas were hand-polished until they became flat and parallel. The length of the samples was adjusted to 20 mm (L=2D, where L is the length of the sample and D is its diameter). Compressive strength was calculated according to equation (2.16), as described in Section 0.

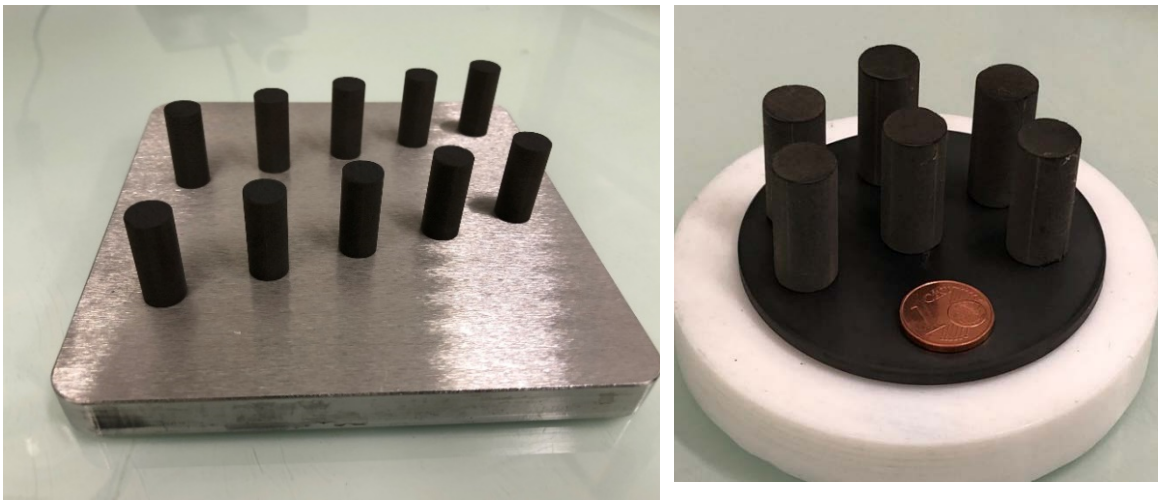

Figure 7.40. SiC cylindrical samples printed for conducting the compressive test.

The compressive tests were performed using a Z100 Universal testing machine (Zwick, Germany) with a 100 kN cell force, and the upper head of the machine was lowered at a rate of 0.5 mm/min until failure occurred.

To improve the mechanical performance of the printed samples, thorough investigation and post-treatments, such as Spark Plasma Sintering (SPS), should be conducted. Seven samples were tested, and the mean of all measurements was calculated. The obtained compressive strength was 1.85 ± 0.36 MPa, which is considered low compared to the 3900 MPa compressive strength of SiC manufactured using conventional techniques [206]. The stress-strain curve for one of the SiC compressive samples is depicted in Figure 7.41. The low performance in compression revealed the need to carry out postprocessing to enhance the sintering and densifications of SiC particles after D-PBSLP. Spark Plasma Sintering (SPS) is an ideal candidates for enhancing the densification of SiC powder after D-PBSLP.

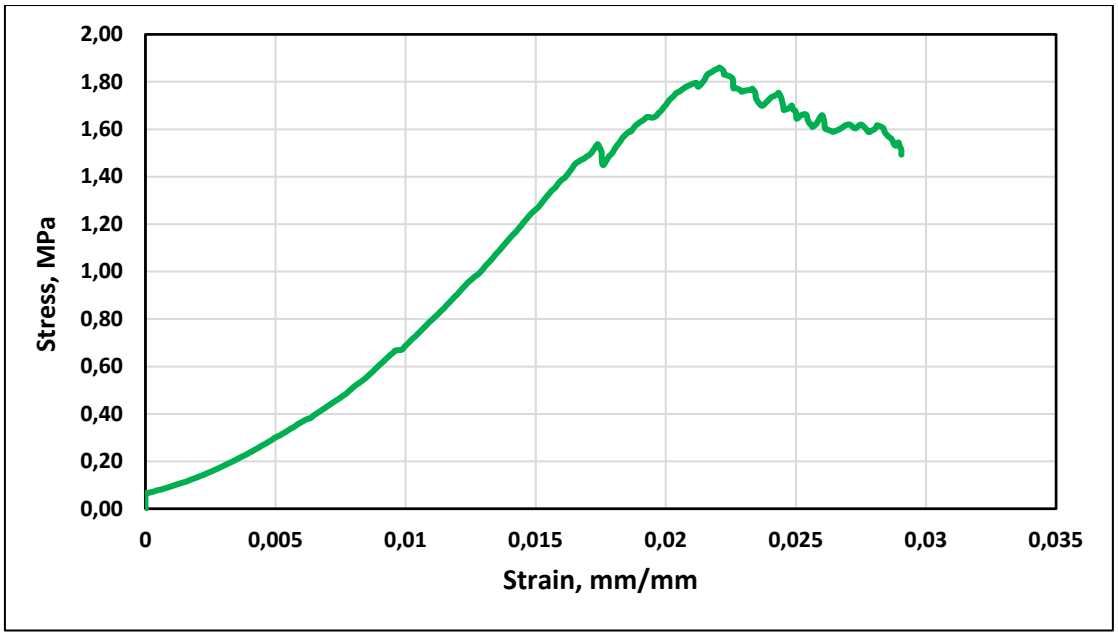

Figure 7.41. Stress-strain curve for SiC sample under compression test.

7.6. Conclusion

In this chapter, the D-PBSLP of SiC was studied experimentally and numerically, as was the case when investigating the PBSLP of alumina. Since SiC Powder has a high absorption rate for the employed laser, it was utilized without modification as feedstock. Using the developed numerical model, it was possible to predict the laser power, scanning speed, and hatching space for varying layer thicknesses. The scanning strategies were the first experimentally investigated parameter, and various strategies were examined as they were available in the Phoenix printer. This research led to the conclusion that the inclined zigzag

should be considered for the D-PBSLP of SiC, as it could circumvent nearly all of the difficulties encountered by the other scanning strategies.

Afterwards, the scanning speed was analyzed based on various layer thicknesses, including 22, 30, and 40 µm. For the D-PBSLP of SiC, it was determined that low layer thickness values and slow scanning speeds are recommended. The process parameters were optimized using laser power and scanning speed as input parameters, and the optimal combination of process parameters was obtained, resulting in a relative density of approximately 90 %.

The compressive test was then utilized to evaluate the mechanical performance of the SiC printed samples. The results indicated that the printed sample's compressive strength was significantly lower than the values reported in the literature. Additional postprocessing should be applied such as SPS to improve the mechanical performance of SiC components printed with the D-PBSLP technique.

8. CONCLUSION AND FUTURE PROSPECTS

General conclusion

The work presented in this dissertation seeks to investigate and improve additive manufacturing (AM) of ceramics materials using the PPBSLP technique, as well as to comprehend the obstacles that prevent the successful application of this technique to ceramics materials. Alumina and SiC were chosen as the model materials for this dissertation, in which they were investigated and studied in depth. Unfortunately, and in contrast to other AM techniques, the PBF of any ceramic material must be investigated separately, as each material has its behaviour when it comes to PBSLP fabrication. Following is a summary of the general conclusions reached throughout the chapters of this dissertation.

Due to the numerous dependent process parameters, the PBSLP technique is considered complicated; therefore, we required a tool to guide us through the research. A simulation is a powerful tool because it allows one to observe the effects of changes like reality. As described in chapter 2, it was decided to establish and develop a numerical model to simulate the PBSLP technique. As described in chapter 4, the developed numerical model was then validated using alumina and SiC as model materials to ensure that the numerical model would produce accurate results.

Chapter 5 used the numerical model to comprehensively understand the PBSLP technique and what occurs during the scanning process, with varying process parameter values and multi-layer deposition and scanning. We determined the process window for alumina and SiC, considering the laser source type. Using a set of the obtained parameters, the model demonstrated a heat accumulation during the multi-layer process, which is the cause of the high thermal stress and cracking development. Controlling the temperature by adjusting the laser's power and scanning speed and applying preheating to the ceramic layer powder is essential for overcoming the thermal stress and cracks that have developed.

Chapter 6 focused on alumina, for which a numerical model was used to determine the appropriate process parameters based on the values available at the BCRC printer (SLM 125,

Renishaw®, UK). Using the obtained parameters as a guide for the experimental study, alumina samples were successfully printed using these values. As described in the literature review presented in chapter 2, the first parameter investigated was the scanning strategies, as it plays a significant role in controlling the heat distribution with the printed layer, and the quality of the scanning process is highly dependent on it. The investigation of scanning strategies led to the recommendation of the Linear 45° scanning strategy for alumina PBSLP, which was also considered for the other investigation. Experiments were conducted to determine the optimal scanning speed range for alumina PBSLP, as scanning speed is a crucial parameter. The results indicated that alumina should be scanned at high speed, and a relative density of approximately 84% was obtained.

Taguchi optimization and Pareto ANOVA were used to determine the optimal process parameters for achieving a relative density of 94.5 %. Due to the porous structure of the spray-dried alumina powder used as a feedstock in this study, this high relative density was accompanied by numerous defects in the form of a wavy surface on the sample's top surface, which can be overcome by employing a solid spherical alumina powder, as described in chapter 6. The microhardness and compressive tests were then used to evaluate the mechanical performance. The printed samples had the same hardness as those produced by conventional techniques but had a compressive strength of only 140 MPa, which is considered extremely low when compared to the 3000 MPa produced by conventional techniques, and this low compressive strength was a result of the cyclic damage experienced along the building's direction.

SiC PBSLP was investigated in chapter 7 using the same procedure as alumina PBSLP, and this study is considered the first to print SiC material without any feedstock preparation directly, achieving the ultimate goal of ceramics AM, which is a one-step AM process. Initially, the numerical model was used to determine the appropriate process parameters within the range of the SLM printer (ProX® DMP200, 3D Systems, US) at CIRIMAT. The investigation into scanning strategies led to the conclusion that the inclined zigzag strategy should be used for SiC PBSLP because it could nearly overcome all the obstacles encountered by other scanning strategies. The scanning speed was the second parameter to be investigated using the numerical model as a guide. All the specified values of laser power and scanning speed (100, 250, and 500 mm/s) at various layer thicknesses (22, 30, and 40 µm) were able to print SiC samples successfully; however, using a low layer thickness with

low scanning speed yielded the most promising results, achieving a relative density of approximately 85%. The Taguchi and Pareto ANOVA technique was then used to determine the optimal value for each process parameter through optimising process parameters. The optimization led to the identification of this optimal set with a 90% relative density.

Finally, the mechanical performance was evaluated using the compressive test, and the printed sample demonstrated a poor performance compared to the literature results. This led us to conclude that postprocessing is required to improve mechanical performance, and this is proposed for a future study.

Future prospects

Numerous factors must be considered for alumina and SiC PBSLP to progress further. For alumina, developing a feedstock with a solid structure and good flowability is crucial, as this will significantly aid in overcoming the top surface defects observed. In addition, the sources of the cyclic damage along the printing direction should be accurately identified and resolved. Overcoming this cyclic damage will have a significant impact on improving the mechanical performance of the sample.

For SiC, the feedstock should be modified with a technique such as spray-drying or another technique to produce a spherical powder with good flowability. In addition, a suitable post-processing technique should be considered in order to improve mechanical performance.

Lastly, the packing density of the powder bed should be increased by optimizing the particle size distribution of the feedstock using particle packing models; this applies to both alumina and SiC.

REFERENCES

1. Valášková, M. (2015). Clays, clay minerals and cordierite ceramics - a review. *Ceramics – Silikáty* 59 (4) 331-340.

2. Langer, J., Hoffmann, M. J., and Guillon, O. (2009). Direct comparison between hot pressing and electric field-assisted sintering of submicron alumina. *Acta Materialia*, 57(18), 5454-5465. https://doi.org/10.1016/j.actamat.2009.07.043

3. Canakci, A., and Varol, T. (2014). Microstructure and properties of AA7075/Al–SiC composites fabricated using powder metallurgy and hot pressing. *Powder Technology*, 268, 72-79. https://doi.org/10.1016/j.powtec.2014.08.016

4. Deckers, J., Shahzad, K., Vleugels, J., and Kruth, J. P. (2012). Isostatic pressing assisted indirect selective laser sintering of alumina components. *Rapid Prototyping Journal*, 18(5), 409-419. https://doi.org/10.1108/13552541211250409

5. Dong, S., Katoh, Y., and Kohyama, A. (2003). Preparation of SiC/SiC Composites by Hot Pressing, Using Tyranno-SA Fiber as Reinforcement. *Journal of the American Ceramic Society*, 86(1), 26-32. https://doi.org/10.1111/j.1151-2916.2003.tb03272.x

6. Rezaie, A., Fahrenholtz, W. G., and Hilmas, G. E. (2007). Effect of hot-pressing time and temperature on the microstructure and mechanical properties of ZrB2–SiC. *Journal of Materials Science*, 42(8), 2735-2744. https://doi.org/10.1007/s10853-006-1274-2

7. Yang, W. S., Fuso, L., Biamino, S., Vasquez, D., Bolivar, C. V., Fino, P., and Badini, C. (2012). Fabrication of short carbon fibre reinforced SiC multilayer composites by tape casting. *Ceramics International*, 38(2), 1011-1018. https://doi.org/10.1016/j.ceramint.2011.08.024

8. Menzler, N. H., Tietz, F., Uhlenbruck, S., Buchkremer, H. P., and Stöver, D. (2010). Materials and manufacturing technologies for solid oxide fuel cells. *Journal of Materials Science*, 45(12), 3109-3135. https://doi.org/10.1007/s10853-010-4279-9

9. Jang, I., and Kelsall, G. H. (2022). Fabrication of 3D NiO-YSZ structures for enhanced performance of solid oxide fuel cells and electrolysers. *Electrochemistry Communications*, 137, 107260. https://doi.org/10.1016/j.elecom.2022.107260

10. Internet: ISO/ASTM 52900:2021 Additive manufacturing — General principles — Fundamentals and vocabulary. URL: https://www.iso.org/standard/74514.html, retrieved 11 April 2020.

11. Hull, Charles W. (2015). The birth of 3D printing. *Research-Technology Management*, 58(6), 25-30. https://doi.org/10.5437/08956308X5806067

12. Azlin, M. N. M., Ilyas, R. A., Zuhri, M. Y. M., Sapuan, S. M., Harussani, M. M., Sharma, S., Afiqah, A. N. (2022). 3D Printing and Shaping Polymers, Composites, and Nanocomposites: A Review. *Polymers*, 14(1), 180. https://doi.org/10.3390/polym14010180.

13. Sturm, L. D., Williams, C. B., Camelio, J. A., White, J., and Parker, R. (2017). Cyber-physical vulnerabilities in additive manufacturing systems: A case study attack on the .STL file with human subjects. *Journal of Manufacturing Systems*, 44, 154-164. https://doi.org/10.1016/j.jmsy.2017.05.007

14. Attaran, M. (2017). The rise of 3-D printing: The advantages of additive manufacturing over traditional manufacturing. *Business Horizons*, 60(5), 677-688. https://doi.org/10.1016/j.bushor.2017.05.011.

15. Gong, X., Anderson, T. and Chou, K. (2012). *Review on powder-based electron beam additive manufacturing technology.* International Symposium on Flexible Automation, 45110, 507-515. https://doi.org/10.1115/ISFA2012-7256

16. Lemu, H.G. (2018). On opportunities and limitations of additive manufacturing technology for industry 4.0 era. *International Workshop of Advanced Manufacturing and Automation*, 484, 106-113. https://doi.org/10.1007/978-981-13-2375-1_15

17. Lopez Taborda, L. L., Maury, H., and Pacheco, J. (2021). Design for additive manufacturing: a comprehensive review of the tendencies and limitations of methodologies. *Rapid Prototyping Journal*, 27(5), 918-966. https://doi.org/10.1108/RPJ-11-2019-0296.

18. Internet: Manufacturing REPORT. (2022). Which Additive Manufacturing Process Is Right for You? URL: https://manufacturing.report/articles/which-additive-manufacturing-process-is-right-for-you, retrieved on 16 July 2021.

19. Guo, N., and Leu, M. C. (2013). Additive manufacturing: technology, applications and research needs. *Frontiers of Mechanical Engineering*, 8(3), 215-243. https://doi.org/10.1007/s11465-013-0248-8.

20. Grossin, D., Montón, A., Navarrete-Segado, P., Özmen, E., Urruth, G., Maury, F., … Bertrand, G. (2021). A review of additive manufacturing of ceramics by powder bed selective laser processing (sintering / melting): Calcium Phosphate, Silicon Carbide, Zirconia, Alumina, and their composites. *Open Ceramics*, 100073. https://doi.org/10.1016/j.oceram.2021.100073.

21. Zocca, A., Colombo, P., Gomes, C. M., and Günster, J. (2015). Additive Manufacturing of Ceramics: Issues, Potentialities, and Opportunities. *Journal of the American Ceramic Society*, 98(7), 1983-2001. https://doi.org/10.1111/jace.13700

22. Dev Singh, D., Mahender, T., and Raji Reddy, A. (2021). Powder bed fusion process: A brief review. *Materials Today: Proceedings*, 46, 350-355. https://doi.org/10.1016/j.matpr.2020.08.415.

23. Sachs, E., Cima, M., Williams, P., Brancazio, D., and Cornie, J. (1992). Three-Dimensional Printing: Rapid Tooling and Prototypes Directly from a CAD Model. *Journal of Engineering for Industry*, 114(4), 481-488. https://doi.org/10.1115/1.2900701.

24. Parupelli, S. K., and Desai, S. (2019). A Comprehensive Review of Additive Manufacturing (3D Printing): Processes, Applications and Future Potential. *American Journal of Applied Sciences*, 16(8), 244-272. https://doi.org/10.3844/ajassp.2019.244.272.

25. Gonzalez, J. A. (2016). Characterization of ceramic components fabricated using binder jetting additive manufacturing technology. *Ceramics International*, 42(9), 10559-10564. https://doi.org/10.1016/j.ceramint.2016.03.079

26. Du, W., Ren, X., Ma, C. and Pei, Z. (2017), November. Binder jetting additive manufacturing of ceramics: A literature review. *ASME International Mechanical Engineering Congress and Exposition*, (58493). https://doi.org/10.1115/IMECE2017-70344

27. Du, W., Ren, X., Pei, Z., and Ma, C. (2020). Ceramic Binder Jetting Additive Manufacturing: A Literature Review on Density. *Journal of Manufacturing Science and Engineering*, 142(4). https://doi.org/10.1115/1.4046248.

28. Lv, X., Ye, F., Cheng, L., Fan, S., and Liu, Y. (2019). Binder jetting of ceramics: Powders, binders, printing parameters, equipment, and post-treatment. *Ceramics International*, 45(10), 12609-12624. https://doi.org/10.1016/j.ceramint.2019.04.012.

29. Chen, Q., Juste, E., Lasgorceix, M., Petit, F., and Leriche, A. (2022). Binder jetting process with ceramic powders: Influence of powder properties and printing parameters. *Open Ceramics*, 9, 100218. https://doi.org/10.1016/j.oceram.2022.100218.

30. Ziaee, M., and Crane, N. B. (2019). Binder jetting: A review of process, materials, and methods. *Additive Manufacturing*, 28, 781-801. https://doi.org/10.1016/j.addma.2019.05.031.

31. Mohamed, O. A., Masood, S. H., and Bhowmik, J. L. (2015). Optimization of fused deposition modeling process parameters: a review of current research and future prospects. *Advances in Manufacturing*, 3(1), 42-53. https://doi.org/10.1007/s40436-014-0097-7

32. Bernard, A., and Fischer, A. (2002). New Trends in Rapid Product Development. *CIRP Annals*, 51(2), 635-652. https://doi.org/10.1016/S0007-8506(07)61704-1.

33. Internet: Microfluidics by Additive Manufacturing for Wearable Biosensors: A Review. (2022). URL: https://www.mdpi.com/1424-8220/20/15/4236/htm, retrived on 24 June 2021.

34. Chaudhary, R. P., Parameswaran, C., Idrees, M., Rasaki, A. S., Liu, C., Chen, Z., and Colombo, P. (2022). Additive manufacturing of polymer-derived ceramics: Materials, technologies, properties, and potential applications. *Progress in Materials Science*, 128, 100969. https://doi.org/10.1016/j.pmatsci.2022.100969.

35. Colombo, P., Mera, G., Riedel, R., and Sorarù, G. D. (2010). Polymer-Derived Ceramics: 40 Years of Research and Innovation in Advanced Ceramics. *Journal of the American Ceramic Society*, 93(7), 1805-1837. https://doi.org/10.1111/j.1551-2916.2010.03876.x.

36. Smirnov, A., Podrabinnik, P. A., Babushkin, N. N., Kuznetsova, E. V., Pristinskiy, Y. O., and Khmyrov, R. S. (2022). Development of Al2O3 and PLA ceramic-polymer filament for 3D printing by fused deposition modelling method. *AIP Conference Proceedings*, 2467(1), 020047. https://doi.org/10.1063/5.0092881.

37. Internet: Alumina Zetamix Filament. URL: https://zetamix.fr/en/produit/zetamix-alumina-filament/, retrieved on 23 June 2021.

38. Hwa, L.C., Rajoo, S., Noor, A.M., Ahmad, N., Uday, M.B. (2019). 3D printing of ceramics: A review. *Journal of the European Ceramic Society*, 39(4), 661-687. https://doi.org/10.1016/j.jeurceramsoc.2018.11.013.

39. Rasaki, S. A., Xiong, D., Xiong, S., Su, F., Idrees, M., and Chen, Z. (2021). Photopolymerization-based additive manufacturing of ceramics: A systematic review. *Journal of Advanced Ceramics*, 10(3), 442-471. https://doi.org/10.1007/s40145-021-0468-z.

40. Zhang, F., Li, Z., Xu, M., Wang, S., Li, N., and Yang, J. (2022). A review of 3D printed porous ceramics. *Journal of the European Ceramic Society*, 42(8), 3351-3373. https://doi.org/10.1016/j.jeurceramsoc.2022.02.039.

41. Tuan Rahim, T. N. A., Abdullah, A., Md Akil, H., Mohamad, D., and Rajion, Z. (2017). The improvement of mechanical and thermal properties of polyamide 12 3D printed parts by fused deposition modelling. *Express Polymer Letters*, 11, 963-982. https://doi.org/10.3144/expresspolymlett.2017.92

42. Cesarano, J. (1998). A Review of Robocasting Technology. *MRS Online Proceedings Library (OPL)*, 542. https://doi.org/10.1557/PROC-542-133.

43. Solís Pinargote, N. W., Smirnov, A., Peretyagin, N., Seleznev, A., and Peretyagin, P. (2020). Direct Ink Writing Technology (3D Printing) of Graphene-Based Ceramic Nanocomposites: A Review. Nanomaterials, 10(7), 1300. https://doi.org/10.3390/nano10071300.

44. Saied, M. A. (2009). Effect of glass joins on performance of layered dental ceramic systems (Ph.D.). University of Maryland, College Park, United States -- Maryland. https://www.proquest.com/docview/304921185/abstract/332C882EB694AD6PQ/1.

45. Franco, J., Hunger, P., Launey, M. E., Tomsia, A. P., and Saiz, E. (2010). Direct write assembly of calcium phosphate scaffolds using a water-based hydrogel. *Acta Biomaterialia*, 6(1), 218-228. https://doi.org/10.1016/j.actbio.2009.06.031.

46. García-Tuñon, E., Barg, S., Franco, J., Bell, R., Eslava, S., D'Elia, E.,Saiz, E. (2015). Printing in Three Dimensions with Graphene. *Advanced Materials*, 27(10), 1688-1693. https://doi.org/10.1002/adma.201405046.

47. He, G., Hirschfeld, D. A., Cesarano III, J., and Stuecker, J. N. (2001). *Robocasting and Coifing of Functionally Graded Si3N4-W Materials*. 25th Annual Conference on Composites, Advanced Ceramics, Materials, and Structures: B: Ceramic Engineering and Science Proceedings- John Wiley and Sons, 119-12). https://doi.org/10.1002/9780470294703.ch15.

48. Balani, S. B., Ghaffar, S. H., Chougan, M., Pei, E., and Şahin, E. (2021). Processes and materials used for direct writing technologies: A review. *Results in Engineering*, 11, 100257. https://doi.org/10.1016/j.rineng.2021.100257.

49. Internet: Robocasting - Direct Ink Writing. (2022), URL: https://euroceram.org/en/eu/robocasting-direct-ink-writing, retrieved on 23 September 2021.

50. Cesarano, J. I., King, B. H., and Denham, H. B. (1998). Recent developments in robocasting of ceramics and multilateral deposition (No. SAND-98-2195C; CONF-980826). *Sandia National Lab. (SNL-NM), Albuquerque, NM (United States)*. https://www.osti.gov/biblio/290950.

51. Hardin, J. O., Ober, T. J., Valentine, A. D., & Lewis, J. A. (2015). Microfluidic printheads for multimaterial 3D printing of viscoelastic inks. *Advanced materials*, 27(21), 3279-3284.

52. Gratson, G. M., Xu, M., and Lewis, J. A. (2004). Direct writing of three-dimensional webs. *Nature*, 428(6981), 386-386. https://doi.org/10.1038/428386a.

53. Melchels, F. P. W., Feijen, J., and Grijpma, D. W. (2010). A review on stereolithography and its applications in biomedical engineering. *Biomaterials*, 31(24), 6121-6130. https://doi.org/10.1016/j.biomaterials.2010.04.050.

54. Lü, L., Fuh, J. Y. H., and Wong, Y. S. (2001). Fundamentals of Laser-Lithography Processes. *Laser-Induced Materials and Processes for Rapid Prototyping. Boston, MA: Springer US*, 9-38 https://doi.org/10.1007/978-1-4615-1469-5_2.

55. Allen, B. G., and Halloran, J. W. (1997). Stereolithography of ceramic suspensions. *Rapid Prototyping Journal*, 3(2), 61-65. https://doi.org/10.1108/13552549710176680

56. Schwentenwein, M., and Homa, J. (2015). Additive Manufacturing of Dense Alumina Ceramics. *International Journal of Applied Ceramic Technology*, 12(1), 1-7. https://doi.org/10.1111/ijac.12319.

57. Schweiger, J., Bomze, D., and Schwentenwein, M. (2019). 3D Printing of Zirconia–What is the Future? *Current Oral Health Reports*, 6(4), 339-343. https://doi.org/10.1007/s40496-019-00243-4.

58. Altun, A. A., Prochaska, T., Konegger, T., and Schwentenwein, M. (2020). Dense, Strong, and Precise Silicon Nitride-Based Ceramic Parts by Lithography-Based Ceramic Manufacturing. *Applied Sciences*, 10(3), 996. https://doi.org/10.3390/app10030996.

59. Internet: 3D Print ceramic pieces on your SLA 3D printer. (2018). URL:. https://www.3dnatives.com/en/ceramic-resin300520184/, retrived on 23 July 2021.

60. Gmeiner, R., Mitteramskogler, G., Stampfl, J., & Boccaccini, A. R. (2015). Stereolithographic ceramic manufacturing of high strength bioactive glass. *International Journal of Applied Ceramic Technology*, 12(1), 38-45.

61. Choi, J.-W., Kim, H.-C., and Wicker, R. (2011). Multi-material stereolithography. *Journal of Materials Processing Technology*, 211(3), 318-328. https://doi.org/10.1016/j.jmatprotec.2010.10.003

62. Ding, G., He, R., Zhang, K., Xie, C., Wang, M., Yang, Y., and Fang, D. (2019). Stereolithography-based additive manufacturing of gray-colored SiC ceramic green body. *Journal of the American Ceramic Society*, 102(12), 7198-7209. https://doi.org/10.1111/jace.16648.

63. Nazemosadat, S. M., Foroozmehr, E., and Badrossamay, M. (2018). Preparation of alumina/polystyrene core-shell composite powder via phase inversion process for indirect selective laser sintering applications. *Ceramics International*, 44(1), 596-604. https://doi.org/10.1016/j.ceramint.2017.09.218.

64. Zhang, K., Liu, T., Liao, W., Zhang, C., Yan, Y., and Du, D. (2018). Influence of laser parameters on the surface morphology of slurry-based Al2O3 parts produced through selective laser melting. *Rapid Prototyping Journal*, 24(2), 333-341. https://doi.org/10.1108/RPJ-12-2016-0201.

65. Montón, A., Abdelmoula, M., Küçüktürk, G., Maury, F., Grossin, D., and Ferrato, M. (2021). Experimental and numerical study for direct powder bed selective laser processing (sintering/melting) of silicon carbide ceramic. *Materials Research Express*, 8(4), 045603. https://doi.org/10.1088/2053-1591/abf6fc.

66. Abdelmoula, M., Zarazaga, A. M., Küçüktürk, G., Maury, F., Grossin, D., and Ferrato, M. (2022). Scanning Strategy Investigation for Direct Powder Bed Selective Laser Processing of Silicon Carbide Ceramic. *Applied Sciences*, 12(2), 788. https://doi.org/10.3390/app12020788.

67. Montón Zarazaga, A., Abdelmoula, M., Küçüktürk, G., Maury, F., Ferrato, M., and Grossin, D. (2022). Process parameters investigation for direct powder bed selective laser processing of silicon carbide parts. *Progress in Additive Manufacturing*, 1-16, https://doi.org/10.1007/s40964-022-00305-7.

68. Sing, S. L., Yeong, W. Y., Wiria, F. E., Tay, B. Y., Zhao, Z., Zhao, L.,Yang, S. (2017). Direct selective laser sintering and melting of ceramics: A review. *Rapid Prototyping Journal*, 23(3), 611-623. https://doi.org/10.1108/RPJ-11-2015-0178.

69. Internet: Additive manufacturing of ceramics. (2022). URL: https://www.mtm.kuleuven.be/onderzoek/siem/Ceramics/research/additive-manufacturing/ceramics, retrived on 12 July 2021.

70. Ferrage, L., Bertrand, G., and Lenormand, P. (2018). Dense yttria-stabilized zirconia obtained by direct selective laser sintering. *Additive Manufacturing*, 21, 472-478. https://doi.org/10.1016/j.addma.2018.02.005.

71. Zou, Y., Li, C.-H., Liu, J.-A., Wu, J.-M., Hu, L., Gui, R.-F., and Shi, Y.-S. (2019). Towards fabrication of high-performance Al2O3 ceramics by indirect selective laser sintering based on particle packing optimization. *Ceramics International*, 45(10), 12654-12662. https://doi.org/10.1016/j.ceramint.2019.02.203.

72. Liu, R.-Z., Chen, P., Wu, J.-M., Chen, S., Chen, A.-N., Chen, J.-Y., Li, C.H. (2018). Effects of B4C addition on the microstructure and properties of porous alumina ceramics fabricated by direct selective laser sintering. *Ceramics International*, 44(16), 19678-19685. https://doi.org/10.1016/j.ceramint.2018.07.220.

73. Qiu, Y.-D., Wu, J.-M., Chen, A.-N., Chen, P., Yang, Y., Liu, R.-Z., Li, C.-H. (2020). Balling phenomenon and cracks in alumina ceramics prepared by direct selective laser melting assisted with pressure treatment. *Ceramics International*, 46(9), 13854-13861. https://doi.org/10.1016/j.ceramint.2020.02.178.

74. Juste, E., Petit, F., Lardot, V., and Cambier, F. (2014). Shaping of ceramic parts by selective laser melting of powder bed. Journal of Materials Research, 29(17), 2086-2094. https://doi.org/DOI: 10.1557/jmr.2014.127.

75. Sachs, E., Cima, M., and Cornie, J. (1990). Three-Dimensional Printing: Rapid Tooling and Prototypes Directly from a CAD Model. *CIRP Annals*, 39(1), 201-204. https://doi.org/10.1016/S0007-8506(07)61035-X.

76. Marcus, H. L., Beaman, J. J., Barlow, J. W., & Bourell, D. L. (1990). Solid freeform fabrication-powder processing. *American Ceramic Society Bulletin*, 69(6), 1030-1031.

77. Yves-Christian, H., Jan, W., Wilhelm, M., Konrad, W., and Reinhart, P. (2010). Net shaped high performance oxide ceramic parts by selective laser melting. *Physics Procedia*, 5, 587-594. https://doi.org/10.1016/j.phpro.2010.08.086.

78. Verga, F., Borlaf, M., Conti, L., Florio, K., Vetterli, M., Graule, T., Wegener, K. (2020). Laser-based powder bed fusion of alumina toughened zirconia. *Additive Manufacturing*, 31, 100959. https://doi.org/10.1016/j.addma.2019.100959.

79. Navarrete-Segado, P., Frances, C., Grossin, D., and Tourbin, M. (2022). Tailoring hydroxyapatite microspheres by spray-drying for powder bed fusion feedstock. *Powder Technology*, 398, 117116. https://doi.org/10.1016/j.powtec.2022.117116.

80. Lv, X., Ye, F., Cheng, L., Fan, S., and Liu, Y. (2019). Binder jetting of ceramics: Powders, binders, printing parameters, equipment, and post-treatment. *Ceramics International*, 45(10), 12609-12624. https://doi.org/10.1016/j.ceramint.2019.04.012.

81. Du, W., Ren, X., Ma, C., and Pei, Z. (2019). Ceramic binder jetting additive manufacturing: Particle coating for increasing powder sinterability and part strength. *Materials Letters*, 234, 327-330. https://doi.org/10.1016/j.matlet.2018.09.118.

82. Gonzalez, J. A., Mireles, J., Lin, Y., & Wicker, R. B. (2016). Characterization of ceramic components fabricated using binder jetting additive manufacturing technology. *Ceramics International*, 42(9), 10559-10564.

83. Kunchala, P., and Kappagantula, K. (2018). 3D printing high density ceramics using binder jetting with nanoparticle densifiers. *Materials and Design*, 155, 443-450. https://doi.org/10.1016/j.matdes.2018.06.009.

84. Moghadasi, M., Du, W., Li, M., Pei, Z., and Ma, C. (2020). Ceramic binder jetting additive manufacturing: Effects of particle size on feedstock powder and final part properties. *Ceramics International*, 46(10, Part B), 16966-16972. https://doi.org/10.1016/j.ceramint.2020.03.280.

85. del-Mazo-Barbara, L., and Ginebra, M.-P. (2021). Rheological characterization of ceramic inks for 3D direct ink writing: A review. *Journal of the European Ceramic Society*, 41(16), 18-33. https://doi.org/10.1016/j.jeurceramsoc.2021.08.031.

86. Conzelmann, N. A., Gorjan, L., Sarraf, F., Poulikakos, L. D., Partl, M. N., Müller, C. R., and Clemens, F. J. (2020). Manufacturing complex Al 2 O 3 ceramic structures using consumer-grade fused deposition modelling printers. *Rapid Prototyping Journal*, 26(6), 1035-1048. https://doi.org/10.1108/RPJ-05-2019-0133.

87. Nevado, P., Lopera, A., Bezzon, V., Fulla, M. R., Palacio, J., Zaghete, M. A., Garcia, C. (2020). Preparation and in vitro evaluation of PLA/biphasic calcium phosphate filaments used for fused deposition modelling of scaffolds. *Materials Science and Engineering: C*, 114, 111013. https://doi.org/10.1016/j.msec.2020.111013.

88. Abdullah, A. M., Rahim, T. N. A. T., Hamad, W. N. F. W., Mohamad, D., Akil, H. M., and Rajion, Z. A. (2018). Mechanical and cytotoxicity properties of hybrid ceramics filled polyamide 12 filament feedstock for craniofacial bone reconstruction via fused deposition modelling. *Dental Materials*, 34(11), 309-316. https://doi.org/10.1016/j.dental.2018.09.006.

89. Abdullah, A. M., Rahim, T. N. A. T., Mohamad, D., Akil, H. M., and Rajion, Z. A. (2017). Mechanical and physical properties of highly ZrO2 /β-TCP filled polyamide 12 prepared via fused deposition modelling (FDM) 3D printer for potential craniofacial reconstruction application. *Materials Letters*, 189, 307-309. https://doi.org/10.1016/j.matlet.2016.11.052.

90. Singh, N., Singh, R., and Ahuja, I. P. S. (2018). On Development of Functionally Graded Material Through Fused Deposition Modelling Assisted Investment Casting from Al2O3/SiC Reinforced Waste Low Density Polyethylene. *Transactions of the Indian Institute of Metals*, 71(10), 2479-2485. https://doi.org/10.1007/s12666-018-1378-9.

91. Li, K., and Zhao, Z. (2017). The effect of the surfactants on the formulation of UV-curable SLA alumina suspension. *Ceramics International*, 43(6), 4761-4767. https://doi.org/10.1016/j.ceramint.2016.11.143.

92. Liu, X., Zou, B., Xing, H., and Huang, C. (2020). The preparation of ZrO2-Al2O3 composite ceramic by SLA-3D printing and sintering processing. *Ceramics International*, 46(1), 937-944. https://doi.org/10.1016/j.ceramint.2019.09.054.

93. Revilla-León, M., Methani, M. M., Morton, D., and Zandinejad, A. (2020). Internal and marginal discrepancies associated with stereolithography (SLA) additively manufactured zirconia crowns. The *Journal of Prosthetic Dentistry*, 124(6), 730-737. https://doi.org/10.1016/j.prosdent.2019.09.018.

94. Fu, X., Zou, B., Xing, H., Li, L., Li, Y., and Wang, X. (2019). Effect of printing strategies on forming accuracy and mechanical properties of ZrO2 parts fabricated by SLA technology. *Ceramics International*, 45(14), 17630-17637. https://doi.org/10.1016/j.ceramint.2019.05.328.

95. Cano-Vicent, A., Tambuwala, M. M., Hassan, Sk. S., Barh, D., Aljabali, A. A. A., Birkett, M.,Serrano-Aroca, Á. (2021). Fused deposition modelling: Current status, methodology, applications, and future prospects. *Additive Manufacturing*, 47, 102378. https://doi.org/10.1016/j.addma.2021.102378.

96. Shahzad, A., and Lazoglu, I. (2021). Direct ink writing (DIW) of structural and functional ceramics: Recent achievements and future challenges. *Composites Part B: Engineering*, 225, 109249. https://doi.org/10.1016/j.compositesb.2021.109249.

97. Dehurtevent, M., Robberecht, L., Hornez, J.-C., Thuault, A., Deveaux, E., and Béhin, P. (2017). Stereolithography: A new method for processing dental ceramics by additive computer-aided manufacturing. *Dental Materials*, 33(5), 477-485. https://doi.org/10.1016/j.dental.2017.01.018.

98. Yves-Christian, H., Jan, W., Wilhelm, M., Konrad, W., and Reinhart, P. (2010). Net shaped high performance oxide ceramic parts by Selective Laser Melting. *Physics Procedia*, 5(2), 587-594. https://doi.org/10.1016/j.phpro.2010.08.086.

99. Wilkes, J., Hagedorn, Y. C., Meiners, W., and Wissenbach, K. (2013). Additive manufacturing of ZrO2-Al2O3 ceramic components by selective laser melting. *Rapid Prototyping Journal*, 19(1), 51-57. https://doi.org/10.1108/13552541311292736.

100. Liu, Q., Danlos, Y., Song, B., Zhang, B., Yin, S., and Liao, H. (2015). Effect of high-temperature preheating on the selective laser melting of yttria-stabilized zirconia ceramic. *Journal of Materials Processing Technology*, 222, 61-74. https://doi.org/10.1016/j.jmatprotec.2015.02.036.

101. Khmyrov, R. S., Protasov, C. E., Grigoriev, S. N., and Gusarov, A. V. (2016). Crack-free selective laser melting of silica glass: single beads and monolayers on the substrate of the same material. International *Journal of Advanced Manufacturing Technology*, 85(5-8), 1461-1469. https://doi.org/10.1007/s00170-015-8051-9.

102. Zheng, Y., Zhang, K., Liu, T. T., Liao, W. H., Zhang, C. D., and Shao, H. (2019). Cracks of alumina ceramics by selective laser melting. *Ceramics International*, 45(1), 175-184. https://doi.org/10.1016/j.ceramint.2018.09.149.

103. Gan, M. X., and Wong, C. H. (2017). Properties of selective laser melted spodumene glass-ceramic. *Journal of the European Ceramic Society*, 37(13), 4147-4154. https://doi.org/10.1016/j.jeurceramsoc.2017.04.060.

104. Song, B., Dong, S., Liao, H., and Coddet, C. (2012). Process parameter selection for selective laser melting of Ti6Al4V based on temperature distribution simulation and experimental sintering. *International Journal of Advanced Manufacturing Technology*, 61(9-12), 967-974. https://doi.org/10.1007/s00170-011-3776-6.

105. Pham, D. T., Dimov, S. S., and Petkov, P. V. (2007). Laser milling of ceramic components. *International Journal of Machine Tools and Manufacture*, 47(3-4), 618-626. https://doi.org/10.1016/j.ijmachtools.2006.05.002.

106. Ramesh Kumar, C., and Nagarajan, G. (2012). Performance and emission characteristics of a low heat rejection spark ignited engine fuelled with E20. *Journal of Mechanical Science and Technology*, 26(4), 1241-1250. https://doi.org/10.1007/s12206-012-0206-0.

107. Chemistry of alumina, reactions in aqueous solution and its application in water treatment. (2004). *Advances in Colloid and Interface Science*, 110(1-2), 19-48. https://doi.org/10.1016/j.cis.2004.02.002.

108. Khashaba, U., Othman, R., and Najjar, I. M. (2020). Development and characterization of structural adhesives for aerospace industry with alumina nanoparticles under shear and thermo-mechanical impact loads. *Proceedings of the Institution of Mechanical Engineers, Part G: Journal of Aerospace Engineering*, 234(2), 490-507. https://doi.org/10.1177/0954410019875557.

109. Freihofer, G., Newkirk, A. V., Gupta, A., Seal, S., and Raghavan, S. (s. f.). *Optical Stress-sensing Alumina Nanocomposite Coatings for Aerospace Structures*. 55th AIAA/ASME/ASCE/AHS/ASC Structures, Structural Dynamics, and Materials Conference. American Institute of Aeronautics and Astronautics. https://doi.org/10.2514/6.2014-0159.

110. Burger, W., and Kiefer, G. (2021). Alumina, Zirconia and Their Composite Ceramics with Properties Tailored for Medical Applications. *Journal of Composites Science*, 5(11), 306. https://doi.org/10.3390/jcs5110306.

111. Benzaid, R., Chevalier, J., Saâdaoui, M., Fantozzi, G., Nawa, M., Diaz, L. A., and Torrecillas, R. (2008). Fracture toughness, strength, and slow crack growth in a ceria stabilized zirconia–alumina nanocomposite for medical applications. *Biomaterials*, 29(27), 3636-3641. https://doi.org/10.1016/j.biomaterials.2008.05.021.

112. Liu, Q., Danlos, Y., Song, B., Zhang, B., Yin, S., and Liao, H. (2015). Effect of high-temperature preheating on the selective laser melting of yttria-stabilized zirconia ceramic. *Journal of Materials Processing Technology*, 222, 61-74. https://doi.org/10.1016/j.jmatprotec.2015.02.036.

113. Shishkovsky, I., Yadroitsev, I., Bertrand, Ph., and Smurov, I. (2007). Alumina–zirconium ceramics synthesis by selective laser sintering/melting. *Applied Surface Science*, 254(4), 966-970. https://doi.org/10.1016/j.apsusc.2007.09.001.

114. Fayed, E. M., Elmesalamy, A. S., Sobih, M., and Elshaer, Y. (2018). Characterization of direct selective laser sintering of alumina. *The International Journal of Advanced Manufacturing Technology*, 94(5-8), 2333-2341. https://doi.org/10.1007/s00170-017-0981-y.

115. Fan, Z., Lu, M., and Huang, H. (2018). Selective laser melting of alumina: A single track study. *Ceramics International*, 44(8), 9484-9493. https://doi.org/10.1016/j.ceramint.2018.02.166.

116. Zhang, K., Liu, T., Liao, W., Zhang, C., Zheng, Y., and Shao, H. (2018). *Simulation of the thermal behavior and analysis of solidification process during selective laser melting of alumina.* 2018 International Solid Freeform Fabrication Symposium. University of Texas at Austin. http://dx.doi.org/10.26153/tsw/17184

117. Chen, Q., Guillemot, G., Gandin, C.-A., and Bellet, M. (2017). Three-dimensional finite element thermomechanical modeling of additive manufacturing by selective laser melting for ceramic materials. *Additive Manufacturing*, 16, 124-137. https://doi.org/10.1016/j.addma.2017.02.005.

118. Sadler, L. Y., and Shamsuzzoha, M. (1997). Response of silicon carbide to high-intensity laser irradiation in a high-pressure inert gas atmosphere. *J. Mater. Res.*, 2(1), 147-160. https://doi.org/10.1557/JMR.1997.0022

119. Meyers, S. (2019), Additive Manufacturing of Technical Ceramics: Laser Sintering of Alumina and Silicon Carbide; Unpublished PhD thesis, KU Leuven-Faculty of Engineering Science: Leuven, Belgium 19-64.

120. Kimoto, T., & Cooper, J. A. (2014). Fundamentals of silicon carbide technology: growth, characterization, devices and applications. Singapore: John Wiley & Sons, 301-365.

121. Renotte, E., Bastin, C., Bernard, F., Bernat, A., Boitrel, Jm., Bougoin, M., Wolfs, F. (2019). *Full-SiC derotator optics for MET image: preliminary design and verification approach*. International Conference on Space Optics — ICSO 2018, 303. https://doi.org/10.1117/12.2536223.

122. Leray, C., Ferriere, A., Toutant, A., Olalde, G., Peroy, J.-Y., Chéreau, P., and Ferrato, M. (2017). *Design and proof of concept of an innovative very high temperature ceramic solar absorber*, AIP Conference Proceedings, 030032. https://doi.org/10.1063/1.4984375.

123. Kimoto, T., and Cooper, J. A. (2014). Fundamentals of silicon carbide technology: growth, characterization, devices and applications. *John Wiley and Sons*.

124. Daviau, K., and Lee, K. K. M. (2017). Decomposition of silicon carbide at high pressures and temperatures. *Physical Review B*, 96(17), 1-10. https://doi.org/10.1103/PhysRevB.96.174102.

125. Song, S., Gao, Z., Lu, B., Bao, C., Zheng, B., and Wang, L. (2020). Performance optimization of complicated structural SiC/Si composite ceramics prepared by selective laser sintering. *Ceramics International*, 46(1), 568-575. https://doi.org/10.1016/j.ceramint.2019.09.004.

126. Ghosh, S. K., and Saha, P. (2011). Crack and wear behavior of SiC particulate reinforced aluminum-based metal matrix composite fabricated by direct metal laser sintering process. *Materials and Design*, 32(1), 139-145. https://doi.org/10.1016/j.matdes.2010.06.020.

127. Hon, K. K. B., and Gill, T. J. (2003). Selective laser sintering of SiC/polyamide composites. *CIRP Annals - Manufacturing Technology*, 52(1), 173-176. https://doi.org/10.1016/S0007-8506(07)60558-7.

128. Xiong, B. W., Yu, H., Xu, Z. F., Yan, Q. S., Zheng, Y. H., Zhu, P. L., and Chen, S. N. (2013). Study on dual binders for fabricating SiC particulate preforms using selective laser sintering. *Composites Part B: Engineering*, 48, 129-133. https://doi.org/10.1016/j.compositesb.2012.09.092.

129. Christian Nelson, J., Vail, N. K., Barlow, J. W., Beaman, J. J., Bourell, D. L., and Marcus, H. L. (1995). Selective Laser Sintering of Polymer-Coated Silicon Carbide Powders. *Industrial and Engineering Chemistry Research*, 34(5), 1641-1651. https://doi.org/10.1021/ie00044a017.

130. Fu, H., Zhu, W., Xu, Z., Chen, P., Yan, C., Zhou, K., and Shi, Y. (2019). Effect of silicon addition on the microstructure, mechanical and thermal properties of Cf/SiC composite prepared via selective laser sintering. *Journal of Alloys and Compounds*, 792, 1045-1053. https://doi.org/10.1016/j.jallcom.2019.04.129.

131. Jin, L., Zhang, K., Xu, T., Zeng, T., and Cheng, S. (2018). The fabrication and mechanical properties of SiC/SiC composites prepared by SLS combined with PIP. *Ceramics International*, 44(17), 20992-20999. https://doi.org/10.1016/j.ceramint.2018.08.134.

132. Xiong, H., Xiong, B., Yu, H., Zhao, J., Zheng, Y., Luo, Y., Zhu, P. (2013). Effects of binders on dimensional accuracy and mechanical properties of SiC particulates preforms fabricated by selective laser sintering. *Composites Part B: Engineering*, 44(1), 480-483. https://doi.org/10.1016/j.compositesb.2012.04.003.

133. Birmingham, B. R., and Marcus, H. L. (1993). *Solid Freeform Fabrication of Silicon Carbide Shapes by Selective Laser Reaction Sintering*, International Solid Freeform Fabrication Symposium, http://hdl.handle.net/2152/65073.

134. Hon, K. K. B., and Gill, T. J. (2003). Selective Laser Sintering of SiC/Polyamide Composites. *CIRP Annals*, 52(1), 173-176. https://doi.org/10.1016/S0007-8506(07)60558-7.

135. W. Löschau, R. Lenk, S. Scharek, M. Teichgraber, S. Nowotny, and C.Richter. (1999). Prototyping of Complex-Shaped Parts and Tools of Si/SiC-Ceramics, *Advances in science and technology*, 567-573. https://doi.org/10.1002/3527607293.ch24.

136. Meyers, S., De Leersnijder, L., Vleugels, J., and Kruth, J.P. (2018). Direct laser sintering of reaction bonded silicon carbide with low residual silicon content. *Journal of the European Ceramic Society*, 38(11), 3709-3717. https://doi.org/10.1016/j.jeurceramsoc.2018.04.055.

137. Meyers, S., Leersnijder, L. D., Vleugels, J., and Kruth, J.P. (2018). Increasing the Silicon Carbide Content in Laser Sintered Reaction Bonded Silicon Carbide, *Ceramic Transactions Series*, 207-215. https://doi.org/10.1002/9781119423829.ch18.

138. Regenfuss, P., Streek, A., Hartwig, L., Klötzer, S., Brabant, Th., Horn, M., Exner, H. (2007). *Principles of laser micro sintering. Rapid Prototyping Journal*, 13(4), 204-212. https://doi.org/10.1108/13552540710776151.

139. Streek, A., Regenfuss, P., Ullmann, F., Hartwig, L., Ebert, R., & Exner, H. (2006). *Processing of silicon carbide by laser micro sintering.* International Solid Freeform Fabrication Symposium. https://hdl.handle.net/2152/80123

140. Birmingham, B.R. and Marcus, H.L. (1993), *Solid freeform fabrication of silicon carbide shapes by selective laser reaction sintering (SLRS)*. International Solid Freeform Fabrication Symposium. http://hdl.handle.net/2152/65073

141. Meyers, S. (2019), *Additive Manufacturing of Technical Ceramics: Laser Sintering of Alumina and Silicon Carbide*; Unpublished PhD Thesis, KU Leuven-Faculty of Engineering Science, Leuven, Belgium, 39-65.

142. Groth, R., and Kauer, E. (1961). Absorption freier Ladungsträger in α-SiC-Kristallen, *physica status solidi (b)*, 1(5), 445-450. https://doi.org/10.1002/pssb.19610010504.

143. Moser, D., Beaman, J., and Fish, S. (2016). *Multi-Layer Computational Modeling of Selective Laser Sintering Processes.* Proceedings of the ASME 2014 International Mechanical Engineering Congress and Exposition IMECE2014, 1-11. https://doi.org/10.1115/IMECE2014-37535

144. Pham, D. T., Dimov, S. S., and Petkov, P. V. (2007). Laser milling of ceramic components. *International Journal of Machine Tools and Manufacture*, 47(3-4), 618-626. https://doi.org/10.1016/j.ijmachtools.2006.05.002

145. Internet: Touloukian, Y. S. (1966). Thermophysical properties of high temperature solid materials, URL: https://apps.dtic.mil/sti/citations/AD0649953, retrieved on 11 September 2021.

146. Tairov, Y. M., & Tsvetkov, V. F. (1978). Investigation of growth processes of ingots of silicon carbide single crystals. *Journal of crystal growth*, 43(2), 209-212..

147. Zhang, K., Liu, T., Liao, W., Zhang, C., Zheng, Y., and Shao, H. (2018). *Simulation of the Thermal Behavior and Analysis of Solidification Process During Selective Laser Melting Of Alumina*, International Solid Freeform Fabrication Symposium. University of Texas at Austin, 1808-1820. http://dx.doi.org/10.26153/tsw/17184

148. ANSYS Inc. (2013). ANSYS FLUENT Theory Guide. Release 18.2, 15317, 373-464. https://doi.org/10.1016/0140-3664(87)90311-2.

149. ANSYS Inc. U.S.A. (2009). Theory Reference for the Mechanical APDL and Mechanical Applications. *Knowledge Creation Diffusion Utilization*, 3304, 724-746. https://doi.org/10.1016/S0920-3796(88)80092-9

150. Abdou, M.A., Hadid, A.H., Raffray, A.R., Tillack, M.S., Iizuka, T., Gierszewski, P.J., Puigh, R.J., Sze, D.K. and Picologlou, B. (1988). Modeling, analysis and experiments for fusion nuclear technology. *Fusion Engineering and Design*, 6, 3-64. https://doi.org/10.1016/S0920-3796(88)80092-9

151. Internet: Ho, C. Y. (1977). Thermophysical and Electronic Properties Information Analysis Center (TEPIAC): A Continuing Systematic Program on Tables of Thermophysical and Electronic Properties of Materials. URL: https://apps.dtic.mil/sti/citations/ADA038198, retrieved on 23 October 2021.

152. Huang, Q., Bando, Y., Xu, X., Nishimura, T., Zhi, C., Tang, C., Golberg, D. (2007). Enhancing superplasticity of engineering ceramics by introducing BN nanotubes. *Nanotechnology*, 18(48). https://doi.org/10.1088/0957-4484/18/48/485706.

153. Michael Bauccio. (1994), ASM Engineered Materials Reference Book, ASM International Second Edition., Ohio: ASM International, 193-251.

154. Urruth, G., Maury, D., Voisin, C., Baylac, V., and Grossin, D. (2022). Powder bed selective laser processing (sintering / melting) of Yttrium Stabilized Zirconia using carbon-based material (TiC) as absorbance enhancer. *Journal of the European Ceramic Society*, 42(5), 2381-2390. https://doi.org/10.1016/j.jeurceramsoc.2021.12.042.

155. Juste, E., Petit, F., Lardot, V., and Cambier, F. (2014). Shaping of ceramic parts by selective laser melting of powder bed. *Journal of Materials Research*, 29(17), 2086-2094. https://doi.org/10.1557/jmr.2014.127

156. Navarrete-Segado, P., Frances, C., Tourbin, M., Tenailleau, C., Duployer, B., and Grossin, D. (2022). Powder bed selective laser process (sintering/melting) applied to tailored calcium phosphate-based powders. *Additive Manufacturing*, 50, 102542. https://doi.org/10.1016/j.addma.2021.102542

157. Navarrete-Segado, P., Frances, C., Grossin, D., and Tourbin, M. (2022). Tailoring hydroxyapatite microspheres by spray-drying for powder bed fusion feedstock. *Powder Technology*, 398, 117116. https://doi.org/10.1016/j.powtec.2022.117116

158. Wilkes, J., Hagedorn, Y., Meiners, W., and Wissenbach, K. (2013). Additive manufacturing of ZrO 2 -Al 2 O 3 ceramic components by selective laser melting. *Rapid Prototyping Journal*, 19(1), 51-57. https://doi.org/10.1108/13552541311292736

159. Sordelet, D. J., and Akinc, M. (1988). Sintering of Monosized, Spherical Yttria Powders. *Journal of the American Ceramic Society*, 71(12), 1148-1153. https://doi.org/10.1111/j.1151-2916.1988.tb05807.x

160. Naglieri, V., Gutknecht, D., Garnier, V., Palmero, P., Chevalier, J., and Montanaro, L. (2013). Optimized Slurries for Spray Drying: Different Approaches to Obtain Homogeneous and Deformable Alumina-Zirconia Granules. *Materials*, 6(11), 5382-5397. https://doi.org/10.3390/ma6115382

161. Kong, P. C., and Lau, Y. C. (1990). Plasma synthesis of ceramic powders. *Pure and Applied Chemistry*, 62(9), 1809-1816. https://doi.org/10.1351/pac199062091809

162. Boulos, M. (2004). Plasma power can make better powders. *Metal Powder Report*, 59(5), 16-21. https://doi.org/10.1016/S0026-0657(04)00153-5

163. Lukasiewicz, S. J. (1989). Spray-Drying Ceramic Powders. *Journal of the American Ceramic Society*, 72(4), 617-624. https://doi.org/10.1111/j.1151-2916.1989.tb06184.x

164. Faqih, A. M. N., Mehrotra, A., Hammond, S. V., and Muzzio, F. J. (2007). Effect of moisture and magnesium stearate concentration on flow properties of cohesive granular materials. *International Journal of Pharmaceutics*, 336(2), 338-345. https://doi.org/10.1016/j.ijpharm.2006.12.024

165. Hirschberg, C., Sun, C. C., Risbo, J., and Rantanen, J. (2019). Effects of Water on Powder Flowability of Diverse Powders Assessed by Complimentary Techniques. *Journal of Pharmaceutical Sciences*, 108(8), 2613-2620. https://doi.org/10.1016/j.xphs.2019.03.012

166. Santos, L. C. D., Condotta, R., & Ferreira, M. D. C. (2018). Flow properties of coarse and fine sugar powders. *Journal of Food Process Engineering*, 41(2), e12648.

167. Li, L. G., Zhuo, H. X., Zhu, J., and Kwan, A. K. H. (2019). Packing density of mortar containing polypropylene, carbon or basalt fibres under dry and wet conditions. *Powder Technology*, 342, 433-440. https://doi.org/10.1016/j.powtec.2018.10.005

168. Internet: Another choice for 3D printing in metal laser sintering: Renishaw, (2022). URL: https://www.makepartsfast.com/another-choice-for-3d-printing-in-metal-laser-sintering-renishaw/, retrieved on 15 September 2021.

169. Internet: ProX DMP 200. (2022). URL: https://support.3dsystems.com/s/prox-dmp-200?language=en_US, retrieved on 1 November 2021.

170. There's more than one way to measure powder particle size! (2003). *Metal Powder Report*, 58(11), 26-31. https://doi.org/10.1016/S0026-0657(03)01124-X

171. Campos, M., and Ferreira, M. (2013). A Comparative Analysis of the Flow Properties between Two Alumina-Based Dry Powders. *Advances in Materials Science and Engineering*, 2013, 1-7. https://doi.org/10.1155/2013/519846

172. Šimek, M., Grünwaldová, V., & Kratochvíl, B. (2017). Comparison of compression and material properties of differently shaped and sized paracetamols. *KONA Powder and Particle Journal*, 34, 197-206.

173. Internet: Ali, A. S. (2020). Application of Nanomaterials in Environmental Improvement. In (Ed.), Nanotechnology and the Environment. IntechOpen. URL: https://www.intechopen.com/chapters/71346, retrieved on 11 November 2021.

174. McCusker, L. B., Von Dreele, R. B., Cox, D. E., Louër, D., and Scardi, P. (1999). Rietveld refinement guidelines. *Journal of Applied Crystallography*, 32(1), 36-50. https://doi.org/10.1107/S0021889898009856

175. Hamdan, A., Sarhan, A. A. D., and Hamdi, M. (2012). An optimization method of the machining parameters in high-speed machining of stainless steel using coated carbide tool for best surface finish. *The International Journal of Advanced Manufacturing Technology*, 58(1), 81-91. https://doi.org/10.1007/s00170-011-3392-5

176. Sayuti, M., Sarhan, A. A. D., Fadzil, M., and Hamdi, M. (2012). Enhancement and verification of a machined surface quality for glass milling operation using CBN grinding tool—Taguchi approach. *The International Journal of Advanced Manufacturing Technology*, 60(9-12), 939-950. https://doi.org/10.1007/s00170-011-3657-z

177. Tanaydin, S. (1998). Robust Design and Analysis for Quality Engineering. *Technometrics*, 40(4), 348-349. https://doi.org/10.1080/00401706.1998.10485564

178. Ghani, J. A., Choudhury, I. A., and Hassan, H. H. (2004). Application of Taguchi method in the optimization of end milling parameters. *Journal of Materials Processing Technology*, 145(1), 84-92. https://doi.org/10.1016/S0924-0136(03)00865-3

179. Karan, S., and Gupta, S. P. S. (2005). Vickers microhardness studies on solution-grown single crystals of magnesium sulphate hepta-hydrate. *Materials Science and Engineering: A*, 398(1-2), 198-203. https://doi.org/10.1016/j.msea.2005.03.016

180. American Society for Testing and Materials. (2013). Standard Test Method for Monotonic Compressive Strength Testing of Continous Fiber-reinforced Advanced Ceramics with Solid Rectangular Cross-section Test Specimens at Ambient Temperatures. *ASTM International*. https://doi.org/10.1520/C1424-15R19.

181. Edith Wiria, F., Fai Leong, K., and Kai Chua, C. (2010). Modeling of powder particle heat transfer process in selective laser sintering for fabricating tissue engineering scaffolds. *Rapid Prototyping Journal*, 16(6), 400-410. https://doi.org/10.1108/13552541011083317

182. Zhang, H., and LeBlanc, S. (2018). Processing Parameters for Selective Laser Sintering or Melting of Oxide Ceramics. *Additive Manufacturing of High-performance Metals and Alloys - Modeling and Optimization. InTech*, 10, 1-44, https://doi.org/10.5772/intechopen.75832

183. Hwa, L. C., Rajoo, S., Noor, A. M., Ahmad, N., and Uday, M. B. (2017). Recent advances in 3D printing of porous ceramics: A review. *Current Opinion in Solid State and Materials Science*, 21(6), 323-347. https://doi.org/10.1016/j.cossms.2017.08.002

184. B09 Committee. Test Methods for Flow Rate of Metal Powders Using the Hall Flowmeter Funnel. *ASTM International*. https://doi.org/10.1520/B0213-13

185. Guerin, E., Tchoreloff, P., Leclerc, B., Tanguy, D., Deleuil, M., and Couarraze, G. (1999). Rheological characterization of pharmaceutical powders using tap testing, shear cell and mercury porosimeter. *International Journal of Pharmaceutics*, 189(1), 91-103. https://doi.org/10.1016/S0378-5173(99)00243-4

186. Harnby, N., Hawkins, A. E., and Vandame, D. (1987). The use of bulk density determination as a means of typifying the flow characteristics of loosely compacted powders under conditions of variable relative humidity. *Chemical Engineering Science*, 42(4), 879-888. https://doi.org/10.1016/0009-2509(87)80046-5

187. Internet: MXBAOHENG Flow Ability Tester Hall Flowmeter for Metal Powder: Tools and Home Improvement. (2022). URL: https://www.amazon.com/MXBAOHENG-Professional-Ability-Tester-Flowmeter/dp/B072Q66MD6, retrieved on December 8, 2021.

188. Internet: Iso Astm Mpif Hall Flowmeter As-300 By Aimsizer Buy Iso Astm Mpif Hall Flowmeter. (2022). URL: https://www.exportersindia.com/aimsizerscientific/iso-astm-mpif-hall-flowmeter-as-300-by-aimsizer-china-248547.htm, retrieved on December 8, 2021.

189. Juste, E., Petit, F., Lardot, V., and Cambier, F. (2014). Shaping of ceramic parts by selective laser melting of powder bed. *Journal of Materials Research*, 29(17), 2086-2094. https://doi.org/10.1557/jmr.2014.127

190. Enneti, R. K., Morgan, R., and Atre, S. V. (2018). Effect of process parameters on the Selective Laser Melting (SLM) of tungsten. *International Journal of Refractory Metals and Hard Materials*, 71, 315-319. https://doi.org/10.1016/j.ijrmhm.2017.11.035

191. Khorasani, A., Gibson, I., Awan, U. S., and Ghaderi, A. (2019). The effect of SLM process parameters on density, hardness, tensile strength and surface quality of Ti-6Al-4V. *Additive Manufacturing*, 25, 176-186. https://doi.org/10.1016/j.addma.2018.09.002

192. Bidare, P., Bitharas, I., Ward, R. M., Attallah, M. M., and Moore, A. J. (2018). Fluid and particle dynamics in laser powder bed fusion. *Acta Materialia*, 142, 107-120. https://doi.org/10.1016/j.actamat.2017.09.051

193. Scipioni Bertoli, U., Wolfer, A. J., Matthews, M. J., Delplanque, J.-P. R., and Schoenung, J. M. (2017). On the limitations of Volumetric Energy Density as a design parameter for Selective Laser Melting. *Materials and Design*, 113, 331-340. https://doi.org/10.1016/j.matdes.2016.10.037

194. Tonelli, L., Fortunato, A., and Ceschini, L. (2020). CoCr alloy processed by Selective Laser Melting (SLM): effect of Laser Energy Density on microstructure, surface morphology, and hardness. *Journal of Manufacturing Processes*, 52, 106-119. https://doi.org/10.1016/j.jmapro.2020.01.052

195. Xue, Y., Luo, Z., Han, S., Cai, D., and Liu, H. (2022). Mechanism analysis of laser coloring of Ti alloy by optical simulation. *Optik*, 254, 168650. https://doi.org/10.1016/j.ijleo.2022.168650

196. Abdo, B. M. A., Anwar, S., El-Tamimi, A. M., and Nasr, E. A. (2019). Experimental Analysis on the Influence and Optimization of μ-RUM Parameters in Machining Alumina Bioceramic. *Materials*, 12(4), 616. https://doi.org/10.3390/ma12040616

197. Muhammad, R., Kumar, B., and Chaskar, A. (2017). Synthesis, Characterization and Mechanical Properties of Alumina-Zirconia Nanocomposite Particles. *IOSR Journal of Mechanical and Civil Engineering*, 14(03), 40-46. https://doi.org/10.9790/1684-1403074046

198. Acharya, S., Bysakh, S., Parameswaran, V., and Kumar Mukhopadhyay, A. (2015). Deformation and failure of alumina under high strain rate compressive loading. *Ceramics International*, 41(5, Part B), 6793-6801. https://doi.org/10.1016/j.ceramint.2015.01.126.

199. Yablokova, G., Speirs, M., Van Humbeeck, J., Kruth, J.-P., Schrooten, J., Cloots, R., Luyten, J. (2015). Rheological behavior of β-Ti and NiTi powders produced by atomization for SLM production of open porous orthopedic implants. *Powder Technology*, 283, 199-209. https://doi.org/10.1016/j.powtec.2015.05.015

200. Spierings, A. B., Voegtlin, M., Bauer, T., and Wegener, K. (2016). Powder flowability characterisation methodology for powder-bed-based metal additive manufacturing. Progress in Additive Manufacturing, 1(1-2), 9-20. https://doi.org/10.1007/s40964-015-0001-4

201. Beakawi Al-Hashemi, H. M., and Baghabra Al-Amoudi, O. S. (2018). A review on the angle of repose of granular materials. *Powder Technology*, 330, 397-417. https://doi.org/10.1016/j.powtec.2018.02.003

202. Geldart, D., Abdullah, E. C., Hassanpour, A., Nwoke, L. C., and Wouters, I. (2006). Characterization of powder flowability using measurement of angle of repose. *China Particuology*, 4(3), 104-107. https://doi.org/10.1016/S1672-2515(07)60247-4

GAZİ GELECEKTİR...